GEMS & GEMOLOGY

SUMMER 2017
VOLUME LIII

THE QUARTERLY JOURNAL OF THE GEMOLOGICAL INSTITUTE OF AMERICA

Russia's Lomonosov Diamond Mine

Carbonado Diamond

PL Mapping of Optical Defects in HPHT Synthetics

Sapphire Inclusions Chart

GEMS & GEMOLOGY

gia.edu/gems-gemology

Subscriptions
Copies of the current issue may be purchased for $29.95 plus shipping. Subscriptions are $79.99 for one year (4 issues) in the U.S. and $99.99 elsewhere. Canadian subscribers should add GST. Discounts are available for group subscriptions, GIA alumni, and current GIA students. To purchase print subscriptions, visit store.gia.edu or contact Customer Service. For institutional rates, contact Customer Service.

Database Coverage
G&G is abstracted in Thomson Reuters products (Current Contents: Physical, Chemical & Earth Sciences and Science Citation Index—Expanded, including the Web of Knowledge) and other databases. For a complete list of sources abstracting *G&G*, go to gia.edu/gems-gemology, and click on "Publication Information."

Manuscript Submissions
Gems & Gemology, a peer-reviewed journal, welcomes the submission of articles on all aspects of the field. Please see the Author Guidelines at gia.edu/gems-gemology or contact the Managing Editor. Letters on articles published in *G&G* are also welcome. Please note that Field Reports, Lab Notes, Gem News International, Micro-World, and Charts are not peer-reviewed sections but do undergo technical and editorial review.

Gems & Gemology is published quarterly by the Gemological Institute of America, a nonprofit educational organization for the gem and jewelry industry.

Postmaster: Return undeliverable copies of *Gems & Gemology* to GIA, The Robert Mouawad Campus, 5345 Armada Drive, Carlsbad, CA 92008.

Our Canadian goods and service registration number is 126142892RT.

About the Cover

The lead article of this issue examines Russia's Lomonosov mine, which is located in a Proterozoic zone in the Baltic Shield craton. Proterozoic tectonic processes are thought to be responsible for the fancy-color diamonds found at this source. The distinctive purplish pink melee diamonds on the cover are part of Lomonsov's production. Photo by Robert Weldon/GIA, courtesy of Diarough.

Printing is by L+L Printers, Carlsbad, CA.
GIA World Headquarters The Robert Mouawad Campus 5345 Armada Drive Carlsbad, CA 92008 USA

ISSN 0016-626X

GEMS & GEMOLOGY

Summer 2017
VOLUME 53, No. 2

pg. 162

pg. 201

pg. 219

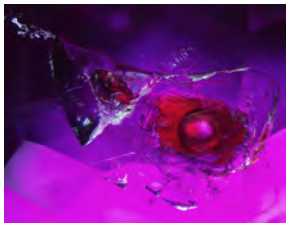

pg. 244

Editorial

143 **Visit Europe's First Diamond Mine**
Duncan Pay

Feature Articles

144 **Geology and Development of the Lomonosov Diamond Deposit, Northwestern Russia**
Karen V. Smit and Russell Shor
Reviews diamond discoveries at the Lomonosov deposit, as well as the geology of the Arkhangelsk kimberlite province.

168 **Carbonado Diamond: A Review of Properties and Origin**
Stephen E. Haggerty
Presents a detailed examination of about 800 samples of carbonado diamond from Brazil and the Central African Republic, including possible models for its genesis.

Notes and New Techniques

180 **Photoluminescence Mapping of Optical Defects in HPHT Synthetic Diamond**
Lorne C. Loudin
Demonstrates the importance of this method in identifying diamond treatments, based on the analysis of PL maps acquired from a brownish orange HPHT synthetic diamond.

190 **An Update on Tourmaline from Luc Yen, Vietnam**
Nguy Tuyet Nhung, Le Thi Thu Huong, Nguyen Thi Minh Thuyet, Tobias Häger, Nguyen Thi Le Quyen, and Tran Thi Duyen
Reviews the characteristics of tourmaline from pegmatites in the Luc Yen district of northern Vietnam.

204 **Characterization of Mg and Fe Contents in Nephrite Using Raman Spectroscopy**
Xiaoyan Feng, Yong Zhang, Taijin Lu, and Hui Zhang
Evaluates the usefulness of Raman spectroscopy in distinguishing the color varieties of nephrite based on the relative ratio of Mg to Fe concentration.

Charts

213 **Inclusions in Natural, Synthetic, and Treated Sapphire**
Nathan D. Renfro, John I. Koivula, Jonathan Muyal, Shane F. McClure, Kevin Schumacher, and James E. Shigley
Provides a visual guide to the internal features of natural, synthetic, and treated sapphires.

Field Reports

215 **Big Sky Country Sapphire: Visiting Montana's Alluvial Deposits**
Tao Hsu, Andrew Lucas, Robert E. Kane, Shane F. McClure, and Nathan D. Renfro
Documents a visit to the upper Missouri River and Rock Creek sapphire mining areas.

Regular Features

189 **Thank You, Donors**

228 **Lab Notes**
Concentric inclusions in diamond • Unusual fluorescence distribution in diamond • Cat's-eye kornerupine • Natural conch "rosebud" pearls • Partially hollow *Tridacna* blister pearls with shells attached • Atypical bead-cultured pearls with unusual nacre growth • Punsiri heat treatment on basalt-related blue sapphire • CVD synthetic imitating natural diamond • Parcel with one-third CVD synthetic melee • CVD synthetic overgrowth on natural diamond • HPHT synthetic diamond melee in jewelry

240 ***G&G* Micro-World**
Iridescence in aquamarine • Chlorapatite crystals in quartz • "Christmas tree" internal feature in diamond • Cosalite inclusions in quartz • Kyanite in diamond • Red oil treatment of Burmese ruby • Concentric "eyes" in sapphire • Quarterly crystal: Molybdenite phantoms in quartz

247 **Gem News International**
Ethiopian sapphire • Mexican gem-quality common opal • Raspberry-red garnet with black core • "Sango" akoya cultured pearl from Japan • Tektite with large fluid inclusion • Dyed freshwater cultured pearls imitating South Sea cultured pearls • "Starburst Stone" chatoyant glass • Titanium nitride coating of chalcedony bead necklace • Tri-color-change synthetic cubic zirconia • Errata

Visit Europe's **First Diamond Mine**

If variety is the spice of life, you'll appreciate our Summer 2017 issue. We offer six diverse articles featuring Russia's Lomonosov diamond mine, carbonado, photoluminescence (PL) mapping, Vietnamese tourmaline, nephrite color determination, and Montana sapphire. In addition, we provide a full-color wall chart of characteristic sapphire inclusions.

In August 2016, GIA's Dr. Karen Smit and Russell Shor were fortunate enough to visit Russia's Lomonosov diamond mine. This deposit is located about 60 miles (100 km) north of the historic port of Arkhangelsk, at a northerly latitude much like Canada's Diavik mine. In our lead article, they share insight into its geology, operations, and diamond production. Rooted in younger Proterozoic rocks—similar to Australia's off-craton Argyle lamproite pipe—Lomonosov's two kimberlite pipes produce a high proportion of small gem-quality diamonds, including a tiny amount of highly valuable fancy colors, including pink.

Named for its resemblance to charcoal, carbonado is one of the most intriguing diamond forms. In our second paper, Prof. Stephen Haggerty of Florida International University reviews his findings from a study of hundreds of examples from the only known sources: Brazil and the Central African Republic. He evaluates origin theories, including terrestrial and extraterrestrial models.

"Photoluminescence mapping shows great promise for detecting sophisticated diamond color treatments."

High-speed PL mapping can plot the distribution of optical centers in diamond. In his study, GIA research associate Lorne Loudin examines an unusual irradiated HPHT synthetic diamond of mixed type. He demonstrates a clear correlation between concentration of optical centers and diamond growth sectors, confirming that the technique shows great promise for detecting sophisticated diamond color treatments.

Luc Yen tourmaline is the subject of our next paper, from Nguy Tuyet Nhung of the Gemmological Center of the Vietnam Gemstone Association and a team of researchers. They survey the gem's distribution in the area, its geology, and suitability for use as gems, carvings, or mineral specimens. In our fifth paper, Xiaoyan Feng, senior engineer at NGTC in Beijing, and her research team use Raman spectroscopy to investigate and define color boundaries in nephrite from China and Taiwan.

Following the Winter 2016 emerald wall chart, we present the next in the series, which features some characteristic internal features of natural, treated, and synthetic sapphire. The chart is from the same team of inclusion specialists, led by GIA's Nathan Renfro and John Koivula.

In our final article, Tao Hsu and her coauthors survey alluvial sapphire production in the U.S. state of Montana. They note the prevalence of small-scale mining and the importance of gem tourism, but indicate that larger, mechanized operations are expanding production at these sources.

Our Lab Notes section offers entries on melee-size CVD synthetics in parcels and jewelry, CVD synthetic overgrowth on natural diamond, and non-nacreous "rosebud" conch pearls. Topics in our Micro-World section include kyanite in diamond and molybdenite "phantoms" in quartz, while GNI features new gem finds such as Ethiopian sapphires and common opal from Mexico.

Please enjoy the Summer edition!

Duncan Pay | Editor-in-Chief | dpay@gia.edu

Geology and Development of the Lomonosov Diamond Deposit, Northwestern Russia

Karen V. Smit and Russell Shor

The Siberian craton in Russia hosts many of the country's famous diamond mines. The Lomonosov mine, however, occurs within the boundaries of a different craton—the Baltic shield, most of which lies in Europe. Unlike many diamond mines in South Africa, Canada, and Siberia, the Lomonosov deposit is not in a stable Archean geologic setting. Similar to the Argyle diamond mine in Australia, Lomonosov is in a younger Proterozoic orogenic (or mountain-building) region. Fancy pink diamonds at both these localities likely relate to these Proterozoic tectonic processes. Along with other diamond mines in Proterozoic geologic regions, the Lomonosov deposit (and its fancy-color diamond inventory) demonstrates that the diamond potential of these regions should not be overlooked.

Russia has been a major diamond producer for more than half a century. Most of its diamond mines occur in the semi-autonomous Sakha Republic within the geological bounds of the Siberian craton. However, over the last 12 years, Alrosa, a public joint-stock company (with both government and private ownership) operating through its subsidiary Severalmaz, has started development and mining at the Lomonosov diamond deposit, the first Russian diamond mine outside the Siberian craton. This deposit occurs in the northwest of the country within the Baltic shield (part of the larger East European craton). Since this region is part of the European continent, Lomonosov is Europe's first diamond mine.

Alrosa's Lomonosov deposit comprises six kimberlites that form part of the Zolotitsa kimberlite field, itself part of the larger Arkhangelsk kimberlite province. Two of the six kimberlites—Arkhangelskaya and Karpinskogo I—are currently being mined. They are distinctive for their high percentage of gem-quality colorless goods as well as their production of fancy-color diamonds, especially pink and purple (figure 1).

See end of article for About the Authors and Acknowledgments.
Gems & Gemology, Vol. 53, No. 2, pp. 144–167,
http://dx.doi.org/10.5741/GEMS.53.2.144

In August 2016, the authors visited the Lomonosov deposit to document this exciting new diamond locality. The visit included tours of the kimberlite open-pit operations, the processing plant, and the preliminary diamond sorting facilities in the city of Arkhangelsk. The authors also visited Alrosa's central diamond sorting and sales operation, the United Selling Organisation (USO) in Moscow. This article discusses the Lomonosov diamond production within the wider context of Russian diamond mining. Details are also provided on the deposit's nontraditional geological setting, which can be linked to the color origin of its pink and purple diamonds.

HISTORY OF DIAMOND MINING IN RUSSIA

Russia is the world's largest diamond producer by volume, responsible for around 30% of the world's diamond output each year. In 2015 alone, 41.9 million carats of diamonds were mined in Russia, valued at US$4.23 billion, according to Kimberley Process figures. Of these diamonds, 95% were mined and sold by Alrosa. By production value, Alrosa is second only to De Beers. Approximately 90% of Alrosa diamonds are mined in northeastern Siberia in the Republic of Sakha (formerly Yakutia), while a growing share (now 5%) is mined in northwestern Russia near the port of Arkhangelsk (Alrosa Annual Report 2015). Alrosa does not operate exclusively in Russia and has a stake

Figure 1. The Lomonosov deposit produces a variety of fancy-color diamonds, including pink and purple diamonds. Similar to the pink diamonds from Argyle, these likely relate to their Proterozoic geologic setting, unlike many other deposits that occur in stable Archean regions. Photo by Kevin Schumacher.

in Angola's Catoca mine, which accounts for approximately 5% of the company's diamond production.

There are a few Russian diamond mines not operated by Alrosa. The largest, the Grib mine, is located near Lomonosov in the Arkhangelsk region and operated by the Russian oil conglomerate Lukoil through its subsidiary Arkhangelskgeoldobycha. The Grib mine officially opened in 2014, around 15 years after it was first discovered. It yielded approximately 3 million carats in 2016 and is expected to produce around 4 to 5 million carats annually beginning in 2017. Lukoil recently agreed to sell the Grib mine to Otkritie Holding, with the deal expected to close in mid-2017 ("Lukoil concludes agreement…," 2016).

Although diamonds had been found in various locations around the country for more than 150 years, the possibility of finding commercial quantities in Russian territory was first raised in 1938 by scientists at Leningrad State University (now Saint Petersburg State University), who conducted a study comparing the geology of the Soviet Union with that of diamondiferous regions around the world.

Russian geologists began their search for diamonds in earnest in 1949, noting their strategic value for industrial uses. Around the same time, the United States began building a strategic stockpile of industrial diamonds, mainly from the Belgian Congo (now the Democratic Republic of Congo), for these same reasons. After five years of following garnet indicator minerals, a small team of geologists headed by Larissa Popugaeva found the first kimberlite near the Daldyn River in Yakutia in 1954. The first kimberlite pipe was subsequently named Zarnitsa. While Zarnitsa was not economic at the time—development only began in 2002—Popugaeva's find led to the discovery of the Mir pipe in 1955. Mir was the first diamond mine developed in Russia, and production commenced in 1959. Russian engineers constructed the town of Mirny nearby to house workers and provide infrastructure for the operation. The Udachnaya pipe, about 250 miles north of Mir and the country's most productive diamond mine by volume, was discovered two years later (Erlich, 2013).

Kimberlite pipes near Arkhangelsk in northwestern Russia were first discovered in the 1960s through airborne geophysical surveys (Stanikovskiy et al., 1974). Magnetic and gravity surveys are commonly used during kimberlite exploration to image the subsurface, as they can distinguish areas that have anomalous rock compositions (such as kimberlite) from the surrounding country rock. Kimberlites will show up as circular magnetic or gravity anomalies that can be seen even if they are buried by younger cover. Any potential kimberlite targets identified through these surveys must be confirmed by drilling, and the kimberlites in the Lomonosov deposit were all drilled in the early 1980s. The deposit itself is named after the eighteenth-century scientist Mikhail Lomonosov, one of the founders of Moscow State University. The Grib mine was named for Vladimir Grib, one of the Russian geologists who discovered diamonds in the area.

After bulk sampling at Lomonosov was completed in 1987, the Soviet central government gave its clearance to develop the deposit. However, the breakup of the Soviet Union in 1991 and the result-

ing political and financial uncertainty delayed the project for years. The new Russian government's priorities for diamond production were focused on existing operations in the Republic of Sakha that could generate quick revenues. As a result, development of the Lomonosov deposit did not begin until 2003.

When the first Russian diamonds appeared in the market in 1961, they were sold through De Beers Consolidated Mines' marketing arm, the Diamond Trading Company (DTC). At that time, however, the African continent was in the midst of an independence movement, with many former colonies becoming sovereign states. The Soviet Union was eager to forge strategic partnerships with these emerging nations, so the officials who managed the USSR's mineral production ended its formal sales contract with the DTC in 1963. Nevertheless, the Soviet Union continued to sell the majority of its production through De Beers for the next 35 years, using a subsidiary and a financial firm in Switzerland as intermediaries. Neither the DTC nor Russia have ever acknowledged this arrangement or released production figures from this time (Shor, 1993, 2009).

In the mid-1960s, the Soviet government directed a portion of Russian diamond production toward building a polishing industry that would generate employment and added value. It also stockpiled a portion of the production for strategic purposes and as a buffer in the event its mines became depleted. The first Russian-polished diamonds began appearing in the market in the late 1960s. By 1980, Russia accounted for an estimated 25% of world output by value (Even-Zohar, 2007). That year also marked the discovery of potential diamond sources in the Arkhangelsk region in the European part of Russia.

Russia's rough diamond production neared 15 million carats annually as 1990 approached, second only to Botswana. Nearly all of its output was from Yakutia, namely the Udachnaya, Aikhal, and Internationalaya pipes. Production at Mir had been suspended to clear flooding in the pit and develop an underground shaft. The Arkhangelsk deposits were still under exploration. Under Mikhail Gorbachev, the Soviet government reorganized its diamond mining and marketing operations, previously managed by various agencies, into a single organization named Glavalmazzoloto, while continuing its relationship with De Beers (Even-Zohar, 2007).

In 1991, the Soviet Union dissolved. Eleven of the republics became autonomous states, while four republics, including Yakutia, were granted semi-autonomous status as part of the newly formed Russian Federation. Yakutia changed its name to Sakha Republic afterward. In the fall of 1992, the central government created a new diamond administration agency and recognized Sakha's semi-autonomous status by giving it substantial equity in its diamond operations (Shor, 1993). The new agency, Almazy Rossii-Sakha, gave the Republic of Sakha 40.5% equity and the right to market 20% of its production. The central government held 32.5%, with the remainder held by other government agencies. The following year, the agency name was shortened to Alrosa, and a subsidiary named Severalmaz ("Northern Diamond") was created to oversee exploration in the Arkhangelsk region (Shor, 1993). Alrosa currently owns 99.6% of Severalmaz shares.

The Russian Federation and Alrosa formalized their relationship with De Beers in 1996 after several years of disorganization, which saw large-scale "leakages" of rough diamond sales outside De Beers' network that had threatened to destabilize the market (Even-Zohar, 2007). In 2006, De Beers and Alrosa began phasing out their sales agreement in yearly increments, largely due to pressure from the European Union. Since then, all of Alrosa's rough production has been marketed directly to diamond manufacturers and dealers (Even-Zohar, 2007). The sales agreement formally ended in 2009.

In 2011, Alrosa reorganized into a semi-government/private equity company (termed a public joint-stock company) and in 2013 issued an initial public offering of its stock. The sale netted US$1.3 billion, selling 22.07% of the company to private investors and leaving the central government with 43.93% equity, Sakha Province with 25%, and 8% held by various municipalities within Sakha (Alrosa Annual Report 2013).

Today, Alrosa operates 42 Russian diamond deposits: 16 primary sources and 26 alluvial sites (Alrosa Annual Report 2015). The major primary deposits in Sakha are Mir (which opened in 1957), Udachnaya (1971), Internationalaya (1971), Aikhal (1971), Jubilee (1986), Nyurbinskaya (2002), Komsomolskaya (2002), Zarnitsa (2002), and Botyobinskaya (under development). The two pipes at the Lomonosov deposit are Arkhangelskaya (2005) and Karpinskogo I (2014).

CRATONS

What Is a Craton? Cratons are remnants of Earth's earliest crust that have been largely spared from erosion or destruction by tectonic processes. Cratonic regions worldwide contain crust that is at least 2.5 billion years old (Archean) but may also be signifi-

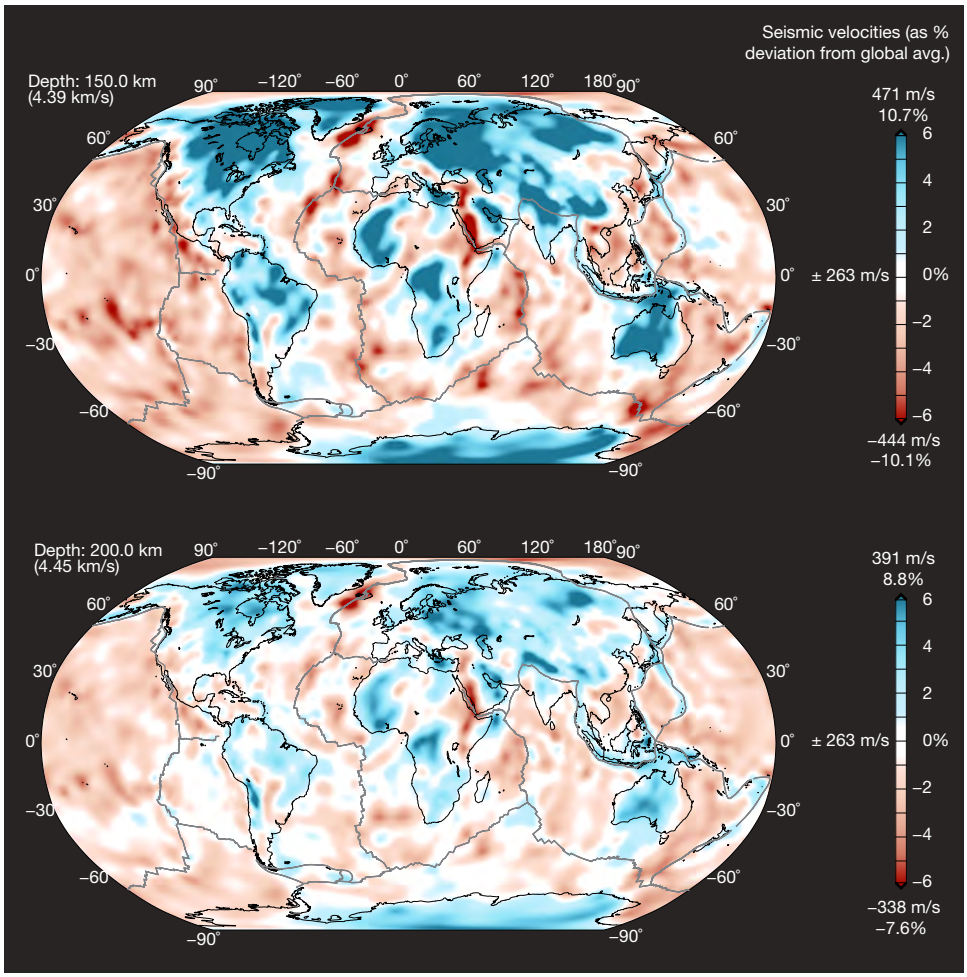

Figure 2. Global seismic shear speed model at depths of 150 km and 200 km (reproduced from Schaeffer and Lebedev, 2013) showing that global diamond-producing areas are all underlain by cratonic lithospheric mantle. These old stable cratonic regions have seismic velocities faster than the global average (shown here by cool colors). Warmer colors represent seismic velocities slower than the global average, indicating tectonically active areas. Major diamond-producing areas such as the Kaapvaal craton (South Africa), Slave craton (northern Canada), Siberian craton (Russia), and the Baltic shield across Scandinavia and western Russia all have fast seismic velocities down to depths of 150–200 km, evidence of deep sub-cratonic lithospheric keels that are conducive to diamond formation.

cantly older—forming within the first 500 million years of Earth's formation 4.56 billion years ago (Connelly et al., 2012). The oldest rocks on Earth occur in four-billion-year-old gneiss units within the larger Acasta Gneiss complex in the Slave craton of northern Canada (Stern and Bleeker, 1998; Reimink et al., 2016) and in the 3.8–4.3 billion-year-old Nuvvuagittuq greenstones in the Superior craton of eastern Canada (O'Neil et al., 2008). The Yilgarn craton of Western Australia has the oldest mineral grains on Earth—4.4 billion-year-old detrital zircons in the Jack Hills conglomerate (Valley et al., 2014).

The long-term stability of cratonic regions is due to their thick continental roots, which are isolated from the convecting mantle. These continental roots are known as the lithospheric mantle keel. Peridotite in the upwelling convecting mantle melts to form basalt at mid-ocean ridges and ocean islands. This melting removes the basaltic melt component from peridotite, leaving the residual peridotite depleted in elements such as Ca, Al, and Fe, as well as H_2O and the heat-producing elements (such as K, U, and Th). Due to its depleted character, this residual peridotite is cooler, less dense (more buoyant), and more rigid than the convecting mantle and therefore remains isolated. Lithospheric mantle keels are typically around 200 km thick and can be recognized in global seismic models by their fast seismic velocities compared to the global average (figure 2). Diamond mining regions across the world, such as those in South Africa, Canada, and Russia, are all underlain by thick continental keels that have "cool" temperature profiles conducive to diamond formation. Diamonds do not form in the lithosphere below portions of geologically young continental crust or in oceanic regions, since the temperature profiles in these regions never intersect into the diamond stability field (see Shirey and Shigley, 2013).

Archean and Proterozoic History of the Baltic Shield. The Baltic (also known as the Fennoscandian) shield, which is part of the much larger East European craton, stretches across Sweden, Finland, and northwestern Russia (Gorbatschev and Bogdanova, 1993).

Figure 3. Simplified geological map of the Baltic (or Fennoscandian) shield in Scandinavia and northwestern Russia. The Baltic shield (part of the larger East European craton) is a stable continental region comprising several cratonic regions—the Norrbotten, Karelian, and Murmansk cratons—that were stabilized during the Proterozoic through mountain-building processes associated with the Lapland-Kola orogen (Daly et al., 2006). The Arkhangelsk kimberlite province lies within the unexposed Lapland-Kola orogen. Basement rocks of the Baltic shield are unexposed in this region due to extensive Proterozoic and Phanerozoic cover rocks, and kimberlites were identified through geophysical surveys. As such, the eastern extent of the Baltic shield is not well defined. Alrosa's Lomonosov diamond deposit is 23 km southwest of the Grib diamond deposit.

It comprises the Archean terranes of the Karelian craton (mostly in Finland) and the Murmansk craton (mostly on the Kola Peninsula), separated by the composite terranes of the Paleoproterozoic Lapland-Kola orogen (figure 3).

The Karelian and Murmansk cratons both have ancient geologic histories, although the Karelian craton appears to be older. It contains crust with an age of at least 3.5 Ga, including some 3.7 Ga zircon grains incorporated from older material (Mutanen and Huhma, 2003; Peltonen et al., 2006). The underlying Karelian lithospheric mantle has similarly old ages—depleted harzburgite *xenoliths* (see box A) have minimum 3 Ga ages (Peltonen and Brügmann, 2006). Crust in the Murmansk craton seems to be much younger; metamorphic gneisses are mostly between 3.0 and 2.6 Ga (Timmerman and Daly, 1995; De Jong and Wijbrans, 2007).

The Baltic shield has an interesting history that is not typical for many diamond-bearing Archean cratons (see the discussion on Clifford's Rule in box B). Archean continents split apart during widespread rifting and ocean formation during the Proterozoic (between 2.5 and 2.1 Ga; Melezhik and Sturt, 1994; Pesonen et al., 2003). Continental breakup was likely due to an upwelling plume of mantle melts, and xenoliths sampled from the deep crust have ages that overlap with this event (Kempton et al., 2001). After a period of seafloor spreading and ocean development—similar to the geologic setting of modern-day Iceland—these Neoarchean terranes were reamalgamated between 1.95 and 1.87 Ga (Gorbatschev and Bogdanova, 1993; Daly et al., 2006).

Closure of the ocean basins was likely through subduction followed by Himalayan-scale mountain building as continents collided. Evidence for subduction includes arc volcanic rocks recognized in the Lapland granulite belt (see figure 3 for location; Meriläinen, 1976; Daly et al., 2001) and lower crustal and mantle eclogite xenoliths from the Grib kimber-

BOX A: ROCKS FROM THE CRATONIC LITHOSPHERIC KEEL

Peridotite is the predominant rock type in the mantle. It contains the minerals orthopyroxene, clinopyroxene, and olivine (figure A-1). Peridotite also contains an aluminous phase that can be either spinel or garnet, depending on depth. At the higher pressure conditions in the diamond stability field, the aluminous phase is always garnet. Peridotite melts to form basalt at mid-ocean ridges and ocean islands. This melting removes the basaltic melt from peridotite, leaving the residual peridotite depleted in elements such as Ca, Al, and Fe. This is because the melt moves upward to dikes that eventually feed shallow magma chambers. Lherzolite, the most fertile peridotite, has not undergone significant melt depletion and will contain some combination of the minerals listed above (figure A-1). With high proportions of melt depletion, clinopyroxene is eventually exhausted in the residual peridotite, resulting in the clinopyroxene-free rock known as harzburgite. With around 40–50% melting, orthopyroxene is also exhausted and olivine dominates the peridotitic assemblage (again, see figure A-1). After these high degrees of melting where most of the Ca, Al, and Fe has been lost, the residual peridotite becomes the most depleted dunite. Importantly, both depleted harzburgite and dunite can be re-enriched by passing melts that could reintroduce many of these minerals and convert peridotite back to fertile lherzolite.

In the absence of rock samples where the full mineral assemblage can be assessed, the relative depletion of the lithosphere can be obtained from the Mg and Fe composition of olivine. This is because the composition of olivine becomes more Mg-rich in residual peridotite that has undergone a higher extent of melting. For example, the most depleted dunitic peridotite will have an Mg# (calculated as Mg/(Mg + Fe) × 100) above 92.8 and fertile lherzolite will have a lower Mg#, around 89–91 (Walter, 1998; Kubo, 2002). These might not look like large differences, but they actually are because the range in olivine compositions in the mantle is small—only about 10% (Mg# from ~85 to 95).

Eclogite is another rock type in the lithospheric mantle, a bimineralic rock consisting of a sodium-rich clinopyroxene known as omphacite and garnet with pyrope (Mg-rich), grossular (Ca-rich), and almandine (Fe-rich) components. There are two main models for the origin of eclogites in the lithospheric mantle: as high-pressure mantle melts or as former oceanic crust that has been subducted and emplaced into the lithosphere (Jacob, 2004). Despite their scarcity in the lithospheric keel, eclogites are frequently sampled by kimberlites and can therefore provide important insights into the role of subduction in the assembly of the lithospheric keel.

Figure A-1. Classification of peridotites and pyroxenites, the rocks found in the lithospheric mantle. The predominant rock type is peridotite, which comprises olivine, clinopyroxene, orthopyroxene, and an aluminous phase (this is spinel at shallower depths and garnet at greater depths of the diamond stability field). All compositions are projected from this aluminous phase, which is not shown. The most fertile (least depleted) peridotite is lherzolite; the most depleted peridotite, dunite, is comprised mostly of olivine. Eclogite has a basaltic bulk composition and at high pressure and temperature in the mantle recrystallizes to only two minerals: Na-rich clinopyroxene and garnet. Eclogites plot in the clinopyroxenite field at the bottom right.

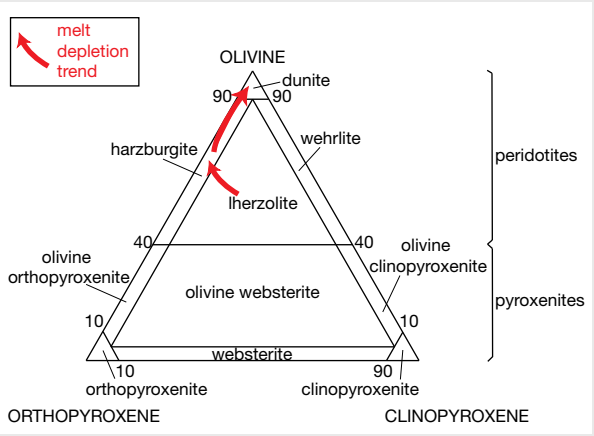

lite (Koreshkova et al., 2014; Shchukina et al., 2015). The resulting Lapland-Kola orogen comprises several different terranes of Archean crust that were reworked during this Paleoproterozoic event (for example, the Kola province, the Belomorian orogen, the Inari terrane, and the Strelna terrane; Daly et al., 2006).

KIMBERLITES

Origin of Kimberlites. Kimberlites are ultramafic volcanic rocks created by extremely explosive volcanic eruptions that originate from great depths below continental regions of the earth. As kimberlites rise through the subcontinental lithospheric mantle, they sample their surrounding rocks and transport them to the surface. When the kimberlite contains pieces of mantle rocks, these foreign pieces are called xenoliths. If the xenoliths fragment during transport, the individual mineral fragments of the xenoliths are called *xenocrysts*. Since the final kimberlite is a mixture of volcanic rock and the foreign materials it

picks up on the way to the surface, they are often regarded as hybrid rocks. During diamond exploration programs, the goal is to determine if these mantle rocks sampled an area of the mantle that is "diamond-stable," increasing the possibility that the kimberlite is economically viable. A kimberlite may predominantly sample shallower mantle within the graphite stability field, or the kimberlite itself may have a composition that is destructive to diamonds, ultimately making the pipe uneconomic to mine. For further information on the origin and eruption of kimberlites, see the detailed review provided in Shirey and Shigley (2013).

Kimberlites on the Baltic Shield. The kimberlites of the Lomonosov mine form part of the Paleozoic Arkhangelsk kimberlite province, which lies northeast of the city of Arkhangelsk. These kimberlites erupted between 390 and 340 Ma into the southeastern extension of the Archean Kola province that was reworked during the Proterozoic Lapland-Kola orogen (Garanin et al., 1999; Shevchenko et al., 2004; Pervov et al., 2005; Kononova et al., 2011; Larionova et al., 2016; see figure 3). This part of the Baltic shield has no exposed cratonic basement rocks. Instead, the rocks at the surface are much younger late Proterozoic to Phanerozoic rocks that overlie the >1.9 billion-year-old cratonic rocks (figure 4).

Other kimberlites in the Baltic shield occur in Finland and Russia (again, see figure 3). In Russia, there are the 1.92 Ga Kimozero kimberlites at Lake Onega (Priyatkina et al., 2014) and the 380–360 Ma Terskii Coast kimberlites in the southern Kola Peninsula (Beard et al., 1998). The 1.2 Ga Kostomuksha kimberlites in Russia are just across the border from Finland's Kuhmo-Lentiira kimberlites, and both these kimberlite fields have similar 1.2 Ga eruption ages and Group II kimberlitic compositions (O'Brien et al., 2007). Also in Finland are the Kuusamo kimberlites, which erupted at 757 ± 2 Ma (O'Brien and Bradley, 2008), and the 626–589 Ma Kaavi-Kuopio kimberlite field (O'Brien et al., 2005). Dublin-based Karelian Diamond Resources is developing the Lahtojoki kimberlite at Kaavi-Kuopia. If successful, it will be the first diamond mine in Finland.

Kimberlites in the Arkhangelsk Region. The Arkhangelsk kimberlite province comprises kimberlites with two distinct source compositions (figure 5). These compositions can reflect either different source depths in the mantle or varying amounts of interaction with the diamond-bearing lithosphere. Nevertheless, kimberlite from each of these groups is currently being mined.

Alrosa's Lomonosov deposit is mining the mica-rich kimberlites of the Zolotitsa field (again, see figure 4), which have enriched isotopic compositions similar to the South African Group II kimberlites (figure 5). Ten pipes in the Zolotitsa field were confirmed by drilling in the early 1980s. Six of these—Pionerskaya, Lomonosovskaya, Pomorskaya, Karpinskogo I and II, and Arkhangelskaya—have economic quantities of diamond and form part of the Lomonosov deposit. The other four kimberlites in the Zolotitsa field (including the Snegurochka kimberlite) are not part of Lomonosov's reserves, as they are currently uneconomic.

All the other kimberlites in the area, including the Grib mine in the Verkhotina kimberlite field, are Fe-Ti-rich kimberlites that are compositionally close to Group I kimberlites (figure 5). Apart from Grib, most of the other Fe-Ti-rich kimberlites are diamond-poor and uneconomic. These include kimberlites in the Shochta field, the Kepino-Pachuga field (e.g., the Zwezdochka, Anomaly 697, and Anomaly 688 kimberlites), and the Mela field, which includes some carbonatites (figure 4; Beard et al., 2000).

In Brief

- Lomonosov is Alrosa's first Russian diamond mine outside of Siberia.
- Production started in 2005, and Alrosa is currently mining only two of six potentially economic kimberlites.
- Similar to Argyle, it occurs in a region that experienced Proterozoic mountain-building.
- These geologic processes may be responsible for the pink-purple diamonds at both localities.

Although the two groups of Arkhangelsk kimberlites appear to be similar in composition to the traditional Group I and Group II kimberlites, a strict distinction into the two groups does not hold up. Arkhangelsk kimberlites actually have transitional isotopic compositions and mineralogical characteristics that lie between the two groups (figure 5; Mahotkin and Skinner, 1998; Beard et al., 2000).

Regardless of their classification, the isotopic compositions can be used to understand why the kimberlites in the Zolotitsa field are significantly more diamond-rich than the Fe-Ti-rich kimberlites. Zolotitsa kimberlites have Sr and Nd isotopic compo-

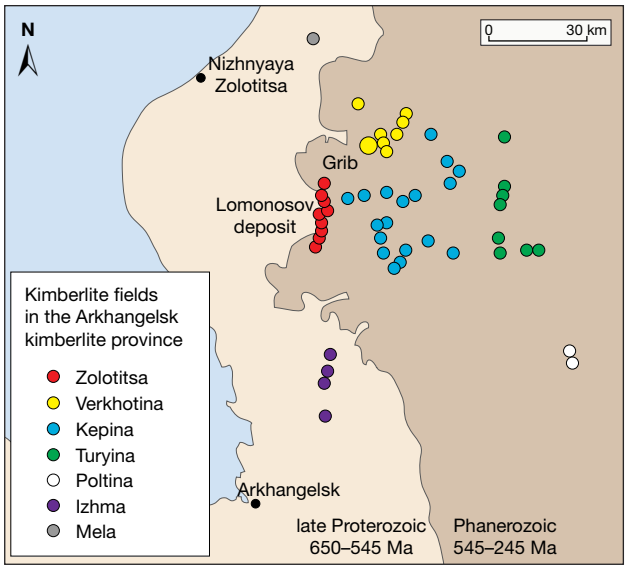

Figure 4. Kimberlitic rocks of the Arkhangelsk kimberlite province, color coded by kimberlite field. These all erupted between 390 and 340 million years ago, near the present-day city of Arkhangelsk in northwestern Russia. Several kimberlites of the Zolotitsa field form the Lomonosov diamond deposit. Aside from these and the Grib kimberlite (in the Verkhotina field), all other kimberlites in this province remain uneconomic. The basement rocks of the Baltic shield (older than 1.9 billion years; figure 1) are not exposed in this area, and the rocks at the surface are younger cover rocks between 650 and 245 million years old.

sitions that lie in the "enriched" quadrant in figure 5. These isotopic compositions can only evolve in the lithospheric keel or crust since they have been isolated from the convecting mantle for billions of years. This isolation allows for isotopic compositions to evolve (through parent-daughter isotopic decay and radiogenic ingrowth) that are distinct from the convecting mantle. "Enriched" isotopic compositions in Zolotitsa diamondiferous kimberlites reflect either their origin in, or interaction with, the diamond-bearing lithospheric mantle. This is in contrast to the isotopic compositions of the Fe-Ti-rich kimberlites, which do not show a strong lithospheric mantle signature but instead are very similar to the convecting mantle (figure 5).

An additional indicator that the Zolotitsa kimberlites are favorable for diamonds is their ilmenite composition. Ilmenites from the Arkhangelskaya kimberlite have compositions that indicate optimal melt conditions for diamond preservation during eruption to Earth's surface, with high MgO and low calculated Fe_2O_3 that indicate low oxygen fugacity (Lehtonen et al., 2009). Kimberlites containing ilmenites that indicate high oxygen fugacities may be destructive to diamonds. Even though the kimberlite may be sampling a diamond-rich portion of the lithosphere, these diamonds may not survive during kimberlite transport to Earth's surface.

THE CRUST AND DIAMONDIFEROUS MANTLE SAMPLED IN THE ARKHANGELSK REGION

Composition of the Lithosphere in the Arkhangelsk Region. Mantle xenoliths and xenocrysts brought to the surface by the Grib kimberlite are predominantly fertile garnet peridotites (around 46% lherzolite), pyroxenites + eclogites (around 11%), and only minor dunites (Kargin et al., 2016; Shchukina et al., 2016; Shchukina et al., 2015), indicating that the mantle keel was not subject to high degrees of melt removal. However, around 14% of the garnets from Grib have high Cr and low Ca contents, so-called G10 compo-

Figure 5. Strontium and neodymium isotopic compositions for kimberlites from Arkhangelsk province, modified from Beard et al. (2000). The estimate for the bulk earth (or convecting mantle) composition is $^{87}Sr/^{86}Sr = 0.7045$ and $^{144}Nd/^{143}Nd = 0.512630$, which is defined as ε_{Nd} of 0 (where ε_{Nd} is a percentage difference from the convecting mantle estimate). The top left quadrant has isotopic compositions that are more depleted than the convecting mantle and includes the source regions for mid-ocean ridge basalts. The bottom right quadrant has isotopic compositions that are more enriched than the convecting mantle. Compositional fields for South African Group I and II kimberlites are from Nowell et al. (2004).

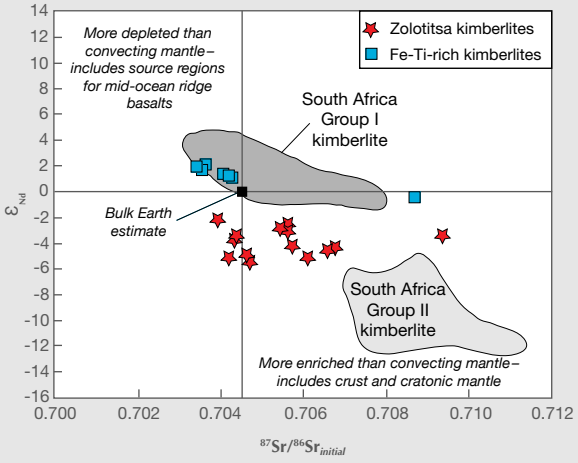

sitions, that show they are from melt-depleted harzburgites, an important diamond stability indicator (Shchukina et al., 2016). In contrast to Grib, the Arkhangelskaya kimberlite at Lomonosov appears to sample roughly equal amounts of pyroxenite-eclogite (37%) and peridotite (33% fertile lherzolite + 4% depleted harzburgite); see figure 6 and Lehtonen et al. (2008, 2009).

Similar to kimberlites elsewhere that sample compositionally diverse eclogites (e.g., Barth et al., 2001, 2002; Aulbach et al., 2007; Smit et al., 2014), Arkhangelskaya has two different suites of eclogites (Lehtonen et al., 2008) that probably had different formation processes. Many of the eclogites from Arkhangelskaya are not derived from depths sufficient for diamond stability (Lehtonen et al., 2008, 2009). Nevertheless, the abundance of low-Mg eclogites that had oceanic crustal protoliths emphasizes the importance of subduction and collisional processes in the formation of this part of the Baltic shield.

Mantle Geotherms in the Arkhangelsk Region. Grib peridotite xenoliths have pressure and temperature (*P-T*) arrays (figure C-1; Shchukina et al., 2012; Shchukina et al., 2015) that define a paleogeotherm (pressure-temperature array at the time of kimberlite eruption, 390 to 340 Ma; box C) corresponding to 35–40 mW/m^2 surface heat flow (i.e., model geotherms, defined in Hasterok and Chapman, 2011). Lomonosov mantle xenoliths are altered compared to fresher xenoliths found at Grib, and there are insufficient fresh xenoliths for inter-mineral geothermobarometry calculations (Lehtonen et al., 2009). However, a paleogeotherm determined to be from Arkhangelskaya clinopyroxene xenocrysts is very similar to the Grib paleogeotherm (figure C-1; Sablukov et al., 1995; Lehtonen et al., 2009). This makes sense considering they are only 23 km apart and erupted at similar times (between 380 and 340 Ma). They are also typical for diamond-bearing cratonic regions worldwide (Mather et al., 2011; Stachel and Luth, 2015). At both Arkhangelskaya and Grib, diamonds are stable at pressures greater than 3.5–4 GPa (below 110–120 km). At shallower depths, any carbon present in the lithosphere will occur as graphite instead.

One difference observed between the paleogeotherms from Grib and Arkhangelskaya is that Grib samples appear to be derived from greater depths in the lithospheric mantle (figure C-1). The two deepest peridotite xenoliths sampled by the Grib kimberlite are derived from >7 GPa/200 km (Lehtonen et al., 2009; Shchukina et al., 2012), whereas the deepest clinopyroxene xenocrysts from Arkhangelskaya are derived from shallower depths (5.5 GPa/170 km). However, garnet xenocrysts from Arkhangelskaya (for which only temperatures can be derived, and therefore are not plotted in figure C-1) have Ni-based tempera-

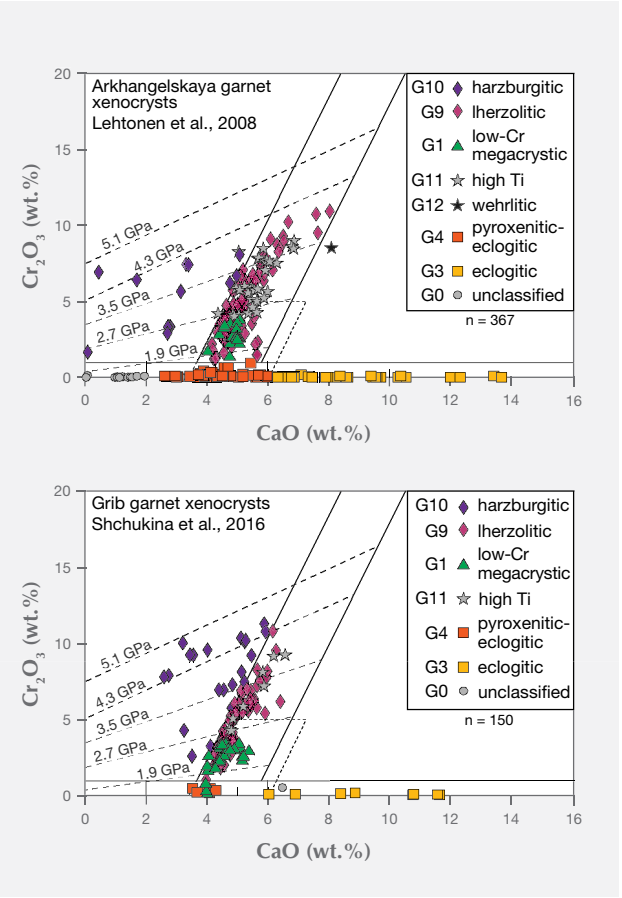

Figure 6. CaO-Cr_2O_3 compositions of garnet xenocrysts from the Arkhangelskaya and Grib kimberlites (Lehtonen et al., 2008; Shchukina et al., 2016). Each garnet xenocryst is color coded according to the composition of the rock from which it was derived. The compositional classification and their fields on the figure (solid lines) are taken from Grütter et al. (2004). Apart from being used to determine the mantle host rock, these compositions can also yield minimum pressures for depth in the lithospheric keel (dashed lines), enabling the diamond-stable portions of the lithospheric sample to be evaluated. Along the paleogeotherm determined for the Arkhangelsk province (figure 8), diamonds are stable above 3.5–4 GPa. The majority of the peridotitic garnets sampled at Arkhangelskaya are derived from pressures lower than 3.5 GPa and were not sampled from lithospheric regions that would contain diamond.

BOX B: CLIFFORD'S RULE AND ITS EXCEPTIONS

Clifford's Rule is a simple diamond exploration strategy based on the observation that diamonds are associated with old cratonic areas that have been tectonically stable since 2.5 Ga (Clifford, 1966). These areas are underlain by thick lithospheric keels that are cooler than the convecting mantle due to ancient melt depletion and have conditions favorable for diamond formation (see the review by Shirey and Shigley, 2013). Clifford's Rule says that although not all kimberlites will be diamondiferous, diamondiferous kimberlites only occur on these old Archean cratons underlain by deep mantle keels.

Contradictions to Clifford's Rule are becoming more prevalent, however, and there are many examples of diamonds mined in regions that have been tectonically active since 2.5 Ga. The splitting apart of continents and their recombination by later collision is common to the history of all continents on Earth. Orogens, which are the result of continental collision, cause rocks to become highly deformed with mineral recrystallization so severe that rocks can take on a "flow" texture. We now understand that diamond-forming fluids can also be introduced into the lithospheric mantle during these collisional processes.

For example, Argyle, one of the world's largest diamond mines and a famous supplier of pink and red diamonds (Shigley et al., 2001), occurs in one such collisional setting—the Proterozoic Halls Creek orogen. Argyle diamonds resided near the base of the lithosphere prior to their transport to the earth's surface. It is in this high-temperature, high-deformation area that Argyle's distinctive brown-pink-red diamonds likely formed (Stachel et al., 2017).

Similarly, the Lomonosov mine occurs within a Proterozoic orogenic setting (for details, see the "Archean and Proterozoic History of the Baltic Shield" section). Subduction-generated rocks have been identified in this part of the Lapland-Kola orogen (Koreshkova et al., 2014; Shchukina et al., 2015), suggesting that subduction played an important role during collision of these terranes and could have been a source of diamond fluids.

It is very possible that Lomonosov's pink-purple-brown diamonds are related to similar processes as the pink-red Argyle diamonds—namely, that they formed from carbon-bearing fluids released into the lithosphere during Proterozoic subduction events and were subsequently deformed in this tectonically active craton-margin setting. An age-dating study on sulfide and/or silicate inclusion–bearing diamonds from the Lomonosov mine would help determine whether this is in fact the case. But the ability to relate a distinctive, important diamond attribute such as pink color to a specific geologic process is a stunning application of basic research into diamond formation that will assist in the exploration for more such precious gems.

After 50 years, Clifford's Rule largely holds true: Most economic diamond deposits are found in association with old cratonic regions. However, the emerging pattern of diamond localities worldwide relative to cratonic regions suggests that exploration programs for economically viable diamondiferous kimberlites should not dismiss areas of the earth adjacent to these stable cratonic settings. For example, the Argyle and Ellendale mines of Australia occur in orogenic belts surrounding the Kimberley craton. Similarly, the Chidliak deposit under development on Baffin Island in northern Canada occurs in a late Archean terrane that was modified during later Paleoproterozoic collisional processes (Whalen et al., 2010). The importance of these diamond mines, including Lomonosov, for diamond exploration is that they show that economic quantities of diamond can occur in these younger Proterozoic regions.

Although diamonds can be associated with non-subduction refertilization events—for example, diamonds from Ellendale and Canada's Victor mine (Smit et al., 2010; Aulbach et al., 2017)—subduction in collisional terranes remains one of the key mechanisms of introducing carbon-bearing fluids into the diamond-forming regions of the deep Earth (e.g., Kesson and Ringwood, 1989). These subduction-derived fluids also introduce nitrogen, one of the main impurities in diamond. Nitrogen-related defects can contribute to a range of colors in diamonds. Examples of such defects include isolated substitutional nitrogen (N_s; C center), N3 (three nitrogens and a vacancy; van Wyk, 1982), H3 (two nitrogens and a vacancy; Davies and Summersgill, 1973; Clark and Davey, 1984), and the NV defects.

tures that indicate they derive from a wide range of depths in the lithosphere—all the way to the base of the lithosphere at 1400°C (Lehtonen et al., 2009).

By extrapolating the linear arrays of calculated *P-T* from both Grib and Arkhangelskaya to where they intersect with the temperature of the convecting mantle (the *mantle adiabat*), a deep lithospheric keel of around 220 km is obtained (figure C-1; Lehtonen et al., 2009). These xenolith-based estimates of lithosphere depth during the Paleozoic (where kimberlite eruption occurred between 390 and 340 Ma) are consistent with present-day seismic evidence of a thick lithosphere more than 200 km below the Baltic shield (figure 3; Schaeffer and Lebedev, 2013).

The final, amalgamated Baltic shield was constructed during the Proterozoic from several older, smaller terranes (see the "Archean and Proterozoic History of the Baltic Shield" section). The thick lithospheric keel (>220 km; figures 4 and C-1) below the Lomonosov mine and the Arkhangelsk kimberlite province was either preserved from the various Archean terranes (such as the Kola province or the Belomorian orogen) during the Lapland-Kola orogen or reestablished after Proterozoic collision.

Age of the Lithosphere in the Arkhangelsk Region. As noted in box B, diamond mining regions worldwide are found in association with cratons that preserve the oldest portions of Earth's crust. Archetypal kimberlites in the Kimberley region of South Africa all erupted through the Archean (>2.5 Ga) crust of the Kaapvaal craton. Similarly, the first kimberlites discovered in Canada, at Lac de Gras, erupted through the ancient crust of the Slave craton.

In contrast, the kimberlites of the Arkhangelsk province erupted through basement crustal rocks that are predominantly of Proterozoic age (<2.5 Ga), probably reflecting Archean crust reworking during 1.95 to 1.87 Ga continental assembly (Lapland-Kola orogen; Daly et al., 2006; Samsonov et al., 2009). Although evidence for older Archean material is found in lower crustal xenoliths from Grib (*magmatic* zircons in granulites with U-Pb ages of 2.72 Ga; Koreshkova et al., 2014), Grib and Pachuga xenoliths also preserve evidence of Proterozoic modification. For example, Grib *metamorphic* zircons all have 1.96 and 1.83 Ga ages (Koreshkova et al., 2014), and Pachuga granulites have 1.9–1.7 Ga Sm-Nd model ages (Markwick and Downes, 2000).

The predominantly Proterozoic crust in the Arkhangelsk region does not exclude the presence of an Archean lithospheric mantle at depth. In northwestern Australia, for example, the Argyle and Ellendale diamond-bearing lamproites erupted through Proterozoic orogens along the margins of the Kimberley craton. However, isotopic analyses of mantle xenoliths and diamond inclusions indicate the presence of Archean mantle lithosphere at both Argyle and Ellendale (Luguet et al., 2009; Smit et al., 2010), suggesting that Proterozoic orogenic activity did not impact deeper portions of the lithosphere.

Since mantle xenoliths from the Arkhangelsk kimberlites have not been extensively dated—unlike the Kimberley craton example given above—it is not known whether the mantle lithosphere has a predominantly Archean or Proterozoic heritage. Some Grib eclogite xenoliths were recently dated to around 2.8 Ga (E. Shchukina, pers. comm., 2016). They are apparently similar in age to Grib lower crustal rocks (Koreshkova et al., 2014), crustal rocks of the Murmansk craton (Timmerman and Daly, 1995; De Jong and Wijbrans, 2007), and eclogites in the Lapland-Kola orogen (Mints et al., 2010; Herwatz et al., 2012); see figure 2 for localities. These preliminary results suggest that although the basement crust in the Arkhangelsk kimberlite province appears to be predominantly Proterozoic, the underlying lithospheric mantle may be much older and was preserved through later collisional processes, similar to the geodynamic setting in the orogenic belts around the Kimberley craton (Luguet et al., 2009; Smit et al., 2010). Without diamond mining that exposes xenoliths and xenocrysts in the kimberlite, it would be impossible to construct this important deep geologic history.

DIAMONDS FROM THE ARKHANGELSK REGION

Diamond Type and Nitrogen-Based Temperatures. Nitrogen, the most common impurity in natural diamonds, is used to classify diamond into different "types." Diamonds with no nitrogen detectable by Fourier-transform infrared (FTIR) spectroscopy are termed type II, whereas diamonds that do contain nitrogen are termed type I. Nitrogen is incorporated into diamond as isolated substitutional nitrogen (N_S; C center). With time and temperature, this nitrogen anneals to form nitrogen pairs (N_2; A center) and nitrogen aggregates (V_1N_4; B center). The conversion from C→A→B centers has been well calibrated so that time-averaged mantle residence temperatures can be calculated (Taylor et al., 1990, 1996). Due to the temperature conditions in the lithospheric mantle, most natural cratonic diamonds contain a combination of A and B centers, termed type IaAB; see Breeding and Shigley (2009) for further details on the type classification of diamonds.

According to Khachatryan and Kaminsky (2003), diamonds from all six kimberlites at Lomonosov are predominantly type IaAB and contain 10–2900 ppma nitrogen. Less than 5% of diamonds from the Lomonosovskaya kimberlite are type II. The same study noted that nitrogen-based temperatures calculated from the percentage of B centers in Lomonosov diamonds are around 1100 ± 50°C. Along the local paleogeotherm (shown in figure C-1), these temperatures indicate that the diamonds were derived from depths between 150 and 170 km, similar to clinopyroxene xenocrysts sampled by the kimberlites.

BOX C: PRESSURE-TEMPERATURE GRADIENTS IN THE LITHOSPHERE (PALEOGEOTHERMS)

Understanding the temperature profile with depth in the lithospheric keel known as a "geotherm" is an important first step toward understanding the diamond-stable portions of the lithosphere. The intersection of the *P-T* array with the thermodynamically determined graphite-to-diamond transition constrains the minimum depth at which diamond will be present in the lithospheric keel (figure C-1). Calculating a geotherm involves routine analyses of major element compositions of constituent minerals in mantle xenoliths. In coexisting minerals such as garnet and clinopyroxene, the relative proportions of elements such as magnesium, iron, and chromium minerals vary systematically with pressure and temperature. Because of this relationship, simple chemical analyses of the minerals can be used to indicate the temperature and pressure at which the minerals equilibrated.

Once a geotherm and the diamond-stable portions of the lithosphere below a diamond prospective area are constrained, these *P-T* conditions can be applied to any diamond indicator mineral. For example, Cr-rich clinopyroxene is known to occur alongside diamonds in the lithospheric keel, but it can also occur at shallower pressures where graphite is stable. If pressures and temperatures are determined for clinopyroxene in diamond exploration samples and compared to the prevailing geotherm, it will become apparent whether these minerals are actually derived from the diamond stability field—in other words, whether the kimberlite is sampling portions of the lithosphere that may contain trace amounts of diamond.

Determining the geotherm also enables geologists to assess the depth of the lithospheric keel at the time of kimberlite eruption. The lithospheric keel is isolated from convection in the asthenosphere because its distinct depleted compositions make it cooler and more buoyant than the convecting mantle. The average temperature in the convecting mantle is around 1300–1400°C (figure C-1) and becomes warmer with increasing depth. Where the deepest samples occur or otherwise where the *P-T* array of the lithosphere (geotherm) intersects with the temperature of the convecting mantle (adiabat), one indication of lithosphere depth is obtained.

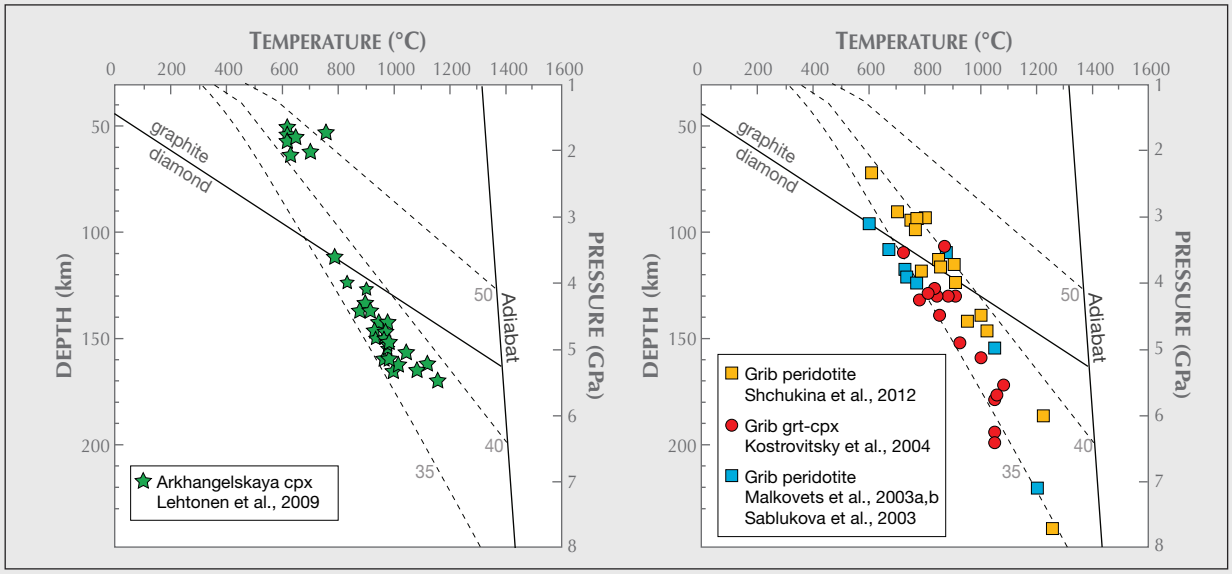

*Figure C-1. Pressure and temperature (*P-T*) data from peridotite xenoliths and xenocrysts from the Arkhangelskaya and Grib kimberlites. For Arkhangelskaya clinopyroxene,* P-T *was calculated using Nimis and Taylor (2000), using data from Lehtonen et al. (2009). For Grib peridotite,* P-T *was calculated using Taylor (1998) and Nickel and Green (1985) using data from Shchukina et al. (2012) and other studies. Gray dashed lines are model* P-T *paths for the mantle known as "geotherms" for different thermal conditions, so cooler (35 mW/m²) and warmer (50 mW/m²) regions can easily be compared (from Hasterok and Chapman, 2011). The graphite-diamond transition, from Day (2012), defines the higher P and T conditions where diamond is expected to crystallize based on experimental studies of graphite transforming to diamond. The* P-T *arrays for both kimberlites are essentially similar and indicate that below the Arkhangelsk kimberlite province, diamonds are stable below 110–120 km depth. Extending the* P-T *trend to the temperature of the convecting mantle (or mantle adiabat) shows that the lithospheric keel is more than 220 km deep under both kimberlites. While this data is useful for comparison between these two kimberlites' diamond favorability, it can also be applied in pre-mining studies to any kimberlite to see if it is sampling mantle that is diamond-stable.*

Mantle Parageneses. Diamonds are metasomatic minerals that form when carbon-bearing fluids or melts infiltrate into either peridotite (depleted harzburgite + fertile lherzolite) or eclogite; carbon isotopic compositions of diamond can be used to distinguish its mantle paragenesis. Carbon isotopic composition is expressed in delta notation, $\delta^{13}C$, where two isotopes of carbon, ^{13}C and ^{12}C, are referenced to a standard and expressed in ‰. The mantle has an average $\delta^{13}C$ value of –5‰ but can extend down to around –9‰. Peridotitic diamonds typically have $\delta^{13}C$ values similar to those of the mantle. Eclogitic diamonds can similarly have so-called mantle values, but also have $\delta^{13}C$ values that extend down to –41‰. These extremely negative $\delta^{13}C$ values reflect carbon input from crustal reservoirs that likely were recycled into the lithospheric mantle through subduction (De Stefano et al., 2009; Smart et al., 2011). Grib diamonds have a narrow range of $\delta^{13}C$ values between –10 and –3‰ that likely reflects their peridotitic nature (Rubanova et al., 2009). Most Lomonosov diamonds have a similar $\delta^{13}C$ range, but a few diamonds have values down to –22.2‰ (Galimov et al., 1994), suggesting mixed peridotitic and eclogitic parageneses.

Mineral inclusions in diamonds can provide information (temperature, depth, and compositional paragenesis) about the environment in which diamonds grew. As suggested from the predominantly mantle-like carbon isotopic compositions (Rubanova et al., 2009), Grib diamonds are predominantly peridotitic and contain both chromite and olivine inclusions. Olivine from Grib has Mg# (calculated as Mg/(Mg+Fe) × 100) between 92 and 94 (Malkovets et al., 2011), indicating its derivation from depleted harzburgitic to dunitic peridotite (i.e., not fertile lherzolite, which would have lower Mg# around 89–91). Grib also has a minor eclogitic diamond population containing typical orange eclogitic garnet inclusions. There have not been many studies on the mineral inclusions from Lomonosov diamonds, so a full comparison of the inclusion characteristics of these two mines is not possible. Interestingly, one study by Sobolev et al. (1997) reported a majoritic garnet inclusion (garnet with excess Si) in a diamond from Lomonosov's Pomorskaya kimberlite. These majoritic garnets are only stable at depths greater than 250 km (Stachel et al., 2005), significantly deeper than the majority of lithospheric diamonds that are derived from depths between 120 and 220 km.

Color and Morphology. Lomonosov produces few very large diamonds. The largest was a 106 ct gray industrial diamond found in February 2011. Between the two kimberlite pipes being mined at Lomonosov, 82% of the diamonds are gem or near-gem quality, which is higher than the global average of 50–60% (Bain & Company, 2013). Diamonds examined by Galimov et al. (1994) and Kudryavtseva et al. (2001), as well as those on display during the authors' visit (figure 7), were predominantly resorbed dodecahedra with only minor octahedral diamonds. Approximately 0.04% of diamond production from the two pipes is fancy color, such as purple, pink, violet, green, yellow, and brown (figures 7–9). For comparison, Argyle produces around 72% brown, 27% colorless to yellow, and <<1% pink-red diamonds (Shigley et al., 2001).

Fancy colors are due to different impurities and defects in the diamond lattice and can be used to understand the geological history of the diamonds. Most near-colorless and yellow diamonds from Lomonosov would be referred to in the gem trade as "cape" diamonds (Garanin et al., 1994). These cape diamonds obtain their color from the N3 defect (three nitrogens and a vacancy; van Wyk, 1982) that forms as a byproduct during the A to B aggregation. By definition, then, all cape diamonds are type IaAB, consistent with FTIR results indicating that Lomonosov diamonds are predominantly type IaAB that have resided at temperatures around 1100 ± 50°C (Khachatryan and Kaminsky, 2003).

From visual color observations, there appear to be two different kinds of green diamonds, similar to Grib (Rubanova et al., 2009), with color originating from both GR1 (neutral vacancy—V^0; Clark and Walker, 1973) and H3 defects (NVN^0; Davies and Summersgill, 1973; Clark and Davey, 1984). GR1 forms through natural and artificial irradiation and also during deformation. Although GR1 occurs in all natural diamonds, the concentration of GR1 is typically too low to detect with visible/near-infrared (Vis-NIR) spectroscopy and therefore does not influence the bodycolor.

GR1 formation related to irradiation is typically imparted relatively late in the diamond's history, when it resides in crust with high concentrations of radioactive minerals. Irradiation sources for natural diamond include radioactive grains such as uraninite, zircon, monazite, and pyrochlore that may be present in either the Archean crust and its sediments or the host kimberlite. However, diamonds can also be irradiated in the lithospheric mantle when radioactive minerals such as monazite and titanite, as well as rare loparite and chevkinite, are trapped in the diamond during growth (Kopylova et al., 1997; Smith and Wong, 2016).

Figure 7. A selection of diamonds from two weeks' production, put on display during the visit to Severalmaz's sorting facility in Arkhangelsk. Diamonds from the Lomonosov deposit are predominantly resorbed dodecahedra, and only a few primary octahedral diamonds were seen. Around 0.04% of the diamond production consists of fancy colors such as yellow, green, purple, pink, and brown. Also on display were gray industrial diamonds. Photos by Karen Smit.

Vacancies are not exclusively related to irradiation. They can also form due to deformation during diamond's residence at high pressures and temperatures in the mantle. H3 normally forms during heating (annealing) of diamonds, which facilitates vacancy migration and trapping at A centers. These vacancies could be from GR1 or vacancy clusters that are normally associated with deformation glide planes in the diamond. A spectroscopic study of Lomonosov green diamonds would be necessary to determine if these particular H3 green diamonds underwent high amounts of deformation.

Although the pink, purple, and brown diamonds from Lomonosov have not been spectroscopically studied, a broad band centered around 550–560 nm is typically responsible for such colors (Raal, 1958; Collins, 1982). The defect structure of the 550 nm band is unknown but generally understood to be related to deformation, since the pink and brown colors are normally concentrated along deformation glide planes in diamonds (Titkov et al., 2008; Gaillou et al., 2010; Howell et al., 2015). For example, the pink and brown Argyle diamonds occur in a Proterozoic orogenic setting along the margin of the Kimberley craton. Their residence at high temperatures in the high deformation zone near the base of the lithosphere (Stachel et al., 2017) resulted in deformation glide planes and the 550 nm band that imparts the pink and brown colors distinctive of Argyle. The Lomonosov diamonds also occur in an area of Proterozoic mountain building (the Lapland-Kola orogen noted above), and it is very likely that these pink and brown diamonds have a color origin similar to the Argyle diamonds that occur in the Proterozoic Halls Creek

Figure 8. Two yellow cuboctahedral diamonds separated during recovery sorting in the processing plant at the Lomonosov mine. Photo by Karen Smit.

Figure 9. A purple-pink Lomonosov diamond weighing approximately 0.4 ct. It was mined in early 2015 and sold for more than US$1.6 million per carat at the Hong Kong tender sale in September of that year. Photo by Russell Shor.

orogen (1.8 Ga; Tyler and Page, 1996). It is remarkable that basic mineralogical and geological research now allows us to understand the geological conditions that create specific color centers in these diamonds.

DEVELOPMENT AND MINING OF THE LOMONOSOV DEPOSIT

Location and Development. The Lomonosov deposit is about 110 km from the White Sea port of Arkhangelsk, which was for centuries Russia's primary deepwater seaport. The deposit is located at around 65°N, a latitude similar to that of the Arctic diamond mining operations in Siberia and northern Canada. Its proximity to the White Sea greatly moderates the climate; the average winter low is –13°C (8°F), compared to –32°C (–25°F) at the Canadian and Siberian mines. Instead of barren tundra, the area hosts dense woods that have served as a source of Russian timber for several centuries.

Mining in the extreme cold of northern Canada and Siberia presents formidable logistical and operational difficulties, as detailed by Shigley et al. (2016), but Lomonosov poses challenges of its own. First, part of the site was built on a partial wetland and groundwater that had softened the soil and rock. This required Severalmaz to truck in tons of hard gravel to shore up the roads leading into the mining pits so they could withstand the weight of the large hauling trucks (Serdyukova, 2013). Then, 63 wells had to be drilled and maintained to continually pump out groundwater at more than 5100 cubic meters per hour (each well pumps nearly 70–80 cubic meters per hour), which is then fed into a canal system surrounding the mining area.

Initial development costs totaled US$385 million, which included a processing plant with an annual capacity of 1 million metric tons of ore (Serdyukova, 2013). Production at Lomonosov started with the Arkhangelskaya pipe in 2005 (figure 10), since it had the largest reserves and the least amount of overburden—about 30 m, compared to the much larger Lomonosovskaya pipe, which was 45 m underground. Production at a second kimberlite pipe—Karpinskogo I—began nine years later in 2014. This was in tandem with the opening of a second plant capable of processing 3 million tons of ore per year.

Mining. Severalmaz employs 1,600 workers. Only the Arkhangelskaya and Karpinskogo I kimberlite pipes are currently being mined (figures 10 and 11), leaving Pionerskaya and Lomonosovskaya in reserve and Karpinskogo II and Pomorskaya under evaluation. Both kimberlite pits are mined using only excavators, without blasting. A fleet of 25 hauling trucks with 35 to 90 metric ton capacity carry the kimberlite ore from each pipe to separate stockpiles. On average, 14 million cubic tons of rock are mined per year, of which only 2 million cubic tons are kimberlite.

The shapes of the Arkhangelskaya, Karpinskogo I, and Karpinskogo II kimberlites and the diamond grade variations are given in figure 11. Current resource estimates show that Karpinskogo I has a grade of 0.6 carats per ton in the upper eruptive levels of the pipe (crater facies), improving to 1.4 carats per ton in the lower non-eruptive or magmatic section (diatreme facies). The Arkhangelskaya kimberlite has a similar resource, with current estimates of 0.5 carats

Figure 10. Open pit of the Arkhangelskaya kimberlite in August 2016, which at the time spanned 1.1 km. Arkhangelskaya was the first of the six kimberlites at Lomonosov to be developed since it had the least overburden and the largest diamond reserve. Photo by Karen Smit.

per ton in the crater facies and 1.06 carats per ton in the diatreme facies. By comparison, the Jwaneng operation in Botswana, the world's richest diamond mine by value, averages between 1.2 and 1.4 carats per ton. Russia's largest mine, Udachnaya, averages 1.3 carats per ton (Serdyukova, 2014).

Severalmaz geologists aim to maximize yield by continually sampling kimberlite sections being mined down to 2 m spacing (figure 12), updating diamond grade statistics as they go. This detailed sampling helps them identify high-grade areas in the kimberlite where diamonds are more highly concentrated. The lowest grade that Severalmaz will consider mining is 0.166 carats per ton. The total reserve estimates from all six pipes in the Lomonosov deposit are approximately 167 million carats.

Mining of crater facies kimberlite for the Karpinskogo I and Arkhangelskaya pipes will be completed in December 2017. Severalmaz expects annual production to more than double to approximately 4.6 million carats after 2017 as operations move into the richer diatreme facies and the existing processing plants are expanded. Reserves for both pipes have been determined down to 460 m, yet Severalmaz's current plan is to complete open-pit mining on them by about 2026, when Arkhangelskaya is down to 324 m (currently at 154 m) and Karpinskogo I down to 260 m (currently at 105 m). A decision will then be made about whether it is more profitable to continue mining deeper or to mine one of the other pipes such as Pionerskaya. The predicted grade for Pionerskaya is lower than for Arkhangelskaya and Karpinskogo I,

Figure 11. Geological cross-sections of the Arkhangelskaya, Karpinskogo I, and Karpinskogo II kimberlites. Modified from Severalmaz source material.

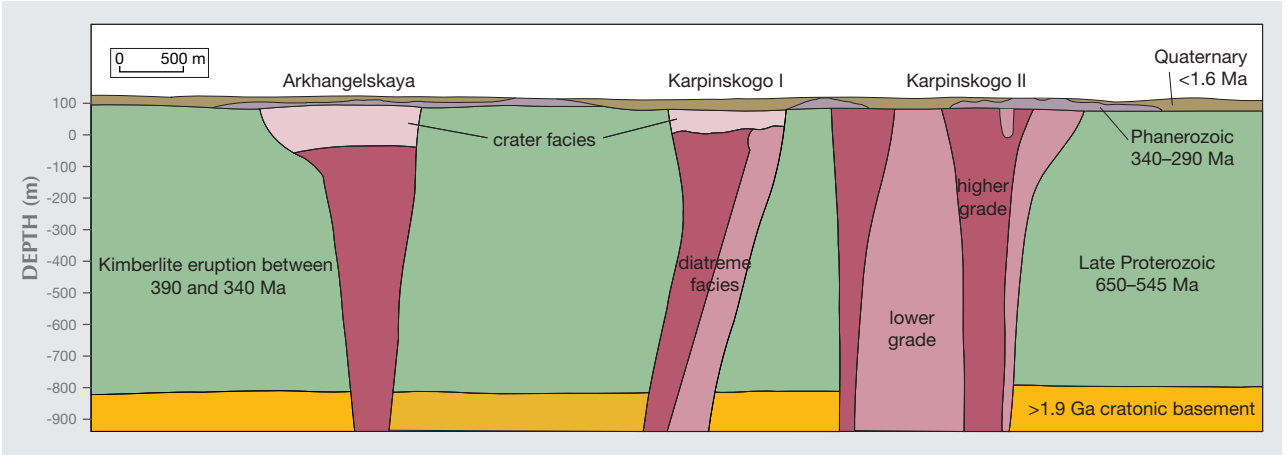

Figure 12. Large-diameter drill core samples of kimberlite from Karpinskogo I, examined by the authors. The fine-grained kimberlite contains highly altered country rock fragments, altered olivine and clinopyroxene macrocrysts, and small mantle xenoliths. Severalmaz continually examines core samples during mining to improve diamond grade estimations. Photos by Karen Smit.

but the diamonds are expected to be of better quality. During the authors' visit, Severalmaz officials said that no decisions had been made about developing the remaining pipes, though a 2017 report to shareholders said that such development was very likely.

RECOVERY AND SORTING OF LOMONOSOV DIAMONDS

Processing Plant. After mining, nearly all of the kimberlite from each pipe is stockpiled for several months in two areas located several hundred meters from mining operations. The weathering of the kimberlite, especially over winter, softens the material, making it much easier to liberate diamonds and reducing the risk of breaking or damaging larger crystals. This weathering technique is as old as systematic diamond mining and was used extensively in the early 1900s in South Africa. While the production profile is different for each pipe, the ore from both pipes is mixed together during processing to obtain uniform grades.

The initial processing phase tumbles the kimberlite in a large rotating mill that breaks the material into smaller pieces measuring about 120 × 25 mm while mixing this material with water (figure 13). This autogenous method of using the kimberlite to crush against itself instead of employing jaw crushers is less damaging to larger diamonds. The maximum size allowed through the mill was determined after a geological study showed that diamonds larger than 120 × 25 mm would likely occur only once every 30 years.

After milling, material is dispatched to hydraulic separators that segregate likely ore material from waste material based on density. The largest pieces out of the hydraulic separators go directly to units that use X-ray fluorescence and X-ray luminescence to identify diamonds. Air jets triggered by the X-ray signals deflect the diamonds into a collector box. The medium-sized pieces are first directed to density separators and then into a thin stream through to the X-ray units, which separate diamonds down to 1.25 mm (sieve size 2, or 0.008 per carat). Material under 1 mm never makes it to the X-ray units and is sent directly to the tailings. Alrosa is developing X-ray transmission technology to identify large diamonds in kimberlite before they undergo recrushing (Alrosa Annual Report 2015).

The waste material is continually sampled for diamonds the recovery process may have missed. During GIA's visit to the processing plant in August 2016, monitors in the recovery control room continually updated the recovery rate, which remained between 97% and 99%. Between 2014 and 2016, mining of the additional kimberlite pipe (Karpinskogo I) and the comple-

Figure 13. During the initial stage of processing, the ore material is sent through a large rotating mill that breaks the material into smaller pieces through autogenous grinding while mixing it with water. This method is designed to minimize the breakage to larger diamonds that often occurs with high-pressure crushing. Photo by Karen Smit.

tion of the new $325 million processing plant increased annual diamond production at Lomonosov from approximately 500,000 to 2 million carats (Serdyukova, 2013; Miller, 2014). Production is expected to increase to 5 million carats after the Pionerskaya and Lomonosovskaya pipes are developed ("Severalmaz recovers first 10 million carats…," 2017).

Diamond Sorting. Every two weeks, diamonds recovered from the Arkhangelskaya and Karponskogo I kimberlite pipes are dispatched to a preliminary sorting facility in the city of Arkhangelsk. Two weeks' production from these two kimberlites averages between 65,000 and 70,000 carats. In the Arkhangelsk sorting facility—overseen by Pavel Grib, the son of the geologist who discovered the Grib kimberlite—the diamonds are sorted manually by weight, color, shape, and clarity. Severalmaz then performs a preliminary valuation for each weight and quality category (for insurance purposes) before shipping the rough diamonds to Alrosa's United Selling Organisation (USO) in Moscow.

At the USO, all incoming rough diamonds from Alrosa's various Russian mines are first weighed and compared against the weights noted from each production region. Diamonds from these different production regions are then sorted by carat, color, shape, and clarity into about 8,000 subcategories of selling lots (Alrosa Annual Report 2015). Sorting is done through a combination of manual and automated operations, though development is continually underway to automate this process as much as possible (Alrosa Annual Report 2015; O. Petrov, pers. comm., 2016).

Diamonds from each production region (including Severalmaz) are kept separate throughout the sorting and sales process and are always sold in separate lots. Severalmaz determines pricing by offering small lots of diamonds, including fancy colors, at tender auctions through Alrosa sales offices. While Severalmaz is generally regarded as an Alrosa subsidiary, unspecified outside owners hold a 0.04% share in the company, necessitating the separate accounting (www.eng.alrosa.ru).

MANUFACTURING OF ALROSA DIAMONDS

Alrosa reserves 5% to 8% of its total diamond production, including Lomonosov goods, for domestic polishing. The vast majority of these are sent to Kristall, its diamond cutting operation, and marketed through the company's polished diamond sales division, which maintains offices in Moscow, Antwerp, New York, and Hong Kong (Alrosa Annual Report 2015).

The first Russian diamond manufacturing unit was founded in 1963 in the city of Smolensk, about 400 km southwest of Moscow. By the 1970s, six additional units had been established in different cities throughout the Soviet Union (www.kristallsmolensk.com/about/history). During that period, the Soviet government earmarked as much as 20% of Russian production to be cut locally and sold primarily through offices in Antwerp, Geneva, and London ("Soviet discounts irk diamond cutters," 1984). While officials never disclosed the exact percentage of diamonds being cut and sold, this polished production (estimated between $230 and $270 million yearly) was sufficient to have a strong effect on world markets by the 1980s (Thompson, 1982).

After the end of the Soviet regime, the government kept control of the operations within Russia proper. This included Kristall Smolensk, which became a sightholder in the mid-1990s after formalizing relations with De Beers. The government also invited foreign diamond manufacturers to open factories in the country. The state-owned Smolensk facility has remained the largest operation, with 2,500 workers producing 600,000 carats yearly by its fiftieth anniversary (Almor, 2013).

Russia's 20 diamond polishing operations produced approximately 300,000 carats worth US$670–$680 million in 2014, the most recent year for which complete figures are available (Leikin, 2016). Three of the operations—including Smolensk, which accounts for 40% of the total polished production—are in the Kristall network. International diamond companies or independent ventures operate the remaining 17 cutting plants. The vast majority of these factories produce smaller sizes ranging from 0.2 to 0.3 carats (Leikin, 2016). As with rough diamonds, the polished goods from Severalmaz and other Alrosa subsidiaries are kept separate through the cutting process and sold separately to diamond wholesalers and large retail chains.

MARKETING AND PRICING OF ALROSA DIAMONDS

In 2015, Alrosa's various operations produced a total of 38.4 million carats, with Severalmaz accounting for about 5%. By volume, Alrosa was responsible for 30% of world production in 2015, compared to De Beers' 22%. It sold 30.1 million carats of rough that year for US$3.55 billion, an average price of just over $103 per carat. This price is relatively low, but at the same time Alrosa's minimum recovery size is much smaller than that of other producers (Leikin, 2016).

The remaining 2015 production was either stockpiled by Alrosa or sold to Gokhran, the Russian government bureau that oversees the country's reserves of precious materials (Alrosa Annual Report 2015). In difficult economic times when demand from Alrosa's clients falls short of production, Gokhran buys the excess and stocks it until the market improves. Indeed, during the 2008–2009 financial crisis, Russia's diamond mines maintained full production, selling as much as US$2 billion to the government bureau, while De Beers and others sharply curtailed their mining output (Shor, 2009).

Between 66% and 70% of the United Selling Organisation's rough sales are sold through a structure similar to De Beers' sight system. A set list of 54 contracted clients, called the Alrosa Alliance, buys rough at monthly sales events in Moscow during the three-year contract life. In 2016, Severalmaz goods were offered every other month in lots separate from Siberian rough. According to Alrosa, these 54 firms represent a sustainable client base of major diamond manufacturers and jewelry retailers. About half of the current Alliance members are Antwerp dealers and manufacturers (figure 14), with most of the remainder from Israel and India. They also include eight Russian manufacturers and three large retailers, Chow Tai Fook (Hong Kong), Signet Group (United States and United Kingdom), and Tiffany & Co. through its Laurelton subsidiary (http://eng.alrosa.ru/operations/sales-policy/).

Alrosa allocates diamonds to each client based on requested size, quality, and rough shape parameters. Its stated policy is to provide long-term contracts to guarantee monthly supply of goods in pre-agreed volumes and assortments, as well as an option to purchase an extra range of goods. This policy is designed to provide stable supplies of rough diamonds and a hedge against diamond price volatility. While Alrosa aims to fully supply requested goods, each contract does contain a provision that there may be periods when it cannot deliver entire allocations of certain types of goods (http://eng.alrosa.ru/operations/sales-policy/).

An additional 25% of Alrosa production, including all rough larger than 10.8 ct and all fancy colors, are sold through tender auctions termed "competitive sales" (Shor, 2014). These are conducted in Alrosa's sales offices (operating as Arcos) in New York, Tel Aviv, Dubai, Antwerp, Hong Kong, and Moscow. Buyers include members of its Alliance or companies from the industry at large that have been vetted. The auctions use electronic bidding confirmed by hard copy, with the lots going to the highest bidders, assuming their offers meet the reserve prices. Most other diamond producers employ more complex bidding systems that average out the top bids (O. Petrov, pers. comm., 2016). For more information on the bidding process, see Shor (2014).

Figure 14. Pink Lomonosov diamonds obtained from Diarough, an Antwerp-based diamond manufacturer. Photo by Kevin Schumacher.

Although Alrosa generally has autonomy over its diamond pricing, the Russian Ministry of Finance remains the final authority (Alrosa Annual Report 2015). Alrosa's management sets rough prices based on market information gleaned from De Beers and Rio Tinto diamond sales, results of other producers' various tender auctions, and the company's own tender auction results. The company takes a very conservative approach and tries to minimize month-to-month price volatility in favor of stability (O. Petrov, pers. comm., 2016). During the second half of 2015, however, the diamond manufacturing industry faced a crisis due to a combination of unsustainably high rough prices, low polished prices, rising

inventories, and declining bank credit. In response, the company reduced its average prices by 15% (Alrosa Annual Report 2015).

In 2016, the company reduced its output by 2% to 37.4 million carats but sold 40.1 million carats (for US$4.3 billion), the difference coming from the 22 million carat stockpile it had accumulated during previous periods of slow demand ("Alrosa caps 2016 output to reduce stocks," 2017). Demand for small diamonds fell sharply at the end of 2016 because of a currency crisis in India. Early in 2017, however, India adjusted to this event, and between January and April 2017, Alrosa sold 16.9 million carats of rough and polished diamonds. These sales figures were up more than 7% compared to the first quarter of 2016. By value, however, sales declined 12.5% to US$1.7 billion as dealers wanted primarily smaller stones ("Alrosa reports sales results…," 2017).

SUMMARY AND CONCLUSIONS

In contrast to many diamond mines in South Africa, Canada, and Siberia, the Lomonosov deposit does not occur within a setting that was stabilized in the Archean. Rather, the kimberlites at Lomonosov erupted within a Proterozoic terrane that records both splitting of the continent and subsequent collision of older Archean terranes. The thick lithospheric keel below this region—a requirement for diamond formation—was either inherited from these Archean subterranes or reestablished during Proterozoic craton assembly. Proterozoic mountain-building in this diamond-producing region of the Baltic shield is seemingly at odds with Clifford's Rule, which states that diamond deposits are found in old cratonic regions that have been stable for at least 2.5 billion years. However, the emerging pattern in many diamond-producing regions is that these Proterozoic terranes can yield economic quantities of diamonds.

Lomonosov produces many fancy-color diamonds, including yellow, brown, pink, violet, and green, and these can be related to the diamonds' geological history, specifically their residence in a lithospheric keel that likely experienced high amounts of deformation related to Proterozoic tectonic processes. Pink-brown diamonds typically result from deformation, either during residency at the base of the lithospheric keel approximately 200 km in the mantle (e.g., Argyle) or possibly during kimberlite eruption. It is hard not to draw parallels between Argyle and Lomonosov, since both localities occur in areas that experienced Proterozoic continental assembly and produce pink, purple, and brown diamonds.

Yellow "cape" diamonds from Lomonosov result from aggregation of nitrogen impurities in the diamonds during what appears to have been a billion-year residency at temperatures above 1100°C in the lithospheric mantle. Green diamonds are likely related to irradiation and annealing, probably late in their history during kimberlite eruption or residence at the earth's surface.

The Lomonosov deposit is the first diamond development in the Baltic shield. Although it is in the early stages of development and only two of six potentially economic kimberlites are being mined, it is already an important source for fancy-color and colorless gem-quality diamonds. While Alrosa's plans to develop the additional kimberlites have not been finalized, Lomonosov will likely remain a significant source of colored and gem-quality diamonds in the coming decades.

ABOUT THE AUTHORS

Dr. Smit (ksmit@gia.edu) is a research scientist with GIA in New York. Mr. Shor (rshor@gia.edu) is a senior industry analyst with GIA in Carlsbad, California.

ACKNOWLEDGMENTS

We would like to thank everyone from Alrosa who made this visit both possible and enjoyable. Evgenia Kozenko and Irina Dolgopolova from Alrosa's international relations department organized this trip and translated during our tour of the operations. Ilya Zezin and Vladimir Kim, deputy and chief geologists, as well as Valery Kalashnikov, chief surveyor at the mine, showed us around the deposit and shared their knowledge. Pavel Grib hosted us at the diamond sorting center in Arkhangelsk. Svetlana Antipina, head of press service at Severalmaz, is also thanked for logistical organization in Arkhangelsk. Anatoly Posadsky and Ludmila Demidova at the United Selling Organisation (USO) in Moscow guided our tour through their facilities. Oleg Petrov, director of the USO, spoke with us on the marketing and selling process. This work benefited from discussions with Elena Shchukina, who along with Jim Shigley and Thomas Stachel provided journal articles that were difficult to access. We thank Evan Smith, Andy Fagan, and Ulrika D'Haenens-Johansson for their comments on the manuscript and Maya Kopylova, Elena Shchukina, and Steve Shirey for constructive comments that improved the final paper. Andrew Schaeffer provided the seismic images in figure 2, and Marianne Georges of Diarough, Antwerp, loaned the pink diamonds used in several figures and the cover photo.

REFERENCES

Almor Y. (2013) The Russian diamond industry celebrates its Jubilee Anniversary. *The International Resource Journal*, http://www.internationalresourcejournal.com/the_russian_diamond_industry_celebrates_its_jubilee_anniversary/

Alrosa Annual Report 2013 (2014) http://www.alrosa.ru/ar2013/?lang=en

Alrosa Annual Report 2015 (2016) http://alrosa.ru/ar2015/en/

Alrosa caps 2016 output to reduce stocks (2017) Diamonds.net, http://www.diamonds.net/News/NewsItem.aspx?ArticleID=58510&ArticleTitle=ALROSA+Caps+2016+Output+to+Reduce+Stocks, Jan. 30.

Alrosa reports sales results in April and January–April 2017 (2017) http://www.rough-polished.com/en/news/106793.html, May 11.

Aulbach S., Pearson N.J., O'Reilly S.Y., Doyle B.J. (2007) Origins of xenolithic eclogites and pyroxenites from the Central Slave Craton, Canada. *Journal of Petrology*, Vol. 48, No. 10, pp. 1843–1873, http://dx.doi.org/10.1093/petrology/egm041

Aulbach S., Stachel T., Creaser R.A., Heaman L.M., Shirey S.B., Muehlenbachs K., Eichenberg D., Harris J.W. (2009) Sulphide survival and diamond genesis during formation and evolution of Archaean subcontinental lithosphere: A comparison between the Slave and Kaapvaal cratons. *Lithos*, Vol. 112S, Proceedings of the 9th International Kimberlite Conference, pp. 747–757, http://dx.doi.org/10.1016/j.lithos.2009.03.048

Aulbach S., Creaser R.A., Stachel T., Chinn I., Kong J. (2017) Re-Os isotope systematics of sulphide inclusions in diamonds from Victor (Superior craton) document mobilisation of volatiles and Os during Rodinia break-up. *Extended Abstracts of the 11th International Kimberlite Conference*, (11IKC-4473).

Bain & Company (2013) The Global Diamond Report. *Journey through the Value Chain*.

Barth M.G., Rudnick R.L., Horn I., McDonough W.F., Spicuzza M.J., Valley J.W., Haggerty S.E. (2001) Geochemistry of xenolithic eclogites from West Africa, Part I: A link between low MgO eclogites and Archean crust formation. *Geochimica et Cosmochimica Acta*, Vol. 65, No. 9, pp. 1499–1527, http://dx.doi.org/10.1016/S0016-7037(00)00626-8

Barth M.G., Rudnick R.L., Horn I., McDonough W.F., Spicuzza M.J., Valley J.W., Haggerty S.E. (2002) Geochemistry of xenolithic eclogites from West Africa, Part 2: origins of the high MgO eclogites. *Geochimica et Cosmochimica Acta*, Vol. 66, No. 24, pp. 4325–4345, http://dx.doi.org/10.1016/S0016-7037(02)01004-9

Beard A.D., Downes H., Hegner E., Sablukov S.M., Vetrin V.R., Balogh K. (1998) Mineralogy and geochemistry of Devonian ultramafic minor intrusions of the southern Kola Peninsula, Russia: implications for the petrogenesis of kimberlites and melilitites. *Contributions to Mineralogy and Petrology*, Vol. 130, No. 3-4, pp. 288–303, http://dx.doi.org/10.1007/s004100050366

Beard A.D., Downes H., Hegner E., Sablukov S.M. (2000) Geochemistry and mineralogy of kimberlites from the Arkhangelsk Region, NW Russia: evidence for transitional kimberlite magma types. *Lithos*, Vol. 51, No. 1-2, pp. 47–73, http://dx.doi.org/10.1016/S0024-4937(99)00074-2

Breeding C.M., Shigley J.E. (2009) The "type" classification system of diamonds and its importance in gemology. *G&G*, Vol. 45, No. 2, pp. 96–111, http://dx.doi.org/10.5741/GEMS.45.2.96

Clark C.D., Davey S.T. (1984) Defect-induced one-phonon absorption in type Ia diamonds. *Journal of Physics C: Solid State Physics*, Vol. 17, No. 15, pp. L399–L403, http://dx.doi.org/10.1088/0022-3719/17/15/003

Clark C.D., Walker J. (1973) The neutral vacancy in diamond. *Proceedings of the Royal Society A*, Vol. 334, No. 1597, pp. 241–257, http://dx.doi.org/10.1098/rspa.1973.0090

Clifford T.N. (1966) Tectono-metallogenic units and metallogenic provinces of Africa. *Earth and Planetary Science Letters*, Vol. 1, No. 6, pp. 421–434, http://dx.doi.org/10.1016/0012-821X(66)90039-2

Collins A.T. (1982) Colour centres in diamond. *Journal of Gemmology*, Vol. 18, No. 1, pp. 37–75.

Connelly J.N., Bizzarro M., Krot A.N., Nordlund A., Wielandt D., Ivanova M.A. (2012) The absolute chronology and thermal processing of solids in the solar protoplanetary disk. *Science*, Vol. 338, No. 6107, pp. 651–655, http://dx.doi.org/10.1126/science.1226919

Daly J.S., Balagansky V.V., Timmerman M.J., Whitehouse M.J., De Jong K., Guise P., Bogdanova S., Gorbatschev R., Bridgwater D. (2001) Ion microprobe U-Pb zircon geochronology and isotopic evidence for a trans-crustal suture in the Lapland-Kola Orogen, northern Fennoscandian Shield. *Precambrian Research*, Vol. 105, No. 2-4, pp. 289–314, http://dx.doi.org/10.1016/S0301-9268(00)00116-9

Daly J.S., Balagansky V.V., Timmerman M.J., Whitehouse M.J. (2006) The Lapland-Kola orogen: Palaeoproterozoic collisions and accretion of the northern Fennoscandian lithosphere. *Geological Society, London, Memoirs*, Vol. 32, No. 1, pp. 579–598, http://dx.doi.org/10.1144/GSL.MEM.2006.032.01.35

Davies G., Summersgill I. (1973) Nitrogen dependent optical properties of diamond. *Diamond Research*. Industrial Diamond Information Bureau, London, pp. 6–15.

Day H.W. (2012) A revised diamond-graphite transition curve. *American Mineralogist*, Vol. 97, No. 1, pp. 52–62, http://dx.doi.org/10.2138/am.2011.3763

De Jong K., Wijbrans J.R. (2007) Apparent partial loss age spectra of Neoarchean hornblende (Murmansk Terrane, Kola Peninsula, Russia): the role of biotite inclusions revealed by $^{40}Ar/^{39}Ar$ laserprobe analysis. *Terra Nova*, Vol. 18, No. 5, pp. 353–364, http://dx.doi.org/10.1111/j.1365-3121.2006.00699.x

De Stefano A., Kopylova M.G., Cartigny P., Afanasiev V. (2009) Diamonds and eclogites of the Jericho kimberlite (northern Canada). *Contributions to Mineralogy and Petrology*, Vol. 158, No. 3, pp. 295–315, http://dx.doi.org/10.1007/s00410-009-0384-7

Erlich E. (2013) The discovery of Zarnitsa: The dawn of Siberian diamonds. *Science First Hand*, Vol. 35, No. 2, https://scfh.ru/en/papers/the-discovery-of-zarnitsa-the-dawn-of-siberian-diamonds/?sphrase_id=1846490

Even-Zohar C. (2007) *From Mine to Mistress: Corporate Strategies and Government Policies in the International Diamond Industry*. Mining Communications Ltd., London.

Gaillou E., Post J.E., Bassim N.D., Zaitsev A.M., Rose T., Fries M.D., Stroud R.M., Steele A., Butler J.E. (2010) Spectroscopic and microscopic characterizations of color lamellae in natural pink diamonds. *Diamond and Related Materials*, Vol. 19, No. 10, pp. 1207–1220, http://dx.doi.org/10.1016/j.diamond.2010.06.015

Galimov E.M., Zakharchenko O.D., Maltsev K.A., Malkin A.I., Pavlenko T.A. (1994) Carbon-isotope composition of diamonds from Arkhangelsk region kimberlite pipes. *Geochemistry International*, Vol. 31, No. 8, pp. 71–78.

Garanin V.K., Dammett H.T., Amtauer G., Kudryavtseva G.P., Fipke C. (1997) Internal structure and spectroscopic characteristics of diamonds from the Lomonosov deposit. *Doklady Akademii Nauk*, Vol. 353, No. 2, pp. 223–227.

Garanin V.K., Grib V.P., Kudriavtseva G.P., Melnikov F.P. (1999) Some characteristics of the M. V. Lomonosov diamond deposit. *Earth Science Frontiers (China University of Geosciences, Beijing)*, Vol. 6, No. 1, pp. 79–82.

Gorbatschev R., Bogdanova S. (1993) Frontiers in the Baltic Shield. *Precambrian Research*, Vol. 64, No. 1-4, pp. 3–21, http://dx.doi.org/10.1016/0301-9268(93)90066-B

Grütter H.S., Gurney J.J., Menzies A.H., Winter F. (2004) An updated classification scheme for mantle-derived garnet, for use by diamond explorers. *Lithos*, Vol. 77, No. 1-4, Proceedings of the 8th International Kimberlite Conference, pp. 841–857, http://dx.doi.org/10.1016/j.lithos.2004.04.012

Hasterok D., Chapman D.S. (2011) Heat production and geotherms for the continental lithosphere. *Earth and Planetary Science Letters*, Vol. 307, No. 1-2, pp. 59–70, http://dx.doi.org/10.1016/j.epsl.2011.04.034

Herwatz D., Skublov S.G., Berezin A.V., Mel'nik A.E. (2012) First Lu-Hf garnet ages of eclogites from the Belomorian Mobile Belt (Baltic Shield, Russia). *Doklady Earth Sciences*, Vol. 443, pp. 377–380.

Howell D., Stern R.A., Griffin W.L., Southworth R., Mikhail S., Stachel T. (2015) Nitrogen isotope systematics and origins of mixed-habit diamonds. *Geochimica et Cosmochimica Acta*, Vol. 157, pp. 1–12, http://dx.doi.org/10.1016/j.gca.2015.01.033

Jacob D.E. (2004) Nature and origin of eclogite xenoliths from kimberlites. *Lithos*, Vol. 77, No. 1-4, pp. 295–316, http://dx.doi.org/10.1016/j.lithos.2004.03.038

Kargin A.V., Sazonova L.V., Nosova A.A., Tretyachenko V.V. (2016) Composition of garnet and clinopyroxene in peridotite xenoliths from the Grib kimberlite pipe, Arkhangelsk diamond province, Russia: Evidence for mantle metasomatism associated with kimberlite melts. *Lithos*, Vol. 262, pp. 442–455, http://dx.doi.org/10.1016/j.lithos.2016.07.015

Kempton P.D., Downes H., Neymark L.A., Wartho J.A., Zartman R.E., Sharkov E.V. (2001) Garnet granulite xenoliths from the Northern Baltic Shield—the underplated lower crust of a Palaeoproterozoic large igneous province? *Journal of Petrology*, Vol. 42, No. 4, pp. 731–763, http://dx.doi.org/10.1093/petrology/42.4.731

Kesson S.E., Ringwood A.E. (1989) Slab-mantle interactions: 2.The formation of diamonds. *Chemical Geology*, Vol. 78, No. 2, pp. 97–118, http://dx.doi.org/10.1016/0009-2541(89)90110-1

Khachatryan G.K., Kaminsky F.V. (2003) "Equilibrium" and "non-equilibrium" diamond crystals from deposits in the East European Platform as revealed by infrared absorption data. *The Canadian Mineralogist*, Vol. 41, No. 1, pp. 171–184, http://dx.doi.org/10.2113/gscanmin.41.1.171

Kononova V.A., Bogatikov O.A., Kondrashov I.A. (2011) Kimberlites and lamproites: Criteria for similarity and differences. *Petrology*, Vol. 19, No. 1, pp. 34–54, http://dx.doi.org/10.1134/S0869591111010024

Kopylova M.G., Rickard R.S., Kleyenstueber A., Taylor W.R., Gurney J.J., Daniels L.R.M. (1997) First occurrence of strontian K-Cr-loparite and Cr-chevkinite in diamonds. *Geologiya I Geofizika,* Vol. 38, No. 2, pp. 382–397.

Koreshkova M.Y., Downes H., Glebovitsky V.A., Rodionov N.V., Antonov A.V., Sergeev S.A. (2014) Zircon trace element characteristics and ages in granulite xenoliths: a key to understanding the age and origin of the lower crust, Arkhangelsk kimberlite province, Russia. *Contributions to Mineralogy and Petrology*, Vol. 167, No. 2, p. 973, http://dx.doi.org/10.1007/s00410-014-0973-y

Kostrovitsky S.I., Malkovets V.G., Verichev E.M., Garanin V.K., Suvorova L.V. (2004) Megacrysts from the Grib kimberlite pipe (Arkhangelsk Province, Russia). *Lithos*, Vol. 77, No. 1-4, pp. 511–523, http://dx.doi.org/10.1016/j.lithos.2004.03.014

Kubo K. (2002) Dunite formation processes in highly depleted peridotite: Case study of the Iwanaidake peridotite, Hokkaido, Japan. *Journal of Petrology*, Vol. 43, No. 3, pp. 423–448, http://dx.doi.org/10.1093/petrology/43.3.423

Kudryavtseva G.P., Tikhova M.A., Gonzaga G.M. (2001) Comparative characteristics of specific morphological features of diamonds from northern and northeastern European Russia (Urals, Timan and Arkhangelsk kimberlite province). *Moscow University Geology Bulletin*, Vol. 56, No. 6, pp. 26–30.

Larionova Y.O., Sazonova L.V., Lebedeva N.M., Nosova A.A., Tretyachenko V.V., Travin A.V., Kargin A.V., Yudin D.S. (2016) Kimberlite age in the Arkhangelsk Province, Russia: Isotopic geochronologic Rb-Sr and $^{40}Ar/^{39}Ar$ and mineralogical data on phlogopite. *Petrology*, Vol. 24, No. 6, pp. 562–593, http://dx.doi.org/10.1134/S0869591116040020

Lehtonen M., O'Brien H., Johanson B., Pakkanen L. (2008) Electron microprobe and LA-ICP-MS analyses of mantle xenocrysts from the Arkhangelskaya kimberlite, NW Russia. *Geological Survey of Finland, Open File Report*, M41.2.

Lehtonen M., O'Brien H., Peltonen P., Kukkonen I., Ustinov V., and Verzhak V. (2009) Mantle xenocrysts from the Arkhangelskaya kimberlite (Lomonosov mine, NW Russia): Constraints on the composition and thermal state of the diamondiferous lithospheric mantle. *Lithos*, Vol. 112S, pp. 924–933, http://dx.doi.org/10.1016/j.lithos.2009.03.008

Leikin I. (2016) Russian diamond manufacturing – before and after the abolition of export duty on diamonds. *Rough & Polished*, http://www.rough-polished.com/en/analytics/104604.html

Luguet A., Jaques A.L., Pearson D.G., Smith C.B., Bulanova G.P., Roffey S.L., Rayner M.J., Lorand J.-P. (2009) An integrated petrological, geochemical and Re-Os isotope study of peridotite xenoliths from the Argyle lamproite, Western Australia and implications for cratonic diamond occurrences. *Lithos,* Vol. 112S, Proceedings of the 9th International Kimberlite Conference, pp. 1096–1108, http://dx.doi.org/10.1016/j.lithos.2009.05.022

Lukoil concludes agreement to sell Grib Diamond Mine (2016) Lukoil press release, http://www.lukoil.ru/api/presscenter/exportpressrelease?id=75774, Dec. 2.

Mahotkin I.L., Skinner E.M.W. (1998) Kimberlites from the Arkhangelsk region - a rock type transitional between kimberlites, melnoites and lamproites. *Abstracts of the 7th International Kimberlite Conference - Cape Town*, pp. 532–535.

Malkovets V., Taylor L., Griffin W., O'Reilly S., Pokhilenko N., Verichev E. (2003a) Cratonic conditions beneath Arkhangelsk, Russia: Garnet peridotites from the Grib kimberlite. *Proceedings of the 8th International Kimberlite Conference, Victoria, BC, Canada*.

Malkovets V., Taylor L., Griffin W., O'Reilly S., Pokhilenko N., Verichev E., Golovin N., Litasov K., Valley J., Spicuzza M. (2003b) Eclogites from the Grib kimberlite pipe, Arkhangelsk, Russia. *Proceedings of the 8th International Kimberlite Conference, Victoria, BC, Canada*.

Malkovets V.G., Zedgenizov D.A., Sobolev N.V., Kuzmin D.V., Gibsher A.A., Shchukina E.V., Golovin N.N., Verichev E.M., Pokhilenko N.P. (2011) Contents of trace elements in olivines from diamonds and peridotite xenoliths of the V. Grib kimberlite pipe (Arkhangel'sk Diamondiferous Province, Russia). *Doklady Earth Sciences*, Vol. 436, No. 2, pp. 219–223.

Markwick A.J.W., Downes H. (2000) Lower crustal granulite xenoliths from the Arkhangelsk kimberlite pipes: petrological, geochemical and geophysical results. *Lithos*, Vol. 51, No. 1-2, pp. 135–151, http://dx.doi.org/10.1016/S0024-4937(99)00078-X

Mather K.A., Pearson D.G., McKenzie D., Kjarsgaard B.A., Priestley K. (2011) Constraints on the depth and thermal history of cratonic lithosphere from peridotite xenoliths, xenocrysts and seismology. *Lithos*, Vol. 125, No. 1-2, pp. 729–742, http://dx.doi.org/10.1016/j.lithos.2011.04.003

Melezhik V., Sturt B. (1994) General geology and evolutionary history of the early proterozoic Polmak-Pasvik-Pechenga-Imandra/Varzuga-Ust'Ponoy greenstone belt in the northeastern Baltic Shield. *Earth Science Reviews*, Vol. 36, No. 3-4, pp. 205–241, https://doi.org/10.1016/0012-8252(94)90058-2

Meriläinen K. (1976) The granulite complex and adjacent rocks in Lapland, northern Finland. *Geological Survey of Finland,* Bulletin 281.

Miller J. (2014) Severalmaz opens second processing plant at Lomonosov. Diamonds.net, http://www.diamonds.net/News/NewsItem.aspx?ArticleID=46389&ArticleTitle=Severalmaz+Opens+Second+Processing+Plant+at+Lomonosov

Mints M.V., Belousova E.A., Konilov A.N., Natapov L.M., Shchipansky A.A., Griffin W.L., O'Reilly S.Y., Dokukina K.A., Kaulina T.V. (2010) Mesoarchean subduction processes: 2.87 Ga eclogites from the Kola Peninsula, Russia. *Geology*, Vol. 38, No. 8, pp. 739–742, http://dx.doi.org/10.1130/G31219.1

Mutanen T., Huhma H. (2003) The 3.5 Ga Siurua trondhjemite

gneiss in the Archean Pudasjärvi Granulite Belt, northern Finland. *Bulletin of the Geological Society of Finland*, Vol. 75, pp. 51–68.
Nickel K.G., Green D.H. (1985) Empirical geothermobarometry for garnet peridotites and implications for the nature of the lithosphere, kimberlites and diamonds. *Earth and Planetary Science Letters*, Vol. 73, No. 1, pp. 158–170, http://dx.doi.org/10.1016/0012-821X(85)90043-3
Nimis P., Taylor W.R. (2000) Single clinopyroxene thermobarometry for garnet peridotites. Part I. Calibration and testing of a Cr-in-Cpx barometer and an enstatite-in-Cpx thermometer. *Contributions to Mineralogy and Petrology*, Vol. 139, No. 5, pp. 541–554, http://dx.doi.org/10.1007/s004100000156
Nowell G.M., Pearson D.G., Bell D.R., Carlson R.W., Smith C.B., Kempton P.D., Noble S.R. (2004) Hf isotope systematics of kimberlites and their megacrysts: New constraints on their source regions. *Journal of Petrology*, Vol. 45, No. 8, pp. 1583–1612, http://dx.doi.org/10.1093/petrology/egh024
O'Brien H., Bradley J. (2008) New kimberlite discoveries in Kuusamo, northern Finland. *Extended Abstracts of the 9th International Kimberlite Conference*, pp. 9IKC–A–00346.
O'Brien H.E., Peltonen P., Vartiainen H. (2005) Kimberlites, carbonatites and alkaline rocks. In M. Lehtninen, P.A. Nurmi, and O.T. Rämö, Eds., *Precambrian Geology of Finland*. Elsevier, Amsterdam.
O'Brien H., Phillips D., Spencer R. (2007) Isotopic ages of Lentiira-Kuhmo-Kostomuksha olivine lamproite-Group II kimberlites. *Bulletin of the Geological Society of Finland*, Vol. 79, pp. 203–215.
O'Neil J., Carlson R.W., Francis D., Stevenson R.K. (2008) Neodymium-142 evidence for Hadean mafic crust. *Science*, Vol. 321, No. 5897, pp. 1828–1831, http://dx.doi.org/10.1126/science.1161925
Peltonen P., Brügmann G. (2006) Origin of layered continental mantle (Karelian craton, Finland): Geochemical and Re-Os isotope constraints. *Lithos*, Vol. 89, No. 3-4, pp. 405–423, http://dx.doi.org/10.1016/j.lithos.2005.12.013
Peltonen P., Mänttäri I., Huhma H., Whitehouse M.J. (2006) Multistage origin of the lower crust of the Karelian craton from 3.5 to 1.7 Ga based on isotopic ages of kimberlite-derived mafic granulite xenoliths. *Precambrian Research*, Vol. 147, pp. 107–123, http://dx.doi.org/10.1016/j.precamres.2006.02.008
Pervov V.A., Larchenko V.A., Minchenko G.V., Stepanov V.P., Bogomolov E.S., Levskii L.K., Sergeev S.A. (2005) Timing and duration of kimberlitic magmatism in the Zimnii Bereg diamondiferous province: Evidence from Rb-Sr age data on kimberlite sills along the Mela River. *Doklady Earth Sciences*, Vol. 407, No. 2, pp. 304–307.
Pesonen L.J., Elming S.-A., Mertanen S., Pisarevsky S., D'Agrella-Filho M.S., Meert J.G., Schmidt P.W., Abrahamsen N., Bylund G. (2003) Palaeomagnetic configuration of continents during the Proterozoic. *Tectonophysics*, Vol. 375, No. 1-4, pp. 289–324, http://dx.doi.org/10.1016/S0040-1951(03)00343-3
Priyatkina N., Khudoley A.K., Ustinov V.N., Kullerud K. (2014) 1.92 Ga kimberlitic rocks from Kimozero, NW Russia: Their geochemistry, tectonic setting and unusual field occurrence. *Precambrian Research*, Vol. 249, pp. 162–179, http://dx.doi.org/10.1016/j.precamres.2014.05.009
Raal F.A. (1958) A new absorption band in diamond and its likely cause. *Proceedings of the Physical Society*, Vol. 71, No. 5, pp. 846–847, http://dx.doi.org/10.1088/0370-1328/71/5/415
Reimink J.R., Chacko T., Stern R.A., Heaman L.M. (2016) The birth of a cratonic nucleus: Lithogeochemical evolution of the 4.02–2.94 Ga Acasta Gneiss Complex. *Precambrian Research*, Vol. 281, pp. 453–472, http://dx.doi.org/10.1016/j.precamres.2016.06.007
Rubanova E.V., Palazhchenko O.V., Garanin V.K. (2009) Diamonds from the V. Grib pipe, Arkhangelsk kimberlite province, Russia. *Lithos*, Vol. 112S, pp. 880–885, http://dx.doi.org/10.1016/j.lithos.2009.04.044
Sablukov L., Sablukov S., Griffin W.L., O'Reilly S.Y., Ryan C.G., Win T.T., Grib V. (1995) Lithosphere evolution in the Arkhangelsk kimberlite province. *Extended Abstracts of the 6th International Kimberlite Conference, Novosibirsk*, pp. 487–489.
Sablukova L.I., Sablukov S., Verichev E., Golovin N. (2003) Mantle xenoliths of the Grib pipe, Zimny Bereg area, Russia. *Extended Abstracts of the 8th International Kimberlite Conference* (FLA-0060).
Samsonov A.V., Larionova Y.O., Sal'nikova E.B. (2009) Isotope geochemistry and geochronology of Paleoproterozoic metakimberlites from Kimozero occurrence (central Karelia). *Proceedings of the 4th Russian Conference on Isotopic Geochronology*, Vol. 2, pp. 158–161.
Schaeffer A.J., Lebedev S. (2013) Global shear speed structure of the upper mantle and transition zone. *Geophysics Journal International*, Vol. 194, No. 1, pp. 417–449, http://dx.doi.org/10.1093/gji/ggt095
Serdyukova A. (2013) The North Diamond: Diamonds in the northwest Russia are a new brilliant spot for the industry. *Rapaport Magazine*, http://eng.alrosa.ru/the-north-diamond-rapaport/
Serdyukova A. (2014) Lucky find in Yakutia. *Rapaport Magazine*, August, pp. 54–57.
Severalmaz recovers first 10 million carats of diamonds at Lomonosov deposit (2017) *Rough & Polished*, http://www.rough-polished.com/en/news/105637.html
Shchukina E.V., Golovin N.N., Malkovets V.G., Pokhilenko N.P. (2012) Mineralogy and equilibrium *P-T* estimates for peridotite assemblages from the V. Grib kimberlite pipe (Arkhangelsk Kimberlite Province). *Doklady Earth Sciences*, Vol. 444, No. 2, pp. 776–781.
Shchukina E.V., Agashev A.M., Golovin N.N., Pokhilenko N.P. (2015) Equigranular eclogites from the V. Grib kimberlite pipe: Evidence for Paleoproterozoic subduction on the territory of the Arkhangelsk diamondiferous province. *Doklady Earth Sciences*, Vol. 462, pp. 497–501.
Shchukina E.V., Agashev A.M., Pokhilenko N.P. (2017) Metasomatic origin of garnet xenocrysts from the V. Grib kimberlite pipe, Arkhangelsk region, NW Russia. *Geoscience Frontiers*, Vol. 8, No. 4, pp. 641–651, http://dx.doi.org/10.1016/j.gsf.2016.08.005
Shevchenko S.S., Lokhov K.I., Sergeev S.A. (2004) Isotope studies in VSEGEI. Prospects of application of results for predicting and search of diamond deposits. *Proceedings of Scientific Practical Conference on Efficiency of Prediction and Search for Diamond Deposits: Past, Present, and Future*, St. Petersburg, pp. 383–387.
Shigley J.E., Chapman J., Ellison R.K. (2001) Discovery and mining of the Argyle diamond deposit, Australia. *G&G*, Vol. 37, No. 1, pp. 26–41, http://dx.doi.org/10.5741/GEMS.37.1.26
Shigley J.E., Shor R., Padua P., Breeding C.M., Shirey S.B., Ashbury D. (2016) Mining diamonds in the Canadian Arctic: The Diavik mine. *G&G*, Vol. 52, No. 2, pp. 104–131, http://dx.doi.org/10.5741/GEMS.52.2.104
Shirey S.B., Shigley J.E. (2013) Recent advances in understanding the geology of diamonds. *G&G*, Vol. 49, No. 4, pp. 188–222, http://dx.doi.org/10.5741/GEMS.49.4.188
Shor R. (1993) Russia to De Beers: We want more control. *Jewelers' Circular Keystone*, Vol. 164, No. 1, pp. 50–60.
Shor R. (2009) Are diamonds Russia's best friend? *Jewellery Chronicles*, May 19, https://jewellerychronicles.wordpress.com/2012/03/09/are-diamonds-russias-best-friend/
Shor R. (2014) Rough diamond auctions: Sweeping changes in pricing and distribution. *G&G*, Vol. 50, No. 4, pp. 252–267, http://dx.doi.org/10.5741/GEMS.50.4.252
Smart K.A., Chacko T., Stachel T., Muehlenbachs K., Stern R.A., Heaman L.M. (2011) Diamond growth from oxidized carbon sources beneath the Northern Slave Craton, Canada: A $\delta^{13}C$–N study of eclogite-hosted diamonds from the Jericho kimberlite. *Geochimica et Cosmochimica Acta*, Vol. 75, No. 20, pp. 6027–

6047, http://dx.doi.org/10.1016/j.gca.2011.07.028
Smit K.V., Shirey S.B., Richardson S.H., le Roex A.P., Gurney J.J. (2010) Re–Os isotopic composition of peridotitic sulphide inclusions in diamonds from Ellendale, Australia: Age constraints on Kimberley cratonic lithosphere. *Geochimica et Cosmochimica Acta*, Vol. 74, No. 11, pp. 3292–3306, http://dx.doi.org/10.1016/j.gca.2010.03.001
Smit K.V., Stachel T., Creaser R.A., Ickert R.B., DuFrane S.A., Stern R.A., Seller M. (2014) Origin of eclogite and pyroxenite from the Victor kimberlite, Canada, and implications for Superior craton formation. *Geochimica et Cosmochimica Acta*, Vol. 125, pp. 308–337, http://dx.doi.org/10.1016/j.gca.2013.10.019
Smith E.M., Wong S.D. (2016) Lab Notes: Diamond inclusion with radiation halo. *G&G*, Vol. 52, No. 1, pp. 69–70.
Sobolev N.V., Yefimova E.S., Reimers L.F., Zakharchenko O.D., Makhin A.I., Usova L.V. (1997) Mineral inclusions in diamonds of the Arkhangelsk kimberlite province. *Russian Geology and Geophysics*, Vol. 38, No. 2, pp. 379–393.
Soviet discounts irk diamond cutters (1984) *Jewelers' Circular Keystone*, 155, D.
Stachel T., Luth R.W. (2015) Diamond formation—Where, when and how? *Lithos*, Vol. 220-223, pp. 200–220, http://dx.doi.org/10.1016/j.lithos.2015.01.028
Stachel T., Brey G.P., Harris J.W. (2005) Inclusions in sublithospheric diamonds: Glimpses of deep Earth. *Elements*, Vol. 1, No. 2, pp. 73–78, pp. http://dx.doi.org/10.2113/gselements.1.2.73
Stachel T., Harris J.W., Hunt L., Muehlenbachs K., Kobussen A., EIMF (2017) Argyle diamonds – how subduction along the Kimberley Craton edge generated the world's biggest diamond deposit. *Society of Economic Geologists Special Publication*, in press.
Stanikovskiy A.F., Danilo M.A., Grib V.P., Sinitsyn A.V. (1974) Explosion pipes of the Onega peninsula. *International Geology Review*, Vol. 16, No. 9, pp. 1009–1017, http://dx.doi.org/10.1080/00206817409471777
Stern R., Bleeker W. (1998) Age of the world's oldest rocks refined using Canada's SHRIMP: The Acasta Gneiss Complex, Northwest Territories, Canada. *Geoscience Canada*, Vol. 25, No. 1, pp. 27–31.
Taylor W.R. (1998) An experimental test of some geothermometer and geobarometer formulations for upper mantle peridotites with application to the thermobarometry of fertile lherzolite and garnet websterite. *Neues Jahrbuch für Mineralogie Abhandlungen*, Vol. 172, pp. 381–408.
Taylor W.R., Jaques A.L., Ridd M. (1990) Nitrogen-defect aggregation characteristics of some Australasian diamonds: Time-temperature constraints on the source regions of pipe and alluvial diamonds. *American Mineralogist*, Vol. 75, pp. 1290–1310.
Taylor W.R., Canil D., Milledge H.J. (1996) Kinetics of Ib to IaA nitrogen aggregation in diamond. *Geochimica et Cosmochimica Acta*, Vol. 60, No. 23, pp. 4725–4733, http://dx.doi.org/10.1016/S0016-7037(96)00302-X
Thompson J. (1982) IDMA attacks Russian diamond threat. *Jewelers' Circular Keystone*, Vol. 153, p. 110.
Timmerman M.J., Daly J.S. (1995) Sm-Nd evidence for late Archaean crust formation in the Lapland-Kola Mobile Belt, Kola Peninsula, Russia and Norway. *Precambrian Research*, Vol. 72, No. 1-2, pp. 97–107, http://dx.doi.org/10.1016/0301-9268(94)00045-S
Titkov S.V., Shigley J.E., Breeding C.M., Mineeva R.M., Zudin N.G., Sergeev A.M. (2008) Natural-color purple diamonds from Siberia. *G&G*, Vol. 44, No. 1, pp. 56–64, http://dx.doi.org/10.5741/GEMS.44.1.56
Tyler I., Page R. (1996) Palaeoproterozoic deformation, metamorphism and igneous intrusion in the central zone of the Lamboo Complex, Halls Creek Orogen. *Geological Society of Australia Abstracts*, Vol. 41, p. 450.
Valley J.W., Cavosie A.J., Ushikubo T., Reinhard D.A., Lawrence D.F., Larson D.J., Clifton P.H., Kelly T.F., Wilde S.A., Moser D.E., Spicuzza M.J. (2014) Hadean age for a post-magma-ocean zircon confirmed by atom-probe tomography. *Nature Geoscience*, Vol. 7, No. 3, pp. 219–223, http://dx.doi.org/10.1038/ngeo2075
Walter M.J. (1998) Melting of garnet peridotite and the origin of komatiite and depleted lithosphere. *Journal of Petrology*, Vol. 39, No. 1, pp. 29–60, http://dx.doi.org/10.1093/petroj/39.1.29
Whalen J.B., Wodicka N., Taylor B.E., Jackson G.D. (2010) Cumberland batholith, Trans-Hudson Orogen, Canada: Petrogenesis and implications for Paleoproterozoic crustal and orogenic processes. *Lithos*, Vol. 117, No. 1-4, pp. 99–118, http://dx.doi.org/10.1016/j.lithos.2010.02.008
van Wyk J.A. (1982) Carbon-12 hyperfine interaction of the unique carbon of the P2 (ESR) or N3 (optical) centre in diamond. *Journal of Physics C: Solid State Physics*, Vol. 15, No. 27, pp. L981–L983.

For More on the Lomonosov Diamonds

To see video detailing the geology, production, and evaluation process at Russia's Lomonosov deposit, visit https://www.gia.edu/gems-gemology/summer-2017-lomonosov-deposit, or scan the QR code on the right.

Carbonado Diamond: A Review of Properties and Origin

Stephen E. Haggerty

Carbonado diamond is found only in Brazil and the Central African Republic. These unusual diamond aggregates are strongly bonded and porous, with melt-like glassy patinas unlike any conventional diamond from kimberlites-lamproites, crustal collisional settings, or meteorite impact. Nearly two centuries after carbonado's discovery, a primary host rock compatible with the origin of conventional diamond at high temperatures and pressures has yet to be identified. Models for its genesis are far-reaching and range from terrestrial subduction to cosmic sources.

Discovered in 1841 in Brazil, carbonado was named by Portuguese diamond prospectors for its resemblance to charcoal (Leonardos, 1937; Dominguez, 1996). Carbonado was found later in the Central African Republic. These two localities, now separated by the Atlantic Ocean and situated on the São Francisco and the Congo cratons, respectively, previously shared a common geological setting for more than a billion years (De Waele et al., 2008) on the supercontinent of Rodinia (figure 1) and its precursor Nuna, also known as Columbia.

Carbonado was prized by the French as a superior polishing material. It was used for drilling during the construction of the Panama Canal and formed part of the U.S. strategic mineral stockpile as recently as 1990. At the height of alluvial mining in Brazil (1850–1870), some 70,000 carats were produced by an estimated 30,000 artisanal miners (Svisero, 1995). A conservative estimate of the recovery from Brazil and the Central African Republic is approximately 2 metric tons (Haggerty, 2014). Four of the five largest diamonds reported from Brazil, ranging in weight from 726 to 3,167 ct, are carbonado (Svisero, 1995). The largest of the five, the Sergio, recovered in 1905, is 61 ct heavier than the largest single-crystal diamond ever reported (the 3,106 ct Cullinan rough).

While earlier investigations of carbonado focused on physical and chemical properties and synthesis, more recent studies have introduced dating techniques, high-resolution microscopy, spectroscopy, and an emphasis on origin (see Haggerty, 2014, for a more comprehensive view). The present study offers a detailed examination of about 800 carbonados from Brazil and the Central African Republic (figure 2), ranging from <1 to 730 ct. These samples showed no significant differences in their texture, superficial appearance, and physical and chemical properties (Haggerty, 2014). This article describes the unusual textural features of carbonado, namely their pores and the presence of glassy diamond as a surface patina, with the aim of assessing the origin of carbonado.

In Brief

- Carbonado, found only in Brazil and the Central African Republic, is distinguished from conventional diamond by its pores, patina, surfaces, and polycrystallinity.
- Although carbonado has been known since 1841, its origin or host rock has yet to be identified.
- The extraterrestrial model of carbonado origin, one of five theories, posits that it formed from carbon-rich, diamond-bearing stellar bodies that were transported to Earth by meteorite about four billion years ago.

See end of article for About the Author and Acknowledgments.
Gems & Gemology, Vol. 53, No. 2, pp. 168–179,
http://dx.doi.org/10.5741/GEMS.53.2.168

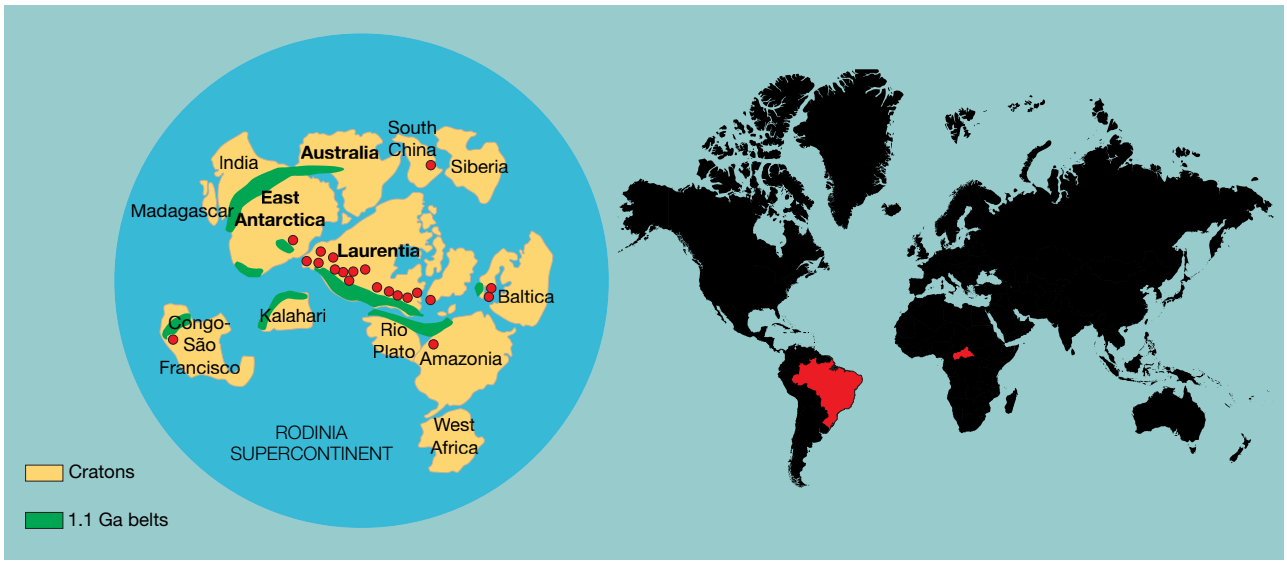

Figure 1. Left: The Congo–São Francisco island in southwest Rodinia, at approximately 1.1 billion years ago (Ga), is the only known site of carbonado that was originally deposited ca. 3.8 Ga on a possibly even smaller cratonic island. Continental masses in Rodinia are underlain by ancient cratons approximately 2.5 to 4.0 Ga. Green zones are 1.1 Ga mountain belts, and the red dots are granite intrusions (Torsvik, 2003).Right: Separation of the microcontinent into two cratonic blocks, now Brazil and the Central African Republic, took place during the breakup of Gondwanaland about 180 million years ago.

CHARACTERISTICS OF CARBONADO

Carbonado is typically found in five major size categories: >200 ct, 75–95 ct, 25–35 ct, 8–15 ct, and 0.25–1.25 ct (see figure 5 of Haggerty, 2014). Sand-sized particles (<1 mm) also occur, and melon-size objects larger than the Sergio are reported but unconfirmed (M. Ozwaldo, pers. comm., 1996). Carbonados are typically equidimensional (in millimeter to centimeter

Figure 2. A: Scene from Chapada Diamantina, the carbonado site in Bahia, Brazil. B: Boulder of Tombodor conglomerate, the carbonado host rock. C: Polished conglomerate surface in a streambed. D: Artisanal mining of Brazilian alluvial carbonado. Photos by Robert Weldon (A and C) and Stephen E. Haggerty (B and D).

Figure 3. The carbonados in the left (118 ct) and center (16.2–52.2 ct) photos are from the Central African Republic, and those on the right (10.8–15.1 ct) are from Brazil. Note the high density of pores, some of which are filled at the surface by crustal infiltrates, and the metallic luster of the glassy melt-like patinas. Photos by Orasa Weldon. GIA Collection numbers 40108–40119; gift of Stephen Haggerty.

sizes), although some are elongated (figure 3); they are seldom rounded.

Carbonado is opaque, composed of randomly oriented diamond crystallites that impede light refraction and increase absorption. Color varies from black and putty gray to shades of brown (figure 3), deep purple to pink, rusty red, and the occasional olive green. Pores (figure 4), an unusual glassy patina (figure 5), highly irregular surfaces (figures 6 and 7), and polycrystallinity (figures 8 and 9) distinguish carbonado from conventional diamonds.

Porosity. As the porosity of an object increases, its apparent density decreases, because the voids take up more and more of the volume. In carbonado, the number of exposed microdiamond cutting points increases with porosity. This was a sought-after property that made carbonado more expensive by weight than diamond at the turn of the twentieth century (Haggerty, 2014). Densities as low as 2.8 g/cm^3 and as high as 3.45 g/cm^3, with most around 3.05 g/cm^3 (Trueb and De Wys, 1969; Haggerty, 2014), are in contrast to gem diamond at 3.52 g/cm^3. Calculated pore concentrations vary between 5% and 15% in volume. The pores persist into the interior of the carbonado and are either spherical or oblate. Some are inferred to be interconnected (Ketcham and Koeberl, 2013), but the material's permeability is very low because the pores are free of infiltrating hydrothermal precipitates that abound in surface pores (again, see figure 4). The spherical pores in carbonado are unlike those in other polycrystalline diamond such as framesite, where the open spaces are at adjoining crystal faces and the shapes are irregularly polyhedral. In other polycrystalline diamonds, the open spaces are microns in width and either radial (in non-gem-quality ballas) or parallel (in fibrous cubes).

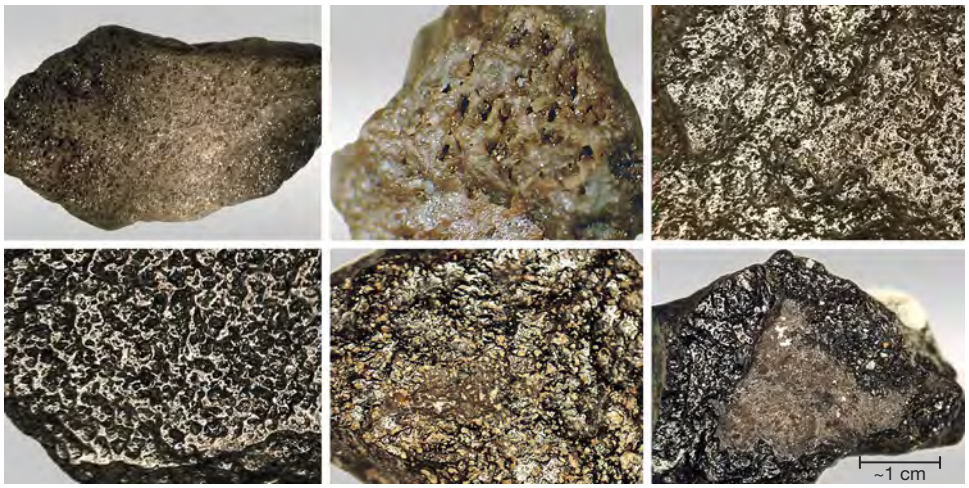

Figure 4. Open pores in carbonado (first five photos) and pores covered by a surface patina of nanodiamond approximately 5 µm thick (lower right). Photos by Stephen E. Haggerty.

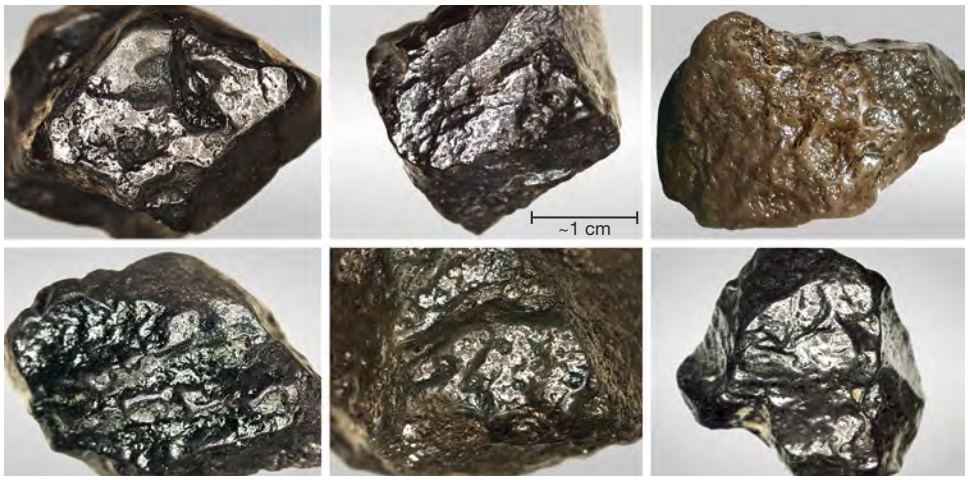

Figure 5. Typical melt-like patinas and flow ornamentation on carbonado. Photos by Stephen E. Haggerty.

Patina. In carbonado, patina surfaces are pervasive (figure 5). Pores in contact with surface patinas are reduced in size, and at 50× magnification they can no longer be distinguished. Glass-like in appearance and similar to synthetic carbon glass (de Heer et al., 2005), these veneers may be dimpled or furrowed, with mounds and flow structures (figures 5 and 6). These textures are akin to those seen in melts in volcanic rocks or in slags from metal processing. But in carbonado, the veneers are diamond that appear to have formed directly from the underlying porous substrates, although diamond coating at a later time is also possible. Contact boundaries between pore-present and pore-absent surfaces are poorly defined, except in cases where patina crusts have splintered off where the contact is sharp, as seen in the lower-right images of figure 6 and in figure 7. Secondary pits and microcraters are pervasive and, in many cases, younger than the patina (figure 7). While pores tend to have sharp outlines (figure 4), craters are rounded with bubbly surfaces or rimmed by smooth ridges (again, see figures 6 and 7). The evidence of flow in both types of voids implies differences in origin. Solid melt marbles are typical. Microcraters, free of ornamentation, grade into texturally soft plastic walls (figures 5 and 6). Slickensides, the striated surfaces known to form on rocks that have been forced to slide along a fracture surface at high pressure as in a fault (figure 7), are of interest because these could only have developed on frictional contact with a body whose hardness was equivalent to another diamond. On the other hand, the patina itself may represent frictional melting (e.g., de Heer et al., 2005; Mitchell et al., 2016; Shumilova et al., 2016a,b; Shiell et al., 2016). Standard diamond testers that measure thermal conductivity give a sharp response to glassy

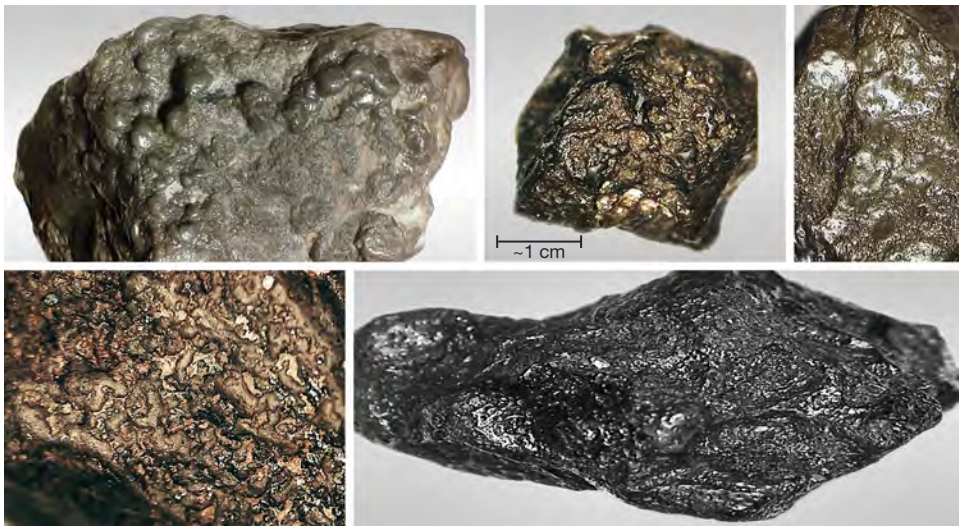

Figure 6. Melt marbles and flow patterns on carbonado. Photos by Stephen E. Haggerty.

Figure 7. Slickenside patterns and melting of vesicular carbonado with later pits and cratering. The melt layer is about 20 µm thick. Photos by Stephen E. Haggerty.

diamond surfaces, less so to the ridges and mounds. The pore-rich surfaces are distinctly sluggish and erratic in response, possibly due to crystal discontinuities of microdiamond grain boundaries.

PHYSICAL AND CHEMICAL PROPERTIES

Octahedra, dodecahedra, tetrahexahedra, and fibrous cubes, all typical of conventional diamond (e.g., Orlov, 1977), are not observed in carbonado. Polycrystalline cubes measuring 5 to approximately 20 µm are common. Encased in very fine diamond (<1–5 µm), the matrix is tightly fused with angular interstices and rounded pores (figure 8). Scanning electron microscopy (SEM) images illustrate the distribution of diamond cleavage surfaces, hopper crystals, skeletal crystallites, re-entrant intergrowths, and layers in single crystals in the open-space pores of carbonado (figures 8 and 9). Trueb and De Wys (1969) and Petrovsky et al. (2010) suggest that the closest analogy to carbonado textures is in synthetically compressed nanodiamond aggregates. Because these structures are found in pores, a more reasonable comparison is with vapor deposition of diamond. The preferred crystal habit of these diamonds is cuboidal, either as single solid cubes or as interpenetrating twins on [111] that follow the fluorite twin law (figure 8). The solid cubes are colorless and, although fine grained, appear to be translucent. Diamond cubes and cuboctahedra are routinely synthesized in metallic catalysts at high pressure and temperature (Burns and Davies, 1992) or by chemical vapor deposition (CVD) under high vacuum and at plasma temperatures (Sato and Kamo, 1992).

X-ray diffraction (XRD) data on crushed carbonado grains are similar to conventional diamonds. Hardness is also similar, but there are data indicating

Figure 8. Brightly reflecting phenocrystic diamond cubes (top row) and twinned diamond clusters (circled) in carbonado. SEM images are black and white. Photomicrographs by Stephen E. Haggerty; SEM images by Sven P. Holbik.

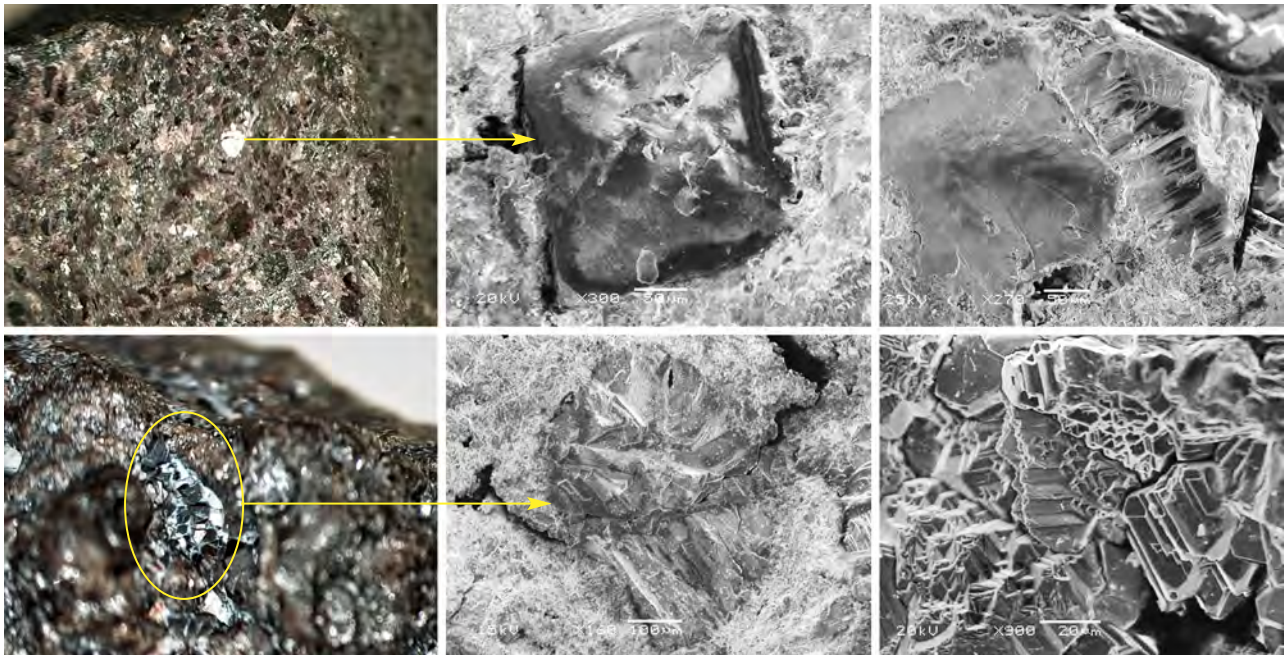

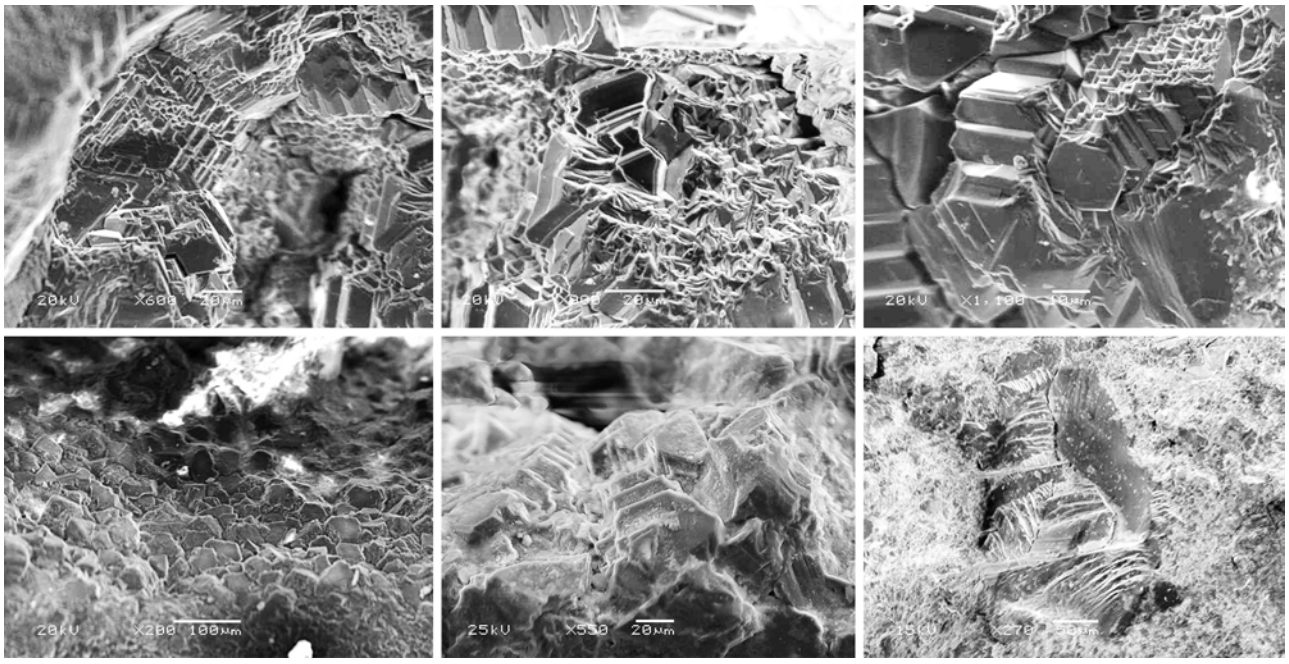

Figure 9. SEM images of euhedral diamonds displaying a variety of morphologies in parallel growth typical of vapor-deposited clusters in the open-space pores of carbonado. Images by Sven P. Holbik.

that carbonado is slightly harder (Haggerty, 2014). Its toughness and tenacity, stemming from the random orientation of microdiamonds, are clearly superior to monocrystalline gem diamond, to the point that carbonado can only be cut by lasers.

Yet another unusual feature of carbonado is the presence of an exotic array of metals (Fe, Ni, Cr, and Ti), metal alloys (Fe-Ni, Fe-Cr, Ni-Cr, and W-Fe-Cr-V), and very unusual minerals, specifically moissanite (SiC) and osbornite (TiN). These phases occur as primary intergranular inclusions or as crystal-controlled oriented intergrowths. They are only stable at the very low oxidation states (Gorshkov et al., 1996; De et al., 1998; Makeev et al., 2002; Jones et al., 2003) that would occur deep within Earth's mantle or other reducing environments such as outer space. By contrast, surface pores and fractures are filled by secondary, low-temperature minerals such as quartz and highly oxidized magnetite, goethite, florencite, and goyazite (Trueb and Butterman, 1969), typical of a more oxidized terrestrial surface growth environment.

Relative to mantle-derived diamonds, carbonado is isotopically light, with $\delta^{13}C = -24$ to -31‰ (Ozima et al., 1991; Shelkov et al., 1997; De et al., 2001). Nitrogen concentrations are low (~20 to 500 ppmw), and $\delta^{15}N$ ranges from –3.6 to 12.8‰ with an average of 3.7‰ (Shelkov et al., 1997; Vicenzi and Heaney, 2001; Yokochi et al., 2008). The coupled isotopic distribution of C and N shows that the compositional field for carbonado is distinctly different from that of conventional diamonds (figure 10).

Figure 11 shows photoluminescence (PL) spectra of carbonado, which are similar to those of irradiated and heated CVD diamond (Clark et al., 1992). The characteristic peaks at 1.945 eV and 2.156 eV are attributed to nitrogen vacancy (NV) defects in type Ib diamonds. Wang et al. (2009) report a substantial amount of nonaggregated N in type Ib diamonds with H2 and H3 defects. Hydrogen-containing defects (H1) and NV defects are also reported by Nadolinny et al. (2003).

Cathodoluminescence of large (approximately 200 μm) monocrystals of diamond in carbonado exhibit orange and green tones (Magee and Taylor, 1999; De et al., 2001; Yokochi et al., 2008). However, blue luminescence in large diamonds, embedded in an orange luminescent matrix of submicron diamond, are also reported (Rondeau et al., 2008). The range in colors is attributed to various N-V (nitrogen-vacancy) defects.

Synchrotron infrared measurements of carbonado have shown the presence of single nitrogen (type Ib) substitution and hydrogen (Garai et al., 2006), in contrast to aggregated N typical of conventional type Ia diamonds that have undergone prolonged high *P-T* annealing in the mantle.

Carbonado has been dated by Ozima and Tatsumoto (1997) and Sano et al. (2002), on samples derived from conglomerates (again, see figure 2) that

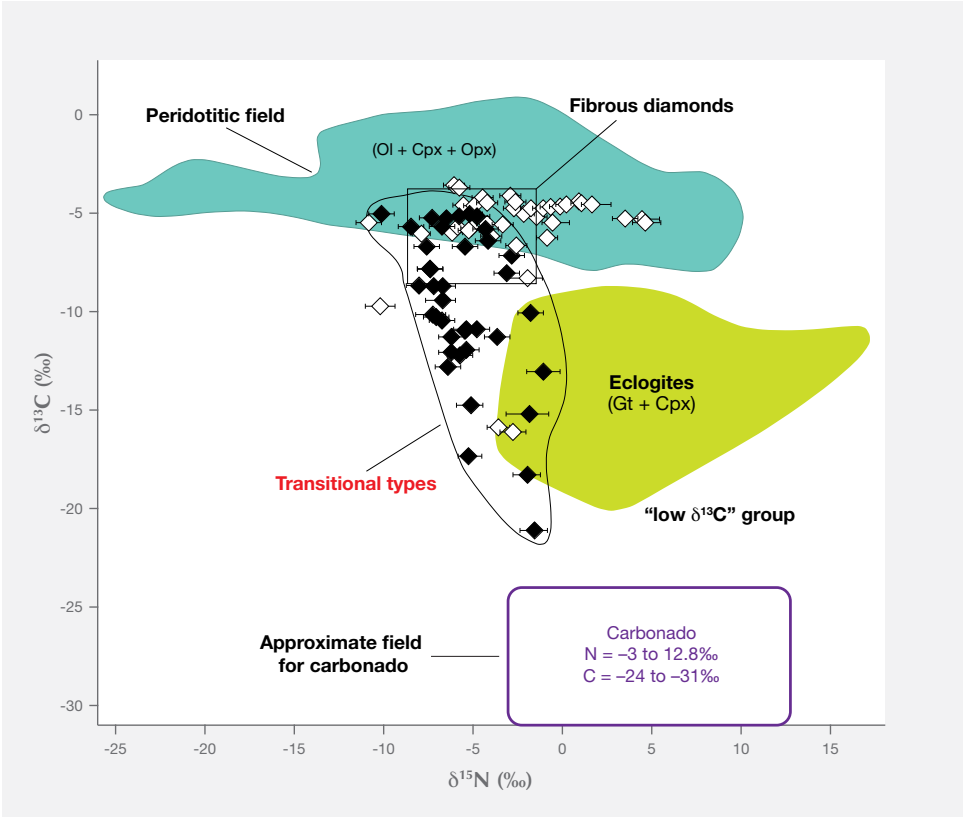

Figure 10. A paired stable isotope plot of C vs. N for conventional diamond (top) and carbonado (bottom). The compositional separation shows that carbonado and deep Earth diamonds are unrelated. Open symbols are for eclogitic diamonds from Kimberley, South Africa; filled symbols are for diamonds from Jwaneng, Botswana; both show extreme variations. The fields for peridotitic (typical inclusions are olivine, clinopyroxene, and orthopyroxene), eclogitic (garnet and clinopyroxene), and fibrous diamonds are from a global database. Data for conventional diamonds are from Cartigny et al. (1998).

have been reworked over a period from at least 1.7 Ga to approximately 3.8 Ga (Pedreira and De Waele, 2008). It is relevant to note that, unlike the dating of conventional diamond, which is based on trapped mineral inclusions (garnet, pyroxene, and sulfides), the age of carbonado discussed in this review was determined directly on diamond. Following a robust chemical protocol of acid dissolution to remove all nondiamond material, the cleansed carbonado was subjected to two different instrumental methods of analyses. Ozima and Tatsumoto (1997) used high-resolution mass spectrometry on carat-sized samples from the Central African Republic, while Sano et al. (2002) employed an ion probe that allowed for micron-sized spot analyses on larger samples from Brazil. Both studies report ages of 2.6–3.8 Ga on implanted radiogenic lead. Although this method of age determination is unconventional, it is important to note that the Archean result is consistent with trapped crustal inclusions (Sano et al., 2002) of zircon (1.7–3.6 Ga), rutile (3.9 Ga), and quartz (3.2 Ga), and with the antiquity of the basement in the São Francisco craton, which is 3.3–3.7 Ga (Barbosa and Sabate, 2004).

In summary, the chemical and physical characteristics of carbonado point to marked similarities with rapidly quenched type Ib diamonds and CVD diamond, both of which contain significant hydrogen. But there are also major differences: carbonado has pores and patinas with distinctions in C and N isotopes, an absence of mantle minerals, and the presence of exotic metal inclusions. Carbonado is unquestionably one of the most unusual forms of diamond ever reported. Because it has never been found in typical diamond-bearing rocks, the many proposed origins are varied, and none are uniformly accepted.

PROPOSED ORIGINS

Theories on the genesis of carbonado fall into five categories:

1. Meteoritic impact (Smith and Dawson, 1985)
2. Growth and sintering in the crust or mantle (Burgess et al., 1998; Ishibashi et al., 2012; Chen and Van Tendeloo, 1999; Heaney et al., 2005; Kagi and Fukura, 2008; Ketcham and Koeberl, 2013)
3. Subduction (De Carli, 1997; Irifune et al., 2004)
4. Radioactive ion implantation of carbon substrates (Kaminsky, 1991; Ozima et al., 1991; Shibata et al., 1993; Kagi et al., 1994; Daulton and Ozima, 1996; Ozima and Tatsumoto, 1997)
5. Extraterrestrial (Haggerty, 1996, 2014)

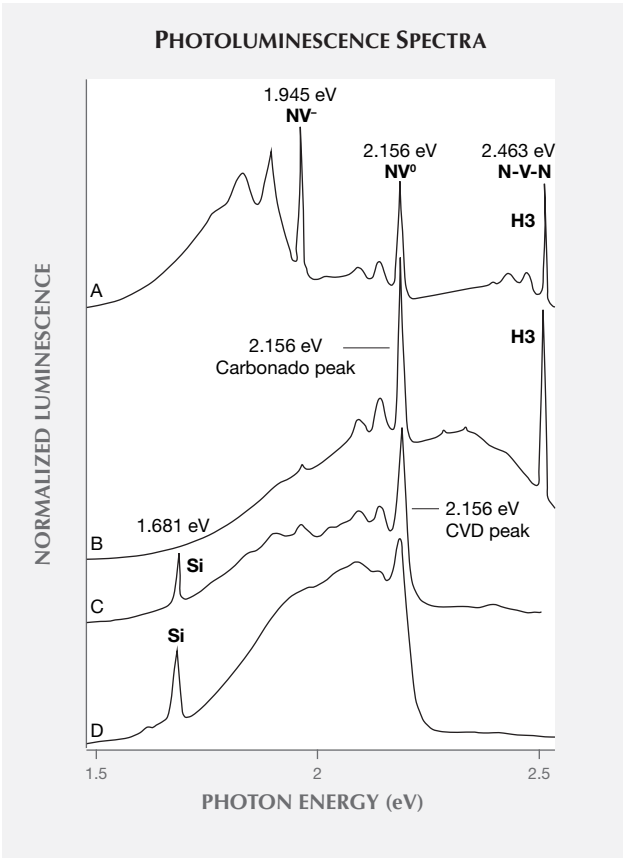

Figure 11. PL spectra illustrating the similarity between carbonado (A and B) and CVD diamond (C) and CVD diamond that has been heated to 1000°C (D). Modified from Clark et al. (1992).

Meteoritic Impact. This model was based on a correlation with the Bangui magnetic anomaly in the Central African Republic. Originally thought to be a buried iron meteorite, it was subsequently shown to be a crustal-derived banded iron ore body (Regan and Marsh, 1982), similar to the magnetic anomaly and giant iron ore deposit in Kursk, Russia (Taylor et al., 2014). Because the C-isotopic composition of carbonado is very light ($\delta^{13}C$ = –21 to –34‰), the presence of biologically derived organic material in the target rocks is assumed. The impact model is unlikely because the C substrate, necessarily of cyanobacteria at ~3.8 Ga, would have been inordinately large (estimated at several cubic km and uncontaminated by crustal material), to account for the estimated two metric tons of carbonado recovered to date (Haggerty, 2014). In addition, the known occurrences of meteorite-impact diamonds (Arizona, United States; Ries, Germany; and Popigai, Russia) are discrete microdiamonds rather than carbonado (Frondel and Marvin, 1967; Hough et al., 1995; Shelkov et al., 1997).

Growth and Sintering in the Crust or Mantle. Some models propose catalytically assisted C-saturated "fluids" in the crust or the mantle. Such fluids provide a source of carbon and a medium capable of drastically decreasing the *P-T* stability limits of diamond from the traditional 5–6 GPa and 1200–1300°C, at a depth of 200 km or more (Shirey and Shigley, 2013). These "fluids" are hydrous, supercritical (i.e., beyond the point of coexisting fluid + vapor), and intensely oxidized so that diamond crystallization is unlikely, and diamond survival even less so. An analogy with loosely aggregated framesite, found in mantle-derived kimberlites, has also been suggested, but is unsatisfactory because the diamonds are semiprecious, free of pores and patina, and lack the highly reduced mineral suite of metals, carbides, and nitrides.

Subduction. Although carbonado is present in metaconglomerates (again, see figure 2), these robustly cemented diamonds are very different from the ultra-high-pressure, subducted, metamorphic diamonds found in continental collision zones in Norway, China, Kazakhstan, Greece, and Germany (Ogasawara, 2005). The diamonds at these localities are single crystals and are armored by zircon, garnet, pyroxene, and amphibole that acted as insulating capsules. Sintering would be necessary to form carbonado. This is possible at high pressures and temperatures in the mantle, but the process would have incorporated one or more mantle minerals such as olivine, garnet, pyroxene, and spinel, none of which are observed. Moreover, the inferred subducted plates are oceanic and basaltic in composition and on transformation at high *P-T* would produce large concentrations of garnet + pyroxene (namely eclogite), which again is not encountered. Transport to Earth's surface is either not considered or is tentatively ascribed to deep mantle volcanic plumes in both the subduction and radiation models (below).

Radioactive Ion Implantation of Carbon Substrates. Radiation-induced diamond is on the scale of nanometers and cannot account for larger diamonds in the micrometer to millimeter size range found in carbonado. Once diamond is formed, low-energy implantation alters the atomic structure and turns the diamond green; high-energy ion doses produce graphite rather than additional diamond (Kalish and Prawer, 1995). There were no coal deposits at 2–3 Ga, and the radia-

tion-induced diamonds recovered from very rare carburanium (U-rich hydrocarbon) are low in abundance and nanometer in size. Proposals of radiation sintering, and even pore formation, are equally untenable.

Extraterrestrial Origin. The extraterrestrial (ET) model was initially proposed because traditional earthbound scenarios failed to account for major characteristics of carbonado, namely diamond porosity, patina, polycrystallinity, rarity, and location (Haggerty, 2014). Pores are incompatible with high-pressure environments; therefore, carbonado cannot have formed under the same conditions in which conventional diamonds form in the mantle at depths of approximately 200 km. The pores in carbonado (again, see figures 3 and 4) are similar to vesicles in basalts that degassed at low pressures under near-surface conditions from a molten or semi-molten magma. This rules out an origin for carbonado in the crust or the mantle, because liquefaction of carbon is not readily accomplished. In fact, diamond is solid in Earth's core (6,380 km and approximately 350 GPa and 7000 K; Bundy et al., 1996; Oganov et al., 2013). Consequently, none of the interpreted melt-like features in carbonado (figures 5–7) can possibly be of terrestrial origin. Furthermore, not a single carbonado has been reported from kimberlite-lamproite suites in the nearly 700 metric tons of diamond mined since about 1900 (Levinson et al., 1992). As noted above, carbonado differs from conventional diamond in several respects:

1. Hydrogen is prominent and N is dispersed, which is the case for <1% of conventional diamonds (i.e., type Ib).
2. Combined N and C isotopes are distinctly not terrestrial (figure 10).
3. There are remarkable similarities to diamonds formed by carbon vapor deposition (figure 11), a process that requires vacuum conditions and plasma temperatures that cannot possibly be accomplished in any natural environment on Earth.
4. Carbonado lacks the characteristic suite of diamond inclusion minerals such as Cr-garnet, Na-Al-pyroxene, Mg-olivine, Mg-chromite, and Fe-Ni-sulfides, and is instead replaced by exotic, reduced metal alloys and minerals.

The ET scenario posits that carbonado originated from carbon-rich, diamond-bearing stellar bodies and/or disrupted C-bearing planets (Haggerty, 2014). All of the characteristic features of carbonado are satisfied: CVD diamond is the sintering glue to microdiamonds in carbonado; the loss of interstellar H produced the pores, and the patina and flow textures are stellar or interstellar high-vacuum melt products. The model further proposes that carbonado was transported to Earth as a large diamond meteorite or as smaller diamond "plums" in a carbonaceous meteoritic matrix, possibly during the Late Heavy Bombardment (3.8–4.2 Ga), in which the inner solar system was pummeled by meteorites (Fassett and Minton, 2013; Abramov et al., 2013). The numerous craters on the moon are considered evidence of the bombardment (Marchi et al., 2013). The theoretical age of this event corresponds to the oldest age determined for carbonado (3.8 ± 1.8 Ga). This would account for its rarity as a single known occurrence on the São Francisco and Congo cratons, which were once joined geologically as the supercontinents of Nuna and Rodinia. Carbonado was undoubtedly widespread during the bombardment, but the carbonado falls were largely into the expansive oceans that existed at that time. Supercontinent disruption and subduction followed, leaving only the preserved remnants of carbonado on an island that is today split between Brazil and the Central African Republic.

The recent discovery of patches of sub-micron diamonds in Libyan desert glass, a high-silica natural glass that is thought to be of cometary origin (Kramers et al., 2013), lends credence to the ET model for carbonado. This view is supported by the growing lines of evidence for (1) synthetically produced diamond-like glass (Shumilova et al., 2016a, b); (2) nanodiamond encased in glassy carbon shells in the interstellar media (Yastrebov and Smith, 2009); and (3) glassy carbon and nanodiamond produced experimentally (Shiell et al., 2016) and in supernova shock waves (Stroud et al., 2011). Another supporting fact is the discovery of asteroid 2008 TC_3, which was tracked upon entering Earth's atmosphere and landed in North Sudan as a fragmented, diamond-bearing ureilite (Miyahara et al., 2015). Unusual in several respects, the meteorite contains diamonds measuring approximately 100 µm. These are exceptionally large for ureilites, whose diamonds typically measure 1–5 µm, and substantially larger than nanodiamonds of pre-solar origin in carbonaceous chondrites. These reports are complemented by the unexpected discovery that Mercury has a crust of graphite, now covered by volcanic rocks but exposed in meteorite craters (Peplowski et al., 2016), that may prove to be diamond bearing.

Figure 12. The origin of carbonado diamond (far right) has yet to be definitively established. Uncovering their formation would represent a scientific breakthrough. Left to right: The 9.49 ct yellow diamond octahedron is a gift of the Oppenheimer Student Collection. The 109.47 ct diamond bort is a gift of Richard Vainer. The 118.01 ct carbonado, a gift of Stephen Haggerty, is from the Central African Republic. GIA Collection nos. 11953, 31602, and 40108. Photo by Robert Weldon/GIA.

CONCLUSIONS

Carbonado (figure 12) is the most unusual form of diamond on Earth. Despite many mineralogical clues not observed in conventional diamonds, its mode of origin remains largely unexplained. Discovering the origin of carbonado would herald a whole new mode of diamond formation and could represent a remarkable form of extraterrestrial carbon delivery to Earth. The extraterrestrial model, although conceptual and supported by astrophysical data, will only be vindicated by the discovery of carbonado in the asteroid belt by remote sensing, or by an observed diamond meteorite fall that is dark in color, porous, and patinaed.

ABOUT THE AUTHOR

Prof. Haggerty is distinguished research professor in the Department of Earth and Environment at Florida International University in Miami.

ACKNOWLEDGMENTS

Fieldwork for this study was supported by a faculty research grant from the University of Massachusetts Amherst, and by De Beers. Laboratory work was supported by the National Science Foundation and Florida International University. Thanks to Jose Ricardo Pisani and the late Jeff Watkins, who provided enormous logistical help and hospitality during fieldwork in Brazil. Thanks also to my many colleagues and critics, from whom I've benefited enormously in active discussions on the controversial issues surrounding the origin of carbonado. And lastly to the reviewers for detailed and constructive comments that led to improvements in presentation. To all I express my sincere appreciation.

REFERENCES

Abramov O., Kring D.A., Mojzsis S.J. (2013) The impact environment of the Hadean Earth. *Chemie der Erde - Geochemistry*, Vol. 73, No. 3, pp. 227–248, http://dx.doi.org/10.1016/j.chemer.2013.08.004

Barbosa J.S.F., Sabate P. (2004) Archean and Paleoproterozoic crust of the São Francisco craton, Bahia, Brazil: Geodynamic features. *Precambrian Research*, Vol. 133, No. 1-2, pp. 1–27, http://dx.doi.org/10.1016/j.precamres.2004.03.001

Bundy F.P., Bassett W.A., Weathers M.S., Hemley R.J., Mao H.U., Goncharov A.F. (1996) The pressure-temperature phase and transformation diagram for carbon; updated through 1994. *Carbon*, Vol. 34, No. 2, pp. 141–153, http://dx.doi.org/10.1016/0008-6223(96)00170-4

Burgess R., Johnson L.H., Mattey D.P., Harris J.W., Turner G. (1998) He, Ar and C isotopes in coated and polycrystalline diamonds. *Chemical Geology*, Vol. 146, No. 3-4, pp. 205–217, http://dx.doi.org/10.1016/S0009-2541(98)00011-4

Burns R.C., Davies G.J. (1992) Growth of synthetic diamond. In J.E. Field, Ed., *The Properties of Natural and Synthetic Diamond*. Academic Press, London, pp. 395–422.

Cartigny P., Harris J.W., Javoy M. (1998) Eclogitic diamond formation at Jwaneng: No room for a recycled component. *Science*, Vol. 280, No. 5368, pp. 1421–1424, http://dx.doi.org/10.1126/science.280.5368.1421

Chen J.H., Van Tendeloo G. (1999) Microstructure of tough polycrystalline natural diamond. *Journal of Electron Microscopy*, Vol. 48, No. 2, pp. 121–129, http://dx.doi.org/10.1093/oxfordjournals.jmicro.a023658

Clark C.D., Collins A.T., Woods G.S. (1992) Absorption and luminescence spectroscopy. In J.E. Field, Ed., *The Properties of Natural and Synthetic Diamond*. Academic Press, London, pp. 35–79.

Daulton T.L., Ozima M. (1996) Radiation-induced diamond formation in uranium-rich carbonaceous materials. *Science*, Vol. 271, No. 5253, pp. 1260–1263, http://dx.doi.org/10.1126/science.271.5253.1260

De Carli P.S. (1997) Carbonado origin: Impact vs. subduction. *Abstract, American Geophysical Union Meeting*, Baltimore, Maryland, S333.

De S., Heaney P.J., Hargraves R.B., Vicenzi E.P., Taylor P.T. (1998) Microstructural observations of polycrystalline diamond: a contribution to the carbonado conundrum. *Earth and Planetary Science Letters*, Vol. 164, No. 3-4, pp. 421–433, http://dx.doi.org/10.1016/S0012-821X(98)00229-5

De S., Heaney P.J., Vicenzi E.P., Wang J.H. (2001) Chemical heterogeneity in carbonado, an enigmatic polycrystalline diamond. *Earth and Planetary Science Letters*, Vol. 185, No. 3-4, pp. 315–330, http://dx.doi.org/10.1016/S0012-821X(00)00369-1

De Waele B., Johnson S.P., Pisarevsky S.A. (2008) Palaeoproterozoic to Neoproterozoic growth and evolution of the eastern Congo Craton: Its role in the Rodinia puzzle. *Precambrian Research*, Vol. 160, No. 1-2, pp. 127–141, http://doi.org/10.1016/j.precamres.2007.04.020

Dominguez J.M.L. (1996) As coberturas plataformais do proterzoico medio e superior (The Middle and Upper Proterozoic). In *Mapa Geologico Do Estado Da Bahia*. Secretaria da Geologia E Recursos Minerais, Salvador, pp. 105–125.

Fassett C.I., Minton D.A. (2013) Impact bombardment of the terrestrial planets and the early history of the solar system. *Nature Geoscience*, Vol. 6, No. 7, pp. 520–524, http://dx.doi.org/10.1038/ngeo1841

Frondel C., Marvin U.B. (1967) Lonsdaleite, a hexagonal polymorph of diamond. *Nature*, Vol. 214, No. 5088, pp. 587–589, http://dx.doi.org/10.1038/214587a0

Garai J., Haggerty S.E., Rekhi S., Chance M. (2006) Infrared absorption investigations confirm the extraterrestrial origin of carbonado diamonds. *The Astrophysical Journal Letters*, Vol. 653, No. 2, pp. L153–L156, http://dx.doi.org/10.1086/510451

Gorshkov A.I., Titkov S.V., Pleshakov A.M., Sivtov A.V., Bershov L.V. (1996) Inclusions of native metals and other mineral phases into carbonado from Ubangi region (Central Africa). *Geology of Ore Deposits*, Vol. 38, pp. 114–119.

Haggerty S.E. (1996) Diamond-carbonado: Models for a new meteorite class of circum-stellar or solar system origin. Abstract, American Geophysical Union, Spring meeting, Baltimore, p. S143.

Haggerty S.E. (2014) Carbonado: Physical and chemical properties, a critical evaluation of proposed origins, and a revised genetic model. *Earth-Science Reviews*, Vol. 130, pp. 49–72, http://dx.doi.org/10.1016/j.earscirev.2013.12.008

Heaney P.J., Vicenzi E.P., De S. (2005) Strange diamonds: The mysterious origins of carbonado and framesite. *Elements*, Vol. 1, No. 2, pp. 85–89, http://dx.doi.org/10.2113/gselements.1.2.85

de Heer W.A., Poncharal P., Berger C., Gezo J., Song Z., Bettini J., Ugarte D. (2005) Liquid carbon, carbon-glass beads, and the crystallization of carbon nanotubes. *Science*, Vol. 307, No. 5711, pp. 907–910, http://dx.doi.org/10.1126/science.1107035

Hough R.M., Gilmour I., Pillinger C.T., Arden J.W., Gilkes K.W.R., Yuan J., Milledge H.J. (1995) Diamond and silicon carbide in impact melt rock from the Ries impact crater. *Nature*, Vol. 378, No. 6552, pp. 41–44, http://dx.doi.org/10.1038/378041a0

Irifune T., Kurio A., Sakamoto S., Inoue T., Sumiya H., Funakoshi K. (2004) Formation of pure polycrystalline diamond by direct conversion of graphite at high pressure and high temperature. *Physics of the Earth and Planetary Interiors*, Vol. 143-144, pp. 593–600, http://dx.doi.org/10.1016/j.pepi.2003.06.004

Ishibashi H., Kagi H., Sakuai H., Ohfuji H., Sumino H. (2012) Hydrous fluid as the growth media of natural polycrystalline diamond, carbonado: Implication from IR spectra and microtextural observations. *American Mineralogist*, Vol. 97, No. 8-9, pp. 1366–1372, http://dx.doi.org/10.2138/am.2012.4097

Jones A.P., Beard A., Milledge H.J., Cressey G., Kirk C., DeCarli P. (2003) A new nitride mineral in carbonado. *Eighth International Kimberlite Conference Abstracts*, Victoria, Canada, p. A95.

Kagi H., Fukura S. (2008) Infrared and Raman spectroscopic observations of Central African carbonado and implications for its origin. *European Journal of Mineralogy*, Vol. 20, No. 3, pp. 387–393, http://dx.doi.org/10.1127/0935-1221/2008/0020-1817

Kagi H., Takahashi K., Hidaka H., Masuda A. (1994) Chemical properties of Central African carbonado and its genetic implications. *Geochimica et Cosmochimica Acta*, Vol. 58, No. 12, pp. 2629–2638, http://dx.doi.org/10.1016/0016-7037(94)90133-3

Kalish R., Prawer S. (1995) Graphitization of diamond by ion impact: Fundamentals and applications. *Nuclear Instruments and Methods in Physics Research Section B*, Vol. 106, No. 1-4, pp. 492–499, http://dx.doi.org/10.1016/0168-583X(95)00758-X

Kaminsky F.V. (1991) Carbonado and yakutite: Properties and possible genesis. In H.O.A. Meyer and O.H. Leonardos, Eds., *Proceedings of the 5th International Kimberlite Conference*, Araxá, Brazil, CPRM Special Publication, pp. 136–143.

Ketcham R.A., Koeberl C. (2013) New textural evidence on the origin of carbonado diamond: An example of 3-D petrography using X-ray computed tomography. *Geosphere*, Vol. 9, No. 5, pp. 1336–1347, http://dx.doi.org/10.1130/GES00908.1

Kramers J.D., Andreoli M.A.G., Atanasova M., Belyanin G.A., Blocke D.L., Franklyn C., Harris C., Lekgoathi M., Montross C.S., Ntsoane T., Pischedda V., Segonyane P., Viljoen K.S., Westraadt J.E. (2013) Unique chemistry of a diamond-bearing pebble from the Libyan Desert Glass strewnfield, SW Egypt: Evidence for a shocked comet fragment. *Earth and Planetary Science Letters*, Vol. 382, pp. 21–31, http://dx.doi.org/10.1016/j.epsl.2013.09.003

Leonardos O.H. (1937) *Diamante e Carbonado no Estado da Bahia*. Metallurgia Servisio De Fomento da Produccao Mineral, Vol. 19, pp. 1–23.

Levinson A.A., Gurney J.J., Kirkley M.B. (1992) Diamond sources and production: Past, present, and future. *G&G*, Vol. 28, No. 4, pp. 234–254, http://dx.doi.org/10.5741/GEMS.28.4.234

Magee C.W., Taylor W.R. (1999) Constraints from luminescence on the history and origin of carbonado. In J.J. Gurney et al., Eds., *Proceedings of the VIIth International Kimberlite Conference*, Red Roof Design Publications, Cape Town, pp. 529–532.

Makeev A.B., Ivanuch W., Obyden S.K., Saparin G.V., Filippov V.N. (2002) Mineralogy, composition of inclusions, and cathodoluminescence of carbonado from Bahia State, Brazil. *Geology of Ore Deposits*, Vol. 44, No. 2, pp. 87–102.

Marchi S., Bottke W.F., Cohen B.A., Wünnemann K., Kring D.A., McSween H.Y., De Sanctis M.C., O'Brien D.P., Schenk P., Raymond C.A., Russell C.T. (2013) High-velocity collisions from the lunar cataclysm recorded in asteroidal meteorites. *Nature Geoscience*, Vol. 6, No. 4, pp. 303–307, http://dx.doi.org/10.1038/ngeo1769

Mitchell T.M., Toy V., Di Toro G., Renner J., Sibson R.H. (2016) Fault welding by pseudotachylyte formation. *Geology*, Vol. 44, No. 12, pp. 1059–1062, http://dx.doi.org/10.1130/G38373.1

Miyahara M., Ohtani E., El Goresy A., Lin Y., Feng L., Zhang J.-C., Gillet P., Nagase T., Muto J., Nishijima M. (2015) Unique large diamonds in an ureilite from Almahata Sitta 2008 TC_3 asteroid. *Geochimica et Cosmochimica Acta*, Vol. 163, pp. 14–26, http://dx.doi.org/10.1016/j.gca.2015.04.035

Nadolinny V.A., Shatsky V.S., Sobolev N.V., Twitchen D.J., Yuryeva O.P., Vasilevsky I.A., Lebedev V.N. (2003) Observation and interpretation of paramagnetic defects in Brazilian and Central African carbonados. *American Mineralogist*, Vol. 88, No. 1, pp. 11–17, http://dx.doi.org/10.2138/am-2003-0102

Oganov A.R., Hemley R.J., Hazen R.M., Jones A.P. (2013) Structure, bonding, and mineralogy of carbon at extreme conditions. In R.M Hazen, A.P. Jones., and J.A. Baross, Eds., *Carbon in Earth*. Reviews in Mineralogy & Geochemistry, Vol. 75. Mineralogical Society of America, Chantilly, VA, pp. 47–77.

Ogasawara Y. (2005) Microdiamonds in ultrahigh-pressure metamorphic rocks. *Elements*, Vol. 1, No. 2, pp. 91–96, http://dx.doi.org/10.2113/gselements.1.2.91

Orlov Y.L. (1977) *The Mineralogy of the Diamond*. John Wiley & Sons, New York, 235 pp.

Ozima M., Tatsumoto M. (1997) Radiation-induced diamond crystallization: Origin of carbonados and its implications on meteorite nano-diamonds. *Geochimica et Cosmochimica Acta*, Vol. 61, No. 2, pp. 369–376, http://dx.doi.org/10.1016/S0016-7037(96)00346-8

Ozima M., Zashu S., Tomura K., Matsuhisa Y. (1991) Constraints from noble-gas contents on the origin of carbonado diamonds. *Nature*, Vol. 351, No. 6326, pp. 472–474, http://dx.doi.org/10.1038/351472a0

Pedreira A.J., De Waele B. (2008) Contemporaneous evolution of the Paleoproterozoic-Mesoproterozoic sedimentary basins of the São Francisco–Congo craton. In R.J. Pankhurst, R.A.J. Trouw, B.B. de Brito Neves, and M.J. De Wit, Eds., *West Gondwana: Pre-Cenozoic Correlations across the South Atlantic Region*. Geological Society of London Special Publication 294, pp. 33–48.

Peplowski P.N., Klima R.L., Lawrence D.J., Ernst C.M., Denevi B.W., Frank E.A., Goldsten J.O., Murchie S.L., Nittler L.R., Solomon S.C. (2016) Remote sensing evidence for an ancient carbon-bearing crust on Mercury. *Nature Geoscience*, Vol. 9, No. 4, pp. 273–276, http://dx.doi.org/10.1038/ngeo2669

Petrovsky V.A., Shiryaev A.A., Lyutoev V.P., Sukharev A.E., Martins M. (2010) Morphology and defects of diamond grains in carbonado: Clues to carbonado genesis. *European Journal of Mineralogy*, Vol. 22, No. 1, pp. 35–47, http://dx.doi.org/10.1127/0935-1221/2010/0022-1978

Regan R.D., Marsh B.D. (1982) The Bangui magnetic anomaly: Its geological origin. *Journal of Geophysical Research: Solid Earth*. Vol. 87, No. B2, pp. 1107–1120, http://dx.doi.org/10.1029/JB087iB02p01107

Rondeau B., Sautter V., Barjon J. (2008) New columnar texture of carbonado: Cathodoluminescence study. *Diamond and Related Materials*, Vol. 17, No. 11, pp. 1897–1901, http://dx.doi.org/10.1016/j.diamond.2008.04.006

Sano Y., Yokochi R., Terada K., Chaves M.L., Ozima M. (2002) Ion microprobe Pb–Pb dating of carbonado, polycrystalline diamond. *Precambrian Research*, Vol. 113, No. 1-2, pp. 155–168, http://dx.doi.org/10.1016/S0301-9268(01)00208-X

Sato Y., Kamo M. (1992) Synthesis of diamond from the vapor phase. In J.E. Field, Ed., *The Properties of Natural and Synthetic Diamond*, pp. 423–469. Academic Press, London.

Shelkov D., Verkhovsky A.B., Milledge H.J., Pillenger C.T. (1997) Carbonado: A comparison between Brazilian and Ubangui sources with other forms of microcrystalline diamond based on carbon and nitrogen isotopes. *Russian Geology and Geophysics*, Vol. 38, No. 2, pp. 315–322.

Shibata K., Kamioka H., Kaminsky F.V., Koptil V.I., Svisero D.P. (1993) Rare earth element patterns of carbonado and yakutite: Evidence for their crustal origin. *Mineralogical Magazine*, Vol. 57, No. 389, pp. 607–611, http://dx.doi.org/10.1180/minmag.1993.057.389.05

Shiell T.B., McCulloch D.G., Bradby J.E., Haberl B., Boehler R., McKenzie D.R. (2016) Nanocrystalline hexagonal diamond formed from glassy carbon. *Scientific Reports*, Vol. 6, No. 1, article no. 37232, http://dx.doi.org/10.1038/srep37232

Shirey S.B., Shigley J.E. (2013) Recent advances in understanding the geology of diamonds. *G&G*, Vol. 49, No. 4, pp. 188–222, http://dx.doi.org/10.5741/GEMS.49.4.188

Shumilova T.G., Isaenko S.I., Tkachev S.N. (2016a) Diamond formation through metastable liquid carbon. *Diamond and Related Materials*, Vol. 62, pp. 42–48, http://dx.doi.org/10.1016/j.diamond.2015.12.015

Shumilova T.G., Tkachev S.N., Isaenko S.I., Shevchuk S.S., Rappenglück M.A., Kazakov V.A. (2016b) A "diamond-like star" in the lab. Diamond-like glass. *Carbon*, Vol. 100, pp. 703–709, http://dx.doi.org/10.1016/j.carbon.2016.01.068

Smith J.V., Dawson J.B. (1985) Carbonado: Diamond aggregates from early impacts of crustal rocks? *Geology*, Vol. 13, No. 5, pp. 342–343, http://dx.doi.org/10.1130/0091-7613(1985)13%3C342:CDAFEI%3E2.0.CO;2

Stroud R.M., Chisholm M.F., Heck P.R., Alexander C.M.O'D., Nittler L.R. (2011) Supernova shock-wave-induced co-formation of glassy carbon and nanodiamond. The *Astrophysical Journal Letters*, Vol. 738, No. 2, pp. L27–L32, http://dx.doi.org/10.1088/2041-8205/738/2/L27

Svisero D.P. (1995) Distribution and origin of diamonds in Brazil: An overview. *Journal of Geodynamics*, Vol. 20, No. 4, pp. 493–514, http://dx.doi.org/10.1016/0264-3707(95)00017-4

Taylor P.T., Kis K.I., Wittmann G. (2014) Satellite-altitude horizontal magnetic gradient anomalies used to define the Kursk magnetic anomaly. *Journal of Applied Geophysics*, Vol. 109, pp. 133–139, http://dx.doi.org/10.1016/j.jappgeo.2014.07.018

Torsvik T.H. (2003) The Rodinia jigsaw puzzle. *Science*, Vol. 300, No. 5624, pp. 1379–1381, http://dx.doi.org/10.1126/science.1083469

Trueb L.F., Butterman W.C. (1969) Carbonado: A microstructural study. *American Mineralogist*, Vol. 54, No. 3-4, pp. 412–425.

Trueb L.F., De Wys E.C. (1969) Carbonado: Natural polycrystalline diamond. *Science*, Vol. 165, No. 3895, pp. 799–802, http://dx.doi.org/10.1126/science.165.3895.799

Vicenzi E.P., Heaney P.J. (2001) The carbon and nitrogen isotopic composition of carbonado diamond: an *in-situ* study. *Eleventh Annual VM Goldschmidt Conference*, A513.

Wang W., Lu R., Moses T. (2009) Photoluminescence features of carbonado diamonds. GIA News from Research, July 21, https://www.gia.edu/gia-news-research-nr72109

Yastrebov S., Smith R. (2009) Nanodiamonds enveloped in glassy carbon shells and the origin of the 2175 Å optical extinction feature. *The Astrophysical Journal*, Vol. 697, No. 2, pp. 1822–1826, http://dx.doi.org/10.1088/0004-637X/697/2/1822

Yokochi R., Ohnenstetter D., Sano Y. (2008) Intragrain variation in $\delta^{13}C$ and nitrogen concentration associated with textural heterogeneities of carbonado. *Canadian Mineralogist*, Vol. 46, No. 5, pp. 1283–1296, http://dx.doi.org/10.3749/canmin.46.5.1283

PHOTOLUMINESCENCE MAPPING OF OPTICAL DEFECTS IN HPHT SYNTHETIC DIAMOND

Lorne C. Loudin

Photoluminescence (PL) mapping provides a means to identify the distribution of optical centers in diamond. To demonstrate the impact of this method on the field of gemology and the study of diamonds, photoluminescence maps were acquired from a laboratory-irradiated brownish orange HPHT synthetic diamond of mixed diamond type. Acquisition time for each PL map was less than four minutes. Analysis of the maps confirmed that optical centers are incorporated in diamond growth sectors, such as {111} octahedral, {100} cubic, {110} dodecahedral, and {113} trapezohedral. The remarkable correlation between optical defects and growth sectors in the sample demonstrates that high-speed photoluminescence mapping is ideal for rapidly determining the distribution of optical defects resulting from both diamond growth and treatments. We anticipate that this technique will allow gemological labs to continue to identify increasingly sophisticated synthetic diamonds and color treatments, helping to ensure consumer confidence in the diamond industry.

In Brief

- Photoluminescence mapping provides an additional tool for gemological laboratories to identify diamond synthetics and color treatments.
- A Raman imaging microscope with an electron-multiplying charge-coupled device can produce PL maps that reveal the spatial distribution of optical defects.
- Analysis of PL maps also reveals information about the nature and formation of these optical defects.

Optical centers in a diamond's crystal lattice, also known as point defects, absorb visible light to produce color (Collins, 1982). In this way, optical centers give rise to the variety of fancy-color diamonds available in the trade. Optical centers can form as a result of impurities in the diamond (such as nitrogen or boron), deformation of the crystal lattice, missing carbon atoms (vacancies), or a combination of these (Collins, 2003; Breeding and Shigley, 2009). Photoluminescence occurs when an optical center is excited to a higher energy state by the absorption of photons and then returns to its ground energy state, emitting light at a specific wavelength or band of wavelengths (Collins, 1992; Eaton-Magaña and Breeding, 2016). There are currently several hundred known optical centers in diamond that produce photoluminescence (e.g., Collins, 1999; Zaitsev, 2001).

Photoluminescence (PL) spectroscopy is a powerful tool used in gemological laboratories to verify whether a specimen is natural or synthetic and determine whether its color origin is natural or due to treatment (Eaton-Magaña and Breeding, 2016). One drawback is that spectra are often collected from a single spot, or a few spots, on the sample surface and therefore represent only a tiny fraction of the entire sample (figure 1). In general, the spectra collected are sufficient for a trained gemologist to determine the diamond's origin, especially when the PL spectra are interpreted in concert with DiamondView images, Fourier-transform infrared (FTIR) spectra, and other absorption and luminescence data. However, as synthetic diamond technology improves for both HPHT- and CVD-grown diamonds (e.g., Moe et al., 2016; Wang and Poon, 2016; Law and Wang, 2016; Eaton-Magaña and Shigley, 2016), and color treatments advance (e.g., Moe et al., 2015; Ardon and Loudin, 2016), gemological laboratories must introduce new techniques to continue to identify all synthetic and treated diamonds.

See end of article for About the Author and Acknowledgments.
GEMS & GEMOLOGY, Vol. 53, No. 2, pp. 180–188,
http://dx.doi.org/10.5741/GEMS.53.2.180

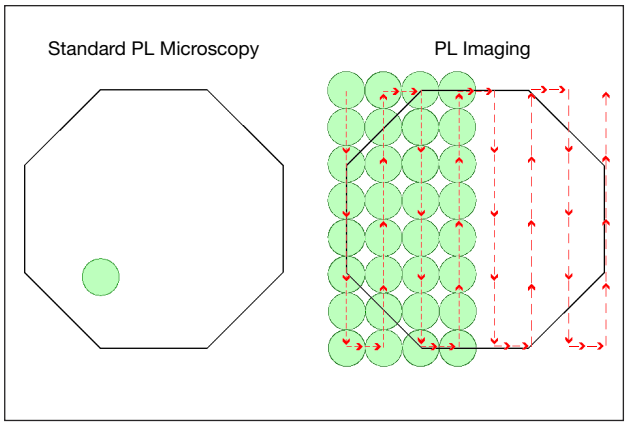

Figure 1. Schematic representation comparing PL methods. With standard PL microscopy, a single spot (shown as a green circle in the figure) is analyzed and represents only a small volume of the actual sample. With PL mapping, numerous spots are collected in a raster pattern (indicated by the dashed red arrows on the right), and the data are interpolated and combined to produce a PL map. Spot size is not to scale.

One useful technique is PL mapping (Eaton-Magaña and Breeding, 2016), which can be used to plot the distribution of an optical defect's intensity. A PL mapping microscope can collect thousands of spectra in a raster pattern by either continuously scanning the sample's surface or by moving from one point to another (pixel to pixel) and collecting a spectrum at each point. The spectral data are then interpolated and combined to produce a map of a defect's distribution (again, see figure 1). PL mapping was first used for gemological purposes in the summer of 2015; the first public demonstration of the technique was by Johnson et al. (2015) at the annual Geological Society of America conference in Baltimore. The technique was further developed by Dieck et al. (2015) to show the distribution of the silicon vacancy (SiV^-) in a CVD synthetic diamond. Ardon and Loudin (2016) used PL mapping to show the influence of focused beam irradiation on the distribution of nitrogen vacancies. Most recently, Johnson and Myagkaya (2017) used PL mapping to show the relationship between SiV^- and Ni^+ in an HPHT synthetic diamond.

One major challenge to implementing a PL mapping technique is that PL emission is temperature dependent. Therefore, the diamond must be cooled to liquid nitrogen temperature (approximately 77 K, or –321°F) to produce sharp PL bands (Collins, 1982; Eaton-Magaña and Breeding, 2016). Overcoming this challenge requires that the diamond be cooled in either a cryogenic stage or an open bath of liquid nitrogen. If the open-bath cooling method is used, then a high-speed mapping technique is needed because the liquid nitrogen boils off and vaporizes at atmospheric temperature and pressure. Using a Raman imaging microscope equipped with an electron-multiplying charge-coupled device (EMCCD), we were able to efficiently produce PL maps in less than four minutes, allowing us to overcome the temperature/time constraints and evaluate the distribution of optical centers in our synthetic diamond sample. Here we present an introduction to PL mapping and demonstrate the technique's effectiveness by reporting the distribution of optical defects in an HPHT synthetic diamond.

MATERIALS AND METHODS

GIA's New York laboratory received an irradiated 1.06 ct Fancy Deep brownish orange HPHT synthetic diamond of mixed type (figure 2) for a synthetic colored diamond grading report. Absorption features typical of both type IIb and type Ib diamonds were observed in the specimen's infrared absorption spectrum (figure 3). The type IIb component, attributed to boron in the diamond lattice, was identified by absorptions at 2803 and 2930 cm^{-1}. The type Ib component, composed of isolated nitrogen in the form of C centers, was identified by

Figure 2. This irradiated 1.06 ct Fancy Deep brownish orange HPHT-grown synthetic diamond of mixed type was examined in the study. Photo by Towfiq Ahmed.

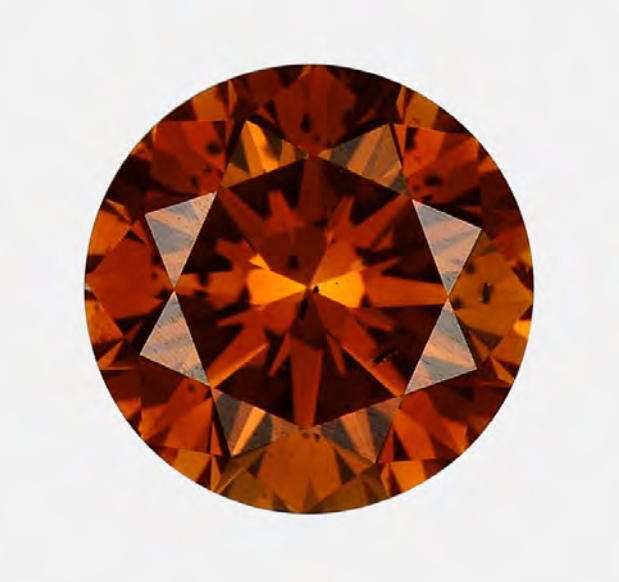

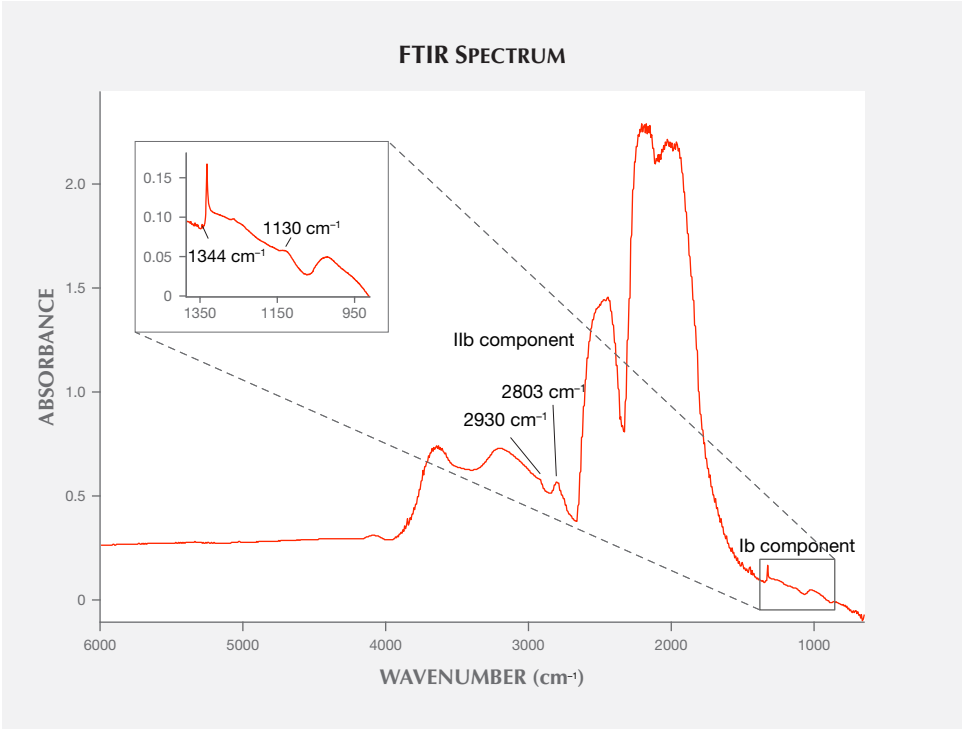

Figure 3. This FTIR spectrum showing both IIb and Ib (inset) peaks in the synthetic diamond sample.

infrared absorptions at 1130 and 1344 cm^{-1}. DiamondView images showed growth sectors corresponding to the {100} cubic, {111} octahedral, {110} dodecahedral, and {113} trapezohedral sectors (figure 4). PL spectra collected using a Renishaw inVia Raman microscope with 488, 514, and 830 nm laser excitation wavelengths revealed several PL features, including well-known defects such as NV^0 at 575 nm and NV^- at 637 nm, as well as several lesser-known defects such as 550.5 nm (figure 5). The combination of well-defined growth sectors and abundant optical defects made this sample well suited for demonstrating the effectiveness of PL imaging microscopy in mapping the distribution of optical defects in diamond.

PL mapping was performed at GIA's New York laboratory. Prior to mapping, the pavilion facets were coated with Pelco colloidal graphite to reduce the amount of light reflecting off the pavilion facet junctions and returning to the table. Additionally, the sample was mounted with the table level. Mapping was conducted using a Thermo Scientific DXRxi Raman imaging microscope with 455, 532, 633, and 780 nm laser excitation wavelengths. The DXRxi is equipped with an Olympus optical microscope and an Andor Technology Newton 970 EMCCD. An Olympus 10×, 0.25 numerical aperture objective lens was used.

The DXRxi uses a continuously moving, variable-speed sample stage driven by a combination of linear magnetic motors and controlled by optical encoders. The stage movement is synchronized with the

Figure 4. This DiamondView image of the synthetic diamond shows the {111}, {100}, {110}, and {113} growth sectors. For an overview of growth sector distribution in HPHT synthetic diamond, please see figure 5 in Welbourn et al. (1996).

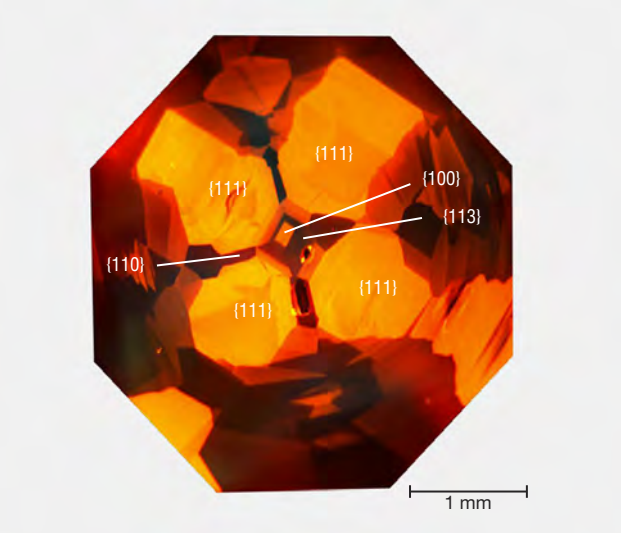

TABLE 1. Analytical conditions and Raman imaging microscope settings for each laser excitation wavelength.

	Laser wavelength (nm)			
	455	532	633	780
Grating (lines/mm)	1200	400	600	400
Laser power (mW)	5.9	0.3	8	24
Exposure time (ms)	1.67	1.67	1.67	8.33
Pinhole aperture size (μm)	50	25	50	50
Pixel size (μm)	15	15	15	25
EM gain	Off	Off	Off	Off
Total spectra	61,005	60,270	59,535	21,756
Collection time (min)	3.4	3.4	3.3	3.8

EMCCD detector exposures so that the spectra are collected at the desired positions with repeatability within 100 nm (A. Rzhevskii, pers. comm., 2016). For each laser excitation, the sample was analyzed at liquid nitrogen temperature to produce sharp PL peaks. The combination of an EMCCD detector and a variable-speed, exposure-synchronized stage allowed the DXRxi to produce high-quality PL maps while maintaining the appropriate temperature and level of liquid nitrogen. Table 1 summarizes the analytical conditions used for each laser excitation. The data were processed using Thermo Scientific's OMNICxi analysis software package, and baseline-corrected peak area profiles were used to produce the observed PL maps.

RESULTS

For each laser excitation wavelength, representative PL maps of the baseline-corrected peak area intensity are shown in figure 6. The maps are interpreted using a color scale. Warmer colors indicate a region that contains a greater intensity of a defect, while cooler colors represent lower intensities of that defect. The

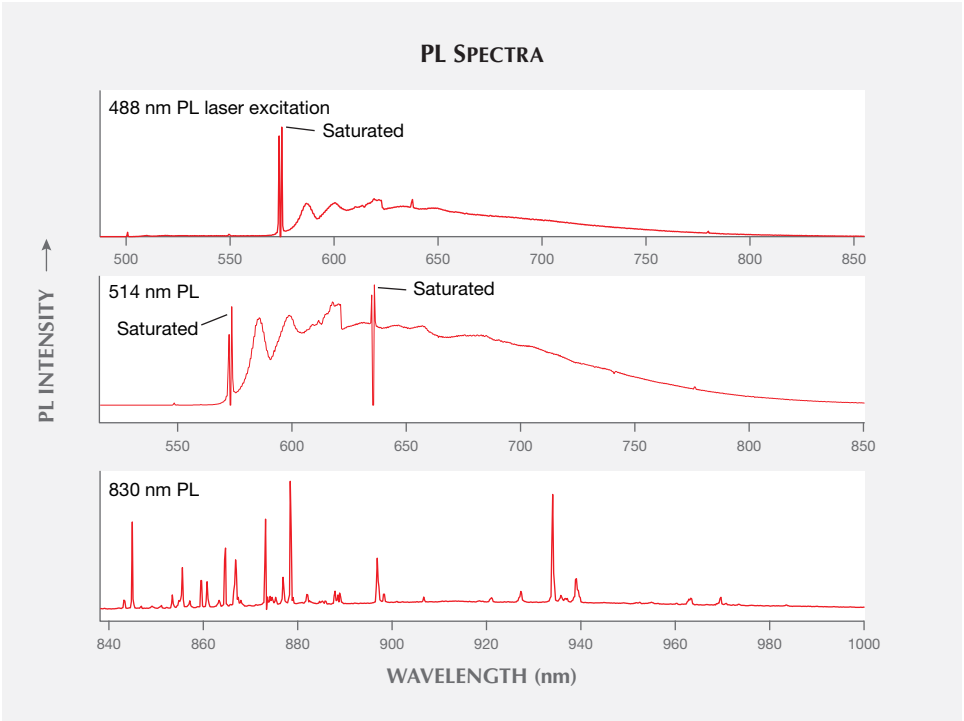

Figure 5. Note the variety of PL peaks in these photoluminescence spectra, specifically at 830 nm excitation.

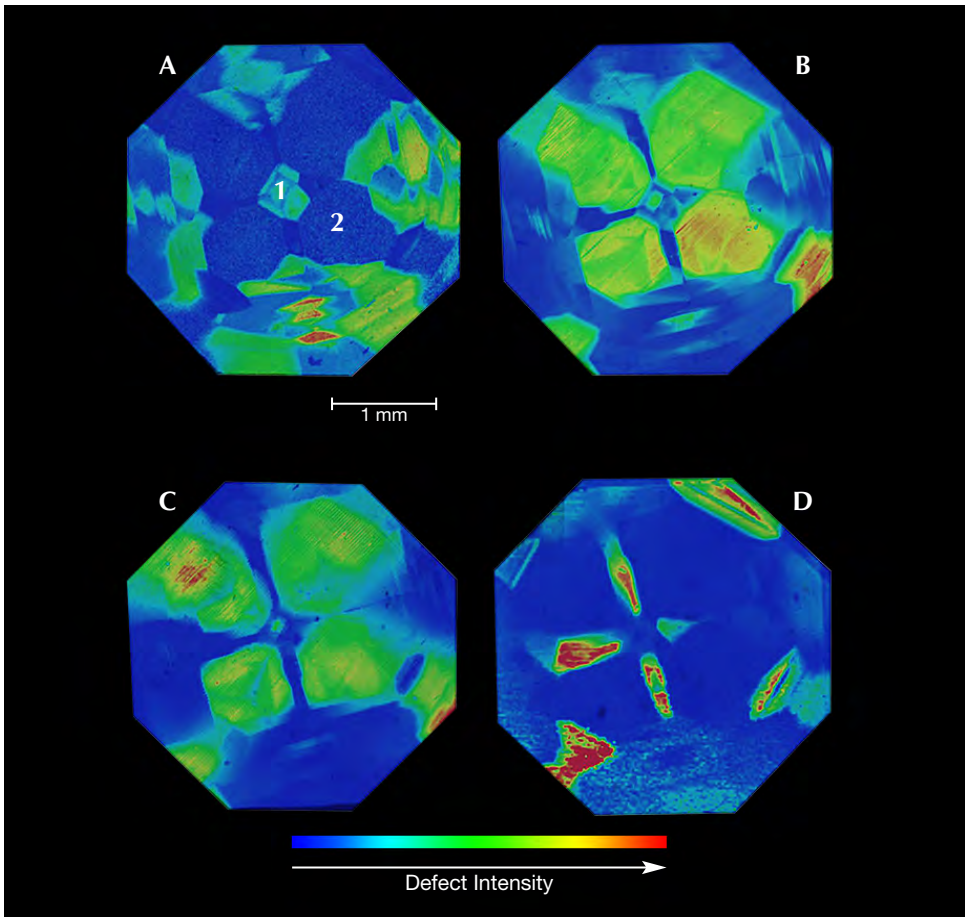

Figure 6. Representative PL images of the baseline-corrected peak area intensity for each laser excitation wavelength. A: The peak area distribution of the 508.8 nm peak (455 nm excitation). Points 1 and 2 represent the regions used for average spectra in figure 7. B: The peak area distribution of the 574.9 nm peak (532 nm excitation). C: The peak area distribution of the 637 nm peak (633 nm excitation). D: The peak area distribution of the 815.1 nm peak (780 nm excitation).

scale for each map depends on the defect's minimum and maximum intensity. To fully interpret the map, the spatial distribution of the defect must be taken in combination with the PL spectra. Figure 7 shows the average spectra from the {100} and {111} growth sectors around points 1 and 2 in figure 6A. Table 2 summarizes the peak area distribution per growth sector for a majority of the peaks observed in the DXRxi spectra. The data presented here are qualitative and are used for the purpose of demonstrating the technique.

The PL map in figure 6A, collected using the 455 nm laser, shows the peak area distribution of a band at 508.8 nm. The four growth sectors in the map—{100}, {111}, {110}, and {113}—correspond to those observed in the DiamondView image in figure 4. The peak area for the 508.8 nm band is greatest in the {100} sector, followed by {113} and {111}, respectively. The 508.8 band is undetectable in {110}. The same distribution is observed for the 470.1 nm peak. A band located at 506.1 nm displays a peak area distribution greatest in {113}; the band is also present in {110}, at approximately half the intensity in {113}. The remaining peaks listed in table 2 for the 455 nm laser were most intense in the {111} growth sector.

The relative peak area distributions for the 532 nm laser are summarized in table 2. Figure 6B shows the peak area distribution for the 575 nm PL band caused by NV^0. For NV^0, the {100}, {111}, {110}, and {113} growth sectors are all visible and correspond with the DiamondView image (again, see figure 4). The NV^0 band has the greatest peak area in the {111} growth sector, with the second-greatest intensity found in {100}. The NV^0 peak area is an order of magnitude lower in the {113} and {110} sectors than in {100}. The peak area distribution for NV^- at 637 nm follows a similar distribution. The peak area intensity of the NV^- center is approximately two times greater in the {111} sector than in {100}. The peak area for the GR1 defect at 741 nm was greatest in the {110} and {113} growth sectors; it was not present in the {111} and {100} sectors. Similar results for both NV^- and GR1 were observed in PL maps obtained using the 633 nm laser.

The peak area distribution for the NV^- center at 637 nm collected using the 633 nm laser is shown in figure 6C. Peak area distributions for the NV^- center

TABLE 2. Relative peak distribution per growth sector measured by the Raman imaging microscope using various laser excitation wavelengths.

Laser	Peak position (nm)	Peak intensity[a] per growth sector
455 nm	470.1	{100}>{113}>{111}>>{110}
	489.4	{111}≥{100}>>{113}
	490.2	{111}>{100}>{113}
	490.9	{111}≥{100}>{113}
	492.0	{111}≥{100}>{113}
	503.2	{111}≥{100}>{113}>>{110}
	506.1	{113}≥{110}
	508.8	{100}>{113}>{111}>>{110} (fig. 6A)
	517.6	{111}>>{110}
	537.8	{111}
532 nm	550.7	{111}>{100}
	574.9	{111}>{100}>>{113}>{110} (fig. 6B)
	636.9	{111}>{100}>>{113}>{110}
	741.0	{110}>{113}
633 nm	637.0	{111}>{100}>{113}≈{110} (fig. 6C)
	648.1	{111}
	662.5	{100}>{111}>>{113}
	676.2	{100}≈{111}>>{113}
	681.1	{100}>{111}>{113}
	684.0	{110}>{113}
	718.2	{111}>{100}>{113}
	741.1	{110}>{113}>{100}>>{111}
780 nm	795.7	{111}
	815.1	{110}>{113}>{100}>{111} (fig. 6D)
	816.9	{111}
	823.8	{110}>{113}>{100}≈{111}
	828.8	{110}>>{113}
	833.0	{110}>>{113}
	843.2	{110}>{100}>{113}>{111}
	845.0	{110}>{113}>{111}>{100}
	849.4	{111}
	853.5	{110}>{113}>>{100}≈{111}
	855.6	{110}>{113}>{111}>{100}
	859.6	{110}>>{113}>{100}
	861.0	{110}>>{111}>{113}>{100}
	864.7	{110}>{113}>{100}≈{111}
	866.7	{110}>{113}>{111}
	873.4	{110}>{113}>{111}>{100}
	878.6	{111}>{100}≈{110}≈{113}
	884.6	{111}
	886.0	{111}
	889.1	{110}>{113}
	897.1	{110}>{111}>{113}>{100}
	898.6	{110}>{113}>{100}
	921.4	{111}
	931.7	{110}
	936.3	{110}
	939.4	{111}
	970.1	{111}

[a] *Baseline-corrected peak area used for comparison*

correlate with the four growth sectors visible in the DiamondView image (figure 4). The peak area intensity for the NV^- center is greatest in the {111} growth sector, nearly double its intensity in {100} and two orders of magnitude greater than in the {110} and {113} sectors. At 633 nm excitation, the GR1 peak at 741 nm was present in all four visible growth sectors. However, the GR1 intensity in {111} and {100} was less than half the GR1 intensity found in the {110} sector.

Meanwhile, the 780 nm excitation revealed the most peaks of any laser used for this study (table 2). Figure 6D shows the peak area distribution for the 815.1 nm peak. The four growth sectors seen in the DiamondView image (again, see figure 4) are visible in the PL image for the 815.1 nm peak area (figure 6D). For the 815.1 nm peak, the {110} sector had the greatest peak area intensity, an order of magnitude greater than in {113}. The peak area intensity in both {111} and {100} was an order of magnitude less than in the {113} sector. Many of the peaks observed using the 780 nm laser and reported in table 2 were most intense in the {110} sector.

DISCUSSION

The data in this study and in previous studies (e.g., Johnson et al., 2015; Dieck et al., 2015; Ardon and Loudin, 2016; Johnson and Myagkaya, 2017) show a clear correlation between the growth features observed in PL maps with DiamondView images. The strong correlation demonstrates the effectiveness of PL mapping in resolving the spatial distribution of optical defects in diamond. The visibility of growth features in the PL maps is a function of both the peak's intensity and its distribution. For example, in this study the 849.4 nm peak is only visible in the {111} growth sector (table 2). Accordingly, the remaining growth sectors cannot be identified using the 849.4 nm peak intensity. Therefore, it is likely that the 849.4 nm peak is preferentially incorporated in the {111} octahedral growth sector. Using similar reasoning, at least 10 peaks from this study are preferentially incorporated in {111} and two peaks in {110} (table 2).

The distribution of the 849.4 nm band also demonstrates the advantage of PL mapping over standard PL. If in a standard PL measurement the instrument operator unknowingly focused on the part of the table corresponding to the {110} sector, then the 849.4 nm peak would not be observed in the spectra. In the same instance, the intensity of the NV^- (637 nm) and NV^0 (575 nm) centers would be lower and the intensity of

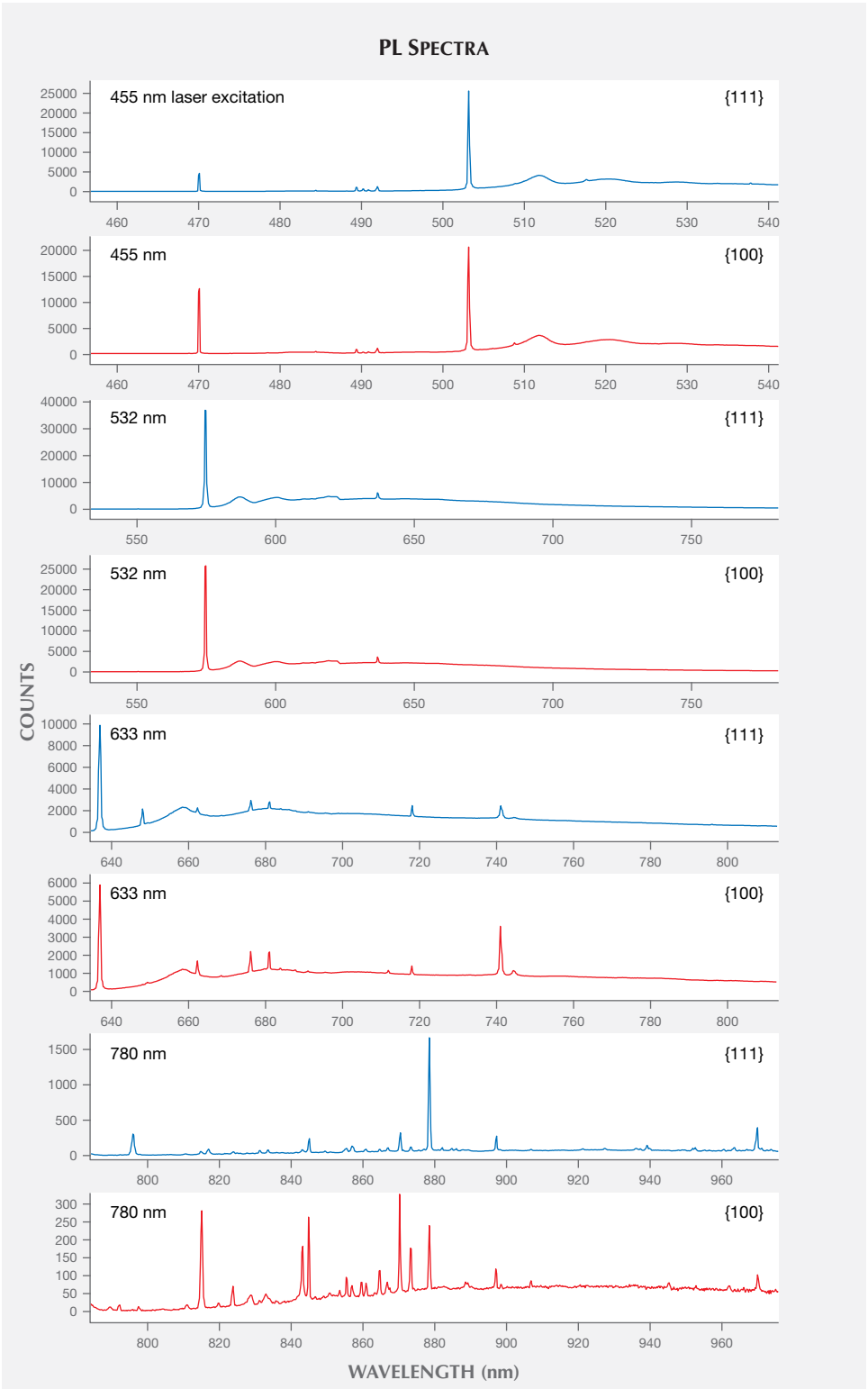

Figure 7. Average PL spectra for the {100} and {111} growth sectors. For each laser excitation, the spectra show that the abundance and intensity of optical defects varies between the {100} and {111} growth sectors.

GR1 (741 nm) would be higher than if the spectra were collected in the {111} sector. This is important to note because, as stated in Eaton-Magaña and Breeding (2016), determining some diamond color treatments relies on the "presence and absence of particular PL peaks." Therefore, PL mapping provides scientists

with a three-dimensional understanding of the diamond's optical defects, its PL intensity, and its spatial distribution.

Finally, to assess the effectiveness of the PL mapping technique introduced in this study, we can compare our data to previous studies that have assigned optical defects to particular growth sectors. The concept of optical defects being incorporated in a specific growth sector is well documented (van Enckevort and Lochs, 1988; Collins et al., 1990; Lawson et al., 1996; Welbourn et al., 1996; Zaitsev, 2001). For instance, the NV^- center is preferentially incorporated in the {111} octahedral sector in HPHT synthetic diamonds (van Enckevort and Lochs, 1988; Zaitsev, 2001). In agreement with the study presented by van Enckevort and Lochs (1988), our results show that the NV^- center is most intense in the {111} octahedral growth sector (table 2). Furthermore, the GR1 intensity was greatest in the {110} growth sector (also in table 2). Comparing the distribution of GR1 to that of the NV^- center, we see a nearly opposite distribution of the two defects. This is expected because a vacancy introduced in the {111} growth sector can readily combine with the available N to form the nitrogen vacancies (Burns et al., 1990). The correlation between our PL maps and the results from previous studies validates the effectiveness of using an EMCCD Raman imaging microscope for rapidly collecting PL maps.

CONCLUSIONS

Using a unique HPHT synthetic diamond of mixed type, our high-speed photoluminescence mapping technique produced images that reveal the intensity variations of PL features between growth sectors. The collected PL images, obtained in less than four minutes each, establish the usefulness of this method in understanding the preferential uptake of impurities and optical defects in diamond growth. We conclude that using an EMCCD Raman imaging microscope is an effective and efficient method for determining the distribution of optical centers in diamond and producing PL maps. This technique will allow scientists to rapidly collect and analyze PL maps in order to better understand the nature and formation of optical defects in diamond and evaluate new criteria for identifying treated and synthetic diamonds.

ABOUT THE AUTHOR

Mr. Loudin is a research associate in diamond advanced testing at GIA in New York.

ACKNOWLEDGMENTS

The author thanks Alexander Rzhevskii of Thermo Fisher Scientific for providing detailed information on the DXRxi EMCCD and instrument automation. The author also thanks A'Dhi Lall and Towfiq Ahmed of GIA's New York lab for collecting the FTIR spectra and acquiring the photo of the sample, respectively. In addition, the author would like to thank three anonymous reviewers, as well as Christopher M. Breeding of GIA in Carlsbad, for providing thoughtful comments and suggestions. The author is grateful to Paul Johnson and Wuyi Wang of GIA's New York lab for their continued support during the development of this PL mapping technique.

REFERENCES

Ardon T., Loudin L. (2016) Lab Notes: Evidence of focused beam irradiation in treated pink diamond. *G&G*, Vol. 52, No. 3, pp. 298–299.

Breeding C.M., Shigley J.E. (2009) The "type" classification system of diamonds and its importance in gemology. *G&G*, Vol. 45, No. 2, pp. 96–111, http://dx.doi.org/10.5741/GEMS.45.2.96

Burns R.C., Cvetkovic V., Dodge C.N., Evans D.J.F., Rooney M.-L.T., Spear P.M., Welbourn C.M. (1990) Growth-sector dependence of optical features in large synthetic diamonds. *Journal of Crystal Growth*, Vol. 104, No. 2, pp. 257–279, http://dx.doi.org/10.1016/0022-0248(90)90126-6

Collins A.T. (1982) Colour centres in diamond. *Journal of Gemmology*, Vol. 18, No. 1, pp. 37–75.

——— (1992) The characterisation of point defects in diamond by luminescence spectroscopy. *Diamond and Related Materials*, Vol. 1, No. 5-6, pp. 457–469, https://doi.org/10.1016/0925-9635(92)90146-F

——— (1999) Things we still don't know about optical centres in diamond. *Diamond and Related Materials*, Vol. 8, No. 8-9, pp. 1455–1462, http://dx.doi.org/10.1016/S0925-9635(99)00013-8

——— (2003) The detection of colour-enhanced and synthetic gem diamonds by optical spectroscopy. *Diamond and Related Ma-*

terials, Vol. 12, No. 10-11, pp. 1976–1983, http://dx.doi.org/10.1016/S0925-9635(03)00262-0
Collins A.T., Kanda H., Burns R.C. (1990) The segregation of nickel-related optical centres in the octahedral growth sectors of synthetic diamond. *Philosophical Magazine Part B*, Vol. 61, No. 5, pp. 797–810, http://dx.doi.org/10.1080/13642819008207562
Dieck C., Loudin L., D'Haenens-Johansson U. (2015) Lab Notes: Two large CVD-grown synthetic diamonds tested by GIA. *G&G*, Vol. 51, No. 4, pp. 437–439.
Eaton-Magaña S., Breeding C.M. (2016) An introduction to photoluminescence spectroscopy for diamond and its applications in gemology. *G&G*, Vol. 52, No. 1, pp. 2–17, http://dx.doi.org/10.5741/GEMS.52.1.2
Eaton-Magaña S., Shigley J.E. (2016) Observations on CVD-grown synthetic diamonds: A review. *G&G*, Vol. 52, No. 3, pp. 222–246, http://dx.doi.org/10.5741/GEMS.52.3.222
van Enckevort W.J.P., Lochs H.G.M. (1988) Photoluminescence tomography as a method to image point-defect distributions in crystals: Nitrogen-vacancy pairs in synthetic diamond. *Journal of Applied Physics*, Vol. 64, No. 1, pp. 434–436, http://dx.doi.org/10.1063/1.341212
Johnson P., Myagkaya E. (2017) Lab Notes: HPHT synthetic diamond with intense green color. *G&G*, Vol. 53, No. 1, pp. 96–98.
Johnson P., Moe K.S., D'Haenens-Johansson U., Rzhevskii A. (2015) Discovery and distribution of the $[Si\text{-}V]^-$ defect in HPHT-grown gem-quality diamonds. *Geological Society of America Abstracts with Programs*. Vol. 47, No. 7, p. 763.
Law B., Wang W. (2016) Lab Notes: CVD synthetic diamond over 5 carats identified by GIA. *G&G*, Vol. 52, No. 4, pp. 414–416.
Lawson S.C., Kanda H., Watanabe K., Kiflawi I., Sato Y., Collins A.T. (1996) Spectroscopic study of cobalt-related optical centers in synthetic diamond. *Journal of Applied Physics*, Vol. 79, No. 8, pp. 4348–4357, http://dx.doi.org/10.1063/1.361744
Moe K.S., D'Haenens-Johansson U., Wang W. (2015) Lab Notes: Irradiated green-blue CVD synthetic diamonds. *G&G*, Vol. 51, No. 3, pp. 320–321.
Moe K.S., Johnson P., D'Haenens-Johansson U., Wang W. (2016) Lab Notes: Largest blue HPHT synthetic diamond. *G&G*, Vol. 52, No. 1, pp. 74–75.
Wang W., Poon T. (2016) Lab Notes: Large blue and colorless HPHT synthetic diamonds. *G&G*, Vol. 52, No. 2, pp. 195–196.
Welbourn C.M., Cooper M., Spear P.M. (1996) De Beers natural versus synthetic diamond verification instruments. *G&G*, Vol. 32, No. 3, pp. 156–169, http://dx.doi.org/10.5741/GEMS.32.3.156
Zaitsev A.M. (2001) *Optical Properties of Diamond: A Data Handbook*. Springer-Verlag, Berlin.

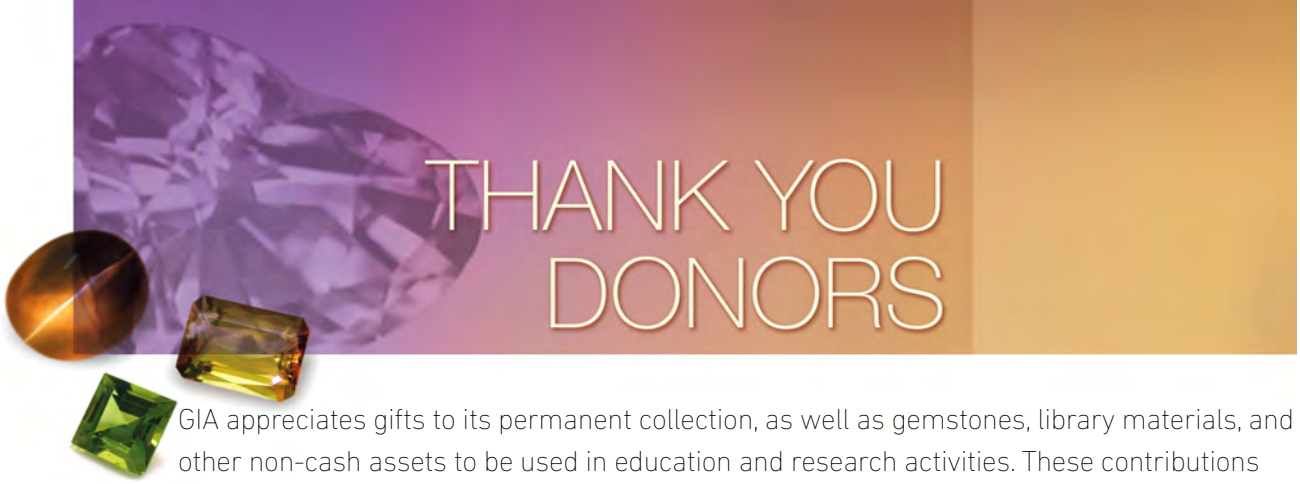

GIA appreciates gifts to its permanent collection, as well as gemstones, library materials, and other non-cash assets to be used in education and research activities. These contributions help GIA further its public service mission while offering donors philanthropic benefits. We extend sincere thanks to all 2016 contributors.

CIRCLE OF HONOR*

$100,000 and higher

Dr. Suman Agrawal
Robert and Marlene Anderson
K.C. Bell
Thomas Cacek
Hauser Family In Memory of Joel and Barbara Hauser
Dr. James Y. Hung
Bill Larson
Dr. Geoffrey A. Smith

2016 DONORS

$50,000 to $99,999

Dr. Suman Agrawal
Dr. Casey Skvorc

$10,000 to $49,999

Dr. J.K. Agrawal
Thomas M. Schneider
Swarovski

$5,000 to $9,999

Scott Lissburger

$2,500 to $4,999

Charles W. Bateman
K.C. Bell
Meg Berry
Dr. James Y. Hung
Linda MacNeil
Dr. Geoffrey A. Smith

$1,000 to $2,499

Cos Altobelli
Scott Guhin
In Memory of Abe and Lillian Joseph
Col. LeRoy R. Peters

$500 to $999

Israel Eliezri
Will Heierman
K.R. Gems & Diamonds International
Tiancheng International Auctioneer Ltd.

Under $500

American Society of Appraisers
Lawrence Beall
Crevoshay
Larry French
In Memory of John Fuhrbach
Jack H. Fulwiler
Al Gilbertson
Georgia Gilbertson
Judith Allen Hall
Jack Hobart
Carolyn S. Jacoby
Qiao Qiao Jiang
Mary Johnson and Mark Parisi
Elyse Karlin
Alf Larsson
Lucara Diamond Corp.
Brent Malgarin
In Memory of Elyga and Mac Mansfield
Mark Mauthner
Montana Tech
Bernd Munsteiner
Renee Newman
In Memory of Orlando Paddock
Penta Gems and Jewelry Co. Ltd.
Poly International Auction
Edgar Rodrigues
Severalmaz
Dr. James Shigley
Karen Simmons
Suh Kwang Sa
Suwa and Sons, Inc.
Trafalgar Square Publishing
In Memory of Alvin Van Valkenburg
John and Andrée Valley

If you are interested in making a donation and receiving tax benefits information, please contact:

MCKENZIE SANTIMER
call: (760) 603-4150
fax: (760) 603-4056
email: mckenzie.santimer@gia.edu

* All are cumulative donations

An Update on Tourmaline from Luc Yen, Vietnam

Nguy Tuyet Nhung, Le Thi Thu Huong, Nguyen Thi Minh Thuyet, Tobias Häger, Nguyen Thi Le Quyen, and Tran Thi Duyen

Since the late 1980s, tourmaline has been collected with ruby, sapphire, spinel, and other minerals from placers along the rivers and streams of Vietnam's Luc Yen district. In 2004, a body of granitic pegmatite containing tourmaline associated with green feldspar was discovered. Several other sites, spreading over an area of more than 100 km^2, were later discovered in the area. Tourmaline from Luc Yen may be colorless, but it also is found in a variety of colors, including gray, pink, green, yellow, brown, and purple. Crystals can reach 20 cm in length and may weigh 2–3 kg or more. Most of the material is of the elbaite species; liddicoatite and uvite are less common. Only a small percentage of the tourmaline is suitable for faceting; the rest is carved or kept as mineral specimens *in situ* for collectors.

Tourmaline is a borosilicate mineral with the extremely complex structural formula $XY_3Z_6(T_6O_{18})(BO_3)_3V_3W$, where the most common ions (or vacancies) at each site are X = Na^+, Ca^{2+}, K+, and vacancy; Y = Fe^{2+}, Mg^{2+}, Mn^{2+}, Al^{3+}, Li^+, Fe^{3+}, and Cr^{3+}; T= Si^{4+}, Al^{3+}, and B^{3+}; B = B^{3+}; V = OH^- and O^{2-}; and W = OH^-, F^-, and O^{2-}. Tourmaline's compositional variability (which mostly occurs at the X, Y, Z, W, and V sites) creates a supergroup of minerals. Gem tourmaline is mined in many places in the world, but is mainly Brazil and Africa. In Vietnam, gem-quality tourmaline (figure 1) has been found with ruby, sapphire, and spinel in the Luc Yen placers since the late 1980s, when crystals were found in the weathering crust by local farmers and construction workers. The first pegmatite body containing colored tourmaline and green feldspar was found at Minh Tien commune and mined in 2004–2005; within a few years, other tourmaline-bearing pegmatite bodies were discovered in Khai Trung (2008–2009), Tan Lap (2009–2010), and An Phu (2011). All of the pegmatite bodies were mined in an unorganized fashion by locals using rudimentary methods. So far, local authorities have banned mining at all the pegmatite bodies, although mining from placers is still permitted (figure 2). A number of published studies have confirmed the presence of gem tourmaline in Luc Yen (see Quoc, 1995; Nhung and Huong, 1996; Ngu, 2001; Nhung et al., 2005, 2010; Blauwet, 2007, 2011; Wilson, 2007; Huong et al., 2012; Long et al., 2013). The material belongs to various species such as elbaite, liddicoatite, dravite, and rossmanite. This paper pre-

Figure 1. This particolor tourmaline crystal, weighing 1400 g and measuring approximately 9.5 × 9.0 × 8.0 cm, was taken from a Luc Yen placer in 1994. Courtesy of Hoi An Gemstone Art Museum.

See end of article for About the Authors and Acknowledgments.
Gems & Gemology, Vol. 53, No. 2, pp. 190–203
http://dx.doi.org/10.5741/GEMS.53.2.190

Figure 2. A farmer digs for tourmaline and other alluvial gemstones in his rice field in Luc Yen's An Phu commune. Photo by N.T. Nhung.

sents an overview of the characteristics of tourmaline from Luc Yen by combining the data published by other authors with the results of this study.

LOCATION AND ACCESS

The Luc Yen district of Yen Bai Province is located in northwest Vietnam, about 270 km from Hanoi. Luc Yen is most easily accessed by driving north from Hanoi along National Highway 2 and then Highway 70 and Route 152 crossing over the Chay River to Yen The, in the center of Luc Yen district (figure 3). It is possible to access the outcrops using a car or motorbike and then walking about 1–2 km. Highway CT05 connecting Hanoi, Yen Bai, and Lao Cai was completed in late 2014, making travel to Luc Yen more convenient.

GEOLOGY

The Luc Yen district covers an area of more than 800 km^2. It is located on both sides of the Chay River and distributed in two geological structure zones within the boundary of the Chay River fault: the Red River zone in the southwest and the Lo Gam zone in the northeast (figure 4).

Gem-quality tourmaline occurs in granitic pegmatite outcrops in the Lo Gam area. This area is composed of Proterozoic rocks, including two mica (biotite and muscovite)-quartz schist intercalated with mica (biotite or muscovite)-quartz schist, with marble lenses and quartzite of Thac Ba formation in the lower part. The upper part is An Phu formation composed of calcite marble, calcite-dolomite marble

Figure 3. This map of northern Vietnam shows the province of Yen Bai outlined in magenta and the Luc Yen district outlined in red. Also shown are numbered highways to Yen Bai.

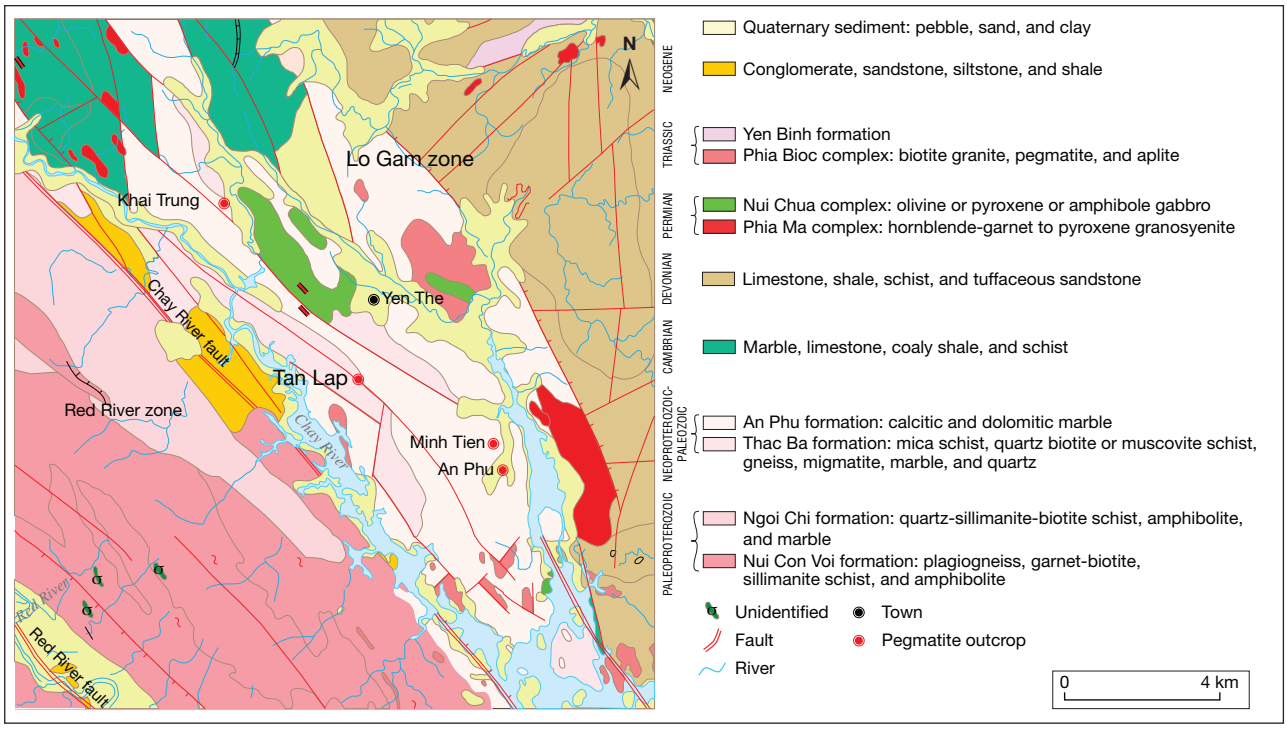

Figure 4. Geological map of Luc Yen showing tourmaline-bearing pegmatite outcrops. Modified after Xuyen (2000) and Vinh (2005).

containing ruby, sapphire and spinel. Quaternary sediments are on the top and include alluvium and diluvium (superficial deposits formed by flooding); gemstones are found in the loose sediments. The exposed magmatic blocks present the changing composition from Paleozoic gabbro, syenite, and granosyenite (Nui Chua and Phia Ma complexes) to Triassic granite (Phia Bioc complex). Pegmatite veins are scattered throughout the area, mainly northwest to southeast, with fewer in the north-south direction. Some are said to be the last phase of above magmatic complexes (Xuyen, 2000), while others are of undetermined age. A few pegmatites throughout Luc Yen were found to contain gem-quality tourmaline, and the Minh Tien pegmatite formed 30.58 Ma (Nhung et al., 2007; Huong et al., 2016). Thus, gem-quality tourmaline-bearing pegmatites do not relate to Paleozoic and Triassic magmatic activities in this region but appeared simultaneously with the displacement of the Red River fault during the Tertiary period.

In Brief

- Tourmaline has been known from Vietnam's Luc Yen district since the 1980s, with pegmatite bodies first exploited in the early 21st century.
- Most tourmaline from this locality is elbaite, with minor amounts of liddicoatite and uvite.
- Only a small percentage of the Luc Yen tourmaline is gem quality. The patterns and sizes, as well as the range of colors due to transition metals, make some specimens suitable for carving or collection.

MATERIALS AND METHODS

The 152 tourmalines from Luc Yen in this study included 90 rough and 62 polished samples. The 90 rough samples, including 30 *in situ* pegmatite pieces and 60 single crystals, were taken from pegmatite bodies and placers by the authors during different field visits in 2004, 2011, 2012, and 2013. Forty-four polished samples were purchased from local people, and the other 18 were loaned by local gem dealers. Refractive index (RI) was measured for 40 samples, and hydrostatic specific gravity (SG) was measured with an electronic balance for 62 samples. UV fluorescence for 40 samples was analyzed using a standard 4-watt long-wave (365 nm) and short-wave (254 nm) UV lamp. Internal features were observed using a standard binocular gemological microscope; solid inclusions were identified in thin sections under a polarizing microscope. Elemental composition of inclusions was analyzed with a JEOL JSM-7600 energy-dispersive

spectroscope (EDS) with an integrated Oxford ISIS microanalyzer. These analyses were performed at the Hanoi University of Natural Science at Vietnam National University, the Gemmological Center of the Vietnam Gemstone Association, and the Institute of Geological Sciences, Vietnam Academy of Science and Technology in Hanoi.

Quantitative chemical analyses were carried out at the Institute of Geosciences at Johannes Gutenberg University in Mainz, Germany. Analyses were performed on seven samples, including three monocolor (green, brown, and pink), three bicolor (light green and light pink; light pink and green; colorless and grayish blue), and one tricolor sample (orange, light yellow, and brown-green). In the four color-zoned samples, chemical analysis was conducted for each color zone, yielding a total of 12 data sets for the seven samples. The chemical analyses were carried out with electron microprobe for Si and laser ablation–inductively coupled plasma–mass spectroscopy (LA-ICP-MS) for all other elements.

Electron microprobe analyses were performed with a JEOL JXA-8900RL instrument equipped with wavelength-dispersive spectrometers, using 20 kV acceleration voltage and 20 nA filament current. The measurements were calibrated with wollastonite as the standard for Si. LA-ICP-MS analysis for all elements except Si and B (including Li, Be, Na, Mg, Al, P, K, Ca, Sc, Ti, V, Cr, Mn, Fe, Co, Ni, Ga, Ge, Rb, Sr, Y, Zr, Nb, Mo, Cs, Ba, La, and Ta) was conducted using an Agilent 7500ce ICP-MS system in pulse counting mode. Ablation was achieved with a New Wave Research UP-213 Nd:YAG laser ablation system, using a pulse repetition rate of 10 Hz, an ablation time of 60 seconds, a dwell time of 10 millisecond per isotope, and a 100 µm crater diameter. On average, three laser spots were measured for each zone of the color-zoned samples. NIST 612 glass was used as a standard. B and H_2O contents were calculated by CLASTOUR software (Yavuz, 2002), which is used to identify varieties of tourmaline on the basis of the classification scheme proposed by Hawthorne and Henry (1999).

MINERALOGICAL AND GEMOLOGICAL CHARACTERISTICS

Crystal Morphology and Structure. Tourmaline from Luc Yen is found in the form of single crystals (figure 5, left) or as multi-crystal aggregates (figure 5, center). Prismatic crystals usually show a combination of hexagonal and trigonal prisms terminated with a pyramid or pinacoid face (figure 5, left). Color-zoned crystals usually have more complex habits, with many prism faces combining to create multiple stripes parallel to the c-axis. Pink tourmaline crystals can form columnar aggregates (figure 5, center) or radiate from a central point (figure 5, right). Individual crystals can reach up to 20 cm in length (Long et al., 2013).

Lattice parameters of 14 different-colored Luc Yen tourmalines were determined (Nhung et al., 2005; 2010) as follows: a = 15.824–15.994 Å, c = 7.091–7.208 Å, c/a = 0.445–0.453 Å. Notably, three of the samples, which had a uniform dark green and dark brown color, gave the high value for the c lattice pa-

Figure 5. Left: A color-zoned tourmaline crystal from the Minh Tien pegmatite, accompanied by mica. Courtesy of Viet Phuong Gemstone Company. Center: This 32 g purple-red tourmaline associated with green feldspar was found in the Minh Tien pegmatite. Right: Radial pink tourmaline crystals associated with violet lepidolite from the Khai Trung pegmatite. This specimen measures 17.0 × 10.5 × 5.0 cm. Photos by T.L. Quyen (left) and N.T. Nhung (center and right).

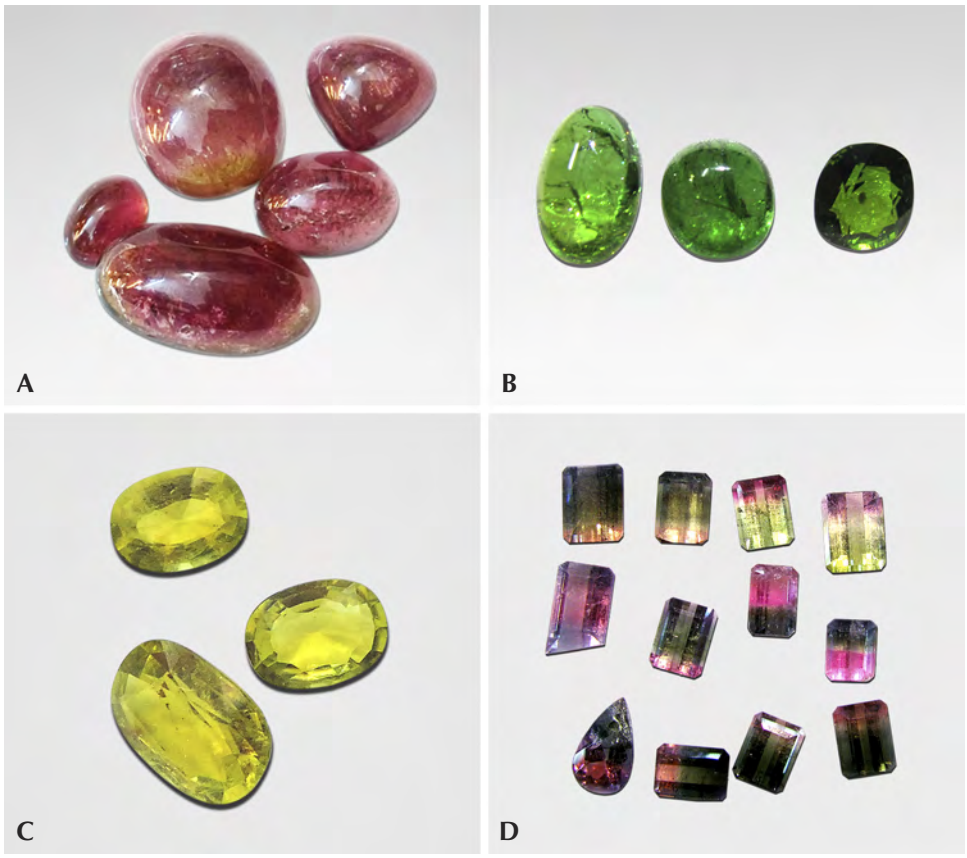

Figure 6. Luc Yen tourmalines come in many colors, including pink (A; 7.0–47.3 ct), green (B; 6.0–63.1 ct), yellow (C; 5.4–9.5 ct), and particolor (D; 1.40–2.58 ct). All these colors were included in the study. Photos by N.T. Nhung.

rameter (7.190–7.208 Å) and the high *c*/*a* ratio (0.451–0.453) that are characteristic for dravite and uvite. The 11 remaining samples, including particolor and homogeneous colored stones, had the lower values (c = 7.091–7.130Å, c/a = 0.445–0.448) characteristic of elbaite.

Visual Appearance and Gemological Properties. Luc Yen tourmalines come in many colors, including pink, green, yellow, orange, red, gray, brown, and black (figure 6), commonly with a mixing of hues (e.g., greenish yellow and brownish red) and a variety of tones and saturations. Many are particolor, with color zoning distributed along the c-axis (figure 6D) or from the center to the periphery (figure 7). Colorless zones are frequently found in particolor material. Sometimes the zoning creates fancy patterns, as seen in figure 8. The color distribution does not follow a

Figure 7. This uncommonly large Luc Yen tourmaline crystal, weighing 1200 g and measuring 12 × 10 × 10 cm, is viewed from different directions. These views show that the color zoning is distributed from core to rim. Courtesy of Hoi An Gemstone Art Museum.

TABLE 1. Gemological properties of tourmaline from Luc Yen, Vietnam.

Property	Observations	Data from the literature: Huong et al. (2012)	Data from the literature: Laurs et al. (2002)
Color (152 samples)	Variety including pink, green, yellow, orange, red, brown often with various hues, tones, and saturations, commonly in zones arranged parallel or perpendicularly to prism faces. Homogeneous colors mostly include pink, green, orange, brown, and black.	Pink, yellow, green, and reddish brown	Pink, red, and yellowish green
Pleochroism (40 samples)	Pink: pink to light pink; light pink to colorless Yellow: yellow to pale yellow Green: green to yellowish green Purple: purple to yellowish red Brown: brown to greenish yellow; brown to reddish brown	Pink: light pink to pink Yellow: yellowish to yellow Green: yellowish green to green Reddish brown: greenish yellow to brownish green	nr
Clarity (152 samples)	Transparent to translucent and opaque crystals	Semitransparent to transparent	nr
Morphology (50 samples)	Prismatic crystals of trigonal symmetry	nr	nr
Optical character (40 samples)	Uniaxial negative	nr	nr
Refractive index (40 samples)	Colorless: n_ω = 1.638–1.640, n_ε = 1.619–1.620 Pink: n_ω = 1.638–1.642, n_ε = 1.620–1.622 Yellow: n_ω = 1.640–1.644, n_ε = 1.623–1.625 Green: n_ω = 1.635–1.645, n_ε = 1.619–1.625 Purple: n_ω = 1.642–1.645, n_ε = 1.622–1.625 Brown: n_ω = 1.638–1.645, n_ε = 1.622–1.626 Brown uvite: n_ω = 1.642–1.645, n_ε = 1.622–1.628 Green uvite: n_ω = 1.638–1.642, n_ε = 1.618–1.620	Pink: n_ω = 1.638–1.639, n_ε = 1.619–1.621 Yellow: n_ω = 1.642–1.646, n_ε = 1.625–1.628 Green: n_ω = 1.635–1.640, n_ε = 1.621–1.625 Reddish brown: n_ω = 1.638–1.644, n_ε = 1.624–1.626	Pink: n_ω = 1.641, n_ε = 1.623 Yellowish green: n_ω = 1.640, n_ε = 1.620 Red: n_ω = 1.647, n_ε = 1.625
Birefringence (40 samples)	Colorless: 0.019–0.020 Pink: 0.018–0.020 Yellow: 0.017–0.019 Green: 0.016–0.020 Purple: 0.018–0.020 Brown: 0.018–0.020 Brown uvite: 0.020–0.023 Green uvite: 0.020–0.022	Pink: 0.018–0.019 Yellow: 0.017–0.018 Green: 0.017–0.019 Reddish brown: 0.016–0.020	Pink: 0.018 Yellowish green: 0.020 Red: 0.022
Specific gravity (62 samples)	Pink, purple-red, brownish red, colorless, gray-blue: 3.05–3.10 Green, greenish yellow, yellow, orange: 3.11–3.02 Brown, green uvite: 3.05–3.10	Pink: 3.05–3.08 Yellow: 3.17–3.19 Green: 3.17–3.20 Reddish brown: 3.06–3.08	nr
Hardness (50 samples)	7.0–7.5	nr	nr
Luster (50 samples)	Vitreous	nr	nr
Cleavage (50 samples)	Poor on {0001} or absent	nr	nr
UV fluorescence (40 samples)			
Short-wave	Greenish yellow, yellow, orange: greenish yellow Other colors: inert	All colors: inert	Pink to red: inert Yellowish green: weak yellow-green
Long-wave	All colors: inert	All colors: inert	All colors: inert
Internal features (40 samples)	Fluid inclusion, gas-fluid inclusion, tube-form inclusion, and solid inclusions including albite, tourmaline, radioactive elements containing inclusions (xenotime or monazite?)	Fluid inclusion, apatite, diopside, quartz	Albite (?), spherical brown particle

Abbreviation: nr = not reported

Figure 8. A cross-section of tourmaline from Luc Yen with a three-pointed star. The slice is approximately 5 cm wide. Photo by T. Häger.

predictable pattern; it may be black in the center and pink in the margin, but may also be red or green in the center and green or black in the periphery. Notably, tourmaline from Minh Tien and An Phu has a wider range of color, while tourmaline from Khai Trung and Tan Lap is mainly pink or purple.

Pleochroism was observed in all samples but was most intense in green, brown, and purple stones (see table 1). The material ranged from transparent to translucent to opaque for some black, brown, and green samples. RI measurements indicated values of n_ε = 1.618–1.628 and n_ω = 1.635–1.645, with a birefringence of 0.016–0.023. SG values ranged from 3.05 to 3.20. Yellow and green tourmalines measured from 3.11 to 3.20, while pink, red, orange, brown, colorless, grayish blue, and other green samples showed values from 3.05 to 3.10. These last green samples were uvite species.

All of the tourmalines were inert to long-wave UV radiation. The pink, red, brown, and black samples were inert to short-wave UV as well, though the green, yellow, and brownish yellow specimens fluoresced yellowish green (see figure 9 and table 1). No phosphorescence was observed in any of the samples.

Internal Features. Most of the Luc Yen tourmalines contained inclusions, such as the gas-filled mirror-like fractures described by Liddicoat (1990). Two-phase (gas + liquid) inclusions were the most common (figure 10, left). Growth tubes were also encountered frequently (figure 10, right). A few pink tourmaline samples contained abundant small solid inclusions of albite and tourmaline (figure 11), with albite being more common. Albite inclusions often showed twinning under a polarizing microscope with crossed polarizers. Tourmaline inclusions had needle or rod forms (figure 11, right). In one faceted green tourmaline sample, we observed reddish brown granular inclusions, presumed to be xenotime or monazite, surrounded by halo tension cracks that might have been caused by radioactive elements within the inclusions. Monazite inclusions were previously reported in a pale pink California tourmaline (see Gübelin and Koivula, 1992). Apatite, quartz, and diopside were also found in Luc Yen tourmaline (Huong et al., 2012).

Table 1 compares the gemological properties of Luc Yen tourmaline from this study with those published elsewhere in the literature.

CHEMICAL COMPOSITION

According to the classification of Hawthorne and Henry (1999), tourmaline-group minerals can be divided into three principal groups based on the domi-

Figure 9. The yellowish green, yellow, and brownish yellow tourmaline from Luc Yen in daylight (left) and under short-wave UV light (right). The brownish yellow sample fluoresces weaker than the green and yellow ones. Photos by N.T. Nhung.

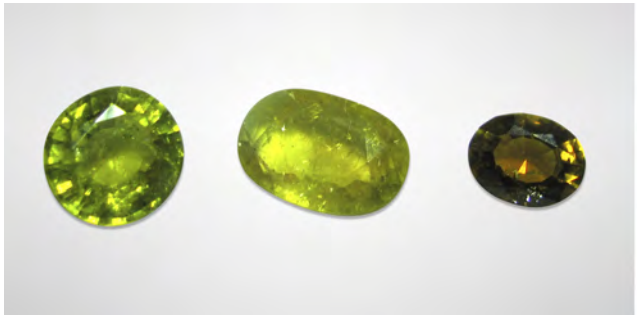

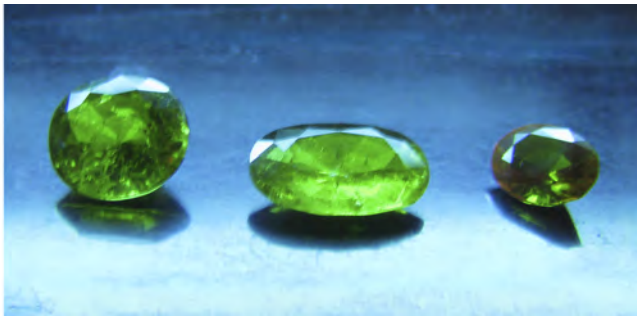

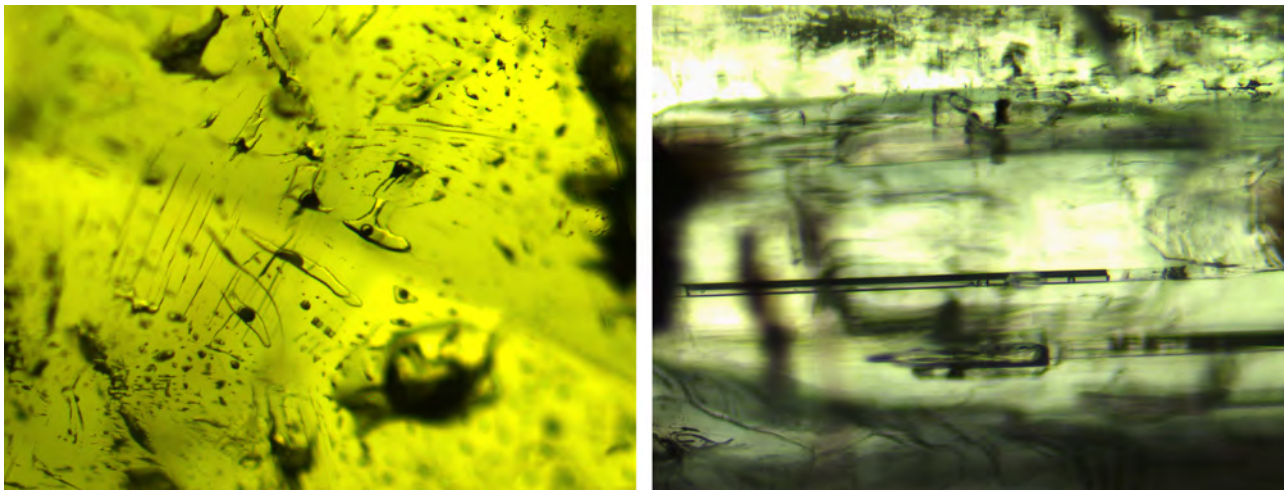

Figure 10. Left: Two-phase (gas + liquid) inclusions link together to form a network of veins known as "trichites" (Gübelin and Koivula, 1992). Right: Growth tubes are encountered frequently in Luc Yen tourmaline. The photos were taken under transmitted light. Photomicrographs by N.T.M. Thuyet; field of view 1.3 mm.

nant occupants at the X-site: alkali tourmalines (Na or K), calcic tourmalines (Ca), and X-site-vacant tourmalines (vacancy). These groups are further divided initially based on the W-site occupancy, and then by the V-site, Y-site, and Z-site occupancies (actual or inferred).

Chemical analyses of seven Luc Yen tourmaline samples ranging from nearly colorless to green, yellow, orange, brown, pink, and grayish blue are shown together with data from the literature (Dirlam et al., 2002; Wilson, 2007; Huong et al., 2012) in table 2 and presented in five ternary composition diagrams (figure 12). The results reveal that all of the samples contained Li. The Li_2O content was quite high (up to 2.58 wt.% in the green zone of sample 2) and was lowest (0.006–0.002 wt.%) in two samples with homogeneous color: sample 3 (brown) and sample 4 (green). Five of the samples (1, 2, 5, 6, and 7) contained high amounts of Li and Na, and the ratio of (Na + K)/(Na + K + Ca) ranged from 0.56 to 0.94, indicating that all of them belonged to the elbaite species (alkaline group). One exception was the pink zone of sample 2, which showed a high amount of Ca with a (Na + K)/(Na + K + Ca) ratio of 0.48, indicating that the pink zone is liddicoatite, a calcium-tourmaline group member. The two specimens with the lowest Li concentrations (samples 3 and 4) were rich in Mg and Ca and therefore classified as uvite, also a calcium-rich tourmaline. Samples 5 and 7 contained notably high Mn (on average 5.17 and 6.49

Figure 11. Abundant small solid inclusions in a pink tourmaline crystal from the Khai Trung pegmatite are seen in transmitted light (left) and in cross-polarized light (center). The small plates are albite, and the rod is a tourmaline inclusion (right). Photomicrographs by N.T. Nhung; field of view 4.2 mm.

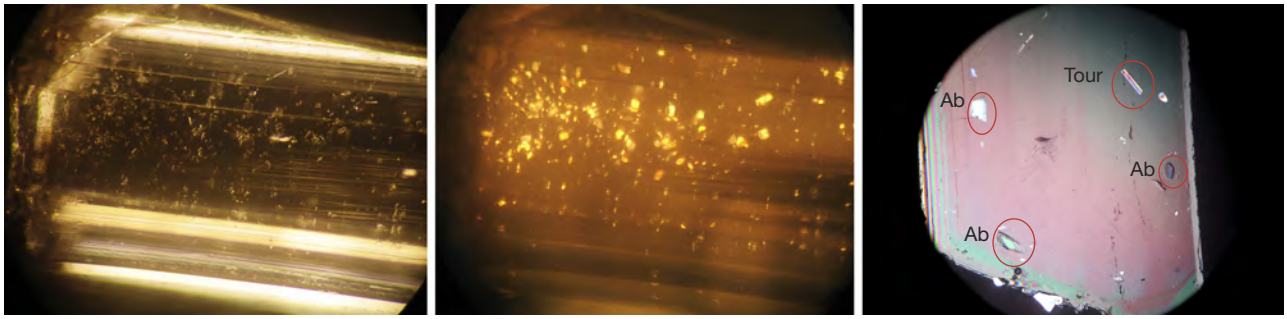

TABLE 2. Chemical composition of tourmaline from Luc Yen, Vietnam.

Location	Minh Tien pegmatite				Luc Yen placer		Minh Tien pegmatite		Khai Trung pegmatite	Minh Tien pegmatite	
Sample number[a]	1a	1b	2a	2b	3	4	5a	5b	6	7a	7b
Color	Light green	Light pink	Light pink	Green	Brown	Deep green	Colorless	Grayish blue	Pink	Orange	Light yellow
Oxide (wt.%)											
SiO_2	36.95	37.15	36.54	35.20	34.72	36.08	33.66	33.94	36.40	35.03	35.46
TiO_2	0.01	<0.01	<0.01	<0.01	0.80	0.40	<0.01	<0.01	<0.01	0.37	0.28
$B_2O_{3\,calc}$	10.971	10.99	11.06	11.15	10.60	10.60	10.71	10.60	11.31	10.67	10.93
Al_2O_3	37.47	38.08	39.61	40.82	31.70	28.48	37.71	37.76	42.65	37.78	37.07
V_2O_3	0.00	<0.01	<0.01	<0.01	0.02	0.15	<0.01	<0.01	<0.01	0.01	<0.01
Cr_2O_3	<0.01	0.00	<0.01	<0.01	0.24	0.68	0.02	0.01	<0.01	0.02	<0.01
FeO	0.40	0.21	0.06	0.77	0.10	0.01	0.18	0.02	<0.01	0.02	0.02
MnO	0.58	0.40	0.17	0.33	<0.01	0.00	5.73	4.62	0.30	6.57	6.47
MgO	<0.01	<0.01	0.00	0.03	11.83	13.75	0.01	<0.01	<0.01	<0.01	<0.01
Li_2O	2.48	2.17	2.29	2.58	<0.01	<0.01	1.99	1.71	2.30	1.21	2.27
CaO	2.11	2.55	1.74	1.28	2.90	3.18	1.56	1.98	0.61	2.47	0.30
Na_2O	1.48	1.30	1.53	1.86	1.49	1.31	2.30	1.92	1.75	2.29	2.40
K_2O	0.02	0.03	0.01	0.03	0.04	0.01	0.05	0.05	0.01	0.03	0.05
H_2O_{calc}	3.27	2.99	3.17	3.63	3.53	3.02	3.15	2.73	3.25	2.74	3.59
F	1.00	1.00	0.90	0.79	0.58	1.21	1.33	1.43	0.63	0.57	0.68
O=F	0.42	0.42	0.38	0.33	0.24	0.51	0.56	0.60	0.26	0.24	0.28
Total	**96.32**	**96.45**	**96.70**	**98.14**	**98.31**	**98.37**	**97.84**	**96.17**	**98.95**	**99.54**	**99.24**
Normalization on the basis of 31 (O, OH, F)											
Si(T)	6.000	6.000	5.916	5.578	5.748	5.94	5.541	5.704	5.677	5.82	5.66
Al(T)	0.000	0.000	0.084	0.422	0.252	0.06	0.459	0.296	0.323	0.18	0.34
Sum(T)	6.000	6.000	6.000	6.000	6.000	6.000	6.000	6.000	6.000	6.000	6.000
Al(Z)	6.000	6.000	6.000	6.000	5.932	5.464	6.000	6.000	6.000	6.000	6.000
Mg(Z)	0.000	0.000	0.000	0.000	0.068	0.536	0.000	0.000	0.000	0.000	0.000
V^{3+}(Z)	0.000	0.000	0.000	0.000	0.000	0.000	0.000	0.000	0.000	0.000	0.000
Cr^{3+}(Z)	0.000	0.000	0.000	0.000	0.000	0.000	0.000	0.000	0.000	0.000	0.000
Sum(Z)	6.000	6.000	6.000	6.000	6.000	6.000	6.000	6.000	6.000	6.000	6.000
Mg(Y)	0.001	0.000	0.000	0.007	2.851	2.838	0.003	0.001	0.001	0.000	0.001
Fe^{2+}(Y)	0.054	0.028	0.008	0.102	0.013	0.001	0.024	0.003	0.001	0.002	0.003
Mn(Y)	0.08	0.056	0.024	0.045	0.001	0.000	0.799	0.657	0.040	0.926	0.875
Al(Y)	1.237	1.483	1.473	1.201	0.000	0.000	0.857	1.183	1.518	1.217	0.633
Ti(Y)	0.001	0.000	0.000	0.000	0.100	0.050	0.000	0.001	0.000	0.046	0.034
Cr^{3+}(Y)	0.000	0.000	0.001	0.000	0.032	0.088	0.002	0.001	0.000	0.002	0.000
V^{3+}(Y)	0.000	0.001	0.001	0.001	0.002	0.019	0.001	0.000	0.000	0.001	0.001
Li(Y)	1.626	1.432	1.494	1.643	0.001	0.004	1.314	1.154	1.440	0.805	1.454
Sum(Y)	2.999	3.000	3.001	2.999	3.000	3.000	3.000	3.000	3.000	2.999	3.001
Ca(X)	0.368	0.449	0.302	0.218	0.514	0.561	0.276	0.356	0.102	0.044	0.052
Na(X)	0.467	0.415	0.481	0.570	0.478	0.419	0.733	0.626	0.530	0.738	0.693
K(X)	0.004	0.006	0.002	0.007	0.008	0.003	0.011	0.010	0.002	0.007	0.010
X-vacancy	0.161	0.130	0.215	0.205	0.000	0.017	0.000	0.008	0.366	0.211	0.245
Sum(X)	1.000	1.000	1.000	1.000	1.000	1.000	1.020	1.000	1.000	1.000	1.000
F	0.516	0.520	0.396	0.396	0.303	0.630	0.692	0.760	0.308	0.299	0.341
OH	3.161	3.160	3.180	3.201	3.232	3.123	3.103	3.080	3.231	3.234	3.220
O	0.323	0.320	0.360	0.403	0.465	0.247	0.205	0.160	0.461	0.467	0.440
(Na + K)/(Na + K + Ca)	0.56	0.48	0.62	0.73	0.49	0.43	0.73	0.64	0.84	0.94	0.93
Species	Elbaite	Liddicoatite	Elbaite	Elbaite	Uvite	Uvite	Elbaite	Elbaite	Elbaite	Elbaite	Elbaite

[a] *For samples 1–7, values represent the average of three points per sample or per color zone. All Fe is reported as FeO. bdl=below detection limit, nr=not reported*

Minh Tien pegmatite	Luc Yen (Huong, 2012)				Minh Tien (Wilson, 2007)						Vietnam (Dirlam, 2002)
7c	8	9	10	11	12	13	14	15	16	17	18
Brown-green	Pink	Green	Reddish brown	Yellow	Pink	Yellow	Gray	Green	Olive	Pink	Red
35.28	36.28	36.97	36.40	36.51	36.62	36.68	36.35	36.35	36.52	36.65	36.54
0.52	bdl	0.25	0.38	0.20	0.03	0.01	bdl	0.14	0.26	bdl	0.02
10.95	11.01	10.84	10.93	11.03	10.97	11.01	10.75	10.85	10.82	11.04	10.95
37.22	40.08	41.63	37.88	42.27	42.17	42.61	38.07	39.15	38.83	42.7	41.02
0.02	bdl	0.12	bdl	0.05	bdl	bdl	bdl	bdl	0.01	bdl	nr
<0.01	bdl	0.26	bdl	bdl	nr	nr	nr	nr	nr	nr	nr
0.04	0.02	0.03	3.2	0.11	0.13	0.15	0.57	4.88	3.4	bdl	0.11
6.44	0.09	0.01	0.37	bdl	0.46	0.02	6.08	0.53	2.18	0.02	1.46
<0.01	0.02	0.02	bdl	0.03	bdl	bdl	bdl	0.03	0.04	bdl	0.04
2.19	2.18	1.92	2.03	2.12	1.95	1.98	1.46	1.53	2.64	1.53	2.04
0.40	2.25	0.47	0.95	0.48	0.65	0.33	1.32	0.16	0.94	1.93	2.04
2.55	1.29	2.57	2.17	2.58	1.77	2.09	1.47	2.45	1.67	0.65	1.08
0.04	0.01	bdl	0.02	bdl	0.02	0.03	0.02	0.04	0.02	0.01	0.02
3.47	3.03	3.49	3.16	3.65	3.24	3.25	3.31	3.12	3.21	3.23	3.32
0.95	0.9	0.14	0.93	0.05	1.16	1.17	0.85	1.32	1.11	1.22	0.98
0.40	0.38	0.06	0.39	0.02	0.49	0.49	0.36	0.55	0.47	0.51	0.41
99.67	**96.78**	**98.66**	**98.03**	**99.06**	**98.68**	**98.84**	**99.90**	**100.29**	**100.07**	**99.00**	99.20
Normalization on the basis of 31 (O, OH, F)											
5.64	5.889	5.88	5.904	5.754	5.802	5.791	5.881	5.843	5.598	5.902	5.801
0.36	0.111	0.120	0.096	0.246	0.198	0.209	0.119	0.157	0.402	0.098	0.199
6.000	6.000	6.000	6.000	6.000	6.000	6.000	6.000	6.000	6.000	6.000	6.000
6.000	6.000	6.000	6.000	6.000	6.000	6.000	6.000	6.000	6.000	6.000	6.000
0.000	0.000	0.000	0.000	0.000	0.000	0.000	0.000	0.000	0.000	0.000	0.000
0.000	0.000	0.000	0.000	0.000	0.000	0.000	0.000	0.000	0.000	0.000	0.000
0.000	0.000	0.000	0.000	0.000	0.000	0.000	0.000	0.000	0.000	0.000	0.000
6.000	6.000	6.000	6.000	6.000	6.000	6.000	6.000	6.000	6.000	6.000	6.000
0.000	0.005	0.005	0.000	0.007	0.000	0.000	0.000	0.007	0.009	0.000	0.009
0.006	0.003	0.004	0.434	0.014	0.017	0.02	0.077	0.656	0.436	0.000	0.015
0.872	0.012	0.001	0.051	0.000	0.062	0.003	0.883	0.072	0.283	0.003	0.196
0.652	1.557	1.684	1.145	1.605	1.675	1.719	1.14	1.259	0.613	2.006	1.475
0.063	0.000	0.030	0.046	0.024	0.004	0.001	0.000	0.017	0.030	0.000	0.002
0.000	0.000	0.015	0.000	0.000	0.000	0.000	0.000	0.000	0.000	0.000	0.000
0.002	0.000	0.015	0.000	0.006	0.000	0.000	0.000	0.000	0.001	0.000	0.000
1.405	1.423	1.228	1.324	1.344	1.242	1.257	0.950	0.989	1.627	0.991	1.302
3.000	3.000	2.982	3.000	3.000	3.000	3.000	3.050	3.000	2.999	3.000	2.999
0.068	0.391	0.080	0.165	0.081	0.110	0.056	0.229	0.028	0.154	0.333	0.347
0.790	0.406	0.792	0.682	0.788	0.544	0.640	0.461	0.763	0.496	0.203	0.332
0.009	0.002	0.000	0.004	0.000	0.004	0.006	0.004	0.008	0.004	0.002	0.004
0.134	0.201	0.127	0.148	0.131	0.342	0.298	0.306	0.201	0.345	0.462	0.317
1.001	1.000	0.999	0.999	1.000	1.000	1.000	1.000	1.000	0.999	1.000	1.000
0.480	0.462	0.070	0.477	0.025	0.581	0.584	0.435	0.671	0.538	0.621	0.492
3.173	3.179	3.310	3.174	3.325	3.140	3.139	3.118	3.11	3.154	3.126	3.169
0.347	0.359	0.620	0.349	0.65	0.279	0.277	0.377	0.219	0.308	0.252	0.339
0.92	0.51	0.91	0.81	0.91	0.83	0.92	0.67	0.96	0.76	0.38	0.49
Elbaite	Elbaite	Elbaite	Elbaite	Elbaite	Elbaite	Elbaite	Elbaite	Elbaite	Elbaite	Rossmanite	Liddicoatite

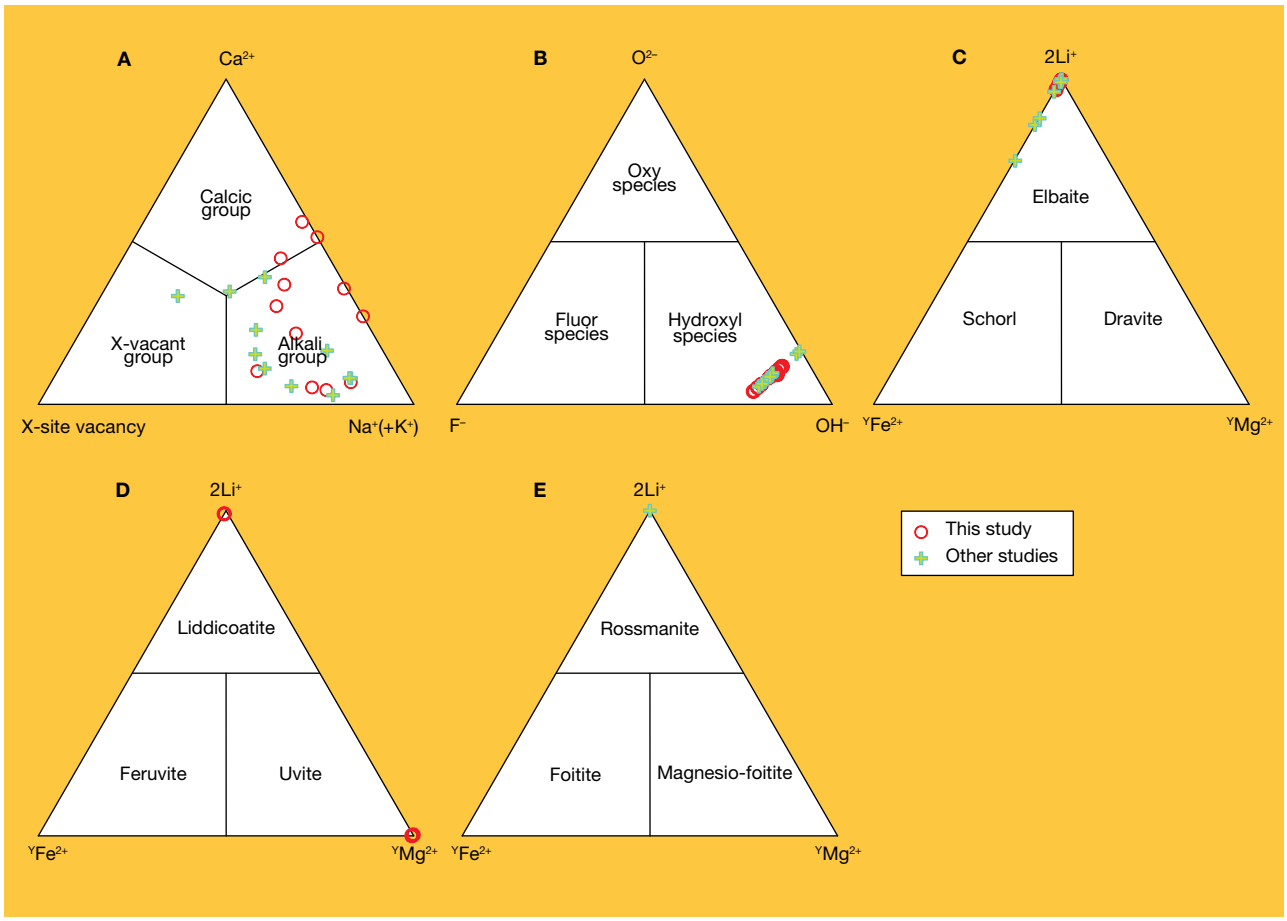

Figure 12. These five ternary composition diagrams (A–E) indicate that most tourmalines from Luc Yen are part of the alkaline group (A, the X-site occupancy); all of them are hydroxyl species (B, the W-site occupancy); all alkaline tourmaline samples are elbaite rich in Li (C, the Y-site occupancy). Two samples of calcic tourmaline are liddicoatite, and the other two are uvite (D, the Y-site occupancy). Only one sample of X-vacant tourmaline is rossmanite (E, the Y-site occupancy).

wt.% MnO, respectively). All samples were in the hydroxyl subclass.

APPLICATIONS

Only 5–10% of the Luc Yen tourmaline production is transparent enough to be faceted for jewelry (figures 6 and 13). The rest is carved (figure 14), taking into consideration the color distribution during processing. Some of the material is large, with beautiful color and relatively high transparency.

Tourmalines with beautiful color but significant fractures or small sizes are often kept in the host rock as mineral specimens (again, see figure 5, left). The tourmaline-bearing pegmatite blocks range from a few kilograms to several hundred kilograms and may contain green feldspar or pink-violet lepidolite (figure 15).

DISCUSSION

The results of 23 chemical analyses—twelve from this study, four from Huong et al. (2012), six from Wilson (2007), and one from Dirlam et al. (2002)—are presented in table 2 and figure 12. Tourmaline from Luc Yen has many different colors that may be homogeneously or heterogeneously distributed in the crystals. Most of them were of the elbaite species, but a few were liddicoatite and uvite. Most of the elbaite and liddicoatite samples were multicolored. Color zoning may appear perpendicular to the c-axis, but in many cases, color zoning is parallel to the c-axis and prism faces, giving different color zones from core to rim. This color zoning distribution is typical for elbaite. A number of studies have confirmed the presence of elbaite in Luc Yen (Nhung et al., 2005; Wilson, 2007; Huong et al., 2012). We also

Figure 13. The centerpiece of this ring is the 7.1 ct green uvite tourmaline from the secondary deposit at Minh Tien. Photo by N.T.L. Quyen, courtesy of Nguyen Huy Truong.

recognized the presence of uvite and liddicoatite. Unlike liddicoatite, uvite has not been reported for watermelon tourmaline samples. In Dirlam et al. (2002) and Laurs et al. (2002), the authors examined the same sample, reportedly from Vietnam. Although no particular locality is indicated, we presume the sample is from Luc Yen, where similar-looking watermelon tourmaline is abundant. The coexistence of elbaite and liddicoatite in one specimen reported by Laurs et al. (2002) is consistent with our study. The species of tourmaline from Luc Yen is determined by its chemical composition (Hawthorne and Henry, 1999). The results of the present study and those from other researchers presented in classification diagrams are quite similar. The difference is the presence of rossmanite reported in Wilson (2007) and uvite in this study. According to the classification of Hawthorne and Henry (1999), sample 3's (Na + K)/(Na + K + Ca) ratio of 0.49 indicates uvite with a high dravite component. This supports the likelihood of a dravite-containing uvite in Luc Yen.

Although we did not detect rossmanite, one of our samples had a high proportion of vacancies (0.366) in the X-site. Thus, the presence of rossmanite in Luc Yen tourmaline is entirely possible (see Wilson, 2007). Transition metal elements such as Fe, Cr, Ti, V, and Mn cause a rich diversity of color in tourmaline (see Fritsch and Rossman, 1987, 1988a, 1988b).

Figure 14. Carved from a cluster of multicolored Minh Tien tourmaline crystals, this Hue Palace statue weighs 2 kg and measures 18 × 10 × 8 cm. It was displayed at the Hue Royal City Festival in April 2016. Courtesy of Hoi An Gemstone Art Museum.

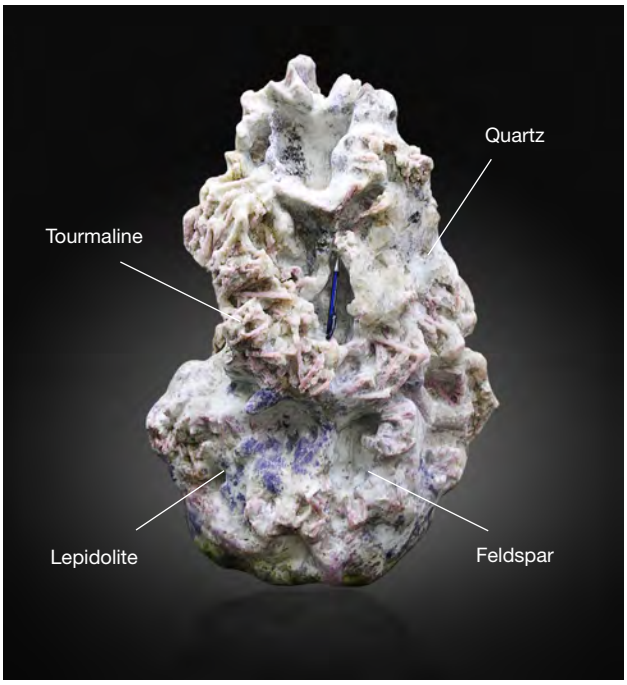

Figure 15. A block of pink tourmaline and violet lepidolite-bearing pegmatite from Khai Trung. This piece weighs approximately 300 kg and was sold to a foreign dealer in 2016. Photo by N.T.L. Quyen.

Tourmaline from Luc Yen has a wide variety of colors, and their relationship with the presence and concentration of transition metal elements should be recognized. The green elbaite samples contained more iron (up to 4.88 wt.% FeO) than the pink elbaite (maximum 0.21 wt.%), which always contained more manganese than iron (see green samples 1a, 2b, 9, 15, and 16 and pink samples 1b, 2a, 6, 8, 12, 17, and 18 in table 2). Orange and yellow elbaite (sample 7) had high manganese content (6.47 and 6.57 wt.% MnO, respectively), similar to the Mn-rich tourmaline from Zambia (Laurs et al., 2007). However, high amounts of manganese were also seen in colorless (sample 5a), grayish blue (sample 5b), and gray (sample 14) tourmaline. Green uvite (sample 4), in contrast to green elbaite, contained lower iron (0.01 wt.% FeO), higher chromium (0.68 wt.% Cr_2O_3), and higher vanadium (0.15 wt.% V_2O_5). Brown uvite (sample 3) contained the highest titanium (0.8 wt.% TiO_2) among all tourmaline samples.

Lepidolite and amazonite are found in association with elbaite, and rarely with liddicoatite-elbaite, in the Luc Yen pegmatites. These minerals contain many rare elements such as Li, Rb, Cs, Ta, and Nb. This suggests that gem tourmaline–bearing pegmatite from Luc Yen might be classified as "rare-element" using the classification by Cerny and Ercit (2005). The ages of feldspar (30.58 Ma) from the Minh Tien tourmaline-bearing pegmatite (Nhung et al., 2007) and of phlogopite (33.6 Ma) associated with ruby from Minh Tien and An Phu marble (Garnier et al., 2002) show that these gemstones were formed by the Cenozoic magmatism related to the India-Eurasia collision in northern Vietnam.

So far, gem-quality green uvite/dravite samples have only been collected from placers in Minh Tien and An Phu, and not from pegmatite host rocks. It is more likely they formed during a metasomatic process when pegmatites were injected into carbonate rocks.

CONCLUSIONS

The study results show that most tourmalines from Luc Yen are elbaite; only a small number are liddicoatite and uvite (dravite). The presence of rossmanite in Luc Yen is also possible, as we found some samples showing a high proportion of vacancies in the X-site. Elbaite and liddicoatite-elbaite have been found in alluvium as well as in pegmatite bodies, while the uvite/dravite has been found only in alluvial placers. The transparent green uvite/dravite has been found in placers from Luc Yen, but its appearance is rare. Tourmalines from this area are rich in color but often contain two-phase (gas + liquid) inclusions, growth tubes, and fractures. Therefore, transparent samples suitable for faceting or cutting are rare. Instead, there are a large number of samples with attractive colors and relatively high transparency that are large enough (up to ten centimeters in some cases) for carving. The gem tourmaline-bearing pegmatite bodies in various parts of Luc Yen indicate considerable potential.

ABOUT THE AUTHORS

Dr. Nhung (nguytuyetnhung@gmail.com) is the director of the Gemmological Center of the Vietnam Gemstone Association in Hanoi. Dr. Huong is a scientist and lecturer at the Institute of Earth Sciences, University of Graz, Austria. Dr. Thuyet is lecturer in geology at Vietnam National University, Hanoi. Dr. Häger is a senior scientist at the Centre for Gemstone Research at Johannes Gutenberg University in Mainz, Germany. He is also a lecturer in gemstone and jewelry design at the University for Applied Sciences, and managing director of the Centre for Gemstone Research, both in Idar-Oberstein, Germany. Ms. Quyen holds a master's degree in mineralogy and works as a gemologist at the Gemmological Center of the Vietnam Gemstone Association. Ms. Duyen is a PhD candidate at the Institute of Earth Sciences of Academia Sinica in Taipei.

ACKNOWLEDGMENTS

The authors thank the Vietnam National Foundation for Science and Technology Development (NAFOSTED) for financial support under Grant No. 105.02–2011.01. The authors are grateful to the Institute of Geosciences at Johannes Gutenberg University in Mainz, Germany, for support in electron microprobe and LA-ICP-MS analyses. The Institute of Geological Sciences, Vietnam Academy of Science and Technology in Hanoi provided support in EDS analyses. Special thanks are given to Prof. Wolfgang Hofmeister of Johannes Gutenberg University. Sincere thanks to Prof. Fuat Yavuz for consulting in the use of the software used to identify Luc Yen tourmaline and Dr. Nguyen Ngoc Khoi for helping to take photomicrographs. Mr. Nguyen Huy Truong of Luc Yen loaned samples for research. Mrs. Diep Mai Phuong from Viet Phuong Gemstone Company in Hanoi, Mr. Hoang Van Suu from Dai Phat Gemstone Company in Hanoi, and Dr. Duong Ba Dung from the Gemstone Art Museum in Hoi An provided images and allowed us to photograph their samples.

REFERENCES

Blauwet D. (2007) The Minh Tien tourmaline mine, Luc Yen mining district, Yen Bai Province, Vietnam. *Mineralogical Record*, Vol. 38, No. 6, pp. 443–452, http://www.mineralogicalrecord.com/detail.asp?id=262

——— (2011) A journey to the exotic locale of Khai Trung, Vietnam, for tourmaline. *Rocks and Minerals*, Vol. 86, No. 6, pp. 518–529, http://dx.doi.org/10.1080/00357529.2011.622230

Cerny P., Ercit T.S. (2005) The classification of granitic pegmatites revisited. *The Canadian Mineralogist*, Vol. 43, No. 6, pp. 2005–2026, http://dx.doi.org/10.2113/gscanmin.43.6.2005

Dirlam D.M., Laurs B.M., Pezzota F., Simmons W.B. (2002) Liddicoatite tourmaline from Anjanabonoina, Madagascar. *G&G*, Vol. 38, No. 1, pp. 28–53, http://dx.doi.org/10.5741/GEMS.38.1.28

Fritsch E., Rossman G.R. (1987) An update on color in gems. Part 1: Introduction and colors caused by dispersed metal ions. *G&G*, Vol. 23, No. 3, pp. 126–139, http://dx.doi.org/10.5741/GEMS.23.3.126

——— (1988a) An update on color in gems. Part 2: Colors involving multiple atoms and color centers. *G&G*, Vol. 24, No. 1, pp. 3–15, http://dx.doi.org/10.5741/GEMS.24.1.3

——— (1988b) An update on color in gems. Part 3: Color caused by band gaps and physical phenomena. *G&G*, Vol. 24, No. 2, pp. 81–101, http://dx.doi.org/10.5741/GEMS.24.2.81

Garnier V., Giuliani G., Maluski H., Ohnenstetter D., Phan T.T., Hoang Q.V., Vu V.T. Schwarz D. (2002) Ar-Ar ages in phlogopites from the marble-hosted ruby deposits in northern Vietnam: Evidence for Cenozoic ruby formation. *Chemical Geology*, Vol. 188, No. 1-1, pp. 39–49, http://dx.doi.org/10.1016/S0009-2541(02)00063-3

Gübelin E.J., Koivula J.I. (1992) *Photoatlas of Inclusions in Gemstones*. 2nd rev. ed., ABC Edition, Zurich, Switzerland.

Hawthorne F.C., Henry D.J. (1999) Classification of the minerals of the tourmaline group. *European Journal of Mineralogy*, Vol. 11, No. 2, pp. 201–215, http://dx.doi.org/10.1127/ejm/11/2/0201

Huong L.T.T.H., Häger T., Hofmeister W., Hauzenberger C., Schwarz D., Long P.V., Khoi N.N., Nhung N.T. (2012) Gemstones from Vietnam: An update. *G&G*, Vol. 48, No. 3, pp. 158–176, http://dx.doi.org/10.5741/GEMS.48.3.158

Huong L.T.T., Nhung N.T., Kien N.D.T., Zubko M., Häger T., Hofmeister W. (2016) Structural investigation of K-feldspar $KAlSi_3O_8$ crystals by XRD and Raman spectroscopy: An application to petrological study of Luc Yen pegmatites, Yen Bai Province, Vietnam. *Acta Physica Polonica A*, Vol. 130, No. 4, pp. 892–893, http://dx.doi.org/10.12693/APhysPolA.130.892

Laurs B.M., Simmons W.B., Falster A.U. (2002) Gem News International: Elbaite-liddicoatite tourmaline from Vietnam. *G&G*, Vol. 38, No. 2, pp. 181–182.

Laurs B.M., Simmons W.B., Rossman G.R., Fritz E.A., Koivula J.I., Anckar B., Falster A.U. (2007) Yellow Mn-rich tourmaline from the Canary mining area, Zambia. *G&G*, Vol. 43, No. 4, pp. 314–331, http://dx.doi.org/10.5741/GEMS.43.4.314

Liddicoat R.T. (1990) *Handbook of Gem Identification*, 12th ed. Gemological Institute of America, Santa Monica, California.

Long P.V., Pardieu V., Giuliani G. (2013) Update on gemstone mining in Luc Yen, Vietnam. *G&G*, Vol. 49, No. 4, pp. 233–245, http://dx.doi.org/10.5741/GEMS.49.4.233

Ngu P.G. (2001) Some characteristics of tourmaline in Vietnam. *Proceedings of the International Workshop on Materials Characterization by Solid State Spectroscopy: Gems and Minerals of Vietnam*, Hanoi, April 4–10, pp. 265–274.

Nhung N.T, Huong V.T. (1996) Gemological characteristics of tourmaline from Luc Yen. *Journal of Geology*, Series A/237, pp. 48–51 (in Vietnamese).

Nhung N.T., Thuyet N.T.M., Anh V.N., Nam N.V. (2005) Gem tourmaline in Luc Yen rare metal pegmatite. *Proceedings of the International Workshop on Gem-Materials and Modern Analytical Methods*, Hanoi, September 26–October 2, pp. 135–145.

Nhung N.T., Khoi N.N., Thuyet N.T.M., Nam N.V., Quynh P.V., Tich V.V. (2007) Establishment of some gemstone deposit types having industrial potential in Vietnam. Project QGTD.05.01 of Hanoi National University (in Vietnamese).

Nhung N.T., Quyen N.T.L., Thuyet N.T.M. (2010) Mineral assemblage of rubellite-bearing pegmatite from Khai Trung, Luc Yen, Yen Bai. *Proceedings of the International Workshop on the Provenance and Properties of Gems and Geo-Materials*, Hanoi, October 17–24, pp. 34–39.

Quoc N.K., Ed. (1995) Origin, Distribution and Potential of Gemstones and Technical Stones of Vietnam. Project KT-01-09 (in Vietnamese).

Vinh N., Ed. (2005) Geology and Mineral Resources of Vietnam, Yen Bai Sheet, Scale 1: 200.000 (F48 XXI). Department of Geology and Minerals of Vietnam, Hanoi.

Wilson W.E. (2007) Tourmaline from the Minh Tien pegmatite, Luc Yen mining district, Yen Bai Province, Vietnam. *Mineralogical Record*, Vol. 38, No. 6, pp. 453–457.

Xuyen T., Ed. (2000) Geology and Mineral Resources Map of Vietnam, Bac Quang Sheet, Scale 1:200.000 (F 48 XV). Department of Geology and Minerals of Vietnam, Hanoi.

Yavuz F., Gultekin A.H., Karakaya M.C. (2002) CLASTOUR: A computer program for classification of minerals of the tourmaline group. *Computers & Geosciences*, Vol. 28, No. 9, pp. 1017–1036, http://dx.doi.org/10.1016/S0098-3004(02)00012-2

Characterization of Mg and Fe Contents In Nephrite Using Raman Spectroscopy

Xiaoyan Feng, Yong Zhang, Taijin Lu, and Hui Zhang

Nephrites with similar hues usually have different ranges of saturation and tone, and color determination with the unaided eye can be problematic. The appearance of impurity ions such as Fe^{2+} influences the color of the material. Raman spectroscopy of 99 nephrite samples of different colors from northwestern China and Taiwan identified their main mineral as either tremolite or actinolite. When the $Mg^{2+}/(Mg^{2+} + Fe^{2+})$ ratio was 0.91 or higher, the mineral was tremolite; when the ratio was less than 0.91, the mineral was actinolite. The features in the M-OH stretching vibration region (3700–3600 cm^{-1}) are important fingerprints of nephrite's composition. Using the relative intensity ratio method, the authors calculated the Mg^{2+} and Fe^{2+} content and the ratio of $Mg^{2+}/(Mg^{2+} + Fe^{2+})$. In this study, the ratio was approximately 1 for white nephrite, 0.98–1 for light green nephrite, 0.90–0.98 for bluish green nephrite, and lower than 0.91 for dark green nephrite. The calculation of relative intensity ratios could provide a standard for nephrite color determination and even the critical evaluation of whiteness.

Nephrite, an amphibole-rich rock, comes in a variety of colors (figure 1). As noted by Zhang (2006), these hues are classified by the Chinese as *baiyu* (white), *qingbaiyu* (white with a slight bluish, greenish, or grayish tint), *qingyu* (bluish green or greenish blue), *biyu* (green to dark green), *huangyu* (yellow), and *tangyu* (brown). Distinguishing the transitions between these color varieties is an important consideration in establishing a nephrite grading standard. Traders once determined the color solely by visual observation, but even a relatively accurate determination requires decades of experience. Major gemological laboratories still do not have a quantitative or semiquantitative boundary between colors. Since the value of fine white nephrite can be significantly higher than material in other hues, whiteness is the most important parameter in evaluating and classifying nephrite that ranges from white and gray to light green. The boundary between white and light grayish to bluish green nephrite is the hardest to identify, and establishing this difference is the focus of our study.

The amphibole group is comprised of double-chain silicates belonging to the monoclinic crystal system. The group's general chemical formula is $A_{0-1}B_2C_5[T_4O_{11}]_2(OH, F, Cl)_2$. The components of the formula are described as A, B, C, T, and OH, with T corresponding to the tetrahedral sites in the unit cell. There are four kinds of sites occupied by cations (figure 2). These sites are C, a composite of five sites made up of two M1, two M2, and one M3 sites; and B, which is two M4 per formula unit. M1 and M3 sites are usually occupied by the Mg^{2+} and Fe^{2+} ions, and M2 sites by a trivalent or tetravalent form of cations with a smaller radius, such as Fe^{3+}. M4 sites are occupied by Ca^{2+}, Na^{+}, and K^{+}, while A sites are occupied by OH^{-} and the remaining Na^{+} and K^{+} cations to balance the valence state. Cations and OH^{-} that occupy M1, M3, and A sites form an ionic bond. Amphiboles are classified into four subgroups de-

In Brief

- Color determination of nephrite jade can be difficult due to ranges of tone and saturation, even within similar hues.
- Since white nephrite tends to be highly valued, establishing a boundary between white and light-colored material is imperative.
- Raman spectroscopy reveals the relative ratio between Mg^{2+} and Fe^{2+} as it pertains to the whiteness of nephrite, providing a measurement for color determination.

See end of article for About the Authors and Acknowledgments.
Gems & Gemology, Vol. 53, No. 2, pp. 204–212,
http://dx.doi.org/10.5741/GEMS.53.2.204

Figure 1. The color varieties of nephrite. Photo courtesy of Beijing Boguan International Auction Co., Ltd.

pending on the occupancy of the B sites: the Mg-Fe-Mn subgroup, the calcic subgroup, the Na-Ca subgroup, and the alkali subgroup (Bragg and Claringbull, 1965; Wang et al., 1982; Leake et al., 1997). Tremolite and actinolite are in the calcic amphibole subgroup.

Nephrite is mainly composed of tremolite, $Ca_2Mg_5[Si_4O_{11}]_2(OH)_2$, and a variable amount of actinolite, Ca_2 (Mg, Fe)$_5[Si_4O_{11}]_2(OH)_2$. When the $Mg^{2+}/(Mg^{2+} + Fe^{2+})$ ratio is 0.91 or higher, the main mineral is tremolite; when the ratio is less than 0.91, it is actinolite (Bragg and Claringbull, 1965; Wang et al., 1982; Leake et al., 1997).

Many researchers exploring the role of Fe and Mg cations in the coordination of tremolite using different spectroscopic methods have pointed out that higher Fe^{2+} content generally produces a deeper green color in tremolite (Liu, 1988; Li and Wu, 1999; Guo and Han, 2002; Lu et al., 2007). On the basis of previous studies and our own Raman spectroscopic investigation of the relative intensity ratio of the spectral features related to M-OH bands, we propose a new method to calculate the relative content of Mg and Fe in the M1 and M3 sites. This method has the potential to define boundaries for nephrite color determination and may allow for evaluation of whiteness.

MATERIALS AND METHODS

Ninety-seven nephrite samples from China (Hetian in the Xinjiang Uygur Autonomous Region and Golmud in Qinghai Province) and two Taiwanese nephrites from Hualian were studied to form a nephrite jade grading standard. Of these, 15 samples showing a range of colors were selected for this study (table 1). One set of nephrite color standards was collected by the Xinjiang Uygur Autonomous

Figure 2. The crystal structure of tremolite. Adapted from Li (2008).

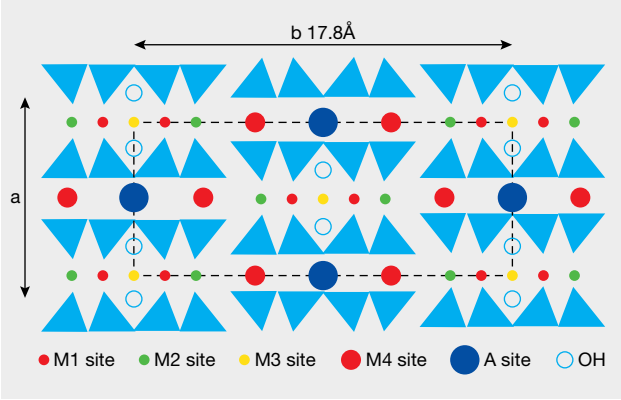

TABLE 1. Chinese nephrite samples examined for color determination.

Sample number	Locality	Size (mm) L × W × H	Color	Chinese term	
H-01	Xinjiang	30.2 × 20.1 × 9.6	White	*Baiyu*	
H-02	Xinjiang	30.3 × 19.9 × 10.2	White	*Baiyu*	
H-03	Xinjiang	30.1 × 20.2 × 10.2	White	*Baiyu*	
H-04	Xinjiang	30.0 × 20.9 × 10.3	White with a slight greenish tint	*Qingbaiyu*	
H-05	Xinjiang	29.7 × 20.0 × 10.2	Bluish green	*Qingyu*	
H-06	Xinjiang	30.3 × 19.8 × 9.5	Dark green	*Biyu*	
H-07	Xinjiang	29.8 × 20.4 × 9.9	Dark green	*Biyu*	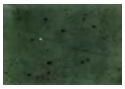
H-08	Xinjiang	30.1 × 19.9 × 10.2	Dark green	*Biyu*	
H-09	Xinjiang	23.0 × 21.4 × 5.3	Dark green	*Biyu*	
Q-01	Qinghai	24.5 × 3.1	White	*Baiyu*	
Q-02	Qinghai	24.5 × 3.1	White with a slight grayish tint	*Qingbaiyu*	
Q-03	Qinghai	24.6 × 3.1	Bluish green	*Qingyu*	
Q-04	Qinghai	24.7 × 3.1	Bluish green	*Qingyu*	
TY-01	Taiwan	9.0 × 7.4 × 3.5	Brown-yellow	*Biyu*	
TY-02	Taiwan	8.6 × 7.1 × 3.4	Brown-green	*Biyu*	

TABLE 2. Main Raman bands of nephrite and their assignments in the 1200–100 cm^{-1} region.

Band position (cm^{-1})	Assignment
1062	Si-O stretching vibration
1031	Si-O stretching vibration
932	Si-O stretching vibration
741	Symmetric Si-O-Si stretching vibration
675	Symmetric Si-O-Si stretching vibration
530	Si-O-Si and O-Si-O bending
516	Si-O-Si and O-Si-O bending
437	Si-O-Si and O-Si-O bending
418	Lattice vibrations
396	Lattice vibrations
372	Lattice vibrations
353	Lattice vibrations
252	Lattice vibrations
225	Lattice vibrations
179	Lattice vibrations
124	Lattice vibrations

Region Product Quality Supervision and Inspection Institute.

The nephrite samples were cut into wafers of different shapes. A Renishaw Raman 1000 spectrometer with a 514.5 nm laser was used at a power of 30–40 mW. To observe both the Si-O and M-OH stretching vibrations, Raman data were acquired with a spectral resolution of 4 cm^{-1} and a scanning time of 20 seconds in the 1200–100 cm^{-1} and 3700–3600 cm^{-1} ranges, respectively. Microprobe analyses were performed on a JEOL JXA-8800 electron microprobe analyzer at the Institute of Mineral Resources, Chinese Academy of Geological Sciences in Beijing. Analysis conditions were 20 kV accelerating voltage, 100 nA beam current, and a 5 μm beam.

RESULTS AND DISCUSSION

Raman Spectra. There are two regions of interest in nephrite's Raman spectrum:

1. The 1200–100 cm^{-1} region: Si-O vibrations are located in this range, where nephrite and other minor minerals can be identified. The main nephrite bands are shown in table 2 (Zou et al., 2002; Lu et al., 2007; Zhao and Gan, 2009). Our samples' Raman spectra essentially match that of tremolite, indicating that this is the main mineral component of these nephrites (figure 3).

   The main Raman peaks of tremolite-dominated nephrite are at 1062, 1031, 932, 741, 675, 530, 516, 437, 418, 396, 372, 353, 252, 225, 179, and 124 cm^{-1} (Zou et al., 2002; Wang et al., 2006).

   With higher Fe content, the tremolite component gradually decreases while actinolite increases; at the same time, the Raman peaks shift accordingly (Lu et al., 2007). Some Raman peaks found in white and dark green nephrite (for instance, the peak near 741 cm^{-1}, which is split into double peaks at 748 and 738 cm^{-1} in white nephrite and shifts to a single 743 cm^{-1} peak in dark green nephrite) shift about 1–5 cm^{-1}, and their intensity diminishes or even disappears (again, see figure 3).
2. The 3700–3600 cm^{-1} region: M-OH stretching vibrations are observed in this range. There are one to three bands, depending on the presence of Fe^{2+} in the M1 and M3 sites (Burns and Strens, 1966; Liu, 1988; Guo and Han, 2002; Lu et al., 2007). The number of peaks and their position also depend on the amount of Fe^{2+} occupying these two sites (table 3 and figure 4).

Raman spectra peak positions from M-OH stretching vibration in the nephrite samples are listed in table 4 and are summarized as follows:

Figure 3. Raman spectra of white nephrite (red trace) and dark green nephrite (black trace). In both types of nephrite, the 748 cm^{-1} peak (see inset A) along with the 530, 516, and 480 cm^{-1} peaks (inset B) shift about 1–5 cm^{-1}, and their intensity diminishes or even disappears due to the presence of Fe.

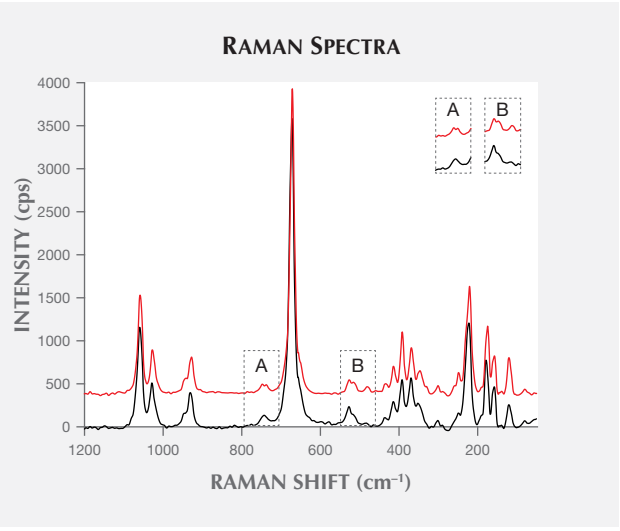

TABLE 3. M-OH stretching bands of nephrite and corresponding cations in the M1 and M3 sites.

Fundamental peak maxima (cm^{-1})		3675	3661	3645
Cation coordinating with OH^-	M1	Mg^{2+}	Mg^{2+}	Mg^{2+}
	M1	Mg^{2+}	Mg^{2+}	Fe^{2+}
	M3	Mg^{2+}	Fe^{2+}	Fe^{2+}

Adapted from Burns and Strens (1966), Liu (1988), Guo and Han (2002), and Lu et al. (2007).

TABLE 4. Peaks from M-OH stretching vibration in nephrite.

Peak position (cm^{-1})	Presence
3675	All samples
3661	H-04, H-05, H-06, H-07, H-08, H-09, Q-02, Q-03, Q-04, TY-01, and TY-02
3645	H-06, H-07, H-08, H-09, Q-03, Q-04, TY-01, and TY-02

1. The white samples (H-01, H-02, H-03, and Q-01) showed a clear 3675 cm^{-1} peak but no 3661 or 3645 cm^{-1} peaks. This indicated very low Fe^{2+} content at the M1 and M3 positions, almost all of which are occupied by Mg^{2+} ions.
2. The slightly greenish white or grayish white nephrite samples (H-04 and Q-02) showed peaks at 3675 and 3661 cm^{-1}. The presence of the 3661 cm^{-1} peak indicated a larger amount of Fe^{2+} ions, but the 3661 cm^{-1} peak in these samples was very weak.
3. The bluish green samples (H-05, Q-03, and Q-04) ranged from light bluish green to deep bluish green. Samples from Xinjiang had a lighter color than those from Qinghai; these lighter-colored samples showed Raman peaks at 3675 and 3661 cm^{-1} but for the most part no 3645 cm^{-1} peak. Both green samples from Qinghai exhibited a 3645 cm^{-1} peak. The 3661 and 3645 cm^{-1} peaks were more intense in the deep green nephrite, indicating that the green color varied with Fe^{2+} content (Lu et al., 2007).
4. The dark green samples showed the 3675, 3661, and 3645 cm^{-1} peaks. This indicated a high Fe^{2+} content, which caused the dark green color.
5. Peaks corresponding to the Fe^{3+} ion of M-OH stretching bands, such as those at 3631, 3651, and 3604 cm^{-1} (Guo and Han, 2002), did not ap-

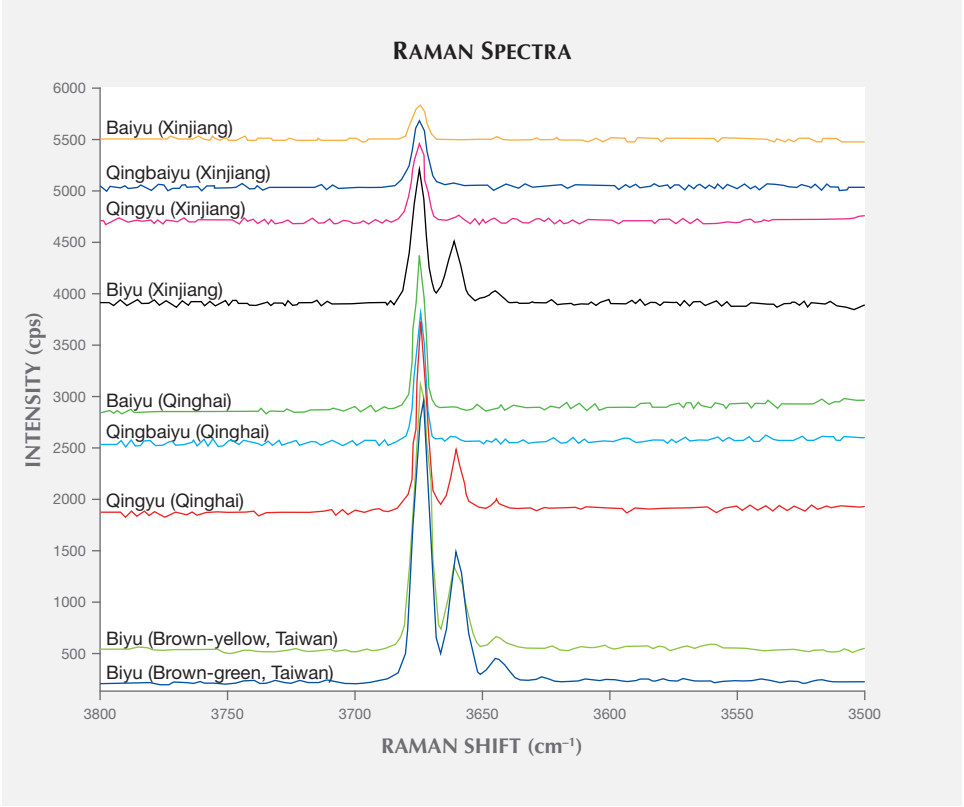

Figure 4. The M-OH stretching bands appear in the 3700–3600 cm^{-1} region in different nephrite colors.

pear in any of the samples. These samples probably contained little or no Fe^{3+}, and Raman spectroscopy could not detect its presence.

The Relative Intensity Ratio Method. We used the relative intensity ratio of the 3675, 3661, and 3645 cm^{-1} peaks to calculate the relative content of Mg^{2+} and Fe^{2+} and the ratio of $Mg^{2+}/(Mg^{2+}+ Fe^{2+})$ in the M1 and M3 sites, and to classify the color of nephrite according to the $Mg^{2+}/(Mg^{2+} + Fe^{2+})$ ratio.

Raman spectroscopy is a powerful tool for quantitative analysis (e.g., Pelletier, 2003). In a study of titanomagnetites, Zinin et al. (2011) used the relative intensity of the Raman peaks to calculate the Ti concentration. In our study, the intensity of Raman spectra was related to sample composition. Based on the intensity of the spectral peaks, we could calculate the relative content of the corresponding cation. On the basis of previous studies, we used Raman spectroscopy to study the relative intensity ratio of the spectral peak in the M-OH bands and devised a new method to calculate the relative content of Mg and Fe in the M1 and M3 sites (figure 5). The color of each nephrite sample was differentiated according to this ratio.

To calculate the relative Fe^{2+} and Mg^{2+} occupying the M1 and M3 sites, we set the relative intensity of the 3675 cm^{-1} peak at 1 ($I_1 = 1$) and used this as a reference for calculation. The relative intensity of 3661 to 3675 cm^{-1} is I_2 ($I_2/I_1 = I_2/1 = I_2$), while the relative intensity of 3645 to 3675 cm^{-1} is I_3 ($I_3/I_1 = I_3/1 = I_3$). Based on the relative amount of Mg^{2+} and Fe^{2+} cations assigned to each peak position (again, see table 3), the relative amount of Mg^{2+} occupying M1 and/or M3 sites in a certain sample is calculated as $I_1 + 2I_2/3 + I_3/3$, while the relative amount of Fe^{2+} is calculated

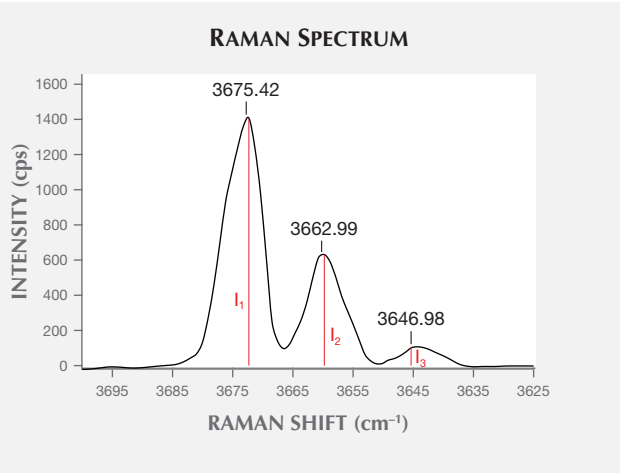

Figure 5. The relative intensities of the three main peaks in the M-OH stretching region are represented by the peak heights as I_1, I_2, and I_3 after baseline correction.

TABLE 5. Calculated relative amounts of Mg^{2+} and Fe^{2+} in the M1 and M3 sites and the $Mg^{2+}/(Mg^{2+} + Fe^{2+})$ ratio.

Sample no.	Nephrite type	Mg^{2+} ($I_1 + 2I_2/3 + I_3/3$)	Fe^{2+} ($I_2/3 + 2I_3/3$)	$Mg^{2+}/(Mg^{2+} + Fe^{2+})$
H-01	White (Baiyu)	1	0	1
H-02	White (Baiyu)	1	0	1
H-03	White (Baiyu)	1	0	1
H-04	White with a slight greenish tint (Qingbaiyu)	1	0	1
H-05	Bluish green (Qingyu)	1.05	0.02	0.98
H-06	Dark green (Biyu)	1.23	0.13	0.90
H-07	Dark green (Biyu)	1.19	0.11	0.91
H-08	Dark green (Biyu)	1.26	0.17	0.88
H-09	Dark green (Biyu)	1.22	0.15	0.89
Q-01	White (Baiyu)	1	0	1
Q-02	White with a slight grayish tint (Qingbaiyu)	1.02	0.01	0.99
Q-03	Bluish green (Qingyu)	1.22	0.14	0.90
Q-04	Bluish green (Qingyu)	1.21	0.12	0.91
TY-01	Brown-yellow (Biyu)	1.21	0.14	0.89
TY-02	Brown-green (Biyu)	1.31	0.19	0.87

TABLE 6. Chemical composition of nephrite samples by electron microprobe analysis (wt.%).

No.	Na_2O	MgO	SiO_2	Al_2O_3	K_2O	CaO	P_2O_5	SO_3	FeO	MnO	ZnO	Cr_2O_3	NiO	TiO_2	Total
H-01	0.132	24.940	57.244	0.067	0.138	13.316	0.027	bdl	0.048	0.021	0.040	bdl	0.012	0.019	96.004
H-02	0.128	25.371	56.594	0.188	0.078	13.201	0.024	0.004	0.062	0.028	0.074	0.009	bdl	0.011	95.772
H-03	0.187	24.034	57.683	0.788	0.186	12.785	0.010	bdl	0.275	bdl	0.136	bdl	0.051	0.017	96.152
H-04	0.159	24.271	57.794	0.472	0.102	12.480	0.044	bdl	0.474	0.076	bdl	0.007	0.026	0.002	95.907
H-05	0.337	24.781	57.593	0.639	0.223	12.094	0.031	0.011	0.636	0.090	0.051	0.041	0.074	bdl	96.601
H-06	0.178	23.028	55.798	0.276	0.094	13.131	bdl	bdl	4.454	0.211	0.05	bdl	0.253	bdl	97.473
H-07	0.147	22.809	55.921	0.381	0.019	13.065	0.021	bdl	3.435	0.172	bdl	0.012	0.126	0.032	96.140
H-08	0.239	22.446	56.115	0.534	0.140	13.108	0.033	0.002	4.154	0.117	bdl	bdl	bdl	0.143	97.031
H-09	1.550	22.740	56.790	0.220	0.460	11.380	bdl	bdl	4.360	0.050	bdl	bdl	bdl	bdl	97.550
Q-01	0.085	23.844	58.576	0.124	0.068	13.826	0.044	bdl	0.074	0.035	0.198	bdl	0.004	0.017	96.895
Q-02	0.074	23.692	58.546	0.211	0.043	13.844	0.007	bdl	0.386	0.060	bdl	bdl	bdl	0.044	96.907
Q-03	0.081	23.233	56.235	0.565	0.021	12.334	0.013	bdl	3.894	0.127	bdl	bdl	bdl	bdl	96.503
Q-04	0.113	23.173	56.298	0.526	0.021	12.920	bdl	bdl	3.725	0.153	bdl	0.024	0.069	bdl	97.022
TY-01	0.080	19.180	59.900	bdl	bdl	12.870	0.010	bdl	3.880	0.170	bdl	0.010	0.030	0.020	96.240
TY-02	0.030	21.300	57.270	0.170	0.010	12.590	0.020	bdl	4.900	0.320	bdl	0.030	0.110	bdl	96.750

bdl: below detection limit

as $I_2/3 + 2I_3/3$. We calculated the relative amounts of Mg^{2+} and Fe^{2+} in all samples and the $Mg^{2+}/(Mg^{2+} + Fe^{2+})$ ratio. The results are summarized in table 5.

According to table 5, the value of $Mg^{2+}/(Mg^{2+} + Fe^{2+})$ varies in samples by color. White nephrite has a value of approximately 1, light green nephrite 0.98–1, bluish green nephrite 0.90–0.98, and dark green nephrite below 0.91. The lower the value of the $Mg^{2+}/(Mg^{2+}+ Fe^{2+})$ ratio, the deeper the green color.

Comparison with Electronic Microprobe Data. To confirm the reliability of the relative intensity ratio method, we analyzed the chemical component of these samples using electron microprobe. The results

TABLE 7. Cation numbers of Mg^{2+} and Fe according to electron microprobe (wt.%) and the $Mg^{2+}/(Mg^{2+} + Fe)$ ratio.

Sample no.	Sample color	Mg^{2+} content	Fe content	$Mg^{2+}/(Mg^{2+} + Fe)$
H-01	White (Baiyu)	0.6186	0.000668	0.999
H-02	White (Baiyu)	0.6292	0.000863	0.999
H-03	White (Baiyu)	0.5961	0.00383	0.994
H-04	White with a slight greenish tint (Qingbaiyu)	0.6020	0.00660	0.989
H-05	Bluish green (Qingyu)	0.6146	0.00885	0.986
H-06	Dark green (Biyu)	0.5711	0.0620	0.902
H-07	Dark green (Biyu)	0.5657	0.0492	0.922
H-08	Dark green (Biyu)	0.5567	0.0578	0.907
H-09	Dark green (Biyu)	0.5640	0.0607	0.899
Q-01	White (Baiyu)	0.5914	0.00103	0.998
Q-02	White with a slight grayish tint (Qingbaiyu)	0.5876	0.00537	0.991
Q-03	Bluish green (Qingyu)	0.5762	0.0542	0.914
Q-04	Bluish green (Qingyu)	0.5747	0.0518	0.917
TY-01	Brown-yellow (Biyu)	0.4757	0.0540	0.899
TY-02	Brown-green (Biyu)	0.5283	0.0682	0.887

are shown in table 6. According to the data, the Fe and Mg^{2+} content and the $Mg^{2+}/(Mg^{2+} + Fe)$ ratio can be calculated, as shown in table 7.

Comparing the $Mg^{2+}/(Mg^{2+} + Fe^{2+})$ ratio obtained using the Raman relative intensity method with electron microprobe results shows good agreement between the two methods, but there is some variance. The variance may be caused by several factors, starting with the different nature of the two methods. Second, the Fe content measured by electron microprobe includes both Fe^{3+} and Fe^{2+}, while the spectral features reflect only Fe^{2+}. In addition, the analyzing spot cannot be exactly the same, because the two instruments do not use the same magnification. Taking this into consideration, the difference of the ratio in these samples is less than 3%, an acceptable variance.

CONCLUSIONS

Raman spectroscopy can help distinguish the color varieties of nephrite (again, see figure 4 and table 5) using the relative ratio of Mg^{2+} to Fe^{2+} concentration. The Fe^{2+} concentration is lowest in white nephrite and highest in dark green nephrite.

Since white nephrite (figure 6) tends to be highly valued, determining a boundary between white and light-colored nephrite is of importance to the trade. According to three relative peak intensity ratios in the M-OH stretching vibration bands, we can classify the color of nephrite to a certain degree. When the Raman spectrum only exhibits a 3675 cm^{-1} peak, the nephrite contains little Fe^{2+}. If the peak is more intense, the nephrite is whiter. The presence of a 3661 cm^{-1} peak is associated with a green tone; it is this peak that separates white nephrite from slightly greenish white, bluish green, and dark green material. The $Mg^{2+}/(Mg^{2+} + Fe^{2+})$ ratio indicates the color of nephrite. The lower the ratio, the deeper the green color. When the relative intensity of the 3661 cm^{-1} peak is stronger, the nephrite has a darker color. The 3645 cm^{-1} peak only appears in dark green and bluish green nephrite. Thus, the method of relative peak intensity ratio of 3675, 3661, and 3645 cm^{-1} and the value of the relative intensity ratio are useful in evaluating nephrite color.

Figure 6. This 30 × 30 × 13 cm carving of high-quality Chinese nephrite from Hetian is shaped like a peach, symbolizing longevity. The design pattern comes from the Chinese fairy tale "Magu Xianshou." Courtesy of Zhiguang You.

ABOUT THE AUTHORS

Ms. Feng is a senior engineer, Mr. Yong Zhang is an engineer, and Dr. Lu is chief researcher at the National Gems & Jewellery Technology Administrative Center (NGTC) in Beijing. Mr. Hui Zhang is the dean of Yunnan Land and Resources Vocational College in Kunming, China.

ACKNOWLEDGMENTS

The authors thank Jie Ke, deputy director of the NGTC, for the support and help at the sample testing stage. Sincere thanks to Yan Ao of Beijing Boguan International Auction Co., Ltd., for providing the lead photo.

REFERENCES

Bragg L., Claringbull G.F. (1965) *Crystal Structures of Minerals,* Vol. 4. G. Bell and Sons, London.

Burns R.G., Strens R.G.J. (1966) Infrared study of the hydroxyl bands in clinoamphiboles. *Science*, Vol. 153, No. 3738, pp. 890–892, http://dx.doi.org/10.1126/science.153.3738.890

Guo L.H., Han J.Y. (2002) The IR analyses of M1 and M3 cation occupation of Hetian jade, Manasi green jade and Xiuyanold jade [J]. *Acta Petrologica et Mineralogica*, No. 21, pp. 68–71.

Leake B.E., Woolley A.R., Arps C.E.S., Birch W.D., Gilbert M.C., Grice J.D., Hawthorne F.C., Kato A., Kisch H.J., Krivovichev V.G., Linthout K., Laird J., Mandarino J., Maresch W.V., Nickel E.H., Rock N.M.S., Schumacher J.C., Smith D.C., Stephenson N.C.N., Ungaretti L., Whittaker E.J.W., Youzhi G. (1997) Nomenclature of amphiboles: Report of the Subcommittee on Amphiboles of the International Mineralogical Association Commission on New Minerals and Mineral Names. *Mineralogical Magazine*, Vol. 61, No. 2, pp. 295–321.

Li S.R. (2008) *Crystallography and Mineralogy*. Geological Publishing House, Beijing, pp. 230 [in Chinese].

Li W.W., Wu R.H. (1999) The colorimetry and chromaticity study of Xinjiang Hetian jade. *Bulletin of Mineralogy, Petrology and Geochemistry*, Vol. 18, No. 4, pp. 418–422.

Liu J.H. (1988) Spectroscopical characteristic and genetical significance of amphiboles in the Ma Keng iron ore deposit. *Journal of Mineralogy and Petrology*, Vol. 8, No. 1, pp. 18–27.

Lu B.Q., Qi L.J., Xia Y.B. (2007) Raman spectra of nephrite cat's eye colors. *Journal of the Chinese Ceramic Society*, Vol. 35, No. 11, pp. 1492–1494.

Pelletier M.J. (2003) Quantitative analysis using Raman spectrometry. *Applied Spectroscopy*, Vol. 57, No. 1, pp. 20A–42A, http://dx.doi.org/10.1366/000370203321165133

Wang C., Yu X.H., Pan F., Chen H., Mo X.X., Zhang J. (2006) Raman spectra for structure of tremolite. *Journal of the Chinese Ceramic Society*, Vol. 34, No. 12, pp. 1508–1513 [in Chinese].

Wang P., Pan Z.L., Weng L.B. (1982) *Systematic Mineralogy (2)*. Beijing.

Zhang B.L. (2006) *Systematic Gemology*, 2nd ed. Geological Publishing House, Beijing, pp. 365–374 [in Chinese].

Zhao H.X., Gan F.X. (2009) The Raman spectroscopic analysis on several nephrite jade from different provenances and the application in non-destructive study of ancient jade artifacts. *The Journal of Light Scattering*, Vol. 21, No. 14, pp. 345–354.

Zinin P., Tatsumi-Petrochilos L., Bonal L., Acosta T., Hammer J., Gilder S., Fuller M. (2011) Raman spectroscopy of titanomagnetites: Calibration of the intensity of Raman peaks as a sensitive indicator for their Ti content. *American Mineralogist*, Vol. 96, No. 10, pp. 1537–1546, http://dx.doi.org/10.2138/am.2011.3745

Zou T.R., Guo L.H., Li W.H., Duan Y.R. (2002) A study on Raman spectra of Hetian jade, Manasi green jade and Xiuyan old jade. *Acta Petrologica et Mineralogica*, Vol. 21, pp. 72–78.

CHARTS

Inclusions in Natural, Synthetic, and Treated Sapphire

Nathan D. Renfro, John I. Koivula, Jonathan Muyal, Shane F. McClure, Kevin Schumacher, and James E. Shigley

Figure 1. Sapphires from a variety of sources. Faceted stones (left to right): 6.36 ct pink/orange (padparadscha), 1.63 ct pink, 4.76 ct violet, 5.43 ct violet purple, 3.03 ct blue, 2.12 ct blue, 8.06 ct yellow, 3.46 ct yellow, 2.00 ct orange, and 1.01 ct deep orange. Crystals (left to right): 9.88 ct pink, 17.80 ct violet, 30.07 ct purple, 42.13 ct blue, 10.84 ct yellow, and 5.86 ct yellow-orange. From the GIA Eduard J. Gübelin Collection and Bill Larson, Pala International. Photo by Robert Weldon/GIA.

This is the second chart in *G&G*'s series focused on micro-features often observed in natural, treated, and synthetic gems. Sapphire (figure 1) was chosen because of its enduring importance within the gem trade. Demand for this gem species has been the driving force behind the development of treatment techniques to improve natural stones and the continued production of inexpensive synthetics.

Natural sapphires, which originate in certain igneous or metamorphic geologic environments are commonly treated to improve their color or clarity. The most common processes involve heat treatment to improve color. Synthetic sapphires have been produced for more than a century, mostly by melt, flux, or hydrothermal solution methods (Hughes, 2017). All of these materials are widely encountered in the jewelry trade.

See end of article for About the Authors.
Gems & Gemology, Vol. 53, No. 2, pp. 213–214,
http://dx.doi.org/10.5741/GEMS.53.2.213

The most essential instrument in separating natural stones from synthetics and treated specimens is the binocular microscope. The information gathered from a brief microscopic observation of an unknown gem is critical for accurate identification—and limited only by the gemologist's own knowledge. No better references exist for understanding the microscopic features of corundum than the three-volume *Photoatlas of Inclusions in Gemstones* by Eduard J. Gübelin and John I. Koivula (1986, 2003, and 2005). Gemologists seeking to understand the many other aspects of gem sapphire, including physical properties and information on the many different localities, should consult *Ruby & Sapphire: A Gemologist's Guide*, by Richard W. Hughes (2017). This is considered the premier reference on the subject.

The selection of photomicrographs chosen for this chart represents the wide variety of inclusion scenes one might encounter in sapphire. Examples of inclusions that may be highly indicative of a particular origin are provided, such as a tourmaline crystal in a sapphire from Kashmir, India. Other images highlight features that may be diagnostic for a particular treatment. A case in point is the "internal diffusion" seen in a heat-treated sapphire, induced as the titanium from rutile silk inclusions was dissolved into the crystal lattice of the host sapphire at high temperatures. This dissolved titanium pairs with iron to increase the amount of blue color in the stone. Synthetics are also represented on the chart, with images of sapphires grown by flux, flame fusion, hydrothermal, and other methods.

We hope the reader will enjoy this look into the micro-features of sapphire and find the images useful and interesting. For more information on sapphire and its inclusions, see our suggested reading list (http://www.gia.edu/gems-gemology/summer-2017-suggested-reading-inclusions-sapphires).

ABOUT THE AUTHORS

Mr. Renfro is analytical manager of the gem identification department and microscopist of the inclusion research department, and Mr. Koivula is analytical microscopist, at GIA in Carlsbad, California. Mr. Muyal is a staff gemologist, Mr. McClure is global director of colored stone services, Mr. Schumacher is a digital resources specialist at the Richard T. Liddicoat Library and Information Center, and Dr. Shigley is distinguished research fellow at GIA in Carlsbad.

REFERENCES

Hughes R.W., with W. Manorotkul and E.B. Hughes (2017) *Ruby and Sapphire: A Gemologist's Guide*. RWH Publishing, Bangkok.

Additional Reading

To access a list of references pertaining to inclusions in natural, synthetic, and treated sapphire, please visit http://www.gia.edu/gems-gemology/summer-2017-suggested-reading-inclusions-sapphires, or scan the QR code to the right.

BIG SKY COUNTRY SAPPHIRE: VISITING MONTANA'S ALLUVIAL DEPOSITS

Tao Hsu, Andrew Lucas, Robert E. Kane, Shane F. McClure, and Nathan D. Renfro

Sapphire has been mined in the western U.S. state of Montana for more than a century and a half. Historically, gem-quality sapphires have been mined commercially in four main areas in southwestern Montana, shown in figure 1: the upper Missouri River gravel bars (1865), Dry Cottonwood Creek (1889), Rock Creek (1892), and Yogo Gulch (1895). Today, the first two areas remain quite active, while operations in Yogo Gulch and Dry Cottonwood Creek have been suspended for many years. To better understand the characteristics of Montana sapphire and record current mining and commercial activities, GIA sent a team to visit the placer deposits at the upper Missouri River and Rock Creek areas in August 2015.

Since the latter half of the 19th century, Montana's history has been intertwined with gold, silver, and copper mining. Corundum was discovered during the course of gold mining activities in southwestern Montana. Before the 1940s, the state's alluvial sapphire deposits were exploited mainly to supply the watch industry, but production fell dramatically with the use of synthetic sapphire in watch bearings (Emmett and Douthit, 1993). Among Montana's secondary deposits, Rock Creek (figure 2) is the only area mined specifically for sapphire from its discovery in 1892 until World War II (Clabaugh, 1952).

While Yogo Gulch is a primary deposit, the placer deposits at Rock Creek, Dry Cottonwood Creek, and the upper Missouri River near Helena have been a matter of speculation among researchers trying to work out the origin of these sapphire crystals. Research indicates that they were carried to the surface by volcanic activity, but their ultimate origin is still an open question, even after about 125 years of searching (e.g., Pratt, 1906; Clabaugh, 1952; Garland, 2002; Berg and Dahy, 2002; Berg, 2014; Zwaan et al., 2015). Due to the lack of significant sapphire-bearing host rock outcrops in these areas, the search and discussion continue. The glamour of the sapphires, the mysteries of their origin, the area's mining history, and the natural beauty of Big Sky country are an intriguing combination (figure 3).

MISSOURI RIVER

Gold miners first discovered Montana sapphire crystals in 1865, in the gravel bars along the upper Missouri River, about 15 miles northeast of Helena. Kunz (1894) reported that the sapphires were found by an "earnest and reliable prospector" named Ed R. Collins in 1865. Collins had some of the Eldorado Bar sapphires cut in New York by Tiffany & Co. and M. Fox & Co., as well as overseas, as part of an effort to locate a potential market. The first scientific reference to these stones was in 1873, when Dr. J. Lawrence Smith described them in the *American Journal of Science*. Smith had some of the sapphires faceted and stated "my opinion is that this locality is a far more reliable source for this gem variety of corundum than any other in the United States that I have yet examined." Today, seven different small-scale commercial operations are active in the Missouri River area, some of which mainly cater to

Figure 1. Sapphire deposits are clustered in southwestern Montana. Active mining operations are at alluvial deposits along the upper Missouri River and Rock Creek. Mining at Dry Cottonwood Creek and Yogo Gulch is suspended.

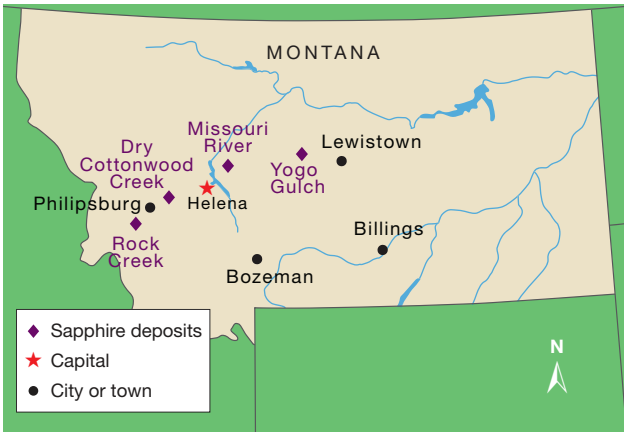

See end of article for About the Authors and Acknowledgments.
GEMS & GEMOLOGY, Vol. 53, No. 2, pp. 215–227,
http://dx.doi.org/10.5741/GEMS.53.2.215

Figure 2. Among all of Montana's secondary sapphire deposits, Rock Creek has been the most productive. Potentate Mining is actively operating on its property in this area. Photo courtesy of Potentate Mining.

tourists. Some of the finer rough is sold to jewelers, gem dealers, and hobbyists who facet these gems. In addition, there are several other areas along the Missouri River where sapphires are mined by hobbyists, including McCune Bar and Gruell's Bar.

Figure 3. A selection of heat-treated Rock Creek sapphires produced by Potentate Mining shows various shades of blue and green. The majority of alluvial sapphires from Montana have bluish and greenish pastel colors prior to heat treatment. Photo by Jeff Scovil, courtesy of Potentate Mining.

On October 8, 1942, President Roosevelt issued War Production Order L-208, which closed all gold mines in the United States. The order was designed to shift gold miners to commodities that were essential to the war effort, such as copper, and to allow the shipment of mining equipment to U.S. allies, including the Soviet Union (Hammett, 1966).

The Perry-Schroeder Mining Co. was given special permission to continue dredging gold on Eldorado Bar throughout the war, because its significant sapphire byproduct had military applications (Ball, 1943). The various non-gem uses included bearings for bombsights and torpedoes, as well as abrasives in grinding wheels. From 1940 to 1944, the Perry-Schroeder gold dredge on Eldorado Bar recovered approximately seven million carats of sapphires of all qualities, most of which were sold for industrial purposes (Clabaugh, 1952).

During this trip, we visited the Eldorado Bar (figure 4) and Spokane Bar deposits, which are active sapphire mining sites. Cass Thompson, owner of the Spokane Bar deposit and one of the six independently owned mines at Eldorado Bar, took the team on a boat tour of Hauser Lake, a reservoir on the Missouri River near Helena. The Missouri River flows from southeast to northwest in this portion of Montana. In addition to

Figure 4. Eldorado Bar is one of the sapphire-bearing gravel bars that have been mined for over 150 years. The operation is visible from the Missouri River. The small gravel mound in the foreground is a tailings pile left by previous miners. Due to the higher river level caused by the 1910 reconstruction of Hauser Dam, the lower part of the tailings pile is submerged. Photo by Andrew Lucas.

other occurrences of known sapphire-bearing gravel, there are at least nine historical sapphire bars (geologically known as strath terraces). These gravel bars, shown in figure 5, have long been known as American Bar, Eldorado Bar, Dana's Bar, McCune Bar, Metropolitan Bar, Spokane Bar, French Bar, Gruell's Bar, and Emerald Bar. Many of these deposits were exploited in the late 1800s and early 1900s, and remnants of the old mining activities can still be found. All of the sapphire deposits are distributed along this approximately

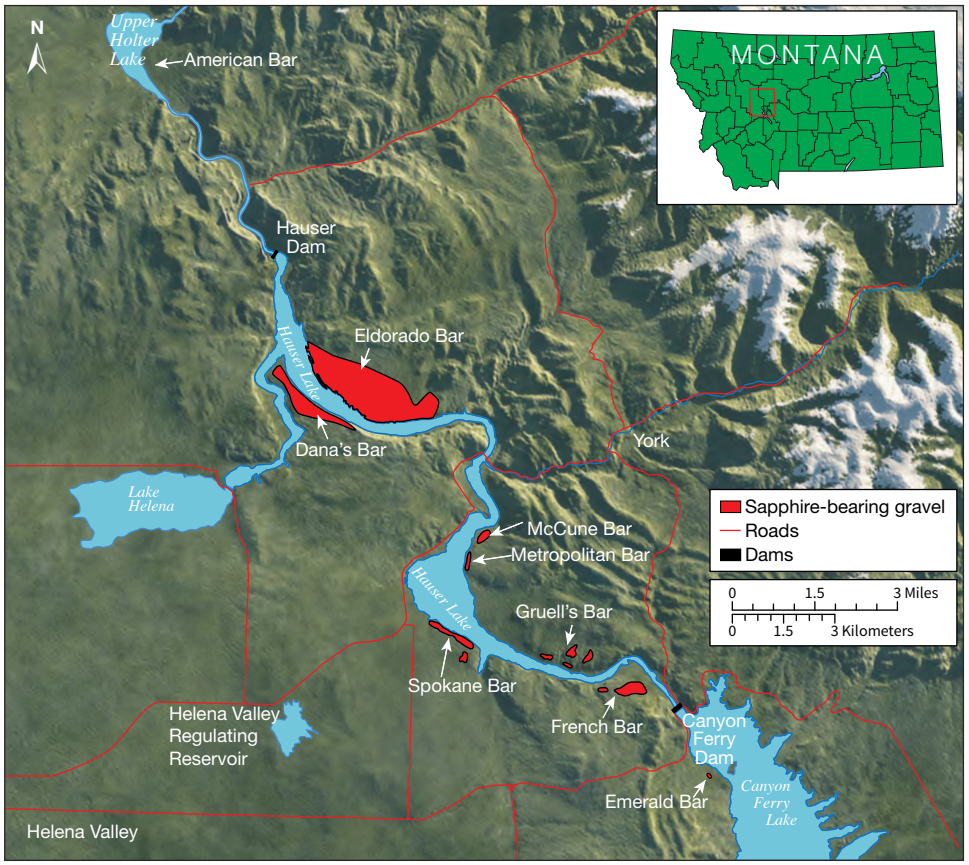

Figure 5. Sapphires have been discovered in gravels in many areas—some very recently—along this northwest-flowing section of the upper Missouri River. This map shows nine of the historic mining areas, seven of which are distributed between the Canyon Ferry Dam and the Hauser Dam. All nine occurrences of sapphire-bearing gravel on this section of the river have also been mined for gold. Sapphires are very rarely found downstream from American Bar. Modified by R. Kane from Berg (2015), with permission, courtesy of the Montana Bureau of Mines and Geology.

14-mile section of the original river. The deposits extend downriver to the northwest from Canyon Ferry Dam to Hauser Dam—essentially all of Hauser Lake—in gravel bars on both sides of the river channel, as well as the riverbed itself. Sapphires are very rarely found northwest of American Bar. When each dam was built, the river level rose dramatically, so the lower layers of many previously exposed gravel bars have been submerged ever since.

Rocks in this area include argillites of the Precambrian Belt series, Paleozoic sedimentary rocks, Tertiary lake sediments and volcanic materials, and Cretaceous or Tertiary intrusives (Clabaugh, 1952). Gravel layers sit directly above the Precambrian Belt series metasedimentary rocks (figure 6). The thickness of the gravel layers varies and at some localities is more than 40 feet. According to Thompson, some gravel bars have a very thick sapphire-bearing layer but are expensive to operate due to extremely thick overburden, as is the case at Dana's Bar and some portions of Eldorado Bar.

At Eldorado Bar, a mine run was prepared for GIA's corundum collection. The team witnessed the entire day's operation as approximately 100 cubic yards of gem-bearing gravel were run through the mechanized processing plant. This process started with gravel extraction in the morning, during which a complete rock profile was exposed (figure 7). Topsoil, overburden sediments, a volcanic ash layer, a gravel layer, and metasedimentary bedrock were observed from top to bottom in the mining pit. The overburden in this particular area is about six feet deep, which makes it relatively easy to remove. Other parts of Eldorado Bar have more than 100 feet of overburden, making these areas uneconomic to mine.

Figure 6. From this angle, brownish Precambrian metasedimentary basement rocks on a portion of Spokane Bar are clearly visible. The sapphire-bearing gravel layers are situated directly above the basement rocks. Photo by Andrew Lucas.

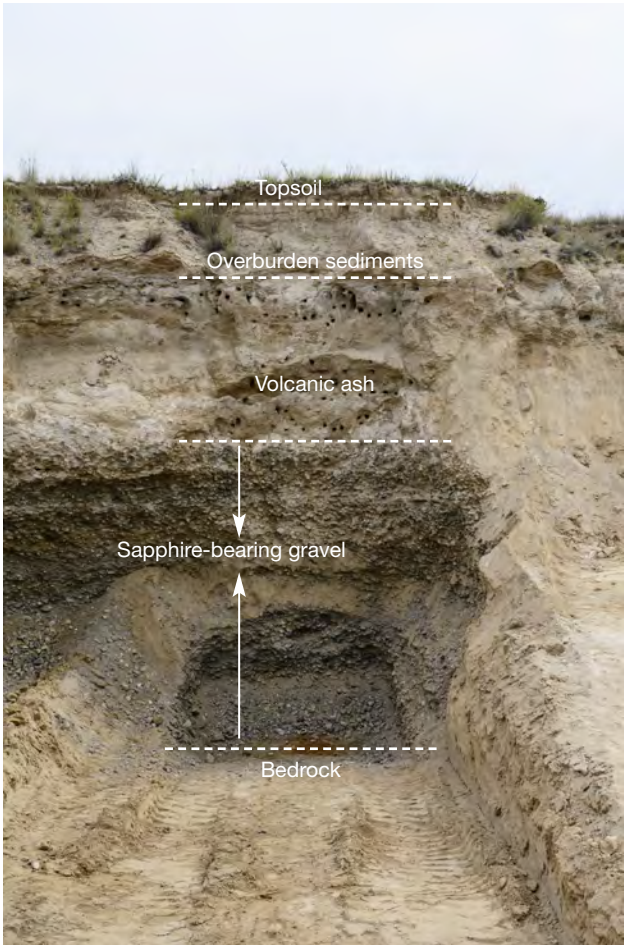

Figure 7. A well-layered lithological profile was exposed at the Eldorado Bar mining site. The sapphire-bearing gravel layer lies between the volcanic ash unit and the brownish Precambrian basement rock. The grains and boulders within the gravel layer are very well sorted. The overburden of this deposit (including the volcanic ash and topsoil layers) is quite shallow and unconsolidated, making it easy to remove. Photo by Andrew Lucas.

Extracted gravels are then transported by front-end loader to a nearby screen separator to get rid of the larger rocks that might break the onsite washing facilities. Materials are fed on a conveyor belt to a rotating trommel (figure 8). The trommel separates the gravel into different size fractions, diverting material over a certain size to the waste piles. At this point the remaining gravels are more likely to contain sapphires. The heavy minerals in the ore, including sapphires, are further concentrated using water, gravity

separation, and a series of screens and jigs, and sluices are used to process the remaining ore.

Many of the sapphires are first removed by hand from the bottom of the mechanized processing plant jigs. All of the concentrate is combed through a second time, either on a light table or by hand jigging in water, and then flipped over onto a table. If this is expertly done, the minerals with the highest specific gravity—sapphires have an SG of 4.00—are concentrated on top in the center of the pile. The authors were informed that currently a small quantity of gold is found with the sapphire. Vast amounts of gold were sometimes recovered in the late 1800s when miners used the highly destructive method of hydraulicking, and in the early 1900s when the Perry-Schroeder dredge was operating (Lyden, 1948). Present-day miners will extract the gold to pay for a portion of the mining costs.

Sapphire crystals from the mines at Eldorado Bar generally have different shades of pastel colors, particularly bluish green and greenish blue. Pink, purple, yellow, deep green, and the rare ruby are found sporadically at this location. Some rather large stones have been recovered. One of the authors (RK) has examined a gem-quality hexagonal tabular crystal weighing nearly 50 ct—it was mounted in a pendant, so the exact weight is unknown.

At the end of our day at Eldorado, a total of 1,045 carats of sapphire were recovered from the mine run, with the largest stone weighing 16.78 ct (figure 9). Also of note was a pink stone weighing 7.86 ct. All of these sapphires are now in the GIA corundum collection in Carlsbad, California.

Today, many of the sapphires mined at the Missouri River deposits are sold—rough and cut—in their natural state. If the transparency is greatly decreased due to dense concentrations of exsolved rutile, they can be heated to change both their transparency and color (figures 10 and 11). Beautiful heat-treated faceted sapphires are produced from Missouri River material.

The origin of sapphires found in the Missouri River gravel bars has been discussed since their discovery in the late 1800s. Pratt (1906) reported a dike containing greenish sapphires about three miles below the Canyon Ferry at French Bar in 1900. A similar rock had been described by Kunz (1890). This rock, called "trachyte rock" by Kunz, came from a dike near the river and above Eldorado Bar. Later, Clabaugh (1952) checked the reported dike location at French Bar and found a similar dike but no sapphires. These reported dikes are still the only source rocks that have ever been proposed. Experts agree that a small outcropping above French Bar containing sapphires in matrix could not have been responsible for the massive quantity of sapphires along the roughly 14-mile stretch of present-day Hauser Lake—there must have been another source or sources. No new origin model has been proposed for the sapphires extracted from the upper Missouri River deposits.

Figure 8. At Eldorado Bar, the washing plant is set up on the gravel bar. Sapphire-bearing gravels are fed through an oversized screen and a trommel, then sorted by a set of jigs and a sluice box for gold and very small sapphire recovery. The operation lies next to the river and some beautiful grassland. Photo by Andrew Lucas.

Figure 9. Four of the best bluish and greenish sapphires mined from Eldorado Bar on the day of the authors' visit. All four show the material's characteristic pastel color, and some clearly display a hexagonal crystal habit even though the surface is worn. The second sapphire from the left, the largest recovered that day, weighs 16.78 ct. Photo by Kevin Schumacher.

Figure 10. Various colors of heated Missouri River sapphires, ranging from 0.16 to 1.65 ct. Courtesy of American Sapphire Company, © Robert E. Kane.

ROCK CREEK

Sapphires were discovered at Rock Creek, popularly known as Gem Mountain, along its tributaries in 1892. The American Gem Mining Syndicate was incorporated in 1901 in the town of Philipsburg, with headquarters in St. Louis, Missouri. The company's top priority was to mine and market sapphires from several different gulches at the huge Rock Creek deposit. While they also maintained sapphire cutting facilities, the bulk of their Rock Creek rough was shipped to the company's factory in Geneva, Switzerland. Most of it was consumed by the watch industry for bearings, with smaller amounts used as industrial bearings and as faceted stones set in jewelry. Large-scale mining took place at Rock Creek between 1906 and 1923.

Mining resumed for a brief time before World War II, until synthetic sapphire took over the watch component market. Since then, Rock Creek sapphires have been extracted solely for jewelry making and mining tourism, with most of the stones undergoing heat treatment. Large-scale mechanized mining and processing facilities have recently been installed, marking the start of a new era of Montana sapphire mining.

Historically, sapphires were mined from Anaconda Gulch and Sapphire Gulch, although many other gulches were also worked (figure 12). Similar to the upper Missouri River area, bedrock in this district is argillite of the Mesoproterozoic Belt Supergroup, overlain by Eocene volcanic rocks from different eruptive events (Berg, 2014). According to Clabaugh (1952), intrusions of either Cretaceous or Tertiary age also occur in this area. The sapphires are found in loose sediments. Currently, two operations are active at Rock Creek: Potentate Mining and Gem Mountain Sapphire Mine. For this trip, the GIA team visited Potentate's mining and washing operations and Gem Mountain's sapphire tourism and heat treatment facilities.

Figure 11. This 32.02 ct crystal is one of the largest high-quality Montana gem sapphires ever recorded. It was discovered at Bruce Scharf's Montana Blue Jewel mine at Eldorado Bar. The stone was heated to intensify its color. It shows strong pleochroism when viewed down the c-axis (left) and at a right angle to the c-axis (right). This consideration is especially important for gem cutters. Courtesy of American Sapphire Company, © Robert E. Kane.

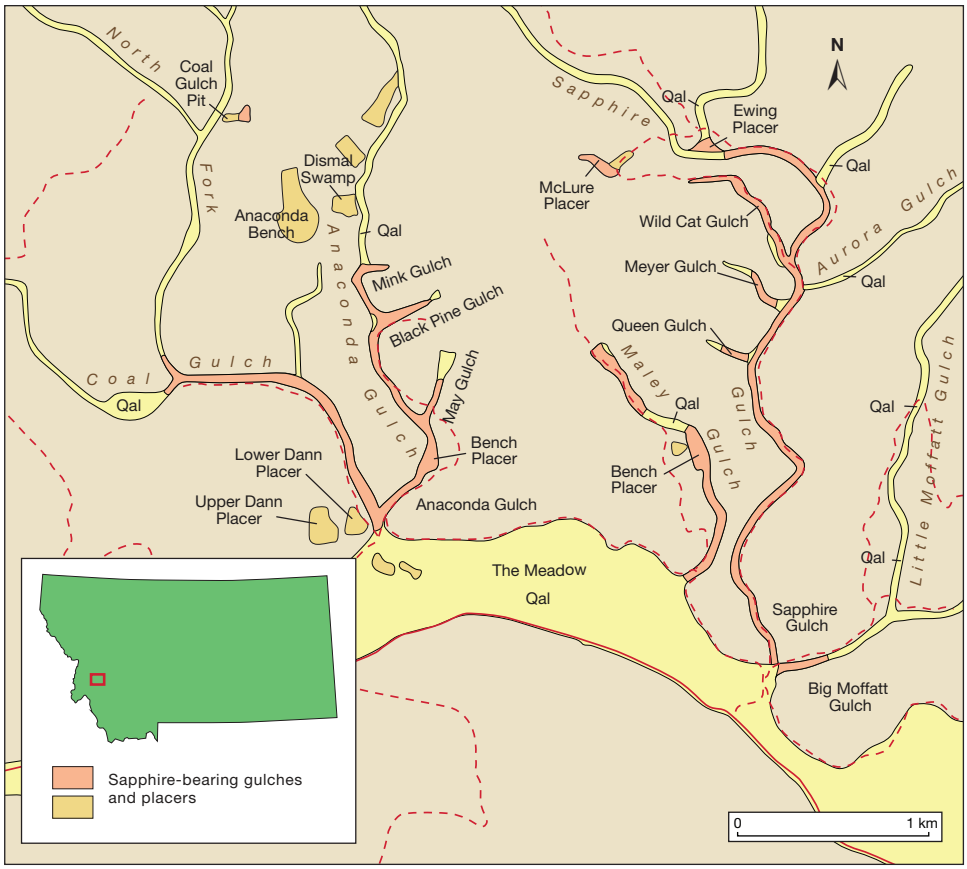

Figure 12. A detailed map shows the main sapphire mining gulches and placers in the Gem Mountain area along the west fork of Rock Creek and its tributaries. From Berg (2014).

At Eureka Gulch, Dr. Keith Barron, geologist and owner of Potentate Mining, described the nature of the sapphire-bearing deposits. Unlike the river gravel layers at the upper Missouri River area, these sapphire-bearing sediments lack the well-defined layering pattern formed by river flows. Instead, gravels and boulders of different sizes are randomly mixed (figure 13). Barron concluded that sapphires are buried in mudflows instead of riverbeds in the Gem Mountain area (Barron and Boyd, 2015). Since mudflow is a rapid mass-wasting process, emplacement can cover both topographic lows and highs. After mudflow emplacement, the local topography is often shaped again by weathering and erosion to form gul-

Figure 13. Dr. Keith Barron, geologist and owner of Potentate Mining, shows the sapphire- and gold-bearing mudflow at Eureka Gulch. Compared to the well-sorted alluvial gravel layer at Eldorado Bar, the ore zones contain much finer-grained soils along with coarser gravel and boulders. Photo by Andrew Lucas.

Figure 14. Dry screening/concentrating plant near Sapphire Gulch. Here, sapphires are mined on the hill slopes and benches rather than the stream beds. Currently, Potentate recovers sapphires from the concentrated +1/8 in. to –1 in. material. They are stockpiling the –1/8 in. undersized material. Photo by Andrew Lucas.

lies and ridges. Today, sapphire-bearing mudflow deposits are found both in gulches and hilltops in Potentate's mining sites. For instance, Potentate set up their dry screening/concentrating operation on a hilltop (bench), and the bulk sampling pit has turned out to be quite productive (figure 14).

Although sapphires have not yet been observed *in situ* in this area, aeromagnetic surveys of the Potentate property also reveal potentially sapphire-bearing igneous bodies beneath the surface. Potentate is mainly working on the Eureka Gulch deposit and bulk sampling the Sapphire Gulch deposit. The former is primarily for gold mining, with sapphire as a by-product, while the latter is focused on sapphire.

Figure 15. Both sapphire and gold are recovered at Potentate's washing plant at Eureka Gulch. The washing plant has a feeder, an oversized screen, multiple conveyer belts, and two sets of jigs, along with a sluice box used mainly to recover gold and very small sapphires. Photo by Andrew Lucas.

Sapphire Gulch material with a size range of 1/8 inch to 1 inch also goes through the washing plant at Eureka Gulch (figure 15). Sapphire concentrates extracted from the jigs are then sorted by hand. The washing plant's capacity is about 50–60 cubic yards (38–46 cubic meters) per hour. After observing the washing process, our team hand-picked sapphire from the jig. About 13–15% of the production had attractive natural colors of blue, greenish blue, yellow, or pink. Most of the remaining sapphires have green and brownish colors that react very well to heat treatment.

Potentate's first mining season at Rock Creek was in 2015, and was very successful. The 2016 mining season near Sapphire Gulch recovered about 220 kilograms of rough sapphire larger than 3.5 mm. According to Potentate marketing director Warren Boyd, the mining operation recovered about 150 kilograms of rough sapphire under 3.5 mm, suitable for very small faceted gemstones and beads. Boyd added that Potentate's objective is to become a major international rough sapphire supplier in the next few years.

Gemstone cutters are important buyers of the rough sapphires mined by Potentate, with stones ranging from 2.5 to 6.0 mm best suited for precision cutting. In today's market, these sapphires will command a premium price if they are custom-faceted or sold in their natural, unheated state. Jeffrey Hapeman of Earth's Treasury (Westtown, Pennsylvania) has faceted many Rock Creek sapphires, applying special cut styles such as "Helena Oval," named after Montana's capital (figure 16). Rachel Abel of Americut Gems is working on heat treating and precision cutting sapphires purchased from Potentate. She uses robotic cutting systems to precisely facet stones ranging from 2.5 to 4.5 mm. The stones are faceted as modified round brilliants and to display the "hearts and arrows" effect seen in some diamonds.

Gem Mountain Sapphire Mine is a diversified business, with a mining site at Rock Creek, a heat treatment facility, a gravel washing site for tourists, and a jewelry store in Philipsburg. The mining at this site is quite different from Potentate's large-scale mechanized operation in the same area. Sapphire-bearing gravels are extracted and transported to the tourist washing site and to the jewelry store for sale.

Figure 16. These sapphires (0.49–4.19 ct) were mined by Potentate in 2015 and faceted by Jeffrey Hapeman of Earth's Treasury. The 0.57 ct pink stone in the front row (second from left) has outstanding brightness and saturation for this deposit. Some of the stones have the "Helena Oval" cut specially designed for Montana sapphire. All of these sapphires are unheated. Photo by Jeffrey Hapeman, courtesy of Earth's Treasury and Potentate Mining.

As the authors witnessed, untreated rough sapphires from Rock Creek generally have more saturated colors than those from the upper Missouri River, but pastel colors are still the most prevalent. Many of the heated stones have color zoning and a brightly colored center that corresponds to lighter or nearly colorless zones in the untreated crystals (figure 17). Local miners call this bright center "yolk." Kunz (1901) noted that Rock Creek sapphires are notable for small colored spots, which when properly cut and positioned can color the entire stone when looking down the table. He also observed that many fancy colors from this area are quite distinct compared to other sources, and that the pink stones in particular can be intensely brilliant. These descriptions matched our own observations (again, see figure 16). Many Rock Creek sapphire crystals show a clear hexagonal habit, similar to those from the Missouri River gravel bars.

The origin of Rock Creek sapphires has drawn the attention of researchers, yet as of this writing, no *in situ* sapphires have been found. In the most recent study on Rock Creek sapphires (Zwaan et al., 2015), the inclusion studies and chemical composition analysis pointed to a plumasitic/metasomatic origin. Palke et al. (2015) performed a study on the glassy melt inclusions in sapphires from both Rock Creek and the Missouri River. The study showed abnormal two-phase inclusions consisting of a glassy solid and a gas. Chemical study indicates that the glassy solid phase is of dacitic to trachydacitic composition. This ongoing study could provide more information on the crystallization of these alluvial sapphires. Previous research by Berg and Cooney (2006) on stones from the same area revealed two characteristic materials attached to the surface: felsite and kaolinite. The study speculated that surface features such as grooves and flats underneath the adhering felsite were from resorption (solution) of the sapphires when they were transported in the felsic magma. Attached kaolinite formed from alteration of feldspars in the volcanic ash also indicates that the sapphires were derived from felsic volcanic rocks.

HEAT TREATMENT OF ROCK CREEK SAPPHIRES

While gemstones have been heated to enhance their quality for thousands of years, a well-controlled high-

Figure 17. A group of heat-treated Rock Creek sapphires under transmitted light. Some of the stones have an intense color, while most show colorless to light yellow color zoning. Locals call the yellow color concentration "yolk." Courtesy of Potentate Mining.

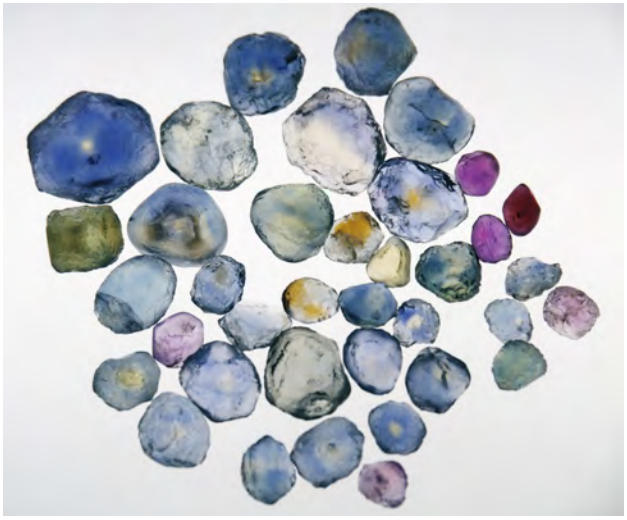

Figure 18. Two scoops of sapphires picked from the jig at Potentate's washing plant. Most of the stones have pale green and bluish hues. Heat treatment can enhance the color of many stones and increase their market value. Photo by Andrew Lucas.

Figure 19. Chris Cooney of Gem Mountain Sapphire Mine operates the electrical furnace used to heat sapphires. The metallic blue cylinder to the right of the control panel houses the sapphire-containing crucibles. Photo by Andrew Lucas.

temperature heating environment has only existed for the past 30–40 years. The authors were offered the opportunity to record the entire process of heat treatment of Rock Creek sapphires at the Gem Mountain facility nearby.

Rock Creek has had considerably higher sapphire production than the other alluvial deposits in Montana over the years, and many people consider it the only alluvial deposit that can be economically mined on a large scale for sapphire alone. Emmett and Douthit (1993) reported that about 8% of Rock Creek sapphires can be marketed as gems, while 65–70% of the production is of pale greenish and bluish colors that are acceptable to the jewelry market (figure 18). Since color is the most important value factor for sapphires, enhancing the stones' color became a priority.

The electrical furnace (figure 19) and the method used are the same as those published in Emmett and Douthit (1993). Today, rough sapphires submitted to Gem Mountain for heat treatment are carefully documented and go through two rounds of heating (figure 20). The first round, called the "fancy burn," is done under an oxidizing environment. After the fancy burn, the stones' color is evaluated; the ones that did not gain satisfactory fancy colors such as yellow, orange, and pink will go to the second round of heating. The second round is the "blue burn," done under a reducing environment. When both rounds of treatment are complete, the stones are reevaluated. Cutting and manufacturing decisions can then be made.

According to Chris Cooney, owner of Gem Mountain Sapphire Mine, about 30–40% of the stones gain a marketable bluish color after the "blue burn" (figure 21). While heating itself risks damage to the stone, the most tedious but most critical step in heat treatment at Gem Mountain is the evaluation of the stones after each round (C. Cooney, pers. comm., 2015). Color zoning and color concentration at the center of many stones further complicate the evaluation process.

Figure 20. Rough sapphires from Rock Creek before and after two rounds of heating. Left: The material before heating. Center: The same sapphires after the oxidizing "fancy burn." Right: The same sapphires after the reducing "blue burn." Photos courtesy of Gem Mountain Sapphire Mine.

Figure 21. After the second round (the "blue burn" heating), about 40% of the stones acquire an attractive blue color. Some stones do not change significantly after two rounds of heating. Photo by Andrew Lucas.

Rough that was treated in an oxidizing environment (producing darker yellow, orange, and pink colors) will often have a dark central color concentration, while many of the stones heated in a reducing environment will have a colorless or very light yellow spot in the center. The concentrated color spots can brighten the entire stone, but sometimes they combine with the bodycolor of the stone, producing unpleasant results. Since many stones are also cut by contractors of Gem Mountain, this evaluation also plays an important role in the process.

Cooney compares the heat treatment of sapphire to cooking, in that procedures are adjusted based on intuition and years of experience. Not all Montana sapphire yields predictable or desirable results from heat treatment; the nature and chemical composition of the stone are critical, as are temperature-time profiles and the conditions inside the furnace (Kane, 2008).

The heating service is not just for the tourists who extract their stones at Gem Mountain. Sapphires sourced elsewhere are also submitted for treatment. Over the years, Cooney has found that sapphires from certain sources achieve better results, while others hardly change color.

MONTANA SAPPHIRE TOURISM

Gem tourism is an essential component, in some cases the only one, of sapphire-related businesses in Montana (figure 22). The authors observed the tourist activities at both Gem Mountain and one of the upper Missouri River operations.

The tourist bucket mining facility at Gem Mountain is about 16 miles southwest of Philipsburg. Gravels removed from the neighboring mining claim by mechanized mining methods are transported to this site, where domestic and international tourists can purchase sapphire-containing "gravel bags" of various sizes. They can either wash their gravels on-site (again, see figure 22) or take them home. Most of the sapphire mines, including Gem Mountain, will mail gravel bags to people who cannot visit in person. Sapphires found can also be evaluated by staff with years of experience. Visitors can choose to keep the stones as they are or have them heat-treated, faceted, or even mounted in jewelry by Gem Mountain's staff. They are encouraged to have larger stones cut and mounted locally to help the local economy. The heat treatment and cutting and manufacturing services set this business apart. Tourists have fun treasure hunting, but also see the whole mine-to-market story happening for themselves.

Figure 22. Visitors of all ages can be found sorting washed and concentrated gravel at Gem Mountain. This boy is carefully putting his just-found sapphire into a tube provided by the operator. Photo by Andrew Lucas.

Figure 23. A visitor at Gem Mountain showed the authors a beautiful pin mounted with natural fancy sapphires she and her family had mined there over the years. Jewelry-making services are easily available in nearby Philipsburg. Photo by Kevin Schumacher.

The authors asked several visitors at the washing site about their experiences at Gem Mountain. We were surprised to see them wearing jewelry mounted with sapphires found there over the years (figure 23). Through our conversations, we learned that many of the tourists have returned repeatedly over the last 10–15 years. They come with family and friends in what has become an annual ritual for some. It is not uncommon to see a couple showing off an engagement ring with their own handpicked sapphire on social media.

At the upper Missouri River operations run by Spokane Bar Sapphire Mine, tourists can purchase gravel bags at the store and wash them on- or off-site. Besides gravel washing, mine owner Cass Thompson and other Montana sapphire miner operators also offer a special mine run service (figure 24). With advance reservations, clients—who range from gemstone wholesalers, to interested clients from outside the gem and jewelry industry—can purchase a certain number of dump truck loads (measured in cubic yards). These will be run through the commercial mechanized mining plant—which can take as long as eight hours for an 80-yard run—which concentrates the gem-bearing gravels along with non-sapphire accessory minerals such as hematite and garnet. These customers come to see the mining process, and at the end of the day they pick up their concentrates from the jig and take them home to sort for fun.

SUMMARY

As one of the "Big Three" colored gemstones, sapphire has always been a focus of exploration and gemological education. The related history, geology, and business models are all of interest to those who trade in sapphire. Montana is one of the few major gemstone sources in the United States. Over the past 150 years, countless people have devoted themselves to prospecting and mining these sapphire sources. The success of these operations has often been difficult to achieve, but the passion for these sapphires has persisted.

Today, the alluvial sapphire deposits are still actively mined. Although small-scale mining still pre-

Figure 24. Cass Thompson (far right) and his colleagues harvest the concentrated mine run purchased by GIA. Sapphire-bearing concentrate is vacuumed from the jig and put into buckets for the clients to take home. Photo by Andrew Lucas.

Figure 25. A group of faceted Rock Creek sapphires and a piece of rough extracted from the jig during the authors' visit to the Potentate operation. The largest faceted stone in this group is the 4.26 ct cushion cut. Photo by Andrew Lucas.

vails in these areas, Potentate Mining's large mechanized operations with heavy investment could change the dynamic of sapphire mining in the Rock Creek area (figure 25). Meanwhile, sapphire tourism is quite important to the local economy.

One thing the different operators have in common is their commitment to protecting the environment. The sapphire mining happens in harmony right next to agriculture land, and we were encouraged to see them taking responsibility for restoring the land. The miners follow state guidelines regarding water and land reclamation. For example, the Eldorado Bar and Potentate Mining pits are refilled after mining. Potentate also plants trees after operations have ceased; water from their washing plants is filtered and restored to potable levels.

As stakeholders in the local economy, the mines maintain good relationships with neighboring farms and businesses. Many miners are from the area and have worked on the sapphire fields for years, so they have an emotional connection to the land and the stones being extracted. Montana sapphire is a gemstone that Americans are proud of. As Cass Thompson put it, "They love the idea of keeping the state of Montana just as beautiful as the sapphires they pull out."

ABOUT THE AUTHORS

Dr. Hsu is technical editor of Gems & Gemology, *Mr. Lucas is manager of field gemology education, Mr. McClure is global director of colored stone services, and Mr. Renfro is the gemological manager of the gem identification department and analytical microscopist in the inclusion research department at GIA in Carlsbad, California. Mr. Kane is president and CEO of Fine Gems International and American Sapphire Company in Helena, Montana.*

ACKNOWLEDGMENTS

The authors thank Chris Cooney of Gem Mountain Sapphire Mine, Dr. Keith Barron and Warren Boyd of Potentate Mining, and Cass Thompson of Spokane Bar Sapphire Mine for providing valuable information about the deposits at each location and giving us the opportunity to record. Prof. Richard Berg of the Montana Bureau of Mines and Geology at Montana Tech generously shared his knowledge of the state's sapphire deposits. The authors also appreciate the videos prepared for this project by Kevin Schumacher of GIA in Carlsbad, California.

REFERENCES

Ball S.H. (1943) Gem Stones. In E.W. Pehrson and C.E. Needham, Eds., *United States Department of the Interior Bureau of Mines, Minerals Yearbook 1942*, Washington, Government Printing Office, pp. 1509–1520.

Barron K.M., Boyd W.F. (2015) The Rock Creek sapphire mine of Montana—A new era. *InColor*, No. 28, pp. 46–57.

Berg R.B. (2014) *Sapphires in the Southwestern Part of the Rock Creek Sapphire District, Granite County, Montana*. Montana Bureau of Mines and Geology Bulletin 135, 86 pp.

—— (2015) Compilation of reported sapphire occurrences in Montana. Montana Bureau of Mines and Geology, Report of Investigation 23, 78 pp.

Berg R.B., Cooney C.F. (2006). The importance of surface features and adhering material in deciphering the geologic history of alluvial sapphires—An example from western Montana. *G&G*, Vol. 42, No. 3, p. 145.

Berg R.B., Dahy J.P. (2002) Montana sapphires and speculation on their origin. In P.W. Scott and C.M. Bristow, Eds., *Industrial Minerals and Extractive Industry Geology*, Geological Society of London, p. 201–206.

Clabaugh S.E. (1952) *Corundum Deposits of Montana*. U.S. Geological Survey Bulletin 983, 100 pp.

Emmett J.L., Douthit T.R. (1993) Heat treating the sapphires of Rock Creek, Montana. *G&G*, Vol. 29, No. 4, pp. 250–272, http://dx.doi.org/10.5741/GEMS.29.4.250

Garland M.I. (2002) The alluvial sapphire deposits of western Montana. PhD thesis, University of Toronto.

Hammett A.B.J. (1966) *The History of Gold*. Braswell Printing Co., Kerrville, Texas, 107 pp.

Kane R.E. (2008) American sapphires: Montana and Yogo. World of Gems Conference 2008, pp. 59–64.

Kunz G.F. (1890) *Gems and Precious Stones of North America*. The Scientific Publishing Co., New York, 365 pp.

—— (1894) Precious stones (Sapphire). In D.T. Day, Ed., *Mineral Resources of the United States, Calendar Year 1893*. United States Geological Survey, Government Printing Office, Washington DC, pp. 692–693.

—— (1901) Precious stones (sapphires in Montana). In D.T. Day, Ed., *Twenty-First Annual Report of the United States Geological Survey to the Secretary of the Interior—1899–1900*. Washington, Government Printing Office, 7 Parts, Part VI (continued), pp. 448–449.

Lyden C. (1948) *The Gold Placers of Montana*. Montana Bureau of Mines and Geology, Montana School of Mines, Memoir No. 26, Butte, Montana, 152 pp.

Palke A., Renfro N., Berg R.B. (2015) Gem News International: Glassy melt inclusions in sapphires from Montana. *G&G*, Vol. 51, No. 3, pp. 329–330.

Pratt J.H. (1906) *Corundum and Its Occurrence and Distribution in the United States*. U.S. Geological Survey Bulletin, 269, 175 pp.

Smith J.L. (1873) Notes on the corundum of North Carolina, Georgia, and Montana, with a description of the gem variety of corundum from these localities. *American Journal of Science*, Series 3, Vol. 6, pp. 180–186, http://dx.doi.org/10.2475/ajs.s3-6.33.180

Zwaan J.C., Buter E., Mertz-Kraus R., Kane R.E. (2015) Alluvial sapphires from Montana: Inclusions, geochemistry and indications of a metasomatic origin. *G&G*, Vol. 51, No. 4, pp. 370–391, http://dx.doi.org/10.5741/GEMS.51.4.370

DIAMOND

With Concentric Inclusions

As a diamond grows, layer by layer, it may incorporate small pieces of the surrounding mantle rocks as mineral inclusions. The three-dimensional arrangement of inclusions in most diamonds has the appearance of being somewhat random, with no discernible pattern. However, GIA's New York laboratory recently examined a noteworthy exception.

A 2.34 ct Fancy Intense yellow-green type IaAB diamond was found to have abundant silicate inclusions with a more systematic pattern delineating growth layers (figure 1). Collectively, the inclusions outline concentric octahedral layers. The growth layers are made even more noticeable by a sort of optical graining that could be caused by layered distortions in the diamond crystal from variations in nitrogen concentration. Many of the individual inclusions have an elongate or flattened oblate shape that conforms to the growth layering (figure 1, bottom). Thus, both the shape of individual inclusions and the collective distribution of multiple inclusions imitate the geometry of concentric octahedral diamond growth. This kind of symmetrical, growth-outlining texture is rarely observed in diamond.

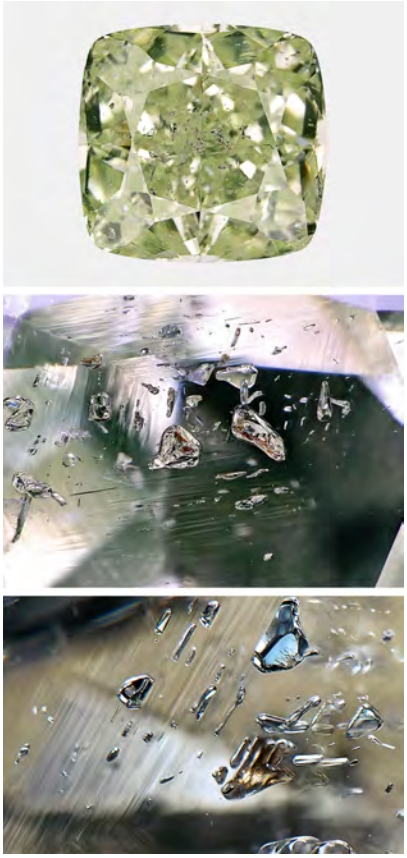

Figure 1. This 2.34 ct Fancy Intense yellow-green diamond (top) contains abundant inclusions that outline concentric octahedral growth layers. Through the table, the layers resemble nested rhombuses (middle, field of view 3.54 mm). The inclusion shapes appear to be controlled by the layering, as seen through the pavilion (bottom, field of view 1.99 mm).

The vibrant orange and green inclusions were identified as almandine-pyrope garnet and omphacitic clinopyroxene, respectively. Such mineral inclusions are distinctive of diamonds grown in an eclogite host rock, one of two common diamond rock types in the lithospheric mantle, the other being peridotite (S.B. Shirey and J.E. Shigley, "Recent advances in understanding the geology of diamonds," Winter 2013 *G&G*, pp. 188–222). Diamonds like this one with eclogitic inclusions are sometimes called E-type, while those with peridotitic inclusions are denoted as P-type.

This is an interesting sample from a geological perspective. There are still many unanswered questions about exactly how diamonds form. Detailed analysis of this sample could provide valuable clues as each layer captures successive chemical snapshots of the diamond growth process. Of particular interest here is the question of how long it takes to make a diamond. It is possible that this diamond grew over the span of millions of years and the inclusions serve as an encrypted record of the process.

Evan M. Smith and Wuyi Wang

With Unusual Fluorescence Distribution

The New York lab recently encountered a round brilliant diamond, weighing just over 2 ct, that displayed little if any reaction to long-wave UV except for a small spot confined to the area around the culet (figure 2, left). This small area appeared to have medium fluorescence intensity. While the laboratory determination of fluorescence strength and color is

Editors' note: All items were written by staff members of GIA laboratories.

Gems & Gemology, Vol. 53, No. 2, pp. 228–239.

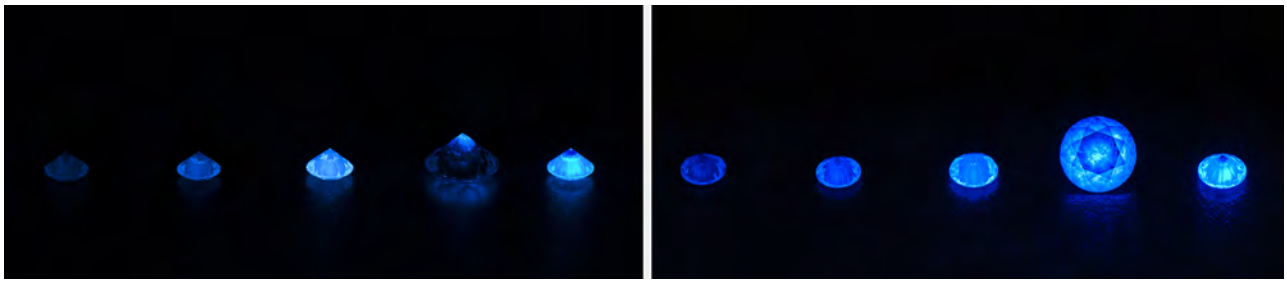

Figure 2. Left: The 2 ct round (second from right) displayed an unusual fluorescence reaction confined to the culet area. Right: When observed face-up, the small fluorescent area by the culet reflected throughout the stone and appeared more intense.

performed in the table-down position, we noticed a very different appearance when the diamond was observed through the crown (figure 2, right). Because of the location of the fluorescent area, it reflected evenly throughout the face-up position and appeared to have higher intensity, at approximately the strong/very strong boundary.

DiamondView imaging revealed that the diamond was cut with its growth zonation parallel to the girdle. We speculate that the area of fluorescence in the rough was larger and more centrally located, indicating that the earlier growth showed more blue fluorescence than the later growth, which was basically inert to UV radiation. With the given orientation and placement of the finished stone in the rough, a part of this fluorescent area remained at the culet in the cut stone, leading to this unusual feature.

Absorption spectra in the infrared region confirmed this to be a type Ia diamond with a high concentration of aggregated nitrogen and spectral features typical of a natural diamond. The N3 defect was detected by the presence of moderate-intensity absorption in the UV-Vis absorption spectrum, which is consistent with this type of diamond. The N3 defect is a well-known cause of blue fluorescence in natural diamonds. Based on past experience, it should be pointed out that the area at the culet with medium-strength blue fluorescence does not necessarily have higher concentrations of the N3 defect. The occurrence of other impurities or lattice distortion could affect fluorescence intensity from the N3 defect as well.

The effect of blue fluorescence on the appearance of D-to-Z diamonds has been debated for more than 25 years. GIA conducted a study on this subject in the 1990s (see T.M. Moses et al., "A contribution to understanding the effect of blue fluorescence on the appearance of diamonds," Winter 1997 *G&G*, pp. 244–259). The study showed that blue fluorescence had little to no impact on color appearance or transparency except in extremely rare examples of "overblues." With this in mind, the 2 ct round brilliant offered an interesting opportunity to revisit the earlier experiment's face-up observations. We compared the diamond, which was graded "H" color, with nonfluorescent diamonds—GIA color master stones—of similar color. As seen in figure 3, no visual difference was observed in the standard color-grading environment. This example supports the conclusion from the 1997 article that the industry would be better served by considering each diamond on its own visual merits.

John King and Wuyi Wang

Figure 3. No visible difference in color appearance or transparency was noted when the fluorescent stone was flanked by nonfluorescent diamonds of similar color in a color-grading environment.

Cat's-Eye KORNERUPINE

A dark, translucent, yellowish green oval cabochon (figure 4) was recently submitted to the New York lab for identification. The 1.44 ct stone displayed an intense chatoyancy.

With a spot refractive index (RI) reading of 1.67 and a hydrostatic specific gravity (SG) of 3.32, the stone was identified as kornerupine, a rare borosilicate mineral found in boron-rich volcanic and sedimentary rocks that have undergone metamorphism (http://rruff.info). Raman spectroscopy confirmed the identification.

Cat's-eye kornerupine is an extremely rare gemstone. Its chatoyancy

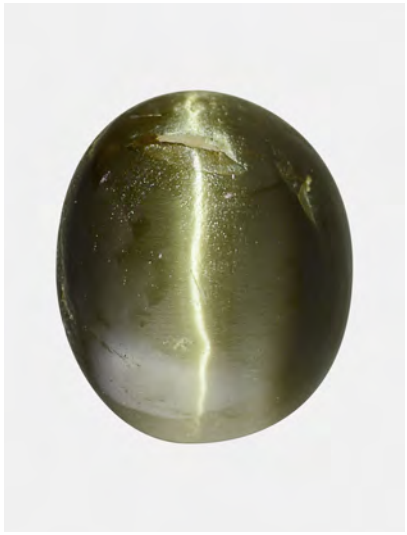

Figure 4. This 1.44 ct yellowish green kornerupine displayed strong chatoyancy.

is caused by rutile and graphite inclusions (H.N. Lazzarelli, *Gemstones Identification: Blue Chart*, 2010, www.gembluechart.com). However, we were unable to identify the needles in this stone using Raman spectroscopy. Fiber-optic illuminated magnification exposed dense clusters of these needles, some displaying iridescence (figure 5). This was GIA's first encounter with this material in more than a decade.

Akhil Sehgal and Daniel Girma

Figure 5. A dense collection of needle inclusions was the cause of the chatoyancy. Field of view 2.08 mm.

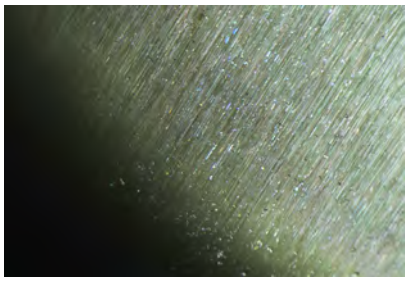

Natural Conch "Rosebud" PEARLS

Non-nacreous conch pearls from *Strombus gigas* are known mainly for their very attractive pink color and distinctive shimmering appeal due to the characteristic flame structures on their surfaces. Although conch pearls are found in various tones of yellow, brown, and white, the most desirable hue is undoubtedly pink with an intense saturation. The flame structures are due to "crosswise arrays of bundles of aragonite laths or fibers that may reflect or absorb the light that falls on the structure, letting it appear bright or dull" (H.A. Hänni, "Explaining the flame structure of non-nacreous pearls," *The Australian Gemmologist*, Vol. 24, No. 4, 2010, pp. 85–88).

In late 2016, GIA's New York lab staff had the opportunity to study part of Susan Hendrickson's conch pearl collection. Among the assortment of conch pearls of various sizes, colors, and shapes, a few "rosebud" specimens caught our attention (figure 6). The term "rosebud" is most commonly used to describe characteristically shaped freshwater nacreous pearls, but this is the first time GIA has examined conch pearls with such shapes (figure 7). The nine pink specimens had roundish outlines with a button-like appearance. But in keeping with the rosebud pearl form, they exhibited differences in the bumps or ridges on their surfaces. Some bumps were rounded and spread out, while others were jagged and tightly grouped. The authors could not locate any reports of rosebud conch pearls in the literature, and the cause of these distinctive surface structures is unknown. One possible explanation is that when a pearl forms in a pearl sac positioned in a region of muscular activity rather than the mantle, it will not form in a smooth symmetrical shape (E. Fritsch and E.B. Misiorowski, "The history and gemology of Queen conch 'pearls'," Winter 1987 *G&G*, pp. 208–221).

All nine samples displayed typical flame structures under magnification (figure 8). Some of them did not exhibit the flames on the bumpy surface, but only within the smoother areas. Microradiography revealed a tight internal structure with uneven outlines corresponding to the bumpy surfaces. The Raman spectra were characteristic of aragonite and clearly showed additional natural polyenic

Figure 6. "Rosebud" conch pearls of various pink tones ranging from 0.93 to 14.72 ct.

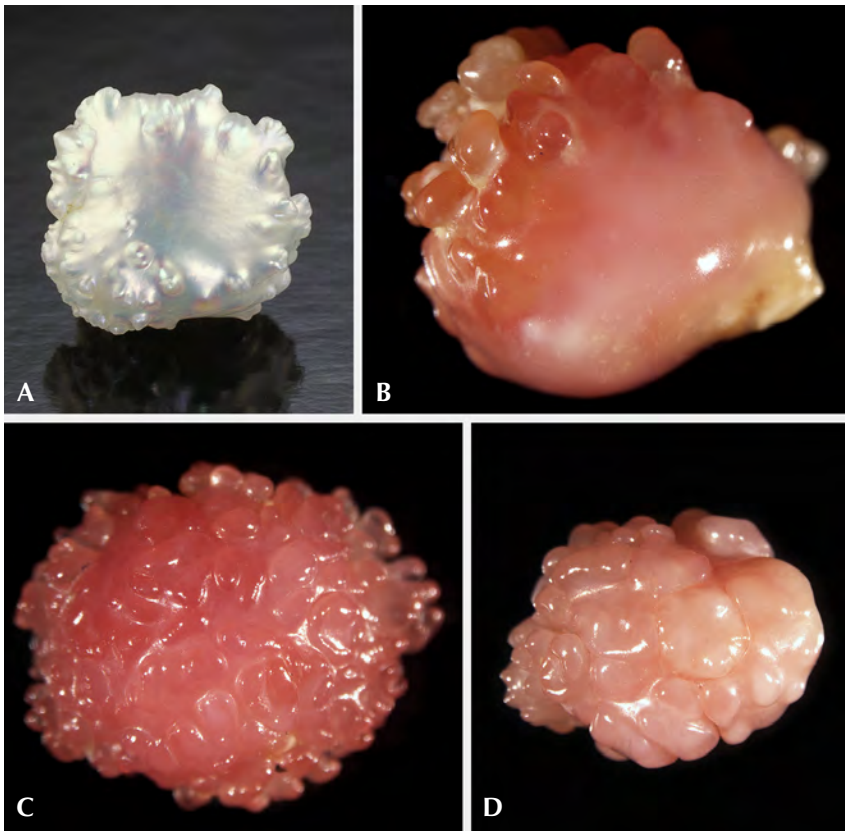

Figure 7. A shape comparison of a 4.90 ct American freshwater pearl exhibiting rosebud form (A) and three conch pearls, weighing 1.30, 0.66, and 0.91 ct (B–D).

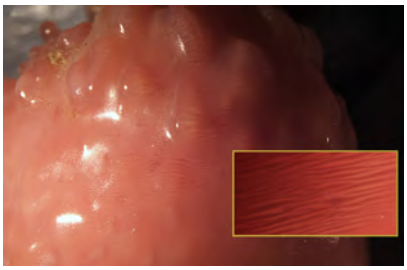

Figure 8. This 6.21 ct rosebud conch pearl shows characteristic flame structure at the surface. Fields of view 10.79 mm and 1.26 mm (inset).

pigment peaks, both as expected for pearls formed in *Strombus gigas* mollusks.

There are records of attempts to cultivate conch pearls (H. Acosta-Salmón and M. Davis, "Inducing relaxation in the queen conch *Strombus gigas* (L.) for cultured pearl production," *Aquaculture*, Vol. 262, No. 1, 2007, pp. 73–77; N. Sturman et al., "Cultured Queen conch pearls—A comparison to natural Queen conch pearls," 32nd *International Gemmological Conference*, Interlaken, Switzerland, 2011; Summer 2015 GNI, pp. 201–202). No further news about the commercial production of cultured conch pearls has reached the market, however. As a result, conch pearls are still highly desirable and valued by the trade and specialty collectors. The opportunity to study such unique and exciting examples of rosebud conch pearls allowed GIA to expand its understanding of rosebud conch pearls for future reference.

Joyce WingYan Ho and Emiko Yazawa

Partially Hollow Tridacna **Blister Pearls with Shells Attached**

GIA sees pearls of all types submitted to its global laboratories. Almost all of them are either loose or mounted in jewelry pieces; however, exceptions are occasionally encountered. The submission of a blister pearl or blister still attached to its shell is such an example (Winter 2015 Lab Notes, pp. 432–434). In January 2017, the Bangkok laboratory received an intact shell with a pearl attached near the adductor muscle area (figure 9, top). The item weighed 2.36 kg. The shell measured 32.0 × 21.0 × 11.5 cm, while the pearl measured 52.0 × 47.5 mm. At the same time and by sheer coincidence, another shell with a similar appearance and a pearl attached to the same area (figure 9, bottom) was submitted to the New York laboratory. This item weighed 806.40 g and the shell measured 20.0 × 13.5 × 9.5 cm, while the pearl measured 80.0 × 50.0 mm.

The exterior of the shell submitted to Bangkok exhibited a light brownish color and appeared roughly triangular in outline with a wavy pattern of thin ridges in rows, while the interior was white to cream with a porcelain-like surface. According to the client, the shell was found in 2014 by fishermen off the coast of Kood Island, a district of Trat Province in eastern Thailand. The shell's features are characteristic of *Tridacna* species mollusks, of which there are a number of varieties (U.E. Hernawan, "Taxonomy of Indonesian giant clams (Cardiidae, Tridacninae)," *Biodiversitas*, Vol. 13, No. 3, 2012, pp. 118–123).

As figure 9 (top right) shows, a blister pearl of similar color is prominently attached to the surface. Observation with a loupe and microscope confirmed that it was naturally attached and untreated. Microscopic examination using a fiber-optic light source confirmed the presence of flame structure on some surface areas

Figure 9. Two Tridacna *species shells with blister pearls in the adductor muscle area. Top: The shell of the specimen submitted to GIA's Bangkok lab weighs 2.36 kg and measures 32.0 × 21.0 × 11.5 cm. The blister pearl measures 52.0 × 47.5 mm (depth unmeasurable). Bottom: The shell of the New York sample weighs 806.40 g and measures 20.0 × 13.5 × 9.5 cm. The blister pearl measures 80.00 × 50.0 mm (depth unmeasurable).*

of the shell and pearl, confirming their non-nacreous or porcelaneous nature. The pearl's flame structure was short and patchy, while that seen on the shell was sharper and more defined. While the pearl's nomenclature may be the source of some debate, we considered it to be a blister pearl, rather than a blister, based on its external appearance, position on the shell, and size (E. Strack, *Pearls*, Ruhle-Diebener-Verlag, Stuttgart, Germany, 2006, pp. 115–127). The shell and pearl were exposed to long-wave UV, with the shell showing a moderate to strong chalky blue reaction with yellowish orange patches near the lip area (figure 10, left), while the blister pearl exhibited a weak to moderate yellowish green color (figure 10, right). This demonstrates how fluorescence in samples may vary from area to area.

However, the most noteworthy feature of the Bangkok specimen was that when the shell was tilted or gently rocked from side to side, a liquid clearly moved within the blister pearl (figure 11, left). The liquid was not viscous and so was most likely water, rather than a thicker liquid such as oil. It is possible that seawater was trapped during the blister pearl's formation or found its way into the "hollow" pearl at a later date. When fiber-optic light was used to illuminate the blister pearl, some of the light was transmitted and made the pearl appear translucent (figure 11, right). This, together with the trapped liquid, proved the pearl was at least partially hollow (see video at http://www.gia.edu/gems-gemology/tridacna-blister-pearls).

To see the extent of the Bangkok blister pearl's void, we examined its internal structure using a real-time X-ray (RTX) machine. Although it was only possible to examine the pearl in one orientation owing to its position and size, the blister pearl quickly revealed its partially hollow form (figure 12, left). The various shades of gray within the white near-oval feature (solid pearl surface) prove that the blister pearl's interior is full of organic matter and/or air since the X-rays passed through with very little obstruction. While hollow or partially hollow pearls—both nacreous and non-nacreous—are not new (N. Sturman, "Pearls with unpleasant odors," GIA Laboratory, Bangkok, 2009, www.giathai.net/pdf/Pearls_with_unpleasant_odours.pdf), this is the first one GIA has encountered with such visible trapped liquid. Although the solid shell attached to the pearl displayed similar gray shades, this coloring relates more to the sample's thickness than anything else. A few small rounded, darker gray patches are voids caused by parasites boring within the shell rather than by structures within the blister pearl.

Figure 10. Exposure to long-wave UV produced a moderate to strong chalky blue reaction with yellowish orange patches in the shell of the Bangkok specimen (left) and a weak to moderate uneven chalky yellowish green reaction in the attached blister pearl (right).

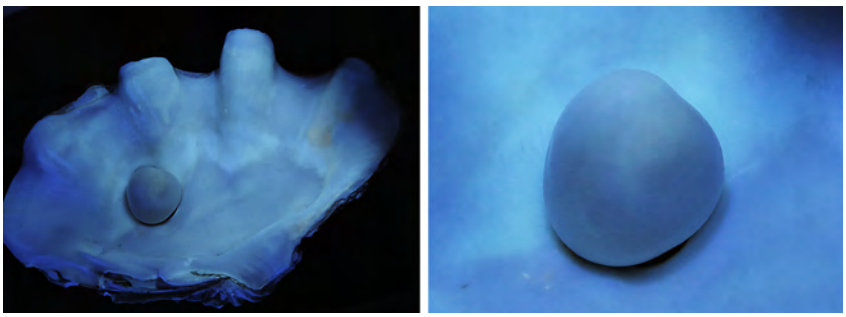

Figure 11. The blister pearl on the Bangkok submission shows a distinct boundary delineating the two phases (liquid and air) within the hollow pearl. The liquid part appears as a darker area and the air as a lighter area (left). Fiber-optic illumination reveals the boundary from a different perspective (right).

Void-like structures in whole or blister pearls from *Tridacna* species mollusks are not unusual (S. Singbamroong et al., "Microradiographic structures of natural non-nacreous pearls reportedly from *Tridacna* (clam) species," *Proceedings of the 5th GIT International Gem and Jewelry Conference*, Pattaya, Thailand, pp. 200–222), and GIA has examined many voids in other non-nacreous pearls. The RTX results proved that the specimen described was a natural blister pearl attached to its shell.

The shell submitted to GIA's New York laboratory is also noteworthy, not only for the coincidental submission, but also because the pearl was larger relative to its host's size than the one examined in Bangkok. The baroque natural blister pearl attached to this rather more colorful shell was also partially hollow, although not to the degree of the Bangkok sample. As the RTX results in figure 12 (right) revealed, the partially hollow blister pearl had a complex internal structure and was less homogenous than the specimen submitted in Bangkok. Unfortunately, no provenance was supplied with the New York sample, so there is no record of where it was found.

Both GIA reports stated that the naturally attached feature on each shell was a natural blister pearl. Many such specimens examined at GIA's labs are submitted as loose examples that have already been removed from their hosts, so it was a welcome change to handle these two shells. In addition, a comment was included on each report informing the clients of the pearl's partially hollow nature and, in the case of the Bangkok submission, the presence of a liquid. The size and appearance of the shells submitted proved they were not *Tridacna gigas* (giant clam), and the report referred to the hosts as *Tridacna* species only.

Nanthaporn Somsa-ard, Areeya Manustrong, and Joyce WingYan Ho

Figure 12. RTX results for the Bangkok sample (left) revealed a hollow pearl with a near-oval white ring marking the solid outline of the pearl's surface. Only parts of the New York pearl (right) were in the field of view at any one time due to its size. Neither appears to be entirely hollow; however, it was not possible to examine the pearls in other orientations due to their size and position on their hosts.

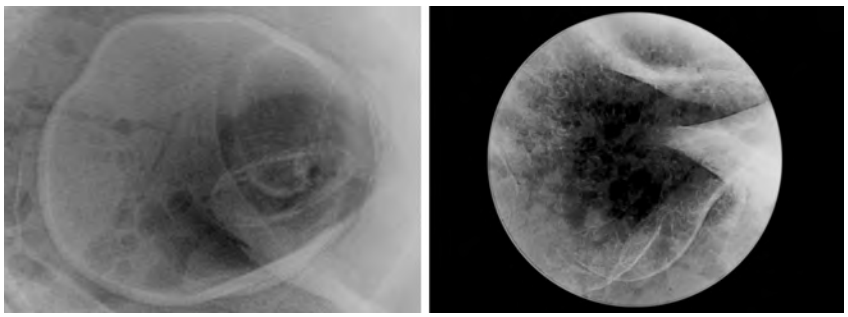

Atypical BEAD-CULTURED PEARLS With Unusual Nacre Growth

Atypical bead-cultured pearls are, by definition, cultured with unconventional beads as opposed to the typical round, predominantly freshwater shell beads. Examples of such atypical bead nuclei are irregularly shaped pieces of shell, ceramic, plastic, wax, coral beads, or even cultured or natural pearls.

Recently, GIA's New York laboratory received 10 loose undrilled pearls for identification. These samples exhibited a brownish bodycolor and measured from 7.17 × 6.92 × 6.42 mm to 12.25 × 9.72 × 9.28 mm (figure 13). Many were unusually lightweight for their size. Microradiographic examination of seven of the pearls revealed atypical bead nuclei (figure 14). The X-ray transparencies of the bead nuclei allowed us to observe faint demarcations and drill holes with varying degrees of clarity in the nuclei.

These atypical bead nuclei permitted some unusual nacre growth to develop within the drill holes, as shown in figure 14C, where the nacre secretion flows into the drill hole. This interesting observation concerning nacre viscosity was also described in recent work on atypical bead culturing experiments (K. Scarratt et al., "Atypical 'beading' in the production of cultured pearls from Australian *Pinctada maxima*," GIA Research & News, Feb. 13, 2017).

Figure 13. The 10 loose pearls submitted for identification. Samples 1, 4, and 5 are conventional bead-cultured pearls, while the rest were cultured with atypical nuclei. Photo courtesy of Aloha Pearls.

To better visualize the unusual nacre growth within the drill hole of the bead in one of the pearls, we used computed X-ray microtomography (μ-CT) and subsequently reconstructed the pearl using computer software (figure 15). The reconstructed image displayed a surface indentation aligned with the bead's drill hole (shown in orange in figure 15, left). Additional nacre growth (shown in green, figure 15, right) filled about half of the drill hole. The yellowish outer region in figure 15 (left) represents the outer nacre of the pearl.

Although this is not the first time GIA has received pearls cultured using X-ray transparent bead nuclei (Fall 2011 Lab Notes, pp. 229–230), the unusual nacre growth pattern within some of the drill holes in this sample group is worthy of note. Three-dimensional rendering using computer software and μ-CT data sets also proved very useful in visualizing the internal structure, further demonstrating the technique's worth as a powerful tool in pearl identification.

Chunhui Zhou and Emiko Yazawa

Punsiri Heat Treatment on Basalt-Related Blue SAPPHIRE

Heat treatment is often applied to sapphire to modify color or improve clarity. One known heat-treatment technique is the Punsiri method, typically applied to metamorphic or low-Fe blue sapphires. This treatment lightens the blue color by heating the stones in an oxidizing atmosphere to diffuse holes and aluminum vacancies into stones with low Ti levels (J.L. Emmett, lectures on corundum at GIA Bangkok, Aug. 28 and Dec. 4, 2010). The main characteristic of Punsiri heat treatment is distinct color zoning observable when the stone is immersed in methylene iodide. The stone will display a pale blue to near-colorless layer corresponding to the girdle outline that surrounds a deep blue core.

Recently, GIA's Bangkok laboratory examined a 1.63 ct blue sapphire, identified by standard gemological testing (RI of 1.760–1.769 and an inert reaction under long- and short-wave UV radiation). Microscopic observation revealed only a few inclusions, consisting of stringers and small healed fractures. We then immersed the stone in methylene iodide and observed Punsiri-type color zoning (figure 16). Fourier-transform infrared (FTIR) spectroscopy is a common technique used in advanced gemological laboratories to determine whether a stone is heated or unheated. When the FTIR spectrum shows Punsiri fea-

Figure 14. Microradiographs of seven pearls revealed atypical beads that were transparent to X-rays. The beads showed faint demarcations and drill holes of varying clarity. Unusual nacre growth that partially filled the drill hole of the bead of one pearl is seen in image C.

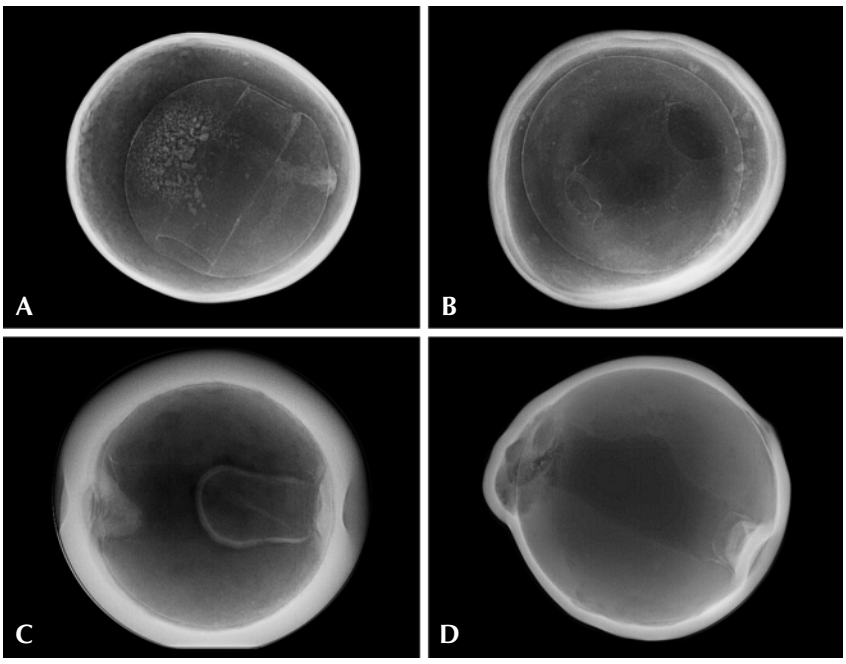

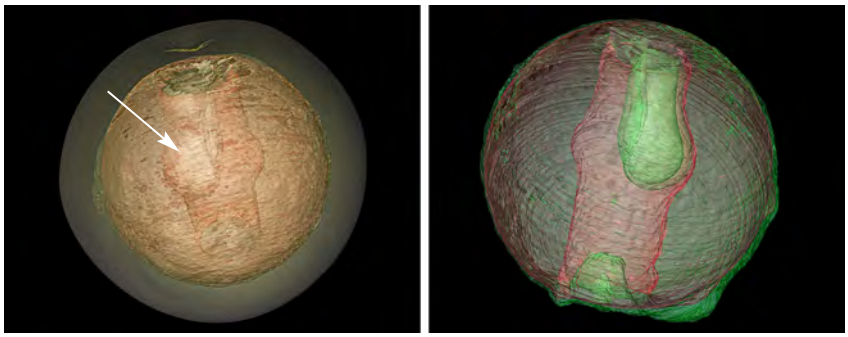

Figure 15. Left: A computed 3-D reconstruction of one of the atypical bead-cultured pearls. The orange area represents the transparent bead revealed by X-rays, with a drill hole partially filled by nacre growth shown by the whitish area (indicated by the arrow). A surface indentation toward the top also corresponds to the orientation of the bead's drill hole. Right: Reconstruction of the internal bead only. The central pink area is the drill hole inside the bead nucleus. The green area represents the nacre growth that formed inside the drill hole.

tures (e.g., multiband structures at 3191, 3064, 2626, and 2412 cm^{-1}; see chapter 4 of R.W. Hughes, *Ruby and Sapphire: A Gemologist's Guide*, RWH Publishing, Bangkok, 2017), this is conclusive for heat-treated metamorphic blue sapphire. However, when the FTIR spectrum does not show these features, it does not necessarily mean the stone has not been heat treated. Such was the case for this stone, which showed signs of heat treatment through its distinctive color zoning and near-colorless rim.

UV-visible near-infrared (UV-Vis-NIR) spectroscopy revealed a broad band at about 880 nm, indicating a blue sapphire of basalt-related origin. Laser ablation–inductively coupled plasma–mass spectrometry (LA-ICP-MS) showed no beryllium and limited amounts of other trace elements: 7 ppma Ti, 860 ppma Fe, and 47 ppma Ga were detected. This is the first time we have observed Punsiri heat treatment on a basalt-related blue sapphire. It was possible to perform the treatment on this sample due to the low amount of Ti, which allowed for faster diffusion. This report demonstrates the importance of the immersion technique in identifying heat treatment.

Sudarat Saeseaw

Figure 16. The 1.63 ct blue sapphire treated by the Punsiri method. Different views show a typical light blue to near-colorless outer layer when the stone is immersed in methylene iodide.

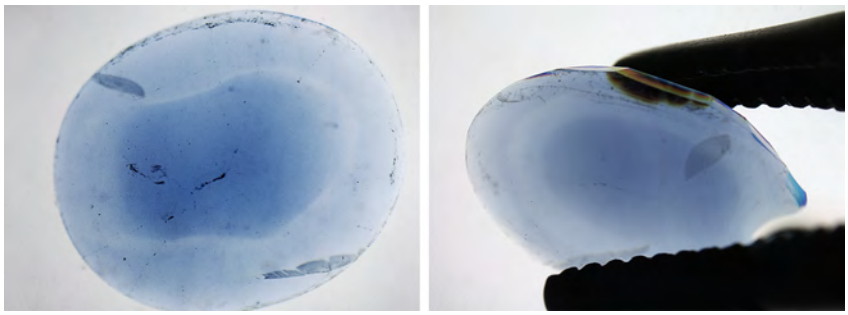

CVD SYNTHETIC DIAMOND
Mimicking Natural Stone

A 0.51 ct round brilliant (figure 17) was recently submitted to GIA's Hong Kong laboratory for update service to verify the results from a diamond grading report issued in 2014. Investigation showed that its properties were much different from the diamond in the original report and that it was actually a CVD synthetic diamond.

The round brilliant submitted (5.18–5.20 × 3.11 mm) had H-equivalent color grade, much lower than the D color of the diamond submitted in 2014 (5.07–5.09 × 3.15 mm). Its IF-equivalent clarity was better than the VVS_1 clarity of the original stone, however. Only pinpoints and blemishes observable with greater than 10× magnification were found in this specimen. A GIA report number inscribed on the girdle was easily identified as a fake (figure 18). A minor difference in weight was also observed: an "increase" from 0.50335 ct to 0.51444 ct.

Infrared absorption spectroscopy identified the synthetic as type IIa and led to further spectroscopic testing. Photoluminescence (PL) spectroscopy was performed at liquid nitrogen temperature, and spectra

Figure 17. This 0.51 ct CVD synthetic diamond, submitted to GIA for update service, yielded some surprising results.

Figure 18. The GIA report number of a natural diamond graded three years earlier was inscribed on the CVD synthetic diamond shown in figure 17.

Figure 19. These 101 CVD synthetic diamonds were mixed into a parcel of 323 diamond melee, representing 31.3% of the stones.

were collected with various excitation wavelengths. A very strong SiV^- doublet observed at 736.6 and 736.9 nm indicated a synthetic diamond. Under the short-wave UV radiation of the DiamondView, the sample showed green fluorescence but, interestingly, none of the obvious layered growth structures that CVD synthetics usually display. All gemological and spectroscopic features confirmed that the stone was CVD synthetic with post-growth HPHT annealing. This is another example of the importance of using a combination of tests and data to identify a stone. GIA's laboratories continue to develop and implement various measures to identify possible fraud.

Billie Law

Melee Diamond Parcel Containing Nearly One-Third CVD Synthetics

In February 2017, a parcel containing 323 colorless to near-colorless diamond melee was submitted to the Mumbai laboratory for screening and color sorting. The average weight of each round brilliant was 0.015 ct, with an average diameter of 1.5 mm. Of this parcel, GIA's fully automated screening and sorting system confirmed that 219 samples were natural, with the remaining 104 samples referred for further testing. Detailed analysis determined that three of the referred stones were natural, and the remaining 101 stones (31.3%) were CVD synthetics (figure 19).

This result is especially remarkable due to the type of synthetic observed. While the undisclosed mixing of HPHT synthetic diamonds in melee has become a primary concern of the diamond trade, CVD synthetics have been very rare in this size group (Fall 2016 Lab Notes, p. 307). The synthetics were color graded using the GIA melee sorting device for research purposes. The majority of the CVD synthetics were G/H (74.3%) in color, though the D–F (20.8%) and I/J (4.9%) color ranges were also represented.

Further analysis was conducted on these synthetics using FTIR and PL spectroscopy (the latter at liquid nitrogen temperature) and DiamondView imaging. Interestingly, the group included both as-grown (10.9%) and treated synthetics (89.1%), indicating that they may have been produced by different laboratories. The treated diamonds showed evidence of annealing at high temperatures for color improvement, probably under HPHT conditions. FTIR revealed that they were all type IIa, with only two samples (1.9%) showing the CVD-specific NVH^0 absorption peak at 3123 cm^{-1}. Several impurity complexes common in CVD synthetic diamonds were detected by PL spectroscopy, including $NV^{0/-}$ (575 and 637 nm, 100%), the 596/597 nm center (4.0%), SiV^- (736/737 nm, 100%), the 883/884 nm Ni-related center (13.9%; see J.P. Goss et al., "The lattice location of Ni in diamond: A theoretical study," *Journal of Physics: Condensed Matter*, Vol. 16, No. 25, 2004, pp. 4567–4578), SiV^0 (946 nm, 29.7%), and H2 (986 nm, 17.8%). The presence of $SiV^{0/-}$ and the 596/597 nm center were particularly indicative of CVD origin, as $SiV^{0/-}$ centers are routinely found in CVD synthetics yet are comparatively rare in other diamond materials. The 596/597 nm center has been observed only in CVD synthetics.

DiamondView imaging further emphasized the variety of CVD synthetics included in this parcel. The fluorescence of the as-grown CVD synthetics ranged from orange to red to pink, as seen in figure 20 (top left), due to emissions from $NV^{0/-}$ centers. The other samples showed the typical blue–green fluorescence associated with high-temperature annealed CVD synthetics (figure 20, top right). In an unusual finding, layered structures suggesting abrupt changes in growth conditions—which may include stopping and restarting growth—were seen in 35.6% of the CVD synthetic melee. These abrupt changes resulted in alterations to the impurity uptakes of the material, producing the layered structures. Layer thicknesses varied

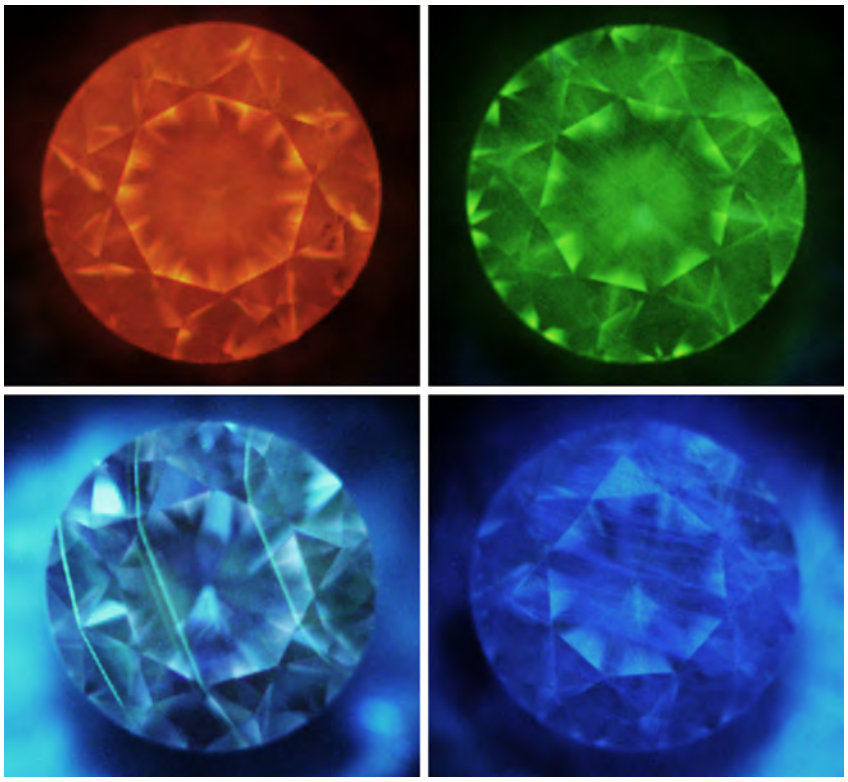

Figure 20. DiamondView images of the 101 CVD synthetic diamonds showed a wide range of patterns and colors, indicative of their different growth and treatment histories. As-grown synthetics showed orange, pink, or red fluorescence (top left), while those treated by high-temperature annealing fluoresced blue or green (top right). Slightly over a third (35.6%) of the synthetics showed layers indicative of changes in growth conditions (bottom left). Those with very high Si content were dominated by blue dislocation bundles (bottom right).

but were generally about 200–500 µm, with samples often showing two or more layers intersecting their table facets (figure 20, bottom left). Such layers are regularly seen in large CVD synthetics (Winter 2015 Lab Notes, pp. 437–439), though they have not been reported for melee-sized goods. Striations and blue dislocation bundles (the latter visible in figure 20, bottom right) were common (45.5% and 19.8%, respectively); certain high-Si synthetic diamonds were dominated by these bundles. Green or blue phosphorescence was observed for 84.2% of the CVD samples.

The substantial undisclosed mixing of CVD synthetic diamonds in this parcel, approaching one-third of the stones, emphasizes the importance of routine testing of melee to identify HPHT and CVD synthetics. GIA's automated melee screening and sorting device was able to successfully separate the natural and CVD synthetic material, providing confidence in the stones' origin and supporting transparency in the industry.

Manisha Bhoir, Priyanka Dhawale, and Ulrika D'Haenens-Johansson

CVD Synthetic Diamond Overgrowth on a Natural Diamond

Nitrogen is the most abundant defect in natural diamonds. It can be observed as single substitutional atoms or in aggregate forms. Boron, on the other hand, is a rare impurity in natural diamonds. It is very unusual to see both nitrogen and boron defects in a single diamond. GIA's New York laboratory recently encountered this in a 0.33 ct diamond graded Fancy blue (figure 21).

The infrared spectrum revealed something very unusual: a mixed type Ia and IIb diamond (figure 22). It also showed a platelet peak at 1367 cm^{-1} and a hydrogen peak at 3107 cm^{-1}. Mixed type Ia and IIb diamond occurs very rarely in nature; one was previously reported in *Gems & Gemology* (Spring 2009 Lab Notes, pp. 55–57). Nitrogen aggregation in this diamond was much higher, however. DiamondView images showed bluish green fluorescence in the face-up view and blue fluorescence in the face-down view (again, see figure 22). Detailed analysis using the DiamondView revealed a yellowish green fluorescence zone at the top of the crown with a sharp boundary in the crown facets (figure 22). PL spectra collected from the table and at the boundary in the crown facets showed emissions from SiV^- defects at 736.3 and 736.9 nm.

Although SiV^- defects can be observed in a natural diamond, the combination of SiV^- defects, a sharp boundary, yellowish green fluorescence, and phosphorescence sug-

Figure 21. This 0.33 ct Fancy blue diamond was confirmed to be a composite of CVD synthetic type IIb diamond overgrowth on a natural type Ia substrate.

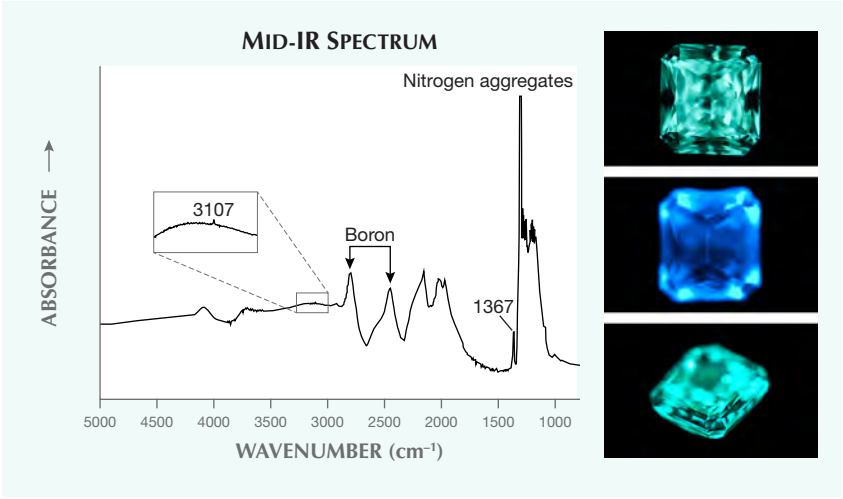

Figure 22. The mid-IR spectrum on the left revealed peaks for nitrogen aggregates and boron defects, along with a platelet peak at 1367 cm^{-1} and hydrogen peak at 3107 cm^{-1}. DiamondView imaging showed bluish green fluorescence in the face-up view (top right) and blue fluorescence in the face-down view (center right). The yellowish green fluorescent top layer was visible in a DiamondView image (bottom right).

gested that the top layer was CVD synthetic diamond. The bottom diamond showed blue fluorescence but no phosphorescence in the DiamondView, consistent with natural type Ia diamond. A distinct boundary line was observed along the interface layer on the crown facets (figure 23). The presence of the overgrowth layer was also clearly revealed through inspection with a variable pressure electron microscope set up to detect both secondary electron and panchromatic cathodoluminescence (CL) emission from the sample, providing topographical and compositional information (again, see figure 23). A distinct interface was visible through the pavilion in reflected light using a fiber-optic light source. A cloud-like inclusion, trapped at the interface layer, was also observed, as well as a dark needle located at or near the interface (figure 23). A small stress halo and a natural surface could be observed in the bottom diamond. The strain pattern throughout the pavilion was consistent with natural type Ia diamond.

The quality of a CVD synthetic depends on the crystallographic orientation and temperature of the seed crystal or substrate during growth. CVD synthetic diamond films have been grown on natural diamond substrates since the early 1960s (W.G. Eversole, U.S. patents 3030187 and 3030188, 1962). Methane and other carbon-containing gases were used, but graphite was deposited along with the CVD synthetic layers. In 1993, CVD synthetic layers were successfully grown on natural type IIa and Ia diamond substrates (see B.G. Yacobi et al., "Preferential incorporation of defects in monocrystalline diamond films," *Diamond and Related Materials*, Vol. 2, No. 2–4, 1993, pp. 92–99). They applied a mixture of CH_4 and H_2 at 80 torr in a microwave plasma-assisted CVD system. Reaction between CH_4 and H_2 produced H atoms, which maintained an sp3-bonded surface and prevented graphitization. The temperature applied to the natural diamond substrate during the CVD growth process of the sample we studied was relatively low, as suggested by the absence of single substitutional nitrogen atoms (N_s^0). It is also in agreement with Yacobi (1993), who applied temperatures of 880°C for CVD growth on type Ia {100} diamond substrates and 1200°C for type Ia {111} diamond substrates. Deposition of a boron-doped CVD synthetic film of <10 microns on a natural gem-quality diamond was reported in 2005 (Summer 2014 Lab Notes, p. 152); however, spectro-

Figure 23. Left: A distinct boundary line indicating an interface (marked with arrows) was seen under the microscope. A dark needle inclusion is located at or near the interface (near the center of the image). Field of view 1.95 mm. Center: An electron microscope image combining secondary electron and cathodoluminescence emissions reveals the presence of an overgrowth layer. Right: The CVD synthetic layer is approximately 80 microns thick.

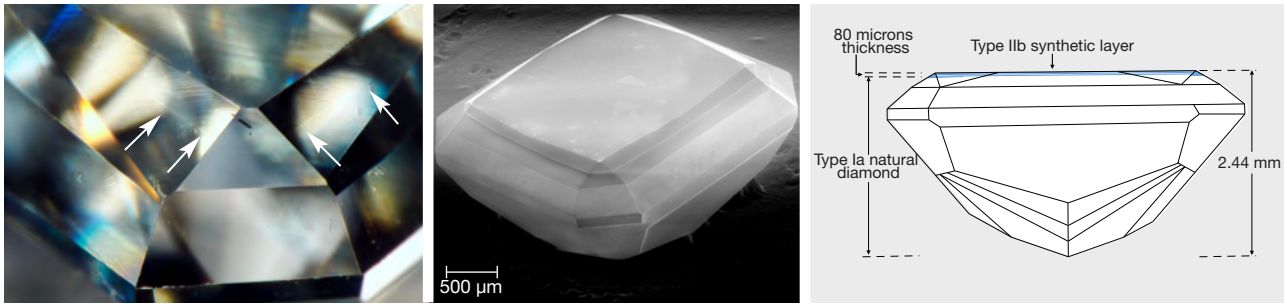

scopic analysis did not show boron and SiV^- defects.

Based on the growth pattern of the natural diamond, it is clear that the type IIb CVD diamond was produced in or very close to {100} orientation. The natural diamond substrate showed no observable inclusions except for a very small stress halo. The thickness of the CVD overgrowth layer was approximately 80 microns (again, see figure 23). FTIR spectroscopy is a bulk analysis, making it very hard to measure and separate IR spectra between a thin CVD layer on top and a thick diamond substrate. However, the fluorescence and phosphorescence reactions suggest that the top synthetic layer contained boron (e.g., boron-doped CVD synthetic) and the bottom diamond contained nitrogen aggregates. The thin layer of type IIb CVD synthetic diamond on the top of this stone effectively introduced Fancy blue color when viewed from its table.

This synthetic overgrowth on a natural diamond with a Fancy color grade is the first GIA has seen. Identification of colored diamonds should be performed very carefully by looking for unusual characteristics, such as a straight boundary line associated with an interface plane, and fluorescence zones with sharp edges in DiamondView images. Examination of this fancy-color composite diamond indicated that similar challenges could exist for colorless and near-colorless diamonds.

Kyaw Soe Moe, Paul Johnson, Ulrika D'Haenens-Johansson, and Wuyi Wang

Figure 24. Among the 70 melee diamonds mounted in this ring, one was confirmed to be an HPHT synthetic diamond.

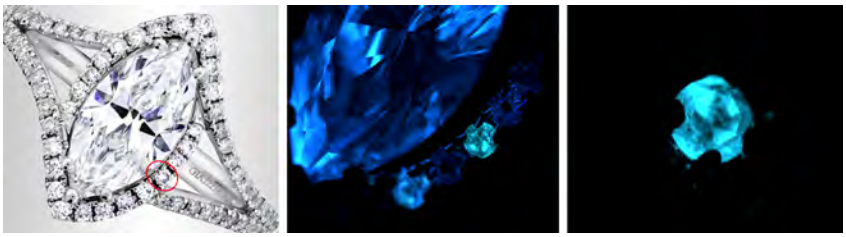

Figure 25. Set near the center marquise diamond, one melee diamond (left, in red circle) showed the blue fluorescence (center) and phosphorescence (right) characteristic of HPHT synthetic diamond.

HPHT SYNTHETIC DIAMOND
Melee Found in Mounted Jewelry

Separation of treated and synthetic diamond melee from natural diamond is challenging work. Diamond melee, which weigh less than 0.2 ct, are often submitted to gemological laboratories in parcels containing hundreds (or more) loose stones. GIA's automatic screening device, introduced in 2016, can separate synthetic and treated diamond melee from natural diamond melee. Identification becomes more challenging when the melee are mounted, due to their small size and the difficulty of accessing them.

In late February 2017, GIA's Hong Kong laboratory received a ring containing 70 melee in addition to a marquise-cut diamond center stone (figure 24). Using a prototype of GIA's new screening device for mounted gems, 69 of the melee passed the test for natural diamond, and one was referred as possible treated or synthetic diamond. The stone in question, which was set next to the center marquise diamond (figure 25, left), had no apparent inclusions. Infrared absorption spectroscopy identified it as a type IIb diamond with an absorption band at 2800 cm^{-1}, indicating the presence of boron as a defect, forming a local vibration mode. Using PL spectroscopy, a very strong doublet peak at 882/884 nm related to nickel impurity was recorded under laser excitation and low temperature. The NV^- center was more prominent than the NV^0 center. Strong blue phosphorescence was also detected (figure 25). These observations confirmed that this was an HPHT synthetic diamond, very similar to melee we have previously tested that were manufactured in China.

How to screen jewelry items with mounted diamonds for quality control is a concern in the industry. GIA's robust instrument for rapid and accurate screening of small diamonds set in mountings will be available in late 2017.

Terry Poon and Wuyi Wang

PHOTO CREDITS
Evan Smith—1; Jian Xin (Jae) Liao—2 and 3; Sood Oil (Judy) Chia—4, 6, 13, and 21; Daniel Girma—5; Tino Hammid—7 (top left); Joyce WingYan Ho—7, 8, and 9 (bottom); Nuttapol Kitdee—9 (top); Promlikit Kessrapong—10; Kwanreun Lawanwong—10; Emiko Yazawa—15; Sudarat Saeseaw—16; Johnny Leung—17, 24, and 25 (left); Tony Leung—17; Billie Law—18; Roxane Bhot—19; Priyanka Dhawale—20; Jemini Naik—20; Kyaw Soe Moe—22 and 23 (left); Ulrika D'Haenens-Johansson—23 (center); Terry Poon—25 (center and right).

Mysterious Iridescence in Aquamarine

Iridescence is a common interference phenomenon seen in many minerals and gems. It occurs when light travels through a stone and interacts with a thin film that has a different refractive index (RI) than the host material, producing a rainbow effect. Iridescence caused by a layered structure occurs on or near the surface of many gems, including iris agate, "rainbow moonstone," and the fossilized ammonite gem known as Ammolite. Iridescence can also indicate the presence of a fracture or cleavage (see Fall 2016 Micro-World, pp. 312–313).

An appealing 40.27 ct aquamarine crystal on calcite matrix owned by Lucas Fassari (Costa Mesa, California) featured eye-visible, cloud-like stringer inclusions that extended from the base of the crystal parallel to the c-axis (figure 1). Inexplicably, examining the stone down through the c-axis with oblique fiber-optic illumination revealed a concealed iridescent, slightly three-dimensional "shimmer" that shifted colors as the light source moved (figure 2; see video at http://www.gia.edu/gems-gemology/iridescence-aquamarine). What was puzzling was that in the iridescent regions there seemed to be no evidence of a break, thin film, liquid inclusion, or other discernible feature that would cause these interference colors. We hypothesize that the cloud-like stringers could be creating dislocations, producing a structure capable of generating interference colors in the localized region just above the stringers.

Figure 1. This 40.27 ct aquamarine contains eye-visible parallel stringers that could be responsible for interference colors seen when the crystal is viewed along the c-axis with a fiber-optic light. Photo by Kevin Schumacher.

About the banner: Partially healed cleavage cracks in a topaz show thin-film interference colors with fiber-optic illumination. Photomicrograph by Nathan Renfro; field of view 2.69 mm.

Editors' note: Interested contributors should contact Nathan Renfro at nrenfro@gia.edu and Jennifer-Lynn Archuleta at jennifer.archuleta@gia.edu for submission information.

Gems & Gemology, Vol. 53, No. 2, pp. 240–246.

Figure 2. The surface of the aquamarine crystal contains a hidden iridescence that is only visible when the light source is at certain angles relative to the surface of the stone. The angle of the oblique fiber-optic illumination in the photo on the left does not make the iridescence visible. As this light is swept across the surface, changing the angle of illumination, colorful iridescent colors appear (center). The appearance of the phenomenon alters along with the angle of illumination (right). The large dark area in the right portion of each image is a reflective void. Photomicrographs by Nathan Renfro; field of view 4.8 mm.

This aquamarine crystal is one of the most interesting the authors have encountered because of its unusual and unexplained iridescence.

Nicole Ahline and Maryam Mastery Salimi
GIA, Carlsbad

Chlorapatite in Quartz

We recently examined a 57.56 ct rock crystal quartz (figure 3) that came from Luciana Barbosa (Gemological Center, Asheville, North Carolina). Said to be from Bahia, Brazil, the transparent and colorless rectangular step-cut gem measured 31.91 × 19.01 × 11.83 mm and hosted two relatively large translucent euhedral crystals. When examined under magnification, these inclusions appeared to be hexagonal prisms, the larger one measuring approximately 7.0 mm in length. Rotation of the microscope's analyzer clearly displayed the crystals' dichroism, which changed from blue to pale yellow (figure 4). Laser Raman microspectrometry was used to identify the inclusions as chlorapatite. This is

Figure 3. This 57.56 ct rock crystal quartz hosts two large euhedral chlorapatite crystals. Photo by Kevin Schumacher.

Figure 4. The blue and pale yellow dichroic colors of a chlorapatite inclusion in quartz are clearly seen in these microscopic views. Photomicrographs by Nathan Renfro; field of view 14.16 mm.

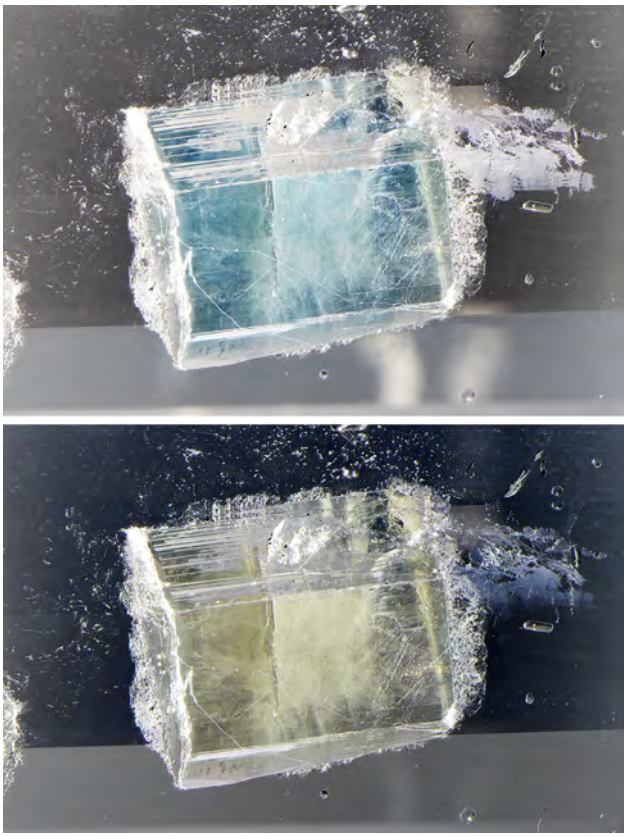

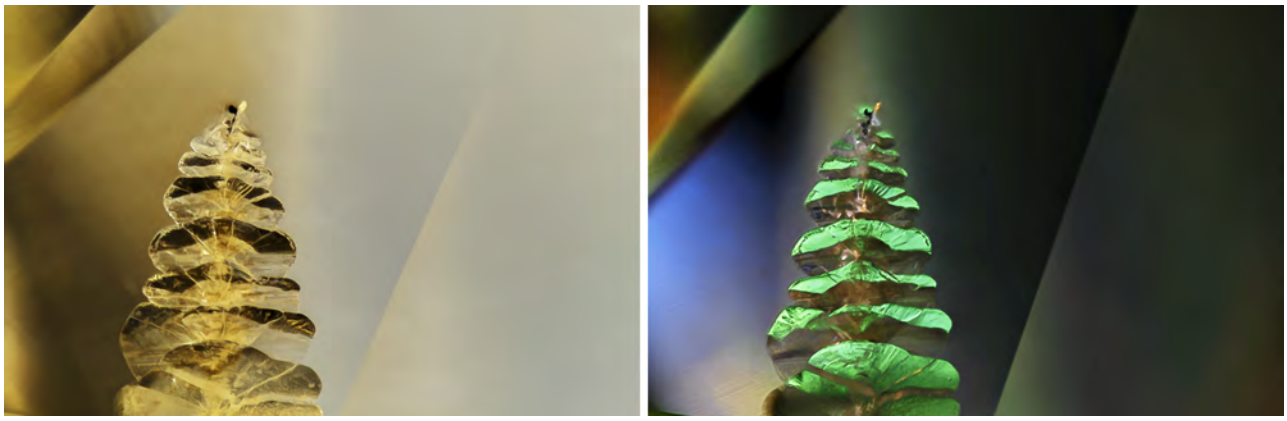

Figure 5. Left: A 3.32 ct fancy-color diamond hosts a laser manufacturing remnant of unusual shape; here, it is seen with diffused fiber-optic illumination. Right: Rheinberg illumination accentuates the LMR's resemblance to an evergreen tree. Photomicrographs by Jonathan Muyal; field of view 2.90 mm.

the first time that we have encountered chlorapatite as an inclusion in quartz.

John I. Koivula
GIA, Carlsbad

Christmas Tree–Shaped Internal Feature In Diamond

A 3.32 ct Fancy yellow marquise diamond recently submitted to GIA's Carlsbad laboratory for color origin determination was of particular interest for its large, eye-visible laser manufacturing remnant (LMR). This LMR extended along a relatively straight path from a star facet through the pavilion and featured lily pad stress fractures stacked in parallel along its length, a composition reminiscent of a Christmas tree preserved within the diamond. With its resulting "green foliage" against a dark blue night, the use of Rheinberg color contrast illumination technique (N. Renfro, "Digital photomicrography for gemologists," Summer 2015 *G&G*, pp. 144–159; Fall 2015 Micro-World, pp. 328–329) dramatically accentuated this already evocative scene (figure 5).

Unlike the remnants of laser drilling used to remove small inclusions, LMRs are an unintended consequence of either carelessness or unpredictable laser optics. As such, they are graded as clarity characteristics that can reduce the overall quality and value of a diamond. LMRs can occur during the laser cutting of a diamond. They appear in a variety of shapes but often resemble the remnants of internal laser drilling (Fall 2013 Lab Notes, p. 174).

Ironically, an accidental feature that might otherwise downgrade a diamond's value can have a positive outcome. This unique and aesthetically pleasing internal feature has created an interesting collector's gemstone, a perfect gift for the Christmas season!

Jonathan Muyal and Troy Ardon
GIA, Carlsbad

Cosalite in Quartz

A search of the gemological literature shows that rock crystal quartz contains a wide variety of unusual and interesting inclusions. Many of those inclusions look alike, so careful analysis is necessary for a positive identification. We recently examined a 16.20 ct cushion-shaped rectangular modified step-cut rock crystal from Kara-Oba, Betpaqdala Plateau, Kazakhstan (figure 6), that was fashioned by Michael E. Gray (Coast-to-Coast Rare Stones, Mendocino, California). Measuring 18.15 × 13.24 × 10.60 mm, it hosted several opaque silvery gray stalks and needles that appeared to have an orthorhombic morphology (figure 7). A fragment cut from the original rough crystal was analyzed by laser Raman microspectrometry and yielded a possible identification as cosalite, a rare orthorhombic lead bismuth sulfide. This was subsequently confirmed by X-ray powder

Figure 6. This 16.20 ct quartz contains an abundance of inclusions. Photo by Kevin Schumacher.

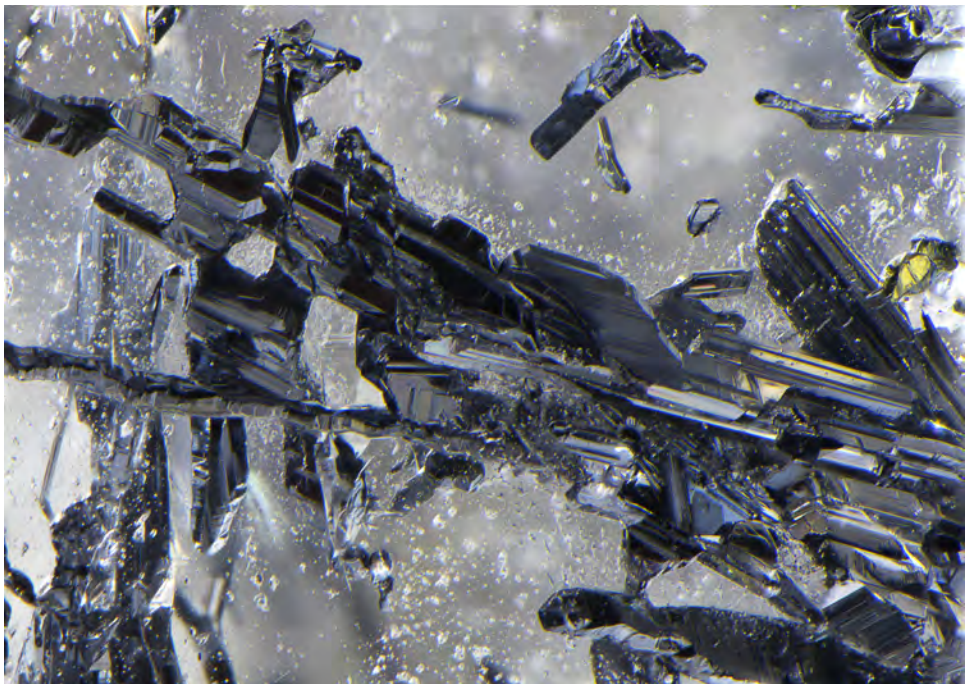

Figure 7. Displaying an orthorhombic morphology, these inclusions were identified as cosalite. Photomicrograph by Nathan Renfro; field of view 4.11 mm.

diffraction. The discovery of such a rare mineral as an inclusion in this stone was a pleasant surprise.

John I. Koivula

Kyanite: A Rare Blue Guest in Diamond

Few landscapes in the micro-world of minerals are as exciting as those encountered within diamonds, which can tell us much about the world from which this most precious of gems originates: the otherwise inaccessible deep earth (J.I. Koivula and E.A. Skalwold, "The microworld of diamonds: Images from the earth's mantle," *Rocks & Minerals*, Vol. 89, No. 1, 2014, pp. 46–51). Of the minerals found as inclusions in diamonds, a few are very deeply colored, due to their strong saturation at any dimension (e.g., red chromium-containing pyrope or a vivid green diopside) or their relatively large size (e.g., olivine crystals that are less saturated with diminishing size, ultimately becoming colorless). While ruby is considered one of the rarest inclusions encountered in diamond, inclusions that are vivid blue hold a similar rank. When discovered in routine examination of a diamond gemstone, they elicit not just breathless appreciation for their exquisite hue, but also anticipation of what they might turn out to be.

So it was with great interest that we examined an intensely saturated rounded blue inclusion within a 2.23 ct diamond (figure 8), a rarity greatly exceeding that of a flawless diamond gemstone. In this case, Raman analysis was used to non-destructively identify the crystal as kyanite, a mineral that occurs only in diamonds of eclogitic origin. This crystal is remarkable for its size (about 0.60 mm long), which in part accounts for its deep color; smaller crystals range from pale blue to colorless. Such colored mineral inclusions in diamonds should not be regarded as imperfections, but rather as hallmarks of beauty and as windows into our planet's deepest secrets. At the very least, they are a compelling invitation from the micro-world to embark on a fascinating scientific adventure.

Elise A. Skalwold
Ithaca, New York

Nathan Renfro and John I. Koivula
GIA, Carlsbad

Figure 8. A deep blue kyanite crystal inside a 2.23 ct diamond identifies its host as being of eclogitic origin. Photomicrograph by Nathan Renfro; field of view 2.18 mm.

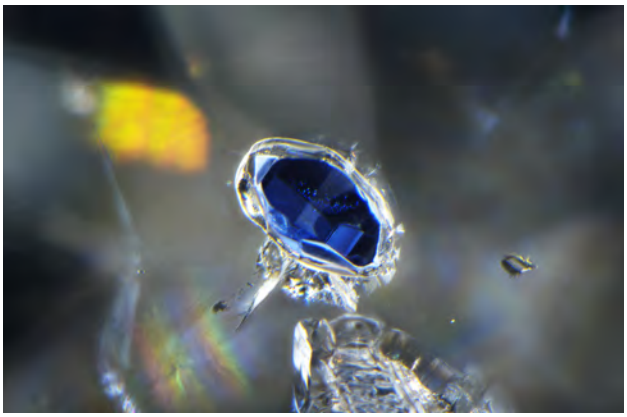

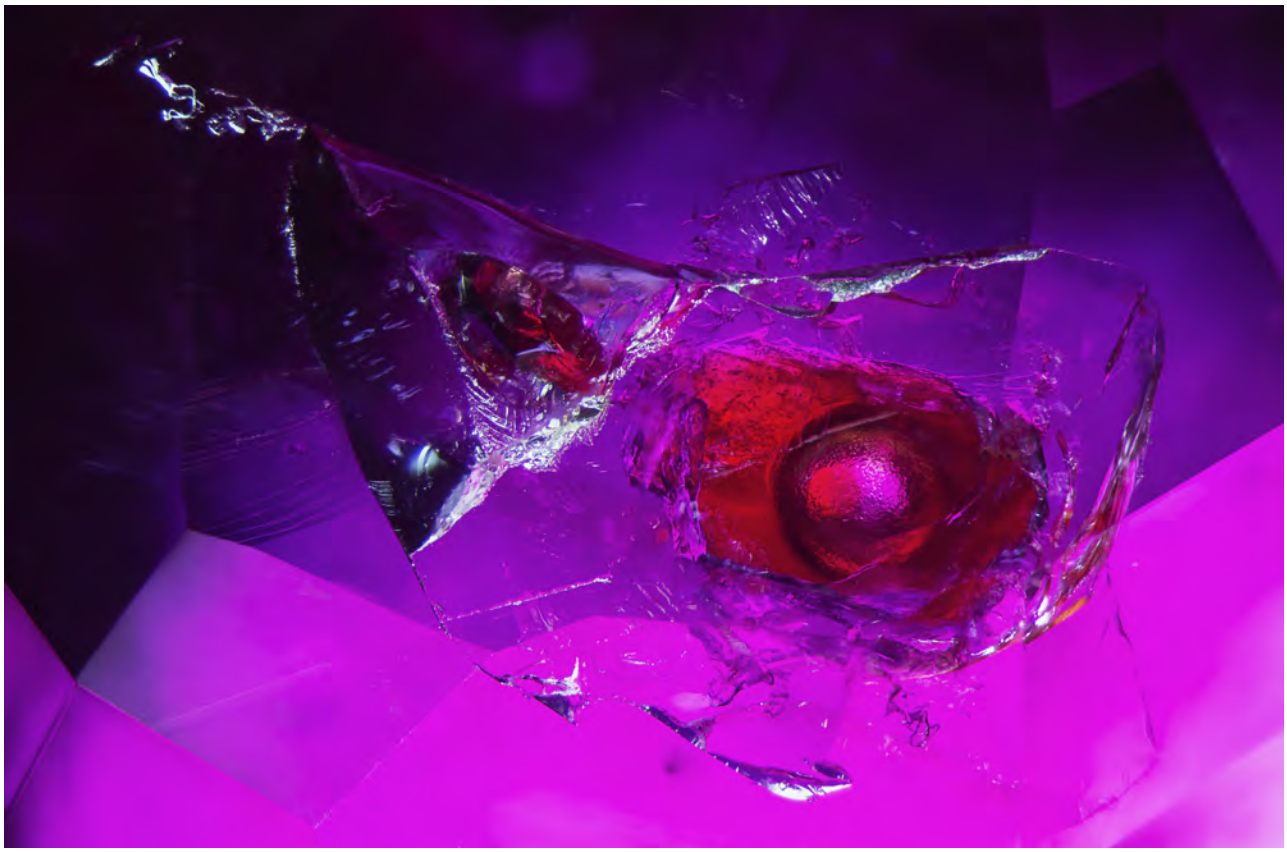

Figure 9. The red color of the oil within the cavity of a ruby displays a remarkable contrast with the bodycolor of the gem. Unlike the flattened bubbles regularly encountered, a rounded bubble attests to the size of the cavity containing the oil. Photomicrograph by E. Billie Hughes; field of view approximately 2.5 mm.

Oiled Ruby: A Remarkable Visual

As laboratory gemologists working in Bangkok, we often encounter gems that have been treated with oil to minimize the appearance of fissures. Most of these stones come from Myanmar, where many vendors consider oiling an accepted standard procedure to enhance their goods, particularly ruby and spinel (http://www.lotusgemology.com/index.php/library/articles/315-lotus-gemology-lab-alert-for-oiled-gems). Furthermore, red oil is commonly used not only to improve clarity, but also to enhance the color of the stone (in Chanthaburi, Thailand, it is sold under the brand name "King Ruby Red Oil"). Often this treatment can be identified by flattened gas bubbles in the fissures or by droplets of oil seeping out of the fissures on the surface when the stone is gently warmed by microscope light or hot point.

Figure 9 shows a small surface-reaching cavity filled with oil in an unheated 1.75 ct ruby from Myanmar. Unlike other examples we have seen, this remarkable gem contained enough of the filler to easily photograph the striking red color of the oil itself within the cavity. With oblique fiber-optic lighting, a stunning image of this enhancement *in situ* was made possible, turning even an otherwise commonplace forensic determination into an aesthetic exploration of the micro-world.

E. Billie Hughes
Lotus Gemology Laboratory
Bangkok

Sapphires With Unusual Radial "Eye" Structure

The Luc Yen district in northern Vietnam produces some remarkable stone varieties, including ruby and red and cobalt-blue spinel. Recently, Geir Atle Gussiås of BalderGems in Luc Yen procured some interesting sapphires from local gem traders. These stones exhibited a radial pattern often accompanied by concentric color zoning. This pattern is commonly seen in minerals that precipitate from fluids such as carbonates and cryptocrystalline silica varieties, but to our knowledge it has never been observed in

Figure 10. This 6.38 ct sapphire from Luc Yen, Vietnam, shows a unique radiating aggregate habit. Photo by Robison McMurtry, courtesy of Lucas Fassari.

corundum. All of Gussiås's samples were opaque and cut as cabochons to display this strange growth pattern. Due to their distinctive appearance, these gems have been called "eye sapphires" in the trade (see figure 10).

The patterns exhibited different forms and sizes but were always a combination of blue and white, with a lower polish quality in the white areas. Raman spectroscopy confirmed that both the white and blue areas were corundum, but the presence of diaspore was detected only in the whiter areas. Some areas also showed a mottled texture and small unidentified black inclusions (figure 11). Laser ablation–inductively coupled plasma–mass spectrometry (LA-ICP-MS) analysis of the sapphire in figure 10 revealed a low iron content, which excludes a basalt-related origin. Epigenetic yellow goethite was found in several fractures on the top of the cabochon. The presence of this mineral was evidence that the stone had not been heat treated (figure 12): Goethite, an iron hydroxide mineral, alters to rust-colored hematite at relatively low temperatures (J.I. Koivula, "Useful visual clue indicating corundum heat treatment," Fall 2013 *G&G*, pp. 160–161). Corundum heat treatments have been performed for centuries and are widely accepted in the trade, but this stone needed no extra enhancement beyond cutting and polishing to reveal its anomalous beauty.

While the cause of this unusual radial aggregate structure remains unknown, it is certainly a welcome novelty in the collector gem market.

Wim Vertriest and Victoria Raynaud
GIA, Bangkok

Hollie McBride
GIA, Carlsbad

Quarterly Crystal: Molybdenite Phantoms in Quartz

Quartz is the most abundant mineral found in the earth's crust. When it forms as solid single crystals, it can serve as a transparent and durable host for a wide variety of mineral inclusions. The two crystals seen in figure 13

Figure 11. This area of the sapphire has a mottled blue and white appearance and hosts unidentified black inclusions. Photomicrograph by Victoria Raynaud; field of view 4.80 mm.

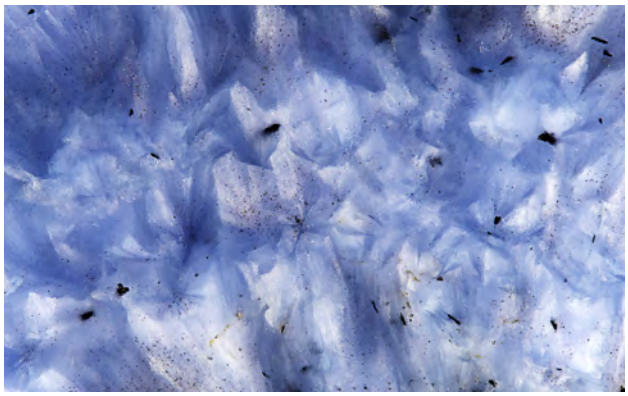

Figure 12. This fracture with epigenetic yellow goethite staining indicates that the sapphire has not been subjected to heat treatment. Photomicrograph by Hollie McBride; field of view 4.79 mm.

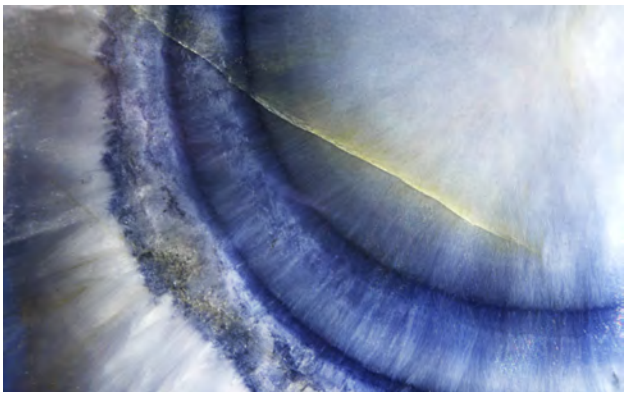

Figure 13. Weighing 378.73 (left) and 294.05 ct (right), these two quartz crystals contain phantoms composed of an abundance of dark silvery gray to black hexagonal inclusions. Photo by Kevin Schumacher.

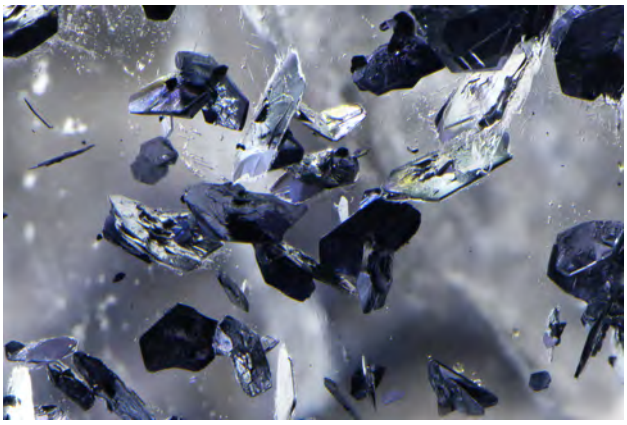

Figure 14. The hexagonal crystals in this phantom plane in quartz were identified through Raman analysis as molybdenite. Photomicrograph by Nathan Renfro; field of view 7.19 mm.

came from collector Terry Szenics (Massapequa, New York), who found them in 2004 as part of a very small discovery at the Confianza mine in the Coquimbo region of Chile.

At a glance, the inclusions in the two crystals looked as though they might be hematite, a common iron oxide. However, laser Raman microspectrometry identified them as molybdenite (figure 14), a hexagonal molybdenum sulfide and a much more unusual inclusion than hematite. The inclusions were situated in the quartz crystals in the form of phantoms that developed through the deposition of the molybdenite on the surface of the quartz. The host then continued to grow, enveloping the molybdenite as inclusion planes tracing the form of the original quartz host.

John I. Koivula

For More on Micro-World

To watch the iridescent "shimmer" of the aquamarine featured in this section, visit https://www.gia.edu/gems-gemology/iridescence-aquamarine, or scan the QR code to the right.

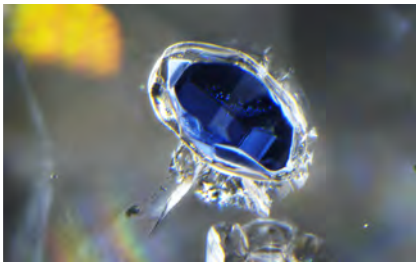

G&G
Gem News International

Contributing Editors
Emmanuel Fritsch, *University of Nantes, CNRS, Team 6502, Institut des Matériaux Jean Rouxel (IMN), Nantes, France* (fritsch@cnrs-imn.fr)
Gagan Choudhary, *Gem Testing Laboratory, Jaipur, India* (gagan@gjepcindia.com)
Christopher M. Breeding, *GIA, Carlsbad* (christopher.breeding@gia.edu)

COLORED STONES AND ORGANIC MATERIALS

Sapphires from northern Ethiopia. Since February 2017, rumors of a newly discovered sapphire deposit in northern Ethiopia have been circulating in the trade. In June, one of the authors (SB-L) visited the mining area, located in the country's Tigray region. The city of Aksum (or Axum), about 35 km south of the Eritrean border, is used as a base for gem merchants. Mining and trading is concentrated around the town of Chila, about 25 km northwest of Aksum. Based on the literature, the alkali basalt field that produces the sapphire stretches into Eritrea, although no sapphires from that area have reached the market. Several sites are active, and about 5,000 miners were working the deposits. All of the deposits are secondary in nature and have yielded rounded crystals. The majority of the rough (figure 1) weighs 2–3 grams, but crystals over 50 g have been reported; the larger ones are usually cracked. Heat treatment experiments are being conducted in Chanthaburi (Thailand) and Beruwala (Sri Lanka) to see how the material reacts. It is estimated that 5–10% of the sapphires do not require heat treatment.

At the end of April, the first parcels started to arrive in Bangkok, and GIA was able to study selected samples donated by author SB-L. The color of the crystals ranged from dark to light blue, and many contained fine rutile particles. Some stones had a trapiche-like pattern. The stones occasionally exhibited a green or yellow color, sometimes combined with blue in bicolor sapphires. All of the sapphires studied by GIA showed strong blue-green pleochroism. The main inclusions were intersecting twinning planes (figure 2), along with crystals, fingerprints, tubules, and bands of rutile particles (figure 3).

Editors' note: Interested contributors should send information and illustrations to Stuart Overlin at soverlin@gia.edu or GIA, The Robert Mouawad Campus, 5345 Armada Drive, Carlsbad, CA 92008.

Gems & Gemology, Vol. 53, No. 2, pp. 247–260.

Trace-element analysis using laser ablation–inductively coupled plasma–mass spectrometry (LA-ICP-MS) was performed on two samples. On each stone we measured 12 spots: six in a clean area and six in a particle-rich area. The clean areas from both stones showed very similar chemical composition, and the same was observed for the particle-rich areas. The compositional ranges of both stones, presented in table 1, clearly show that the chemical concentrations are different between the clean and particle-rich areas. None of the areas contained enough natural Be or Cr to detect with LA-ICP-MS. All samples showed a high Fe concentration. While Ti content was higher than Mg concentration in both areas, the particle-rich areas showed elevated levels of titanium (table 1). The UV-Vis-NIR spectrum shows a broad band around 860 nm, which is typical of basalt-related sapphires (figure 4).

Figure 1. Rough sapphires from a new deposit near Chila, Ethiopia. Photo by Simon Bruce-Lockhart.

TABLE 1. Chemical composition (ppma) of Ethiopian sapphire, obtained by LA-ICP-MS[a].

	^{24}Mg	^{47}Ti	^{51}V	^{57}Fe	^{69}Ga
Clean area	8–9	10–12	0.7–1.0	1362–1450	58–66
Particle-rich area	11–14	15–43	0.6–0.8	1365–1588	57–64

[a] *In total, 12 spots in clean areas and 12 in particle-rich areas were analyzed. Be and Cr were both below detection limit (0.2 and 0.4 ppma, respectively).*

Starting in May, many Sri Lankan dealers have traveled to Ethiopia to buy this material, causing steep price increases in local gem markets. All of the mining around Chila is artisanal, but large volumes of sapphire have been mined in a short time span. Time, and the results of the heat treatments, will show the viability of this deposit.

Wim Vertriest, Vararut Weeramonkhonlert, and Victoria Raynaud
GIA, Bangkok

Simon Bruce-Lockhart
Chanthaburi, Thailand

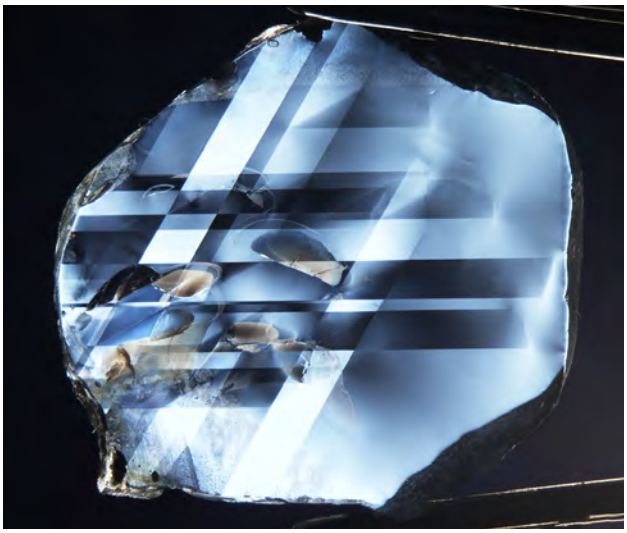

Figure 2. An Ethiopian sapphire wafer with two polished windows perpendicular to the c-axis under crossed polarizers shows two sets of twinning planes. Photo by Victoria Raynaud; field of view 13.4 mm.

New deposits of gem-quality common opal from Michoacán, Mexico. The principal gemological characteristic of precious opal is the play-of-color produced by the diffraction of white light from three-dimensionally stacked layers of microscopic spheres of silica. In comparison, so-called common opal does not show play-of-color but may be valued for its attractive bodycolors. Most play-of-color opals are opal-A (e.g., Australian and Brazilian sedimentary opal), which is amorphous in X-ray diffraction (XRD). Less-studied Mexican volcanic opals, both precious and common, are by contrast opal-CT (for "cristobalite-tridymite"). In these specimens, XRD shows diffraction peaks for highly disordered cristobalite with abundant tridymite stacking (M. Ostrooumov et al., "Spectres Raman des opales: aspect diagnostique et aide a la classification," *European Journal of Mineralogy*, Vol. 11, No. 5, 1999, pp. 899–908). Yet there have been few studies of gemological interest on the microstructure of common opals.

Recently, the author discovered new deposits of common gem opal (figure 5) in the hills near Lake Cuitzeo, in Mexico's Michoacán State. These opals were embedded in volcanic andesitic rocks. They were generally characterized by a medium to light orange to brown color, with no visible inclusions. While these new deposits are considered "common opal" since the material does not show play-of color, some gemologists may also consider the specimens to be fire opal due to the orangy bodycolor. The samples were studied at the Institute of Earth Sciences at the University of Michoacán in Morelia.

Standard gemological testing yielded refractive indices between 1.440 and 1.457 and hydrostatic specific gravities (SGs) ranging from 2.11 to 2.14. The material was inert to both long- and short-wave UV radiation. These properties suggested common opal, which we later confirmed with scanning electron microscopy (SEM), transmission electron

Figure 3. Left: An unidentified crystal surrounded by a fingerprint. Many particles and fine wispy fingerprints can be seen throughout the stone in darkfield lighting. Center: Intersection tubules associated with different types of fingerprints, shown here in fiber-optic lighting, were always found in the twinning planes of the Ethiopian sapphires. Right: Bands of particles seen with fiber-optic lighting. Photomicrographs by Victoria Raynaud; fields of view 1.20 mm (left), 3.60 mm (center), and 1.44 mm (right).

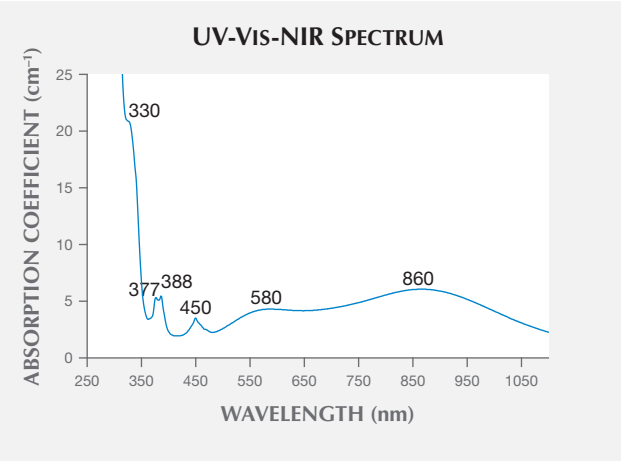

Figure 4. UV-Vis-NIR spectrum of the o-ray of a greenish blue Ethiopian sapphire. Optical path length 1.13 mm.

Figure 6. SEM image of the heterogeneous nanostructure of a common gem opal from the Cuitzeo area in Michoacán. The spheres are too small, irregularly sized, and disorganized to exhibit play-of-color.

microscopy (TEM), atomic force microscopy (AFM), Raman microprobe, and infrared spectroscopy.

Previous research (E. Fritsch et al., "Mexican gem opals: Nano-and micro-structure, origin of colour, comparison with other common opals of gemmological significance," *Australian Gemmologist*, Vol. 21, No. 6, 2002, pp. 230–233) has shown that Mexican opals with play-of-color exhibit a higher degree of organization. In these specimens, nanoparticles measuring about 10–50 nm in diameter form pseudospheres (lepispheres) of appropriate size to diffract visible light (about 200 nm) in a matrix of less acid-soluble silica particles. When examined with a scanning electron microscope, fresh broken surfaces show no particular organization, but after etching with diluted hydrofluoric acid (10% vol. HF), the microscopic arrangement of spheres is revealed. There is a continuum of structures between opals with and without play-of color. In addition to the role of particle size, rounder spheres with a more organized structure display a more noticeable play-of-color with a wider range of colors.

Figure 5. Gem-quality common opal was recently discovered in Michoacán State in western central Mexico. The approximate size of this sample is 15.04 × 7.68 × 5.57 cm. Photo by M. Ostrooumov.

From SEM and AFM images, it is clear that these newly discovered common opals from Michoacán are built from a random aggregation of small, near-spherical grains, averaging 60 to 100 nm in size. (The software we used was ImageJ, an open-source image processing program designed to generate scientific multidimensional images.) The apparent diameter of some grains actually ranges from about 120 to 130 nm (figures 6 and 7). The nanostructure of this common opal explains the absence of play-of-color. In this case, we can consider the following general explanations for the lack of play-of-color:

1. The spheres do not have the same size (heterogeneous structure).
2. The spheres are not perfectly spherical.
3. The spheres are the same size but not well organized.
4. The spheres are too small (<150 nm) or too large (>300 nm) to diffract light.

In some cases two or more of these conditions occur in the same sample.

All Mexican volcanic CT-opals have similar Raman spectra characterized by a very strong general band (apparent maximum toward 325 cm^{-1}) that shows a complex structure with lines of weak to medium intensity (M. Ostrooumov et al., "Spectres Raman des opales: aspect diagnostique et aide a la classification," *European Journal of Mineralogy*, Vol. 11, No. 5, 1999, pp. 899–908). According to theoretical calculations, the normal modes in the 300–350 cm^{-1} range consist mainly of Si-O-Si bending vibrations

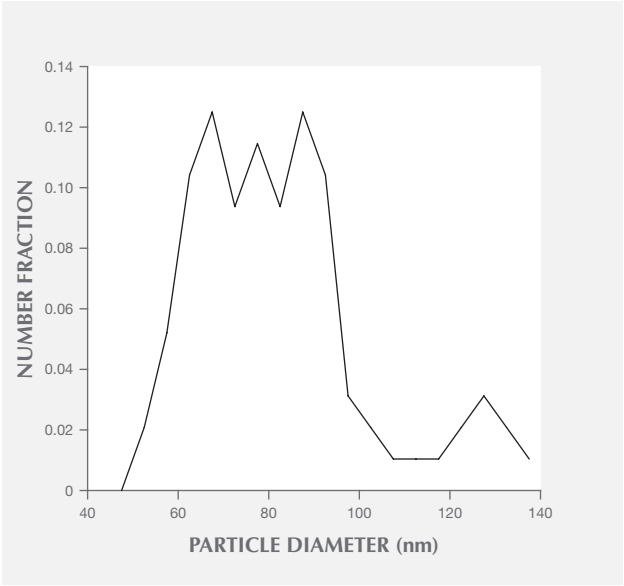

Figure 7. Distribution of particle sphere diameters in the nanostructure of the newly discovered Mexican volcanic opal. Most of the spheres are 60–100 nm, a size too small to diffract light.

of ring atoms. Other principal bands in the Raman spectra of opal from these new deposits are found at about 800 and 960 cm^{-1}, 1069–1086 cm^{-1}, and 1600 and 3200 cm^{-1}. These bands belong to α-tridymite, α-cristobalite, α-quartz, and groups of H_2O and OH.

Infrared absorption bands were observed between 4000 and 400 cm^{-1}, which is typical for all varieties of micro- and non-crystalline opals (C, CT, and A). The three strong bands near 1100, 790, and 480 cm^{-1} are common to all silicates with tetrahedrally coordinated silicon (M. Ostrooumov, "A Raman, infrared and XRD analysis of the instability in volcanic opal from Mexico," *Spectrochimica Acta, Part A*, Vol. 68, No. 4, 2007, pp. 1070–1076). Broadly speaking, in opal-CT only localized Si-O-Si stretching and bending vibrations remain. The distinction between opal-CT and opal-A requires careful inspection of the frequencies of the three strong Si-O bands. In particular, the band at 790 cm^{-1} is always at higher frequency in opal-A than in opal-CT. Broad absorption bands between 3700 and 2700 cm^{-1} are due to fundamental O-H stretching vibrations. For example, a very broad band is present at around 3448–3458 cm^{-1}, with a shoulder at about 3250 cm^{-1} that is generally considered to be related to hydrogen-bonded molecules of water.

Based on TEM results, we have been able to prove that the orange to brown bodycolor of Mexican common opal is due to nano-inclusions of an iron-containing material. It is probably related to hematite, which is often found associated with common opal in nodules. It typically appears as needles measuring 10 to 20 nm wide by 100 to 200 nm long, seen only with TEM.

Mikhail Ostrooumov (ostroum@umich.mx)
University of Michoacán, Institute of Earth Sciences
Morelia, Michoacán, Mexico

Raspberry-red garnet with black core. Raspberry-red grossular garnet mineral specimens have been popular in the collector market since their discovery in 1994 in the Sierra de Cruces range in the State of Coahuila, Mexico. V.W. Lueth and R. Jones ("Red grossular from the Sierra de Cruces, Coahuila, Mexico," *Mineralogical Record*, Vol. 34, No. 6, 2003, p. 73) described the geological environment where the garnet was discovered and the petrological composition of the garnet and matrix (figure 8). An interesting internal characteristic of this type of grossular crystal is its raspberry-red rim and black core with sharp color transition at the core-rim boundary. Lueth and Jones reported that the raspberry-red rim is composed mainly of grossular and the black core contains up to 4.5 wt.% titanium that can be used to calculate additional morimotoite and schorlomite garnet end-member species (table 2). No detailed chemical analysis of the black core was presented, however. To better understand the composition of this type of garnet, we prepared a thin section sliced from the middle of one garnet crystal (see the color-zoned image in

TABLE 2. Cation site occupancies for garnet end members.

End members		Cation site			Anion site
		Dodecahedral	Octahedral	Tetrahedral	
Schorlomite	Schorlomite	Ca_3	Ti_2	Si, Fe^{3+}_2	O_{12}
	Schorlomite-Al	Ca_3	Ti_2	Si, Al_2	O_{12}
Morimotoite	Morimotoite	Ca_3	Ti, Fe^{2+}	Si_3	O_{12}
	Morimotoite-Mg	Ca_3	Ti, Mg	Si_3	O_{12}
	Morimotoite-Fe	Fe^{2+}_3	Ti, Fe^{2+}	Si_3	O_{12}
Grandite	Grossular	Ca_3	Al_2	Si_3	O_{12}
	Andradite	Ca_3	Fe^{3+}_2	Si_3	O_{12}
Kimzeyite	Kimzeyite	Ca_3	Zr_2	$SiAl_2$	O_{12}
	Kimzeyite-Fe	Ca_3	Zr_2	$SiFe^{3+}_2$	O_{12}

Figure 8. A very fine 4.5 × 3.1 × 2.1 cm specimen of raspberry-red grossular from skarn deposits, with crystals approaching 1 cm. The matrix consists of calcite, quartz, wollastonite, and scapolite. Photo by Kevin Schumacher.

the middle of figure 9) for detailed chemical analysis at GIA's Carlsbad laboratory.

The section's chemical composition was obtained with a Thermo Fisher iCAP Q ICP-MS coupled with a New Wave Research UP-213 laser ablation unit. ^{29}Si was used as the internal standard. GSD-1G and GSE-1G were used as external standards. A line of 33 ablation spots was selected to cross the whole section from one outer rim to the opposite outer rim. The black core contained up to 27.91 mol.% morimotoite and up to 4.07 mol.% schorlomite (figure 9). The detailed composition of the black core of spot 7 to spot 15 (the light blue vertical zone in figure 9) is listed in table 3. The black core contained 4.10–5.04 wt.% TiO_2, confirming the analytical results reported by Lueth and Jones, and 4.42–5.49 wt.% FeO_{tot}. It also contained 0.26–0.84 wt.% ZrO_2 that could be used to calculate a distinct kimzeyite garnet end-member species (tables 2 and 3; table 2 gives the composition and site occupancy of the end members). It is the first time a detailed chemical analysis of the black core of this type of raspberry-red garnet has been documented.

Ziyin Sun and Nathan D. Renfro
GIA, Carlsbad

"Sango pearl" from Japan. A type of pink Japanese akoya cultured pearl, introduced about a decade ago and known as "Sango" pearl (figure 10), uses a pink coral nucleus and a *Pinctada fucata* mollusk. It is produced by Matsumoto Pearls, a Japanese pearl farming company based in Uwajima, Ehime Prefecture. *Sango* is the Japanese word for coral, and the species of pink coral used as the nucleus is likely a *Corallium* species, one of the precious corals harvested off the Pacific coast of Japan, especially around southern Kochi Prefecture (N. Iwasaki et al., "Biology of Japanese *Corallium* and *Paracorallium*," *Proceedings of the First International Workshop on Corallium Science, Management, and Trade*, 2009, pp. 68–70). Matsumoto Pearls has successfully combined two beautiful organic gem materials to produce these attractive pink-colored pearls.

The coral nuclei in this study exhibited a pinkish orange color and measured 5.60–5.90 mm in diameter. Under microscopic examination, white layer-like structures and banding as well as polyp-related cavities have sometimes been

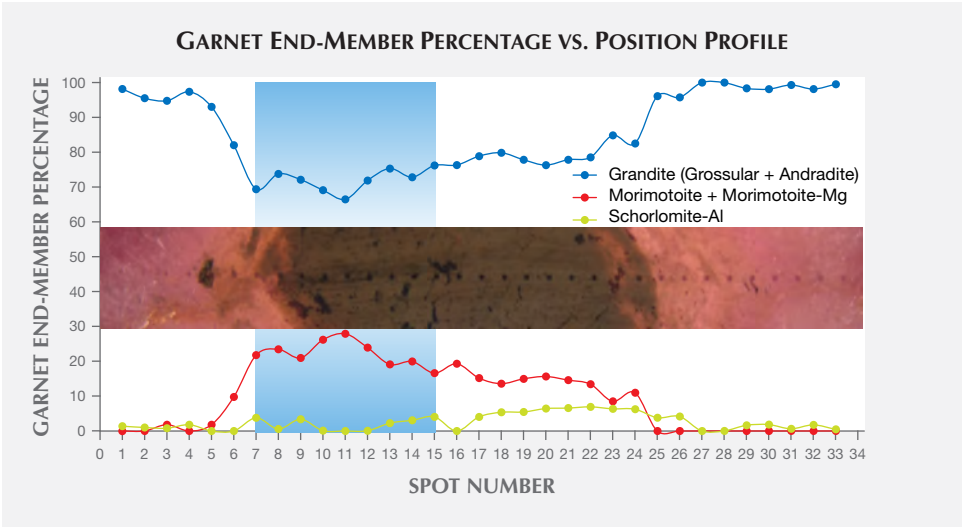

Figure 9. Garnet end-member percentage vs. position profile revealed that the black core of the garnet was rich in morimotoite and schorlomite. The pink rim of the garnet was composed almost entirely of grossular with minor andradite.

TABLE 3. Chemical composition of grandite-morimotoite garnet spots by LA-ICP-MS.

Number of spots	spot 7	spot 8	spot 9	spot 10	spot 11	spot 12	spot 13	spot 14	spot 15
					wt.% oxides				
MgO	1.37	1.13	1.37	1.38	1.32	1.28	1.23	1.23	1.30
Al_2O_3	14.84	14.88	15.48	15.21	15.32	15.30	15.77	15.34	15.85
SiO_2	37.28	38.31	37.86	38.67	38.95	38.71	38.26	37.64	37.69
CaO	34.89	35.99	35.29	34.94	34.20	35.11	35.39	35.23	35.55
TiO_2	5.04	4.28	4.80	4.57	4.80	4.17	4.10	4.51	4.29
V_2O_3	0.02	0.02	0.02	0.02	0.02	0.02	0.02	0.02	0.02
Cr_2O_3	0.02	0.01	0.00	0.00	0.00	0.00	0.00	0.00	0.00
MnO	0.10	0.13	0.14	0.15	0.15	0.16	0.15	0.14	0.15
FeO_{tot}	5.49	4.42	4.62	4.60	4.59	4.81	4.75	5.09	4.66
ZrO_2	0.84	0.73	0.35	0.40	0.57	0.37	0.26	0.71	0.42
Total	99.89	99.90	99.93	99.93	99.92	99.93	99.93	99.91	99.93
					mol.% end members				
Kimzeyite	1.59	1.37	0.66	0.75	0.00	0.70	0.48	1.33	0.79
Schorlomite-Al	3.78	0.59	3.37	0.10	0.00	0.07	2.27	3.08	4.07
Morimotoite	15.21	11.36	12.62	20.55	27.91	18.14	12.15	12.90	7.33
Morimotoite-Mg	6.56	12.08	8.35	5.64	0.00	5.80	6.97	7.05	9.27
Goldmanite	0.05	0.05	0.06	0.06	0.06	0.05	0.05	0.06	0.06
Uvarovite	0.05	0.03	0.00	0.00	0.01	0.00	0.00	0.01	0.00
Spessartine	0.23	0.29	0.31	0.33	0.32	0.34	0.33	0.31	0.33
Pyrope	3.08	0.33	2.48	3.41	3.66	2.98	2.38	2.37	1.89
Almandine	0.00	0.00	0.00	0.00	0.52	0.00	0.00	0.00	0.00
Grossular	59.13	65.13	63.47	64.50	65.28	65.36	66.02	62.75	64.82
Andradite	10.19	8.59	8.57	4.56	0.00	6.44	9.22	10.01	11.33
Remainder[a]	0.06	0.06	0.06	0.05	1.19	0.06	0.07	0.06	0.05
Total	99.93	99.88	99.95	99.95	98.95	99.94	99.94	99.93	99.94

[a]*The "remainder" in the end-member components is what is left over after assigning all the atoms to stoichiometric garnet formula. This value is related to analytical error in the chemical measurements.*

observed. The nuclei also exhibit a weak whitish and stronger whitish fluorescence under short-wave and long-wave UV, respectively. The coral bead's Raman spectrum (figure 11, top) shows strong pigment peaks at 1129 and 1517 cm^{-1} and calcite peaks (e.g., 280 and 713 cm^{-1}), identifying them as *Corallium* species, as in S. Karampelas et al. ("Identification of the endangered pink-to-red *Stylaster* corals by Raman spectroscopy," Spring 2009 *G&G*, pp. 48–52). The full-range photoluminescence spectra closely match that of natural pink coral with natural pigment-related peaks, similar to those in C.P. Smith et al. ("Pink-to-red coral: A guide to determining origin of color," Spring 2007 *G&G*, pp. 4–15). Visible-range reflectance spectra (figure 11, middle) reveal peaks at 468, 482, 590, and 666 nm, like those observed in the spectra of natural coral by C.P. Smith et al. (2007).

Figure 10. Sango pearls (left and center) and a coral bead nucleus (right), each approximately 6 mm in diameter. Photo by Y. Katsurada.

Ten partially drilled Sango pearls examined for this note were of a similar size (5.60–6.00 mm) as the coral beads used as nuclei. No color concentrations were noted down the drill holes or anywhere on their nacreous surfaces using a loupe or microscope. The nacre thickness measured between 120 and 400 microns (0.12–0.40 mm) under the microscope

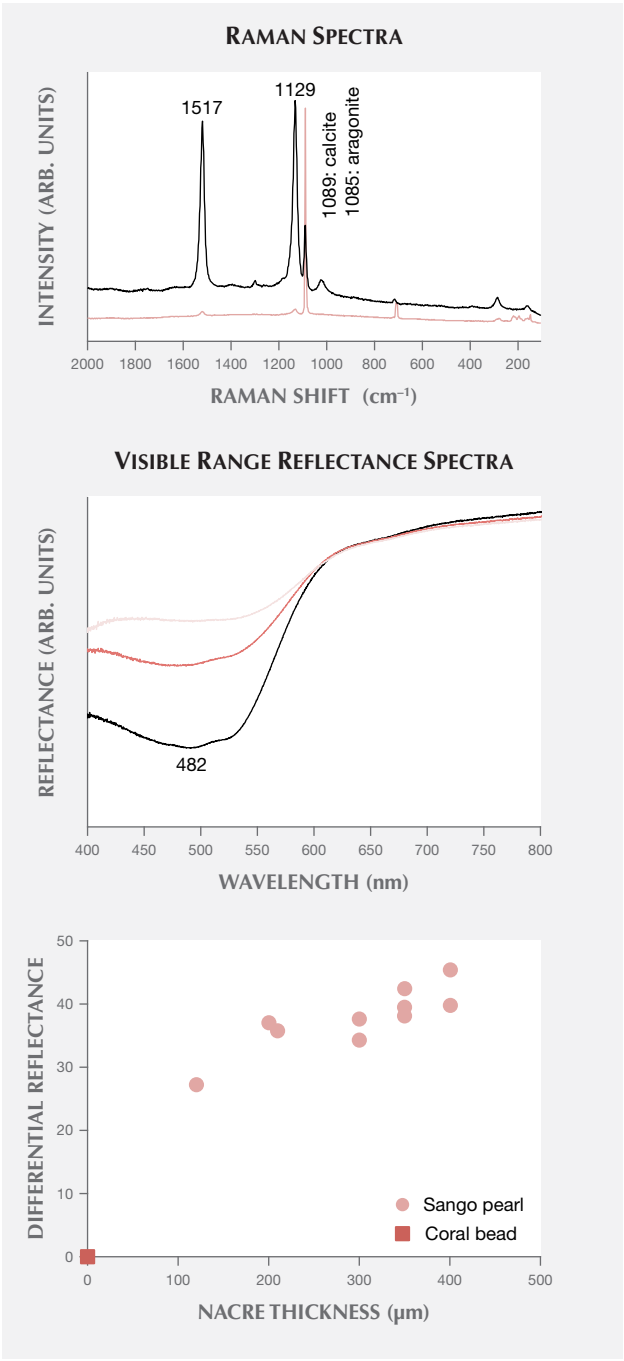

Figure 11. Top: Raman spectra of a coral bead (black trace) and a Sango cultured pearl (pink trace) with pigment-related peaks at 1129 and 1517 cm^{-1}. The bead's peaks are stronger at those wavelengths. Middle: Visible-NIR spectra of a coral bead (black trace) and two Sango cultured pearls showing the different reflectance values obtained. The dark pink trace represents thinner nacre (120 µm thick); the light pink trace is from nacre that is 400 µm thick. Bottom: Plot of the relationship between nacre thickness and the differential reflectance of Sango pearls at 482 nm based on the average reflectance of the coral beads (differential reflectance = $R_{Sango\ pearls} - R_{coral\ beads}$).

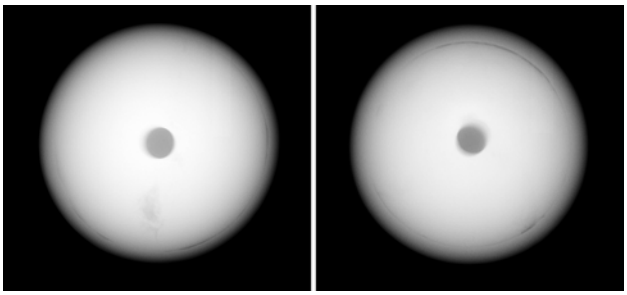

Figure 12. RTX images of Sango cultured pearls showing clear demarcations between the larger coral bead nucleus and thinner nacre overgrowth. The pearl on the left has a thinner nacre than the one on the right.

using a small table gauge. The different nacre thicknesses were also visible in real-time X-ray (RTX) images (figure 12). The pearls exhibited excellent luster, with almost no overtone and very weak orient, and showed a weak yellow to greenish yellow fluorescence under long-wave and short-wave UV radiation, respectively. These observations indicated that the 10 samples' pink coloration was natural, though it remained to be seen whether the pink color originated from the pearls' nacre or the underlying coral beads.

Chemical analysis using an energy-dispersive X-ray fluorescence (EDXRF) spectrometer revealed manganese levels of 0 to 28 ppmw and strontium levels of 1077 to 1719 ppmw, indicating that the pearls formed in a saltwater environment. A useful observation was that pearl color seemed to be related to nacre thicknesses: Thin nacre overgrowth produced a more obvious pink tint, while thicker nacre resulted in a less saturated pink. Likewise, the Raman and visible-range reflectance spectra were also related to the nacre thickness. Raman spectra for pearls with thin nacre showed stronger pigment peaks at approximately 1129 and 1517 cm^{-1}, similar in strength to those noted in the coral beads; only the aragonite-related peaks—and no pigment peaks—were noted in pearls with thicker nacre (see figure 11, top). The visible-range spectra of the pearls possessing thin nacre also matched the coral beads more closely, albeit with a lower reflectance (figure 11, middle), while pearls with thicker nacre had higher reflectance, as would be expected for lighter-colored pearls. By correlating the coral pigments with the maximum visible reflectance spectrum at 482 nm, the point of least reflectance (see figure 11, bottom), the relationship between nacre thickness and the visible spectra of the pearls could be gauged. The intensity at 482 nm indicates that the pink color of Sango pearls most likely originates from their coral nuclei.

While Sango pearls are not the first cultured pearls to use atypical bead nuclei in the form of other gem materials (see K. Scarratt et al., "Atypical 'beading' in the production of cultured pearls from Australian *Pinctada maxima*," *GIA Research News*, 2017, https://www.gia.edu/gia-news-research/atypical-beading-production-cultured-pearls-australian-pinctada-maxima), this is the first time the author has analyzed the detailed color origin of Sango pearls with

Pinctada fucata mollusks as the host. The pearls are known to possess relatively thin nacre overgrowth, which has enabled the creation of the commercial type of akoya cultured pearl using a natural coral nucleus. GIA would classify Sango pearls as atypical bead-cultured pearls.

Kazuko Saruwatari
GIA, Tokyo

Tektite with a large fluid inclusion. Tektites are a form of natural glass related to extraterrestrial impact. When a meteorite hits Earth's surface, the impact site is subjected to tremendous heat and pressure. This causes the rocks to instantly melt and quickly cool, creating a glass with a bulk composition similar to that of the original host rock. Only the most volatile elements will be removed, because their gaseous phases escape easily. This is the case for fluids and gases such as water and carbon dioxide, as well as certain metals. This melting and cooling results in a silica-dominated glass called tektite that is often very dark green to black.

Tektites are common in many parts of the world. The most famous type is probably moldavite, related to an impact in southern Germany. The world's largest tektite area is the Australasian field, which covers Australia (australites), southeast Asia (indochinites), and most of the Indian Ocean. It is related to a single impact 790,000 years ago, although the impact crater has not been identified.

The gem mines in northern Vietnam around Thac Ba Lake, which are famous for ruby and spinel, also yield tektite from secondary deposits. Local dealer Geir Atle Gussiås (BalderGems) procured a large tektite weighing 230.9 g (figure 13) with a very large fluid inclusion. The inclusion contained a mix of gas and liquid, which could be seen under strong illumination (figure 14; see video at http://www.gia.edu/gems-gemology/tektite-inclusion). GIA's Bangkok lab examined this unique piece by comparing it to six tektite samples collected in the mines during several field expeditions to Vietnam.

We examined the specimen and performed density measurements as well as chemical analysis to determine whether it was a real tektite. The surface features and overall shape of the large piece were very similar to the reference samples, although the reference samples were much smaller. The overall color was black, but when strong light was transmitted through the sample, a brown color was observed. The SG of the reference samples ranged from 2.01 to 2.42. This range can be explained by differences in chemical composition, mainly iron concentration, and the amount of gas bubbles in the matrix, which lowers the SG. The SG of the Vietnamese sample was 1.84, indicating an unusual abundance of fluid and/or gaseous inclusions in the sample. Because this tektite was too large to analyze using LA-ICP-MS, its chemical composition, along with those of the reference samples, was revealed with EDXRF. The large tektite had Fe, Sr, Rb, and Zr contents that are comparable to the other Vietnamese tektites.

Figure 13. A large tektite (230.9 g) from Luc Yen, Vietnam, surrounded by six tektite samples from the GIA reference collection. Photo by Wim Vertriest.

We then imaged the internal structure using real-time X-ray microradiography (RTX), a technique commonly used in pearl analysis. Because the device has a small detector, we could not view the whole tektite in one image. The maximum resolution of 4 µm should have been sufficient to pick up any artificial structures such as drill holes. The RTX images show the irregular outline of the tektite's surface and a large bubble with a smooth outline (figure 15). Several smaller negative inclusions are also visible as dark ovals. When the sample was moved under the RTX, the liquid-gas inclusion was clearly seen because of the motion of the liquid.

Since we did not find a drill hole or any signs of man-made glass, we assume that the liquid in the negative inclusion is a natural phenomenon. Since glass is not porous, it seems most likely that the liquid was included during the tektite's formation. Although this could not be proven, this tektite remains a unique specimen.

Wim Vertriest, Vararut Weeramonkhonlert, and Kwanreun Lawanwong
GIA, Bangkok

Figure 14. A close-up view of the tektite sample using very strong backlighting reveals a curved black line, which is the liquid-gas contact. Photo by Wim Vertriest.

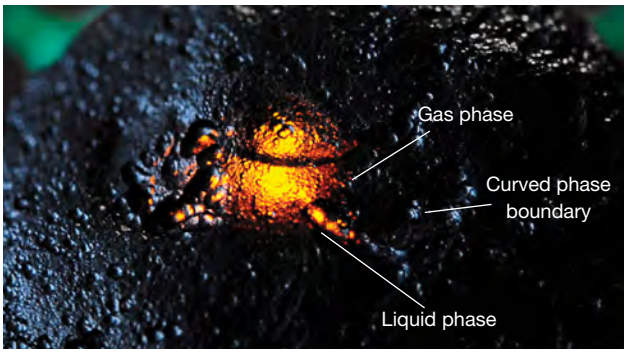

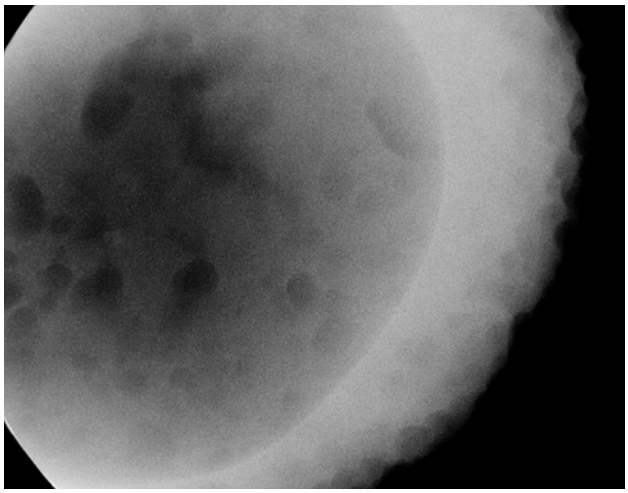

Figure 15. This RTX image shows the tektite's irregular outline on the right side. The very large negative inclusion has a smooth outline. Several other smaller negative pockets can also be seen.

SYNTHETICS AND SIMULANTS

Dyed yellow beaded freshwater cultured pearls imitating South Sea cultured pearls. In the spring of 2017, the Gübelin Gem Lab received a yellow pearl necklace for testing. The size and color of the specimens implied that they were South Sea cultured pearls. The high insurance value appeared to confirm this; however, there were some suspicious color patches that suggested the material had been dyed.

Only a few months earlier, author LK visited the Hong Kong office of Grace Pearls, a large producer with a pearl farm and factory in China, to see their latest batch of freshwater cultured pearls. Grace Pearls developed a proprietary method to grow large freshwater pearls with bead, marketed as "Edison" pearls. These occur in all the known colors of traditional freshwater pearls, typically white, orange, pink, and purple. To complement their color range, they also offer yellow and black treated pearls ranging from approximately 12 to 18 mm.

The goods we saw at Grace Pearls had a wide range of qualities and prices. The lowest price for a strand of Edison pearls was approximately US$100, while the highest-quality yellow dyed pearls go for as much as US$2,000. Prices for top-quality white and pink natural-color pearls may reach up to US$40,000 per strand.

The Gübelin Gem Lab acquired from Grace Pearls a necklace of yellow dyed freshwater bead-cultured pearls to complement our extensive reference collection. The largest of these pearls measured nearly 17 mm. For study purposes, we deliberately chose a low-quality necklace showing color concentrations, slightly irregular colors from pearl to pearl, and slight blemishes on the surface (figure 16).

The grafting process, which Grace Pearls considers a proprietary method, appears to be similar to that of "Kasumigaura pearls" from Japan and "Ming pearls" from China,

Figure 16. Uneven color and blemishes on the surface of a low-quality dyed cultured freshwater pearl necklace obtained from Grace Pearls. Photo by Lore Kiefert.

where the bead is drilled first and a tissue is partly inserted into the drill hole in order to introduce both tissue and bead at the same time during the implantation procedure (H.A. Hänni, "Ming pearls: A new type of cultured pearl from China," *Journal of the Gemmological Association of Hong Kong*, Vol. 32, 2011, pp. 23–24). X-ray images clearly show drill holes in the beads of several of these cultured pearls, mostly in the smaller beads (figure 17), while larger beads, like the one in the center of figure 16, have only one drill hole. This may be due to a possible re-implantation into the pearl sac once the first pearl has been harvested. X-ray fluorescence (XRF) analysis gave Mn and Sr values consistent with those of freshwater pearls.

Upon testing, the necklace submitted by the client showed identical properties: dark yellow color concentrations around drill holes and in cavities, uneven surfaces with various shades of yellow (figure 18, left; see also C.

Figure 17. X-ray image of yellow dyed freshwater cultured pearls. The beads range from approximately 10 to 15 mm in diameter, while nacre thickness varies from <0.2 to >5 mm. Some of the beads show an additional drill hole. Image by Pierre Hardy.

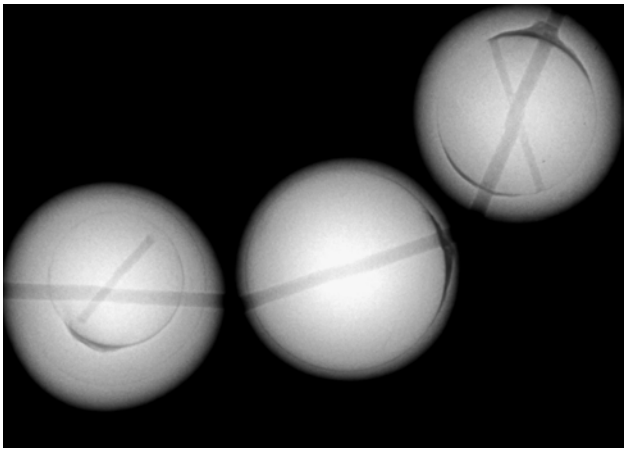

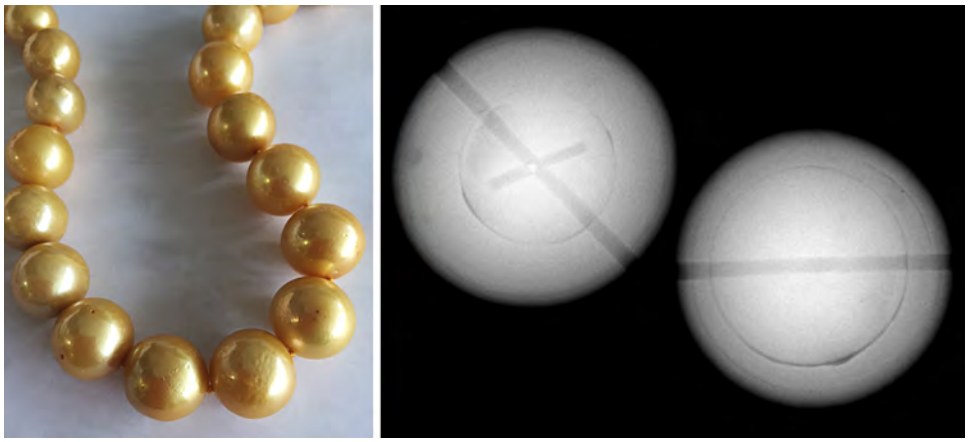

Figure 18. Left: Blemishes and dark color concentrations in cavities on the surface of dyed cultured freshwater pearls in a client-submitted necklace. Photo by Lore Kiefert. Right: An X-ray image of two pearls from the client necklace showing a clear bead. The left pearl displays an additional drill hole in the bead. Image by Pierre Hardy.

Zhou et al., "Update on the identification of dye treatment in yellow or 'golden' cultured pearls," Winter 2012 *G&G*, pp. 284–291), X-rays showing an additional drill hole through the bead in some of the pearls (figure 18, right), and the chemical composition of freshwater pearls (figure 19). This demonstrates the importance of staying informed on new developments in the market.

Lore Kiefert and Pierre Hardy
Gübelin Gem Lab
Lucerne, Switzerland

Figure 19. A plot showing the theoretical distribution of MnO vs. SrO in freshwater and saltwater pearls (after W. Gutmannsbauer and H.A. Hänni, "Structural and chemical investigations on shells and pearls of nacre forming salt- and fresh-water bivalve molluscs," Journal of Gemmology, *Vol. 24, No. 4, 1994, pp. 241–252). The red dots represent values for our reference collection necklace, the yellow dots the values for the client-submitted necklace.*

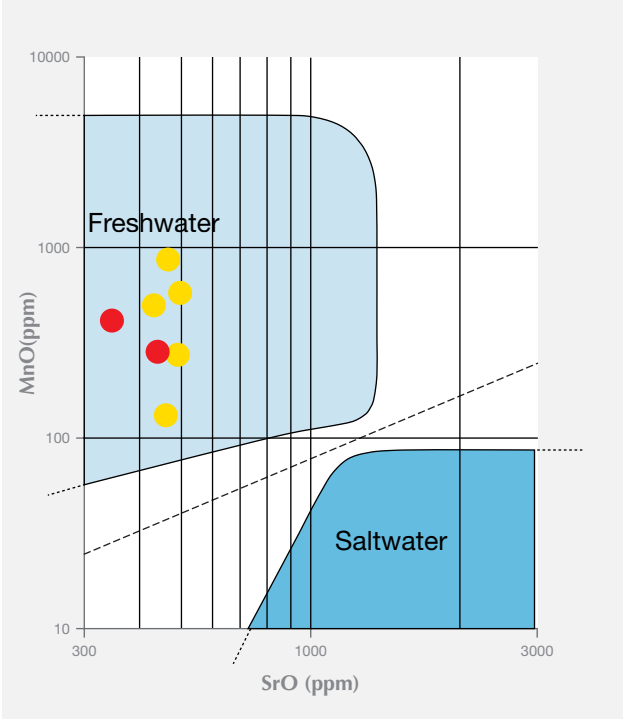

Colorful chatoyant glass. This year at the Tucson gem shows, this author encountered an interesting new product of chatoyant devitrified glass (glass that has converted to a crystalline material) marketed as "Starburst Stone." This material (figure 20) closely resembles the chatoyant glass known as Victoria Stone, which was developed in Japan by Dr. Satoyasu Iimori in the 1950s and produced for almost 40 years (http://victoriastone.sakura.ne.jp/JP-30-88-B.pdf).

John Bennett, in partnership with Artur Birkner (both based in Perth, Western Australia), began developing Starburst Stone in 2013, and this is the first year of commer-

Figure 20. Starburst Stone is a colorful new devitrified glass, reminiscent of the product once marketed as Victoria Stone. Photo by Kevin Schumacher; courtesy of Australian Rough and Tumble.

cially available production (approximately 100 kilograms). This devitrified glass is made from a chemical mixture that is cooled at a rate to facilitate nucleation and growth of dense networks of elongate lath-like crystals, and each batch of glass is colored by the addition of certain metals. Darker blues are achieved by adding cobalt, lighter blue by adding copper, and green by adding chromium to the glass mixture.

Standard gemological testing revealed properties consistent with manufactured glass. The RI was between 1.51 and 1.52 and varied slightly between the different colors tested. The average SG, measured hydrostatically, was 2.62. Raman analysis identified the devitrification product responsible for the chatoyancy as apatite, which was also responsible for the chatoyancy in the devitrified glass product known as Victoria stone.

Dark and light blue, green, and golden Starburst Stones are being manufactured, with additional colors in development. This new ornamental glass showing chatoyancy is a welcome addition to the gem trade. Those interested in the material once sold as Victoria Stone will certainly appreciate this very similar phenomenal glass product.

Nathan Renfro

TREATMENTS

Chalcedony beads coated with titanium nitride. Recently, RAG Gemological Laboratory in Turin received a necklace of unusual metallic appearance (figure 21). The beads showed irregular surfaces that were actually small geodes with shiny and well-shaped crystals. The cavities in the beads (figure 22) were reminiscent of the small quartz-lined holes that are often formed in agates and chalcedony. The necklace consisted of 29 beads ranging from 12.0 to 12.5 mm in diameter, with a total weight of 84 g.

Some loose opaque beads provided by the necklace's owner allowed us to measure the material's density. The value of 2.60 g/cm^3 was in agreement with chalcedony. RI was not measurable on the beads due to their rough surface. No fluorescence reaction was observed under long- or short-wave UV. A sawed bead revealed that the inner part consisted of light gray chalcedony without zonation (figure 23). Observation of the area near the drill holes showed discoloration and the true color of the underlying material. The coating on these grayish gold chalcedony beads in this necklace had an unusual composition. The unusual color and reflectivity of the external surface, clearly not inherent to chalcedony, warranted investigation.

The chemical composition of the bead was confirmed by energy-dispersive spectroscopy (EDS) using a Cambridge Stereoscan 360 scanning electron microscope equipped with an Oxford Inca Energy 200 EDS and a Pentafet detector for the determination of elements from boron to uranium. The results showed homogeneous composition on the sample surface, with titanium, oxygen, and silicon as major elements. No known compound of Ti and Si could explain the nature of the bead's surface or the goldish gray metallic tinge.

Figure 21. The beads in this necklace, ranging in diameter from 12.0 to 12.5 mm, have a submetallic luster and a gray tinge with goldish reflection. Small vugs lined with sparkling crystals are clearly visible in most of the beads. Photos by Raffaella Navone.

Low-acceleration voltage conditions in EDS analysis (4 kV) allowed us to enhance the X-ray emission yield of lighter elements and reduce the penetration depth of the electron beam at around 100 nm into the bead's surface. The EDS spectra at low acceleration voltage showed the presence of nitrogen and titanium, suggesting a coating of titanium nitride (TiN) on the beads. At low potential the electron beam could pass through the thin layer of TiN, so the oxygen and silicon peaks from the underlying silica were still visible in the spectra. We calculated the thickness of the coating by acquiring several EDS spectra at dif-

Figure 22. SEM imaging shows the small, well-shaped quartz crystals within the cavities. The crystal in the lower middle clearly displays the classic "flute" termination typical of quartz. Image by Emanuele Costa; field of view 1 mm.

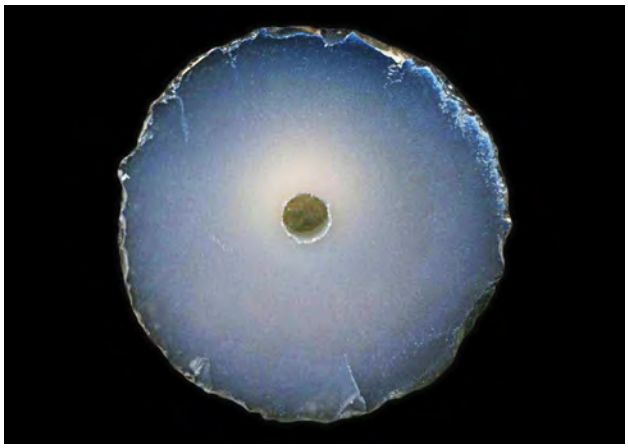

Figure 23. This sawed cross-section clearly demonstrates the homogeneity and light gray color of the chalcedony that constitutes most of the bead. Photo by Emanuele Costa.

ferent acceleration voltages (from 4 to 10 kV). The presence of the silicon peak even at 4 kV suggests that the electron beam could penetrate the layer and generate the signal through the TiN coat. The Casino software package evaluated the corresponding excitation depth of the electron beam using a Monte Carlo simulation. The calculated maximum thickness in our samples was less than 200 nm.

TiN is a very difficult material to analyze due to the presence of nitrogen, which is not always revealed with standard gemological techniques. To confirm the presence of a TiN film coating, we performed micro-Raman investigations. Spectra were obtained using a micro/macro Horiba LabRAM HR 800 (UV-Vis-IR) equipped with an Olympus microscope. The backscattered Raman signal was collected with a 50× objective and the 632.8 nm line of a He-Ne laser. The spectra were collected with multiple and repeated acquisitions to improve the signal-to-noise ratio, but even with these precautions the quality of the spectra is very poor due to the low intensity of Raman response from TiN. The Raman spectrum was recorded from 100 to 1200 cm^{-1}. Spectral manipulation such as baseline adjustment, smoothing, and normalization were performed using LabSpec 5 software. Band component analysis using the Fityk software package enabled the type of fitting function to be selected and specific parameters to be fixed or varied accordingly.

The Raman spectrum of a deposited TiN film is shown in figure 24. The Raman spectrum of the TiN layer can be fitted with Gaussian-Lorentzian peaks at 260, 330, 418, and 584 cm^{-1}. The spectrum is the same as those of TiN films reported, also with very poor quality, in the literature (Y.H. Cheng et al., "Substrate bias dependence of Raman spectra for TiN films deposited by filtered cathodic vacuum arc," *Journal of Applied Physics,* Vol. 92, 2002, pp. 1845–1849). Slight variations in peak position, shape, and relative intensity can be influenced by thickness (C.C. Chen et al., "Raman spectra of titanium nitride thin films," *Chinese Journal of Physics*, Vol. 32, No. 2, 1994, pp. 205–210), treatment time, and deposition temperature of TiN films (R.R.M. de Sousa et al., "Cathodic cage plasma deposition of TiN and TiO_2 thin films on silicon substrates," *Journal of Vacuum Science & Technology A, Vacuum, Surfaces and Films*, Vol. 33, No. 4, p. 041502), as well as substrate bias.

The TiN films also contained a small quantity of crystalline phase of TiO_2 (i.e., brookite) that was identified in the bead coating using Raman spectroscopy. There was a close match between the collected spectrum and that of brookite available in the RRUFF database (R050363). The association of TiN and TiO_2 films is well known and widely studied (de Sousa et al., 2015).

TiN deposition is widely used for the coating of small mechanical parts or tools, giving them a higher resistance to corrosion and scratching. Therefore, TiN films are essential for applications such as wear-resistant coatings, diffusion barriers, and optical coatings. The coating typically produces a golden hue, but other colors are also possible. Even though TiN films are common in industrial applications, this may be the first time such a coating has been reported in gemology.

Emanuele Costa and Erica Bittarello
Department of Earth Sciences, University of Turin
Raffaella Navone
RAG Gemological Laboratory, Turin

Figure 24. Raman spectrum of the TiN film in the 100–800 cm^{-1} region. The Raman bands are related to transverse acoustic (at 260 cm^{-1}), longitudinal acoustic (330 cm^{-1}), second-order acoustic (418 cm^{-1}), and transverse optical (584 cm^{-1}) modes of TiN, respectively (Cheng et al., 2002). The poor quality of the spectrum, despite a long collection time and enhanced sensitivity, is due to the faint response of the TiN to Raman investigation (as well as to the extreme thinness of the coating); it is comparable to the reported spectra available in the literature.

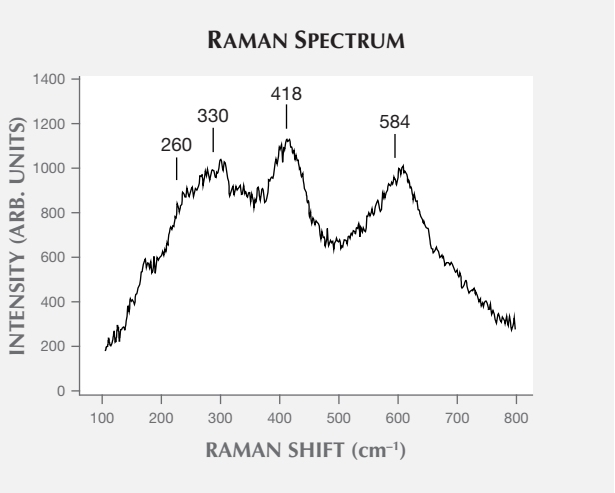

Figure 25. This 68 ct synthetic CZ shows three distinct hues in CIE standard illuminant F10 (left), CIE standard illuminant F9 (center), and CIE standard illuminant D65 (right). Photos by Robison McMurtry.

Tri-color-change holmium-doped synthetic CZ. Colored yttria-stabilized synthetic cubic zirconia (CZ) has been an attractive diamond substitute since the late 1970s (R.T. Liddicoat and J.I. Koivula, "Synthetic cubic stabilized zirconia," Summer 1978 *G&G*, pp. 58–60). The different colors seen in synthetic CZ are caused by the introduction of specific transition metal elements and rare earth elements (K. Nassau, "Cubic zirconia: an update," Spring 1981 *G&G*, pp. 9–19). At this year's Tucson Gem and Mineral Show, the authors obtained an interesting synthetic CZ rough that exhibited an unusual color-change behavior (figure 25). Unlike traditional color-change stones such as alexandrite, color-change corundum, and color-change garnet, this material did not exhibit different colors when illumination alternated between incandescent light and daylight conditions (approximated by CIE standard illuminants A and D65, respectively). Surprisingly, it showed three distinct hues in daylight/incandescent light (yellowish green), in fluorescent lighting corresponding to CIE standard illuminant F9 (green-blue), and in CIE standard illuminant F10 (purplish violet). One wafer with 3.32 mm thickness was polished and analyzed to understand this color-change phenomenon.

The wafer's chemical composition was obtained using a Thermo Fisher iCAP Q ICP-MS coupled with a New Wave Research UP-213 laser ablation unit. LA-ICP-MS analyses were performed in the same spot where the spectroscopic data was collected. Based on its calculated chemical formula of $Zr_{0.52}Y_{0.45}Ho_{0.02}Hf_{0.01}O_{1.79}$ (the formula is nonstoichiometric and calculated by forcing cations to 1 atom per formula), the wafer was a holmium-doped yttria-stabilized CZ (S. Gutzov et al., "High temperature optical spectroscopy of cubic holmium doped zirconia, $Zr_{0.78}Y_{0.21}Ho_{0.01}O_{1.90}$," *Physical Chemistry Chemical Physics*, Vol. 9, No, 4, 2007, pp. 491–496). Holmium was the only detected chromophore, at a concentration of about 7780 ppma.

Visible spectra were collected with a Hitachi U-2910 spectrometer with a 1 nm spectral resolution at a scan speed of 400 nm/min. The wafer's spectrum matched the holmium-doped CZ spectrum reported by Gutzov et al. (2007). The unusual color change under different illuminants can be qualitatively understood by examining figure 26. The violet and orange emission peaks of the F10 illuminant are not absorbed by Ho-doped CZ; however, there is significant absorption by holmium of the green emission peak for the F10 illuminant. This selective absorption of the F10 emissions creates a purplish violet color (figure 26, top). The F9 illuminant has more of a broadband emission,

Figure 26. The UV-Vis-NIR absorption spectrum of holmium-doped synthetic CZ is shown with the relative power distribution curves of CIE illuminant F10 (top), CIE illuminant F9 (middle), and CIE illuminant D65 (bottom).

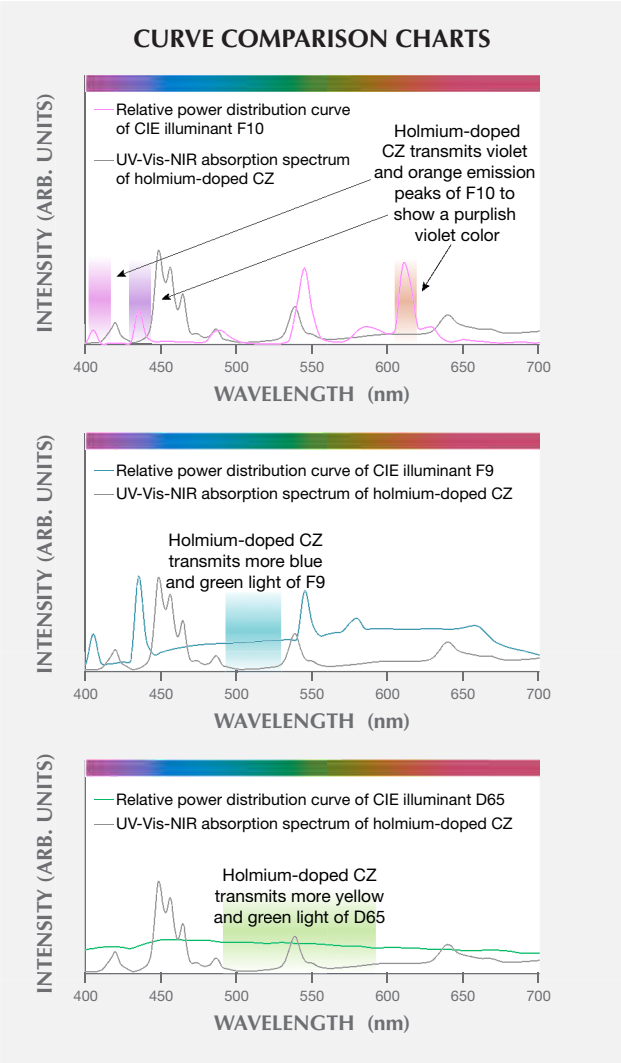

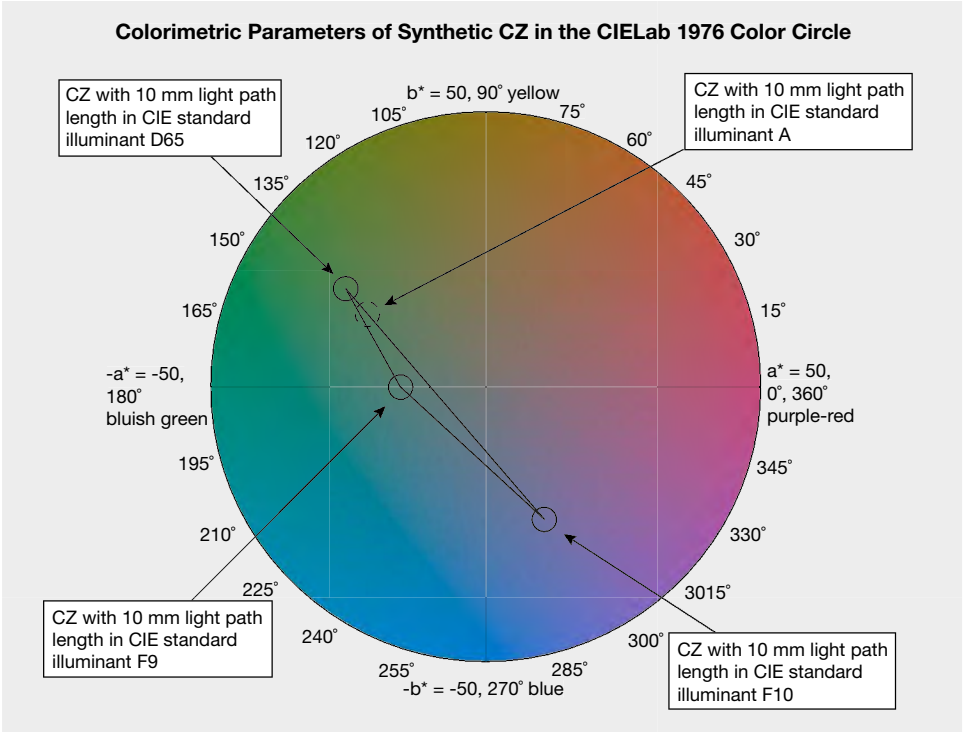

Figure 27. In the CIELab 1976 color circle, the color of holmium-doped synthetic CZ with 10 mm light path length changes from yellowish green in CIE standard illuminant D65 to blue-green in CIE standard illuminant F9 to purplish violet in CIE standard illuminant F10. The hue angle differences are 148.61° between D65 and F10, 34.96° between D65 and F9, and 113.65° between F10 and F9. The chroma differences are 4.73 between D65 and F10, 15.52 between D65 and F9, and 10.79 between F10 and F9. In contrast, the hue angle difference and chroma difference between D65 and A are 3.37° and 5.79, respectively.

which is unaffected by the strong but narrow absorption by holmium of green light at 540 nm. This results in a blue-green color under F9 illumination (figure 26, middle). The D65 illuminant is essentially a broadband emission roughly corresponding to a black body irradiator at 6500 K. Under D65 illumination, a yellowish green color is produced because of the strong absorption of blue light by holmium (figure 26, bottom).

The wafer's visible absorption spectrum was reflection-corrected by subtracting the absorbance value at 850 nm, where no chromophoric absorption is expected, from values for every other data point along the rest of the spectrum. The reflection-loss-corrected visible spectrum can then be used to quantitatively calculate the color of this material at a wide range of path lengths and under different lighting conditions (Z. Sun et al., "Vanadium- and chromium-bearing pink pyrope garnet: Characterization and quantitative colorimetric analysis," Winter 2015 *G&G*, pp. 348–369). There are large differences in the CIE L*, a*, b* color coordinates between D65, F10, and F9 (figure 27). One way to judge the quality of a color-change stone is to plot the color pair in the CIE 1976 color circle. Well-defined color-change pairings show a large hue angle difference, a small chroma difference, and high chroma values. The color coordinates of the material with a 10 mm light path length in D65, F9, and F10 were plotted in the CIE 1976 color circle shown in figure 27; calculated color panels for the illuminants were also placed alongside the faceted material (see online at http://www.gia.edu/gems-gemology/summer-2017-gemnews-holmium-synthetic-cz). The fact that the material shows three distinct hues in three different white lights makes it unique.

Ziyin Sun and Nathan Renfro
Aaron C. Palke
University of Queensland and Queensland Museum
Brisbane, Australia

ERRATA

1. The cover description on the Spring 2017 masthead page was incorrect. The cover photo actually shows a rose-cut diamond brooch, or "stomacher," from France that contains over 10 carats of diamonds set in silver over gold. It has a 1.90 ct center stone and three side stones totaling 5.05 ct. The photo is by Robert Weldon, courtesy of Lang Antique & Estate Jewelry (San Francisco, California).

2. In the Spring 2017 Gem News International section, the cultured pearl market update (pp. 124–126) showed a necklace featuring baroque South Sea cultured pearls (figure 23), which the caption described as "keshi." We would like to clarify that these are baroque, beaded (bead-cultured) pearls and cannot be true keshi pearls, which are pearls produced by a loose tissue piece, or in a pearl sac that previously held a bead or cultured pearl. We are grateful to Prof. Henry A. Hänni for this observation.

Micro-Features of Sapphire

Treated

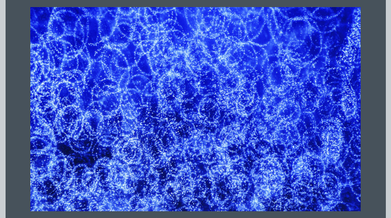

This treated blue sapphire shows "smoke ring" decorated dislocations, a result of beryllium diffusion. Field of view 1.26 mm.

Cobalt-doped lead glass is used to bind colorless corundum in this manufactured product. Blue color concentrations from the cobalt glass and gas bubbles are visible in the microscope. Field of view 7.84 mm.

A whitish altered mineral crystal and discoid tension crack with a healed fringe are proof of heat treatment in this metamorphic blue sapphire. Field of view 2.12 mm.

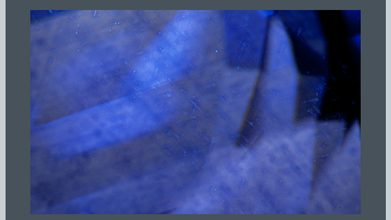

"Internal diffusion" occurs when rutile needles dissolve into the crystal lattice during heat treatment. Titanium from the rutile pairs with iron in the sapphire, increasing the blue color. Field of view 3.00 mm.

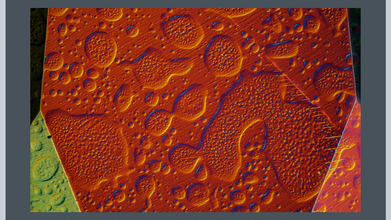

In this false-color image obtained using differential interference contrast microscopy, the surface of the sapphire shows obvious melt damage on the facet surfaces, proving heat treatment. Field of view 1.23 mm.

Natural

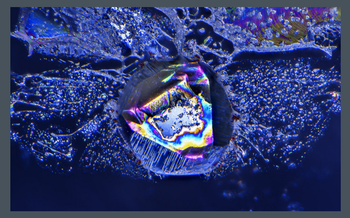

A negative crystal filled with carbonate and analcime minerals shows colorful thin-film interference in this untreated sapphire from Yogo Gulch, Montana. Field of view 1.28 mm.

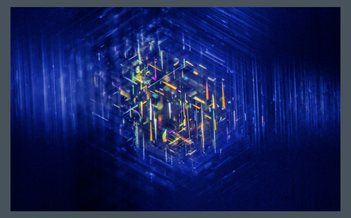

Exsolved rutile needles that are crystallographically aligned in the host Burmese sapphire cause the six-rayed star phenomenon displayed when the stone is viewed using a point light source. Field of view 1.90 mm.

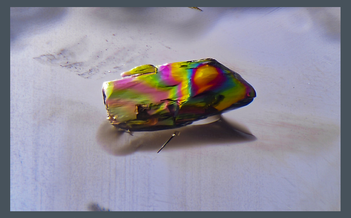

A mica crystal shows colorful interference colors in this sapphire from Sri Lanka, observed under plane-polarized light. Field of view 1.99 mm.

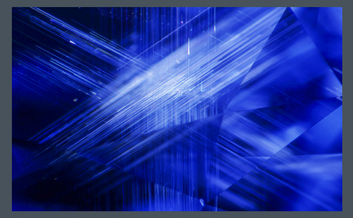

Elongate exsolution silk (i.e., tiny rutile needles) sometimes occurs in sapphires such as this unheated stone from Sri Lanka. Field of view 2.00 mm.

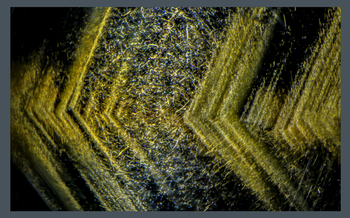

Exsolution mineral needles of rutile and ilmenite are responsible for the golden silk chevron pattern in this star sapphire from Australia. Field of view 2.58 mm.

Protogenetic carbonate crystals are often present in sapphires that form in carbonate-rich rocks such as marble, as seen in this sapphire from Madagascar. Field of view 2.90 mm.

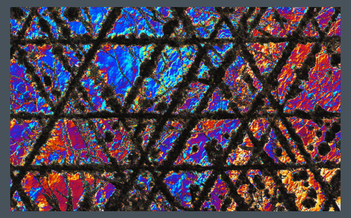

This sapphire from Montana shows an intricate pattern of dissolution along twinning planes when viewed using differential interference contrast microscopy. Field of view 1.44 mm.

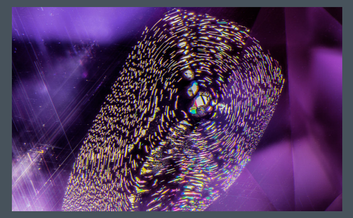

"Fingerprints" are arrays of tiny fluid or multiphase inclusions that result from the thermal healing of cracks in the growth environment, as in this Sri Lankan purple sapphire. Field of view 3.74 mm.

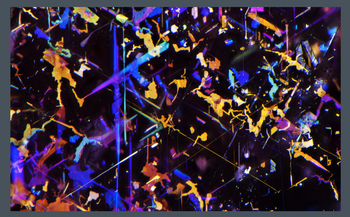

Exsolution rutile, shown in a Sri Lankan sapphire, often displays thin-film iridescence under oblique fiber-optic illumination. This "silk" can form elongate needles, arrowheads, and other shapes. Field of view 1.29 mm.

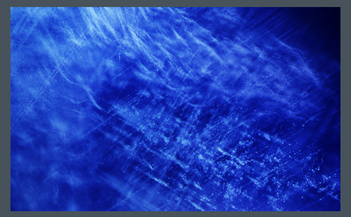

This Kashmir sapphire shows characteristic patterned clouds of tiny inclusions. These sapphires also contain clouds of nanoparticles that result in their highly prized velvety appearance. Field of view 1.90 mm.

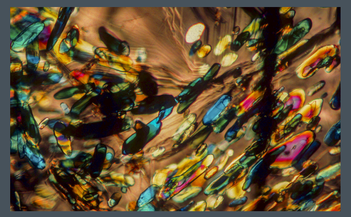

The kyanite inclusions in this Tanzanian sapphire are a rare sight. High-order birefringent colors make for a dramatic inclusion scene when observed using cross-polarized light. Field of view 3.00 mm.

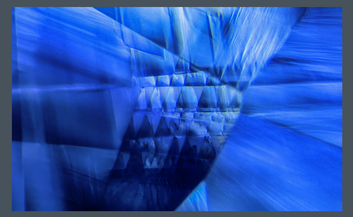

Complex growth patterns known as "graining" are often observed in sapphires. They are particularly evident in some sapphires from Madagascar, such as the example shown here. Field of view 4.00 mm.

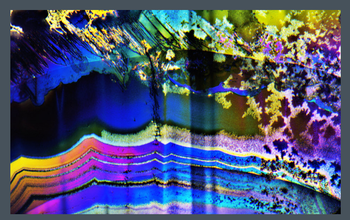

This Australian sapphire has a large crack filled with epigenetic iron oxide staining. Oblique fiber-optic illumination reveals colorful interference colors and agate-like banding. Field of view 1.43 mm.

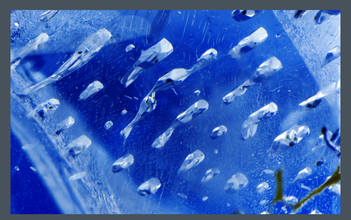

Negative crystals are a common inclusion in sapphires from metamorphic source rocks, such as this Sri Lankan specimen. They often contain a carbon dioxide fluid, graphite, and diaspore crystals. Field of view 2.62 mm.

Bright red pyrochlore crystals are often found in sapphires from Pailin, Cambodia. They sometimes occur as comet-tail inclusions trailed by light-scattering dislocations. Field of view 1.72 mm.

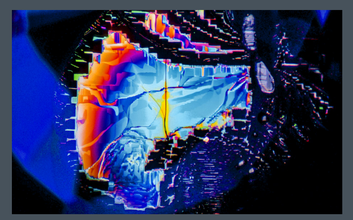

Partially healed cracks occasionally display vibrant interference colors resulting from thin-film interference, as in this Sri Lankan sapphire. Field of view 5.00 mm.

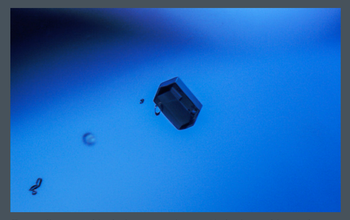

Tourmaline crystal inclusions are unique to Kashmir sapphires. When present, they are highly indicative of Kashmir origin. Field of view 4.69 mm.

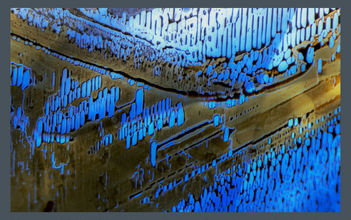

When partially healed cracks reach the surface of a sapphire, iron-rich fluids can deposit epigenetic matter such as limonite in the open spaces, as in this Thai sapphire. Field of view 1.42 mm.

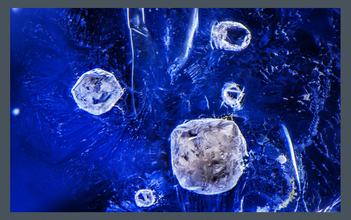

Brownish orange pyrope-almandine-grossular garnets are occasionally found in sapphires from Yogo Gulch and can help confirm this highly prized geographic origin. Field of view 2.04 mm.

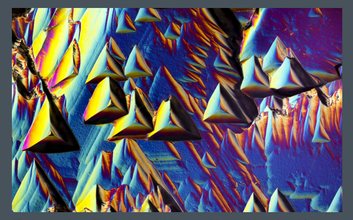

The lamprophyre dike that brought Yogo sapphires to the earth's surface partially dissolved the crystals' surface. Differential interference contrast microscopy shows crystallographic patterns and trigons. Field of view 1.44 mm.

Synthetic

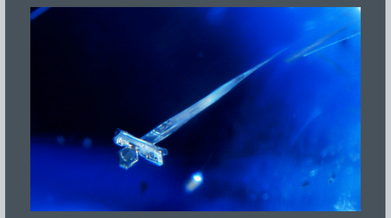

This platinum crystal inclusion in a synthetic sapphire shows a characteristic tapered morphology. This feature is diagnostic of flux growth, as in this Chatham synthetic sapphire. Field of view 1.72 mm.

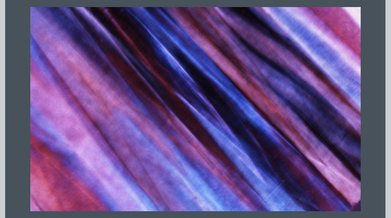

Plato-Sandmeier lines are resolved using cross-polarized light when viewed along the optic axis. They appear as shadowy subparallel striations in flame-fusion pink synthetic sapphire. Field of view 8.68 mm.

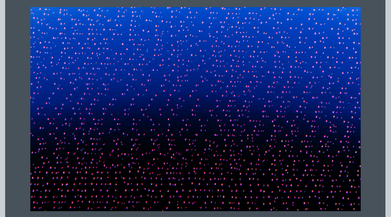

Minute pinpoint gas bubbles are arranged as near-parallel layers in this Czochralski-grown or "pulled" synthetic sapphire, as seen using modified Rheinberg illumination. Field of view 3.00 mm.

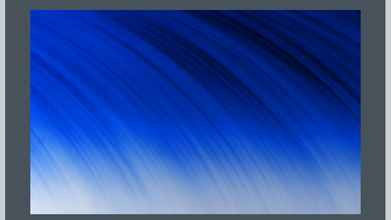

Curved color banding is diagnostic for flame-fusion material, as in this blue synthetic sapphire. Field of view 4.11 mm.

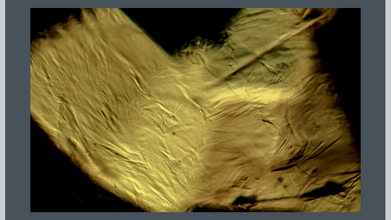

Hydrothermally grown sapphire is a rare synthetic gem material. Observed microscopically, it displays a diagnostic chevron or roiled growth structure, as seen in this yellow example. Field of view 3.00 mm.

This chart contains a selection of photomicrographs of natural, synthetic, and treated sapphires. It is by no means comprehensive. The images show the visual appearance of numerous features a gemologist might observe when viewing sapphires with a microscope.

Published in conjunction with Nathan D. Renfro, John I. Koivula, Jonathan Muyal, Shane F. McClure, Kevin Schumacher, and James E. Shigley (2017), "Inclusions in Natural, Synthetic, and Treated Sapphire," *Gems & Gemology*, Vol. 53, No. 2, pp. 213–214. Photomicrographs by Nathan D. Renfro, John I. Koivula, Jonathan Muyal, and Shane F. McClure.

GIA®